Turbulent mixing driven by variable density and transport coefficients effects

Giovanni Viciconte

Giovanni Viciconte. Turbulent mixing driven by variable density and transport coefficients effects. Other. Université de Lyon, 2019. English. NNT : 2019LYSEC035 . tel-02479835

HAL Id: tel-02479835
https://theses.hal.science/tel-02479835v1

Submitted on 14 Feb 2020

Numéro d'ordre NNT : 2019LYSEC35 Année : 2019

THÈSE de DOCTORAT DE L'UNIVERSITÉ DE LYON
opérée au sein de **L'ÉCOLE CENTRALE DE LYON**

ÉCOLE DOCTORALE n^o 162 : MEGA
Mécanique, Energétique, Génie civil et Acoustique
Spécialité : Mécanique des fluides

Soutenue publiquement le 18/11/2019, par

Giovanni Viciconte

Turbulent mixing driven by variable density and transport coefficients effects

---

Devant le jury composé de :

Mikhael GOROKHOVSKI	Professeur des Universités, École Centrale de Lyon	Président du jury
Luminita DANAILA	Professeur des Universités, Université de Rouen	Rapporteur
Patrick HENNEBELLE	Chercheur, CEA	Rapporteur
Bastien DI PIERRO	Maître de conférences, Université Claude Bernard Lyon 1	Examinateur
Robin J. R. WILLIAMS	Chercheur, AWE	Examinateur
Fabien GODEFERD	Directeur de Recherche, CNRS	Directeur de thèse
Benoît-Joseph GRÉA	Ingénieur de recherche, CEA	Encadrant de thèse

---

Abstract : This thesis is dedicated to the study of turbulent mixing in flows with variable density and non-uniform transport coefficients. We use a new direct numerical simulation (DNS) code based on a two-dimensional domain decomposition, capable of taking into account variable density and diffusive contributions. At first, we consider the case of turbulence in weakly-coupled plasmas under isotropic compression, which can experience a sudden dissipation of kinetic energy due to the growth of the viscosity coefficient due to temperature increase. In this case, in addition to DNS we use a spectral model based on the Eddy-Damped Quasi-Normal Markovian closure. We evidence the sensitivity of the flow dynamics to initial conditions for homogeneous isotropic turbulence and an inhomogeneous spherical turbulent layer. In the latter case, we find, also, the first hint of a sudden diffusion effect. The importance of initial conditions is also shown in the study of the variable density unstably stratified homogeneous turbulence. If the initial density contrasts are sufficiently strong, the large scales of the flow are modified with the consequent modification of the self-similar scaling laws. Finally, we consider an idealized configuration of inertial confinement fusion implosion, with both variable density and transport coefficients effects. During the compression, we evidence the competition between the plasma molecular diffusion, which is enhanced by the temperature increase, and the turbulent diffusion, which on the contrary decreases due to the increased viscous dissipation. In the last phase of the implosion, we highlight a sudden diffusion process, where compressed spherical mixing layers are quickly diffused.

Keywords : Mixing, turbulence, variable density flow, non-uniform transport coefficients, compression, plasma, inertial confinement fusion, DNS, EDQNM

Résumé : Cette thèse est consacrée à l'étude du mélange turbulent dans des écoulements à densité variable et à coefficients de transport non uniformes. Nous utilisons un nouveau code de simulation numérique directe (DNS) basé sur une décomposition bidimensionnelle du domaine, capable de prendre en compte la densité variable et les contributions diffusives. Dans un premier temps, nous considérons le cas de la turbulence dans les plasmas faiblement couplés en compression isotrope, qui peuvent subir une dissipation soudaine d'énergie cinétique due à la croissance du coefficient de viscosité par une augmentation de la température. Dans ce cas, en plus des DNS, nous utilisons un modèle spectral basé sur la fermeture Eddy-Damped Quasi-Normal Markovian. On démontre la sensibilité de l'écoulement aux conditions initiales pour une turbulence homogène isotrope et une couche sphérique turbulente. Dans ce dernier cas, nous trouvons aussi la première indication d'un effet de diffusion soudain. L'importance des conditions initiales est également mise en évidence par l'étude de la turbulence homogène stratifiée instable à densité variable. Si les contrastes de densité initiale sont suffisamment forts, les grandes échelles de l'écoulement sont modifiées avec pour conséquence la modification des lois d'échelle des états autosemblables. Enfin, nous considérons une configuration idéalisée d'implosion de fusion par confinement inertiel, avec des effets de densité variable et des coefficients de transport. Pendant la compression, nous mettons en évidence la compétition entre la diffusion moléculaire du plasma, qui est renforcée par l'augmentation de la température, et la diffusion turbulente, qui au contraire diminue en raison de la croissance de la dissipation visqueuse. Dans la dernière phase de l'implosion, nous mettons en évidence un processus de diffusion soudaine, où les couches de mélange sphériques en compression sont rapidement diffusées.

Mots-clés : Mélange, écoulements à densité variable , coefficients de transport non-uniformes, compression, plasma, fusion par confinement inertiel, DNS, EDQNM

Acknowledgments

Après ces trois ans de thèse il y a beaucoup de gens à remercier pour une raison ou une autre. Je vais commencer par remercier les deux rapporteurs de cette thèse, Luninita Danaila et Patrick Hennebelle pour avoir accepté ce rôle, pour leurs rapports et leurs commentaires ainsi que leurs questions. Je veux aussi remercier Mikhael Gorokhovski pour avoir accepté d'être le président du jury ainsi que pour les questions et discussions qui ont suivi la présentation de mes travaux. I would also like to thank Robin Williams to have agreed to be part of the jury and for his very informative comments and observations which helped to define the final form of this manuscript. Enfin, je voudrais remercier Bastien Di Pierro, tout d'abord pour avoir accepté de faire partie de ce jury et ensuite pour tes suggestions concernant la résolution de l'équation de Poisson. Sans l'idée du GMRES, il y a deux ans, cette thèse aurait été très différente. Bien sûr, si tout s'est bien passé pendant le doctorat, c'est en grande partie grâce à mes deux encadrants, Fabien Godeferd et Benoit-Joseph Gréa. J'ai beaucoup appris grâce à vous, à la fois sur les aspects techniques et théoriques mais aussi sur des autres aspects tels que la rédaction et la présentation orale. Fabien, malgré la distance, tes conseils, toujours ponctuels et appréciés, m'ont facilité la tâche et tes observations n'ont jamais manqué d'améliorer le travail. Last but not least, Benoît-Joseph. Tout d'abord, je tiens à te remercier pour ta confiance. Tant au début, quand tu m'as recruté en thèse, que pendant ces trois ans, quand tu m'as laissé suivre mes inspirations tout en restant toujours présent pour me guider. Puis, de ta rigueur, tu m'as appris la démarche scientifique et «l'ostinato rigore». Et, pour finir, je veux aussi te remercier pour tous les allers-retours que tu as effectué afin de venir me voir, tu as dû parcourir tant de kilomètres au cours de ces trois années. Je veux aussi remercier l'ensemble des membres de "l'équipe turbulence" : Oliver Soulard, Jerome Griffond, Antoine Llor et Denis Souffland pour avoir écouté mes présentations et pour toutes les discussions et conseils qu'ils aient pu me procurer tout au long de ma thèse. Et aussi les physiciens de "équipe Plasma" avec qui j'ai pu interagir : Philippe Arnault, Jean Clérouin et Nicolas Desbiens.

Je remercie l'ensemble de stagiaires et doctorants (ou thésard ou thésitif, à vous de choisir le nom que vous préférez) et post-doctorants avec qui j'ai partagé ces trois ans de thèse : Ulysse, Tristan, Loïc, Luis, Alexandre, Robinson, Augustin, Jean-Baptiste, Raphael, Estelle, Paul, Gerome, Nicolas, Guillaume, Richard, Lucas, Jean-Cedrik, Marie, Grégoire et Mathieu .

En particulier, j'aimerais remercier toutes les personnes du "thesarium", Régis, Aloïs, Luc, Jean-Baptiste, Thibaud, Nils, Yoannis et Gautier.

En particulier je veux remercier Thibaud, même avec tes chansons et tes blagues, cela a toujours été un plaisir de partager tous ces moments avec toi pendant deux ans.

Gautier, je te remercie pour toutes les discussions (sérieuses et moins sérieuses), même

si tu as souvent (sinon toujours) tort, cela a été un plaisir de discuter avec toi.
Paul "7h-19h" Lafourcade, Dr Prat a déjà tout dit dans ses remerciements, donc il ne me reste plus qu'à te remercier de m'avoir toléré durant ces trois années, me donnant un exemple quasi impossible à égaler.
Et enfin Dr. Raphael Prat (oui, je l'ai fait exprès d'oublier la ë, deux fois), avec qui j'ai partagé la totalité de ces trois ans de thèse (je sais que c'était un honneur pour toi). Un merci particulier pour tes appels pour la "pause" de 9 heures, tes conseils en informatique, pour ta bonne humeur, pour toutes les soirées (un gros merci à Sonia, aussi) que tu as organisé et enfin pour avoir su apprécier l'endroit le plus beau du monde a sa juste valeur.

Une pensée particulière pour Aloïs, Augustin et Jean-Baptiste, qui commencent la deuxième année de thèse, profitez-en, parce que en troisième année entre la rédaction et autres choses, vous allez beaucoup plus vous amuser.
E visto che questa tesi é la fusione di tre lingue, (un italiano che ha fatto il dottorato in Francia e scritto la tesi in inglese), voglio chiuderli in italiano.
Da ormai nove anni ho lasciato casa mia e pian piano mi sono spostato verso nord, prima a Torino poi a Lione e infine a Parigi. In questo periodo e in tre città diverse, ho avuto la possibilità di conoscere persone che senza dubbio, e maniera diretta e indiretta, hanno contribuito alla realizzazione di questo lavoro. A partire dai coinquilini torinesi, Donato, Carmine e Marco, quelli di Lione, Alberto, Richard et Mayeul, il gruppo degli italiani "Lionesi", fino agli amici dell'ALJT di Versailles e della box H78 di Montigny le Bretonneaux. Tutti voi avete avuto un ruolo importante e per questo vi saró sempre riconoscente.

Durante questi viaggi e trasferimenti, una cosa é rimasta sempre costante. Il sostegno della tutta la mia famiglia. In particolare, un grazie dal più profonde del cuore va ai miei genitori, Antonio e Elisa, mia sorella Angela e zio Frank, che mi supportano/sopportano da ormai ventotto anni e che in questo periodo non mi hanno mai fatto mancare niente. Nonostante la mancanza di comunicazione e le mie scelte annunciate sempre a cose fatte ("a proposito..."). Senza di voi non solo non sarei arrivato a questo punto, ma non sarei la persona che sono. Le parole non sono sufficienti per esprimere tutta la mia gratitudine, ma tuttavia dovrete accontentarvi.
Alla fine di questa avventura, una parte dei pensieri va a quelli che non ci sono più, in particolare un ringraziamento va a zio Antonio, che non ha potuto assistere alla conclusione di un percorso che abbiamo fatto insieme per otto anni. Una delle cose che mi é mancata e che mi mancherà di piú è la classica telefonata pre-esame, ed è per questo, caro compare, che questa tesi è dedicata a te.

Table des matières

List of Symbols

t	Time
x_i	Position
ω	Vorticity
$\mathbf{u}$	Velocity vector
ρ	Density
P, p	Pressure
∇	Gradient operator
$\nabla\cdot$	Divergence operator
$\nabla\times$	Curl operator
τ	Viscous stress tensor
h	Perturbation amplitude
λ	Perturbation wavelength
g	Acceleration
$\mathcal{A}_t$	Atwood number
δ	Mixing zone size
α	Rayleigh-Taylor mixing zone growth rate
Δu	Shock impulsion
Kn	Knudsen number
E_B	Magnetic energy density
E_{kin}	Kinetic energy density
B	Magnetic field
μ_0	Magnetic permeability constant
ν	Kinematic viscosity
$\mathcal{D}$	Diffusivity
μ	Dynamic viscosity
C_M	Ratio between the turbulence and compression time scales
M_T	Turbulent Mach number
U_i, u_i	Velocity components
$*^B$	Base component of a field $*$
$\tilde{*}$	Variable $*$ in the moving reference frame
$*_0$	Initial value of variable $*$
$\mathcal{S}_{ij}$	Deformation tensor
$\mathcal{S}(t)$	Compression rate
Λ	Compression parameter
Π, π	Reduced pressure

Θ, θ	Logarithm of the density divided by a reference density
N	Buoyancy frequency
$\langle * \rangle$	Volume average of a quantity $*$
$\overline{*}$	Tangential average of a quantity $*$ (depending on r only
L	Mixing zone width
$\mathcal{H}$, G	Self-similar functions
T	Temperature
r	Radial position
T	Mass fraction
n	Number density of particles
k_B	Boltzmann constant
κ	Temperature diffusion coefficient
ϕ	Diffusive flux
M	Atomic mass
Z	Ionization number
FT	Fourier transform
k	Wavenumber
Δt	Time step
K^n	Krilov subspace of size n
$E(k)$	Kinetic energy spectrum
$E_\theta(k)$	Scalar variance energy spectrum
$E\langle u_3\theta\rangle(k)$	Vertical flux spectrum
$\mathcal{K}$	Integrated kinetic energy
Re	Reynolds number
Cp	Compression number
ℓ_I	Integral length scale
β	Growth rate of USHT one-point statistics
Fr	Froude number
$\langle \theta\theta \rangle$	Volume averaged scalar variance
$\langle \theta u_3 \rangle$	Volume averaged vertical flux
b_{ij}	Anisotropy coefficient
Γ	Coupling parameter
h_0	Characteristic length scale of temperature gradient
c	Speed of sound
Ξ	Molecular mixing parameter
r_{01}	Radial position where averaged value of the CH mass fraction reaches a value of 0.01
r_{50}	Radial position where averaged value of the CH mass fraction reaches a value of 0.5

r_{99}	Radial position where averaged value of the CH mass fraction reaches a value of 0.99
$C_{l,\mathcal{K}}$	Kinetic energy angular power spectrum
$C_{l,\mathcal{K}}$	Scalar variance angular power spectrum
q_l	Non dimensional wavenumber

List of Acronyms

RT	Rayleigh-Taylor	4
RM	Richtmyer-Meshkov	6
DNS	Direct Numerical Simulation	9
RANS	Reynolds-Averaged Navier-Stokes	11
BHR	Besnard-Harlow-Rauenzahn	11
ICF	Inertial Confinement Fusion	12
NIF	National Ignition Facility	13
LMJ	Laser Megajoule	13
ALE	Arbitrary Lagrangian Eulerian	14
MHD	Magnetohydrodynamics	15
DT	Deuterium-Tritium	17
CH	Carbon-Hydrogen	17
EDQNM	Eddy Damped Quasi-Normal Markovian	19
HIT	Homogeneous Isotropic Turbulence	19
ILES	Implicit Large Eddy Simulations	25
USHT	Unstably Stratified Homogeneous Turbulence	25
LES	Large Eddy Simulations	36
RDT	Rapid Distortion Theory	27
GMRES	Generalized Minimal Residual	43
SSP	Strong Stability Preserving	43
FFT	Fast Fourier Transform	46
FFTW	Fastest Fourier Transform in the West	46
PDFFT++	Parallel Three-Dimensional Fast Fourier Transforms	47
VD	Variable Density	103
B	Boussinesq	103
PDF	Probability Density Function	119
PIJ	Pseudo-Ion-in-Jellium	122

Chapitre 1

Introduction

Contents

1.1 Turbulent mixing

Mixing is an irreversible process that increases entropy, decreases Gibbs free energy and exergy [Tailleux 2009], and brings homogenization to the molecular level. According to Eckart (1948), mixing in fluids can be thought of as a process in three steps :

1. An initial or entrainment phase, where large volumes of the mixed materials are visible, steep gradients are found at the interface between these regions, which are otherwise smooth. This phase is dominated by the large scales coherent structure of the flow.
2. An intermediate or stirring phase, when distortion caused by advection, provokes a rapid increase in the extension of interfacial surfaces, with the final results to increase the mean value of the initial gradients.
3. A final or diffusion phase where the gradients disappear, and the fluid becomes homogeneous.

Mixing can be laminar or turbulent, with noticeable differences in the stirring phase. The main features that distinguish turbulent from the laminar mixing are the large range of flow scales and the associated greater interfacial surface, which permits to the molecular diffusive effect to proceed more effectively.

Although laminar mixing present interesting application [Erwin 1978], especially in the case where high viscosity prevents the onset of turbulence [Ottino and Chella 1983], the most common mixing processes are driven by turbulence, which is present in many natural and engineering phenomena, with length scales and Reynolds numbers spanning 20 orders of magnitude [Ottino 1990].

Many natural phenomena present turbulent mixing as a crucial factor, from the atmosphere dynamics [Monin and Obukhov 1954], where it is involved in the transport of heat from the subtropical latitudes to the polar regions, to the oceans circulation [Polzin et al. 1997, Mashayek et al. 2017] where it helps sustain the deep global ocean overturning circulation. Also, turbulent mixing has a significant impact on astrophysical processes, from stars [Baglin 1972] to interstellar medium of galaxies [Slavin et al. 1993] where turbulent mixing layer are substantial contributors to interstellar radiations. Moreover, applications involving combustion [Pitz and Daily 1983, Reitz 2002], chemical industry reactors [Nienow et al. 1997], hypersonic propulsion systems [Parent et al. 2002] and inertial confinement fusion [Haines et al. 2014a] are all concerned in some measure by the understanding of this fundamental problem.

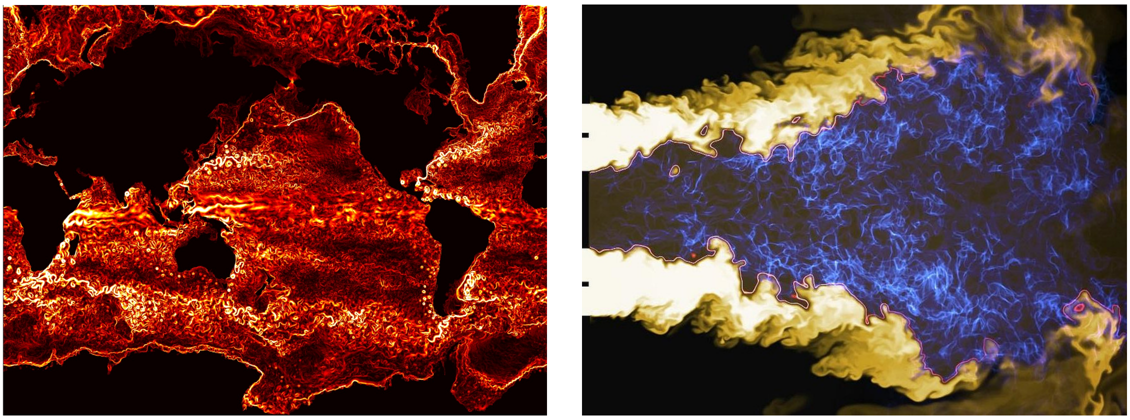

(a) (b)

Figure 1.1 – (a) Numerical simulation of turbulent mixing in the ocean (NASA/Chris Henze) (b) Numerical simulation of the turbulent mixing with chemical reaction in a burner. (Universität Duisburg-Essen)

Dimotakis (2005), in his review, distinguishes between three levels of possible turbulent mixing. Level-1 is the simplest and one of the widely studied ; it involves the mixing of a passive scalar, which does not act back on the flow dynamics. In Level-2, the mixing is coupled to the dynamics of the flow, such as in cases driven by buoyancy forces. The Level-3 mixing produces changes to the fluid, e.g., chemical composition change due to combustion, that in turn modify the flow dynamics.

1.1.1 Buoyancy driven mixing

A classic example of level-2 mixing, which is of interest in this thesis, is caused by buoyancy-driven flows. A case occurring when a fluid with non-uniform density distribution is subjected to pressure gradients or external accelerations, in both stably or unstably stratified configuration, *i.e.* the density of the fluid respectively increases or decreases in the direction of the force.

If one takes the vorticity, ω, equation for flow with non uniform density and constant body forces [Tennekes and Lumley 1972],

$$\partial_t \omega + \mathbf{u} \cdot \nabla \omega = \underbrace{\frac{1}{\rho^2} \nabla \rho \times \nabla p}_{\text{Baroclinic term}} + \underbrace{\omega \cdot \nabla \mathbf{u} - \omega \nabla \cdot \mathbf{u}}_{\text{Vorticity stretching}} + \underbrace{\nabla \times \frac{\nabla \cdot \tau}{\rho}}_{\text{Vorticity diffusion}} \tag{1.1}$$

where $\mathbf{u}$ is the velocity field, ρ the density, p the pressure and τ the viscous stress tensor. The main difference with non-stratified flows is the generation of vorticity from the baroclinic effects, resulting from misalignment between pressure and density gradients.

The stability criterion for non-uniform density fluid can be a tricky question, given the vast difference in possible configurations. For instance, if one considers incompressible flows with a constant pressure gradient, imposed by a constant acceleration, and the density as the only non-uniform quantity, the stability can be determined by the direction of pressure and density gradients.

Otherwise, if the acceleration varies in time, even if it is always in the opposite direction of the density gradient, the configuration can be destabilized by the Faraday instability [Faraday 1831, Gréa and Adou 2018].

Another example is the double diffusion process, due to the simultaneous presence of different scalar species [Huppert and Turner 1981], *i.e.* concentration and temperature. Finally, discarding the incompressible constraint, one has to take into account the entropy [Lighthill 2001].

Stably stratified mixing Within the framework of buoyancy-driven mixing, a great deal of study is devoted to turbulence in stably stratified medium [Fernando 1991]. This field is of particular importance because oceans, lakes, and atmospheres and many astrophysical bodies are stably stratified. This stable stratification would imply in principle that vertical motions are inhibited, imposing a limit to the vertical exchange of matter. Nevertheless, these exchanges happen thanks to the help of turbulent mixing. In stably stratified fluid, the transition to a turbulent state can be caused, for example, by shear flows generating Kelvin-Helmholtz or Homlboe waves, or the breaking of internal waves generated by gravitational restoring forces acting on vertically displaced fluid [Lamb 2014].

Unstably stratified mixing The simplest case of unstable stratification is obtained when density gradients and the acceleration have the opposite direction. In this configuration, the flow evolution and the related mixing mechanism are determined by the pressure gradient imposed by the acceleration profile. If the acceleration is constant, the flow is subjected to the Rayleigh Taylor instability, while if the acceleration is an impulsion, such as a shock wave, the Richtmyer-Meshkov instability takes place.

1.1.1.1 Rayleigh-Taylor

The Rayleigh-Taylor (RT) instability has been individually investigated by Rayleigh (1882) and Taylor (1950), who studied the interface of a heavy fluid of density ρ_2, on top of a light fluid of density ρ_1. It is one of the most common instability mechanism. For example, it is the reason why when one turns a glass over, the water inside falls, even if the atmospheric pressure should be able to keep the water inside the glass. This instability has been the object of extensive study, and different review articles are available [Sharp 1983, Kull 1991, Boffetta and Mazzino 2017, Zhou 2017a]. Studies on this problem have identified three main phases in the evolution of the flow : linear, nonlinear, turbulent.

Linear The theory describing the first phase of the instability was proposed by Rayleigh (1882) and Taylor (1950) who studied the case of incompressible flows. They assumed that the amplitude, h, of the perturbations was small compared to their wavelength, λ. This hypothesis allows to linearize the equations and neglecting the effects of viscosity or surface tension they obtained :

$$h = h_0 \exp\left(t\sqrt{g\frac{2\pi}{\lambda}\mathcal{A}_t}\right) \tag{1.2}$$

where g is the acceleration and $\mathcal{A}_t = \frac{\rho_2-\rho_1}{\rho_2+\rho_1}$. So that the dispersion relation can be written as

$$\zeta^2 = g\frac{2\pi}{\lambda}\mathcal{A}_t, \tag{1.3}$$

which allows us to observe that when acceleration and Atwood number are positive, the flow is unstable, $\omega^2 > 0$, for all perturbation wavelength, and the growth rate increase unbounded when $\lambda \to 0$. When viscosity, surface tension, and compressibility are considered, the dispersion relation is modified. Chandrasekhar (1961) shows that viscosity cannot stabilize the flow, it dampens the small wavelengths growth rate, which nevertheless stays always positive, imposing a maximum to the growth rate for a wavelength $\lambda_{max} > 0$. On the contrary, the same author demonstrates how surface tension is capable of stabilizing an unstable configuration for sufficiently small wavelengths, which nonetheless remains unstable if perturbations have sufficiently long wavelengths. Regarding compressibility, Livescu (2004) proves that it can have both stabilizing and destabilizing effects. In the linear phase, the initial perturbations develop without interacting with each other. However, at some point at the end of this first phase, they reach an amplitude comparable with their wavelength, and nonlinear interactions begin to be relevant, so that linear arguments are no longer valid.

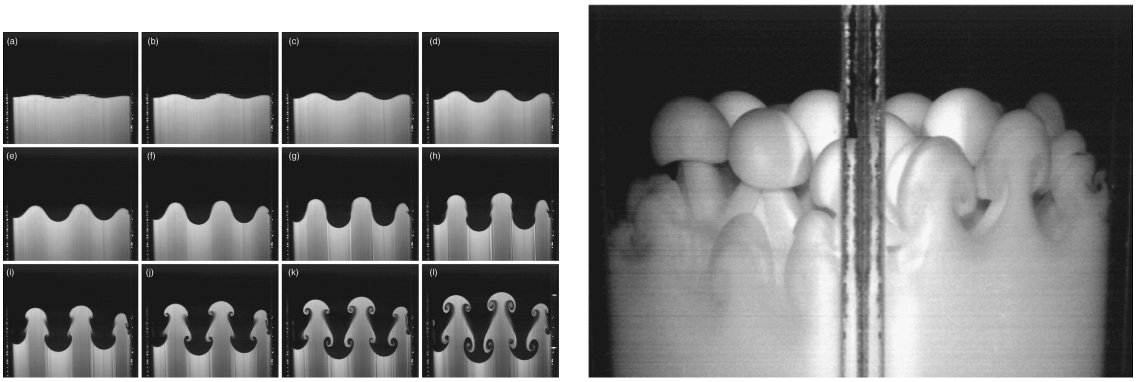

(a) (b)

FIGURE 1.2 – (a) Sequence of images relative to the development of Rayleigh-Taylor instability in the linear and nonlinear phases. The Atwood number is 0.15. (b) Three-dimensional visualization of the structure of the bubbles with the same initial condition of (a). From Wilkinson and Jacobs (2007)

Non-linear When the flow transition in the nonlinear phase, we observe a first qualitative difference depending on the Atwood number. For small density contrasts, $\mathcal{A}_t \ll 1$, the evolution of the light and heavy fluid are similar, and we observe an interpenetrating bubble. When $\mathcal{A}_t \sim 1$, the evolution is asymmetric, the lighter fluid moves into the heavy fluid in the form of bubbles while the heavy fluid in the form of spikes. In this regime Youngs (1984) found that the mixing zone size $\delta = 2h$ has a quadratic dependence on time

$$\delta = \alpha_i \mathcal{A}_t g t^2 .$$

Where α is the mixing zone growth rate. Discussion around this value has gone for 30 years, due to contrasting results obtained in experiments and numerical simulations. A combined effort resulted in the α-group collaboration [Dimonte et al. 2004], which proved that numerical simulation and experiment converged to two different results, with the second value twice as much as the first. This incoherence was connected to the large scale perturbations and confinement effects in the experimental set-up that were not taken into account into numerical computations.

Nowadays discussions around the parameter alpha are still ongoing, for instance Zhou (2017a) in his review after collecting the value of α published after the α-group paper, found a spread of its value depending on Atwood number and initial conditions wavelengths (lower values for short initial wavelength, higher values for large initial wavelength).

Turbulence At the end of the nonlinear phase, the bubbles and spikes begin to interact with each other creating a turbulent mixing regime. This phase addressed by Boffetta and Mazzino (2017) in a recent review paper, present all the characteristic of turbulent mixing from multi-scale properties to the development of the Kolgomorov cascade [Cabot and Cook 2006].

1.1.1.2 Richtmyer-Meshkov

The work on the Richtmyer-Meshkov (RM) instability begins with the theoretical analysis of Richtmyer (1960) and the experimental confirmation of the results by Meshkov (1969). In principle, this instability can be considered as a particular case of RT instability with an impulsion acceleration. As for the Rayleigh-Taylor, this instability has been the object of extensive study and reviews [Brouillette 2002, Zhou 2017a].

As in the case of RT, also for Richtmyer-Meshkov, we can divide the evolution into three phases : linear, nonlinear, turbulent, which can be observed in Figure 1.3.

Linear The theory for the linear phase of the instability was derived by Richtmyer (1960), who assumed that the amplitude, h, of the perturbations was small compared to their wavelength,λ, without the effects of viscosity or surface tension. With these hypotheses we obtain :

$$\frac{dh}{dt} = h_0 \Delta u \frac{2\pi}{\lambda} \mathcal{A}_t \tag{1.4}$$

where Δu is the shock impulsion, h_0, and $\mathcal{A}_t = \frac{\rho_2-\rho_1}{\rho_2+\rho_1}$ are the initial amplitude and the Atwood number just after the shock has impacted the interface. The numerical solution of (1.4) shows that in this phase, the growth of the perturbation is linear in time, unlike the exponential growth of the RT. Moreover, the interface is unstable for every value of the Atwood number, even the negative [Brouillette 2002]. The effects of viscosity and surface tension were considered by Mikaelian (1993), who shows that viscosity induces damping of the perturbation while surface tension oscillations. Short wavelength perturbations oscillate faster but are more damped ; longer-wavelength perturbations oscillate slower and are less damped.

As for the Rayleigh-Taylor, in the linear phase, the initial perturbations develop without interaction with each other, but when their amplitude has increased sufficiently, the nonlinear phase takes place.

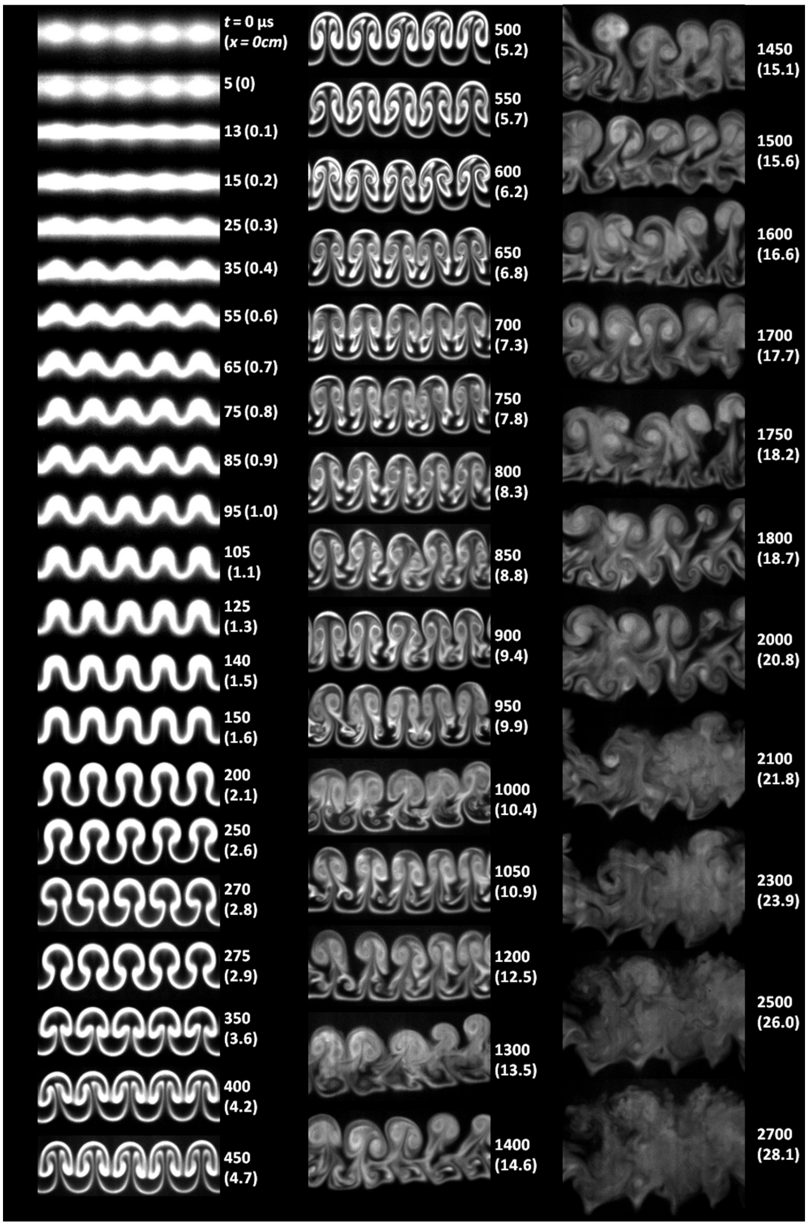

FIGURE 1.3 – Time evolution of Richtmyer-Meshkov instability with an Atwood number of 0.5 and incident shock Mack number of 1.21. The initial condition is on the top-right position. The time is noted near every image, together with the distance traveled in parentheses. These images display the complete evolution of a Richtmyer-Meshkov mixing zone from the initial development to the final turbulent state. Orlicz et al. (2013)

Non-linear We observe the asymmetry between the interpenetration between the two fluids. The heavy fluid tends to the formation of spikes, whereas the light fluid organizes as bubbles. Some analytical tools allow studying this phase for single-mode perturbation [Brouillette 2002]. However, usually, the wavenumbers of the initial perturbation span many orders of magnitude. Also, as the RM flow develops, the Kelvin-Helmholtz instability develops, which further complicates the computational task. Ultimately, a three-dimensional turbulent mixing zone develops on the interface.

At the end of the non-linear stage, the time evolution of the overall mixing zone size h follows power-law $\sim t^{\theta}$ with values of θ ranging from 0.3 to 1, (see Zhou (2017a) for a collection of published values). As for the α coefficient in the self-similar phase of a Rayleigh-Taylor mixing zone, there was a debate on the value of the exponent θ, addressed by the θ-group work [Thornber et al. 2017]. They determined that the growth rate exponent is $\theta = 0.292 \pm 0.009$, in good agreement with prior studies ; however, the exponent is decaying slowly in time.

Turbulence At the end of the nonlinear phase, the bubble and spikes begin to interact with each other creating a turbulent regime. The mixing between the two fluid is intensified, and the interface is no longer visible. Also, the mixing zone size continues to follow the evolution law $\sim t^{\theta}$.

1.1.1.3 Open problems

From the short review on Rayleigh-Taylor and Richtmyer-Meshkov instabilities, we observe similarities in the development and evolution of the flow together with differences. The instability mechanisms are the same, and for both cases, the discussion on the dependence of the long-time flow evolution on certain factors is still ongoing. Here we present some open questions : What is the effect of initial conditions ? How well can these instabilities mix ? Is the anisotropy imposed by the acceleration maintained in the smallest scale of turbulence ? What happens if the acceleration is inverted during the development of the instability ? What is the effect of the Atwood (and Mach) number on the flow ?

Initial condition (IC) influence One of the questions that arise from the study of RT and RM turbulence is about the role of IC, and this question seems to be still open to debate.

In the Rayleigh-Taylor context, this dependence has been used to justify the difference between experimental and numerical studies.
For instance, Ramaprabhu et al. (2005) show that initial perturbation wavelength may influence the late time self-similar evolution, depending on the wavelength. With short wavelengths [Ramaprabhu et al. 2005, Youngs 2013], it seems reasonable to assume a loss of the initial perturbation proprieties, whereas long-wavelengths impose

a dependence on the initial conditions. Banerjee and Andrews (2009) using Direct Numerical Simulation (DNS) concluded that RT mixing has a strong dependence on IC. Whereas the results of Soulard et al. (2015) prove that there is no permanence of large eddies for RT turbulence, which at late times is dominated by nonlinear interaction with loss of information of IC.

For Richtmyer-Meshkov, the influence of initial conditions is likely to be significant in most applications, in particular for the nonlinear and turbulent phases. For example, [Budzinski et al. 1994] prove that changes in the initial interface shape give different patterns during the evolution of the flow.[Thornber et al. 2010] found a dependence on initial conditions for the self-similar exponent θ, which seems to depend, similarly to the RT case, to the range of scale used for the initialization.

Moreover, from a theoretical point of view Soulard et al. (2018), evidence that the initial condition can influence late time flow evolution. They prove the permanence of large eddies, in case of low Atwood number, relating the self-similar growth rate of the turbulent mixing zone to the infrared slope of the velocity spectrum.

Mixing rate The discussion about how the quantification of mixing is another subject of debate, with different quantity proposed (see Zhou (2017a), for instance). One that is widely used is molecular mix fraction Θ [Youngs 1984], which can be linked to α [Gréa 2013].

The value reported for RT turbulence [Ramaprabhu et al. 2005, Youngs 2003; 2013] varies from 0.68 to 0.8. The reasons for the discrepancy are to be found in the dependence on the initial perturbation, with long initial wavelengths that result in a low value of the mixing parameter.

The same quantity can be measured in the RM mixing layer. The range of Θ from numerical simulation goes from $0.3 - 0.8$ [Thornber et al. 2010, Oggian et al. 2015]. This difference can be attributed to differences in initial interface thickness and shape, as well as the characteristics of the initial perturbations, in particular, the range of scale used.

Anisotropy Both RT and RM have a preferential direction imposed by constant or impulsive acceleration so that the question about the anisotropy of the flow has to be addressed.

In general, for RT flows, the large turbulent scales are anisotropic due to the action of gravity, but the flow becomes isotropic at small scales in the core of the mixing layer. However, there are still discussions open, for instance, Livescu et al. (2009) found anisotropy for the largest and smallest scales where the buoyancy effects continue to be significant due to the cancellation between nonlinear transfer and viscous dissipation. Furthermore, Gréa et al. (2016b) show that the level of anisotropy is not very sensitive to initial energy and buoyancy spectra.

For the RM case, Soulard et al. (2018) prove large scales keep their initial anisotropy during the flow evolution, implying that the return to isotropy of the turbulent mixing zone is only partial. These results confirm the observation of Thornber et al. (2010), Lombardini et al. (2012). This anisotropy, is, of course, more significant in the direction of the shock propagation, with the ratio of the component turbulent kinetic energy (TKE) in the parallel and perpendicular directions that tends towards a constant value.

Acceleration inversion and demixing for RT The assumptions made about the direction of the acceleration with respect to the density gradient are not always valid in real applications, for instance, in astrophysical contexts like the Crab nebula [Ebisuzaki et al. 1989]. In this case, one has to reconsider the theoretical results under the light of the variable acceleration, which changes direction during the flow evolution. One of the consequences, for example, is that the expression of the mixing zone width self-similar evolution is no longer valid. When the sign of the acceleration is reversed, there is a partial demixing for miscible fluids and complete demixing for immiscible fluids.

Numerical simulations by Ramaprabhu et al. (2013) show that a deceleration between two acceleration phases destroys the spikes bubbles structures changing the flow topology. It increases the molecular mixing and the rate of return to isotropy within the mixing layer, retarding the following growth towards self-similarity. However, Burlot (2015) shows how the final state of the mixing zone depends on the time between the two acceleration phases.

The role of the Atwood number For RT, as the Atwood number increases, the self-similar constant α increases. On the contrary, the late times' value of the mixing parameters shows no influence on the At. While the small-scale anisotropy may be more persistent for higher Atwood number, which can be explained by the fact that the effects of gravity that cause the anisotropy increase with the Atwood number (for a complete discussion see the corresponding section in Zhou (2017a)).

In the RM case, the self-similar exponent θ seems to have a little dependence on the At, while an increase in Atwood number increases the time needed to reach the self-similar state, and it has the opposite effect of the molecular mixing [Thornber et al. 2010].

Mach number For the RM, the dependence on Mach number has been studied. The experimental results of Weber et al. (2014b) show the relative insensitivity of Θ to the Mach number, which has been confirmed by the numerical simulation of Lombardini et al. (2012).

Others effects Rotation [Scase et al. 2017], chemical reactions [Chertkov et al. 2009], and magnetic field [Chandrasekhar 1961] are among the effects that are sometimes present in applications where they can influence the evolution of the buoyancy-driven instability.

1.1.2 Converging Geometry

Rayleigh-Taylor or Richtmyer-Meshkov instability have been mostly studied in a planar geometry, a simplified setting useful to understand the fundamental driving processes. However, in some applications, for instance, inertial confinement fusion compression, the interface geometry can be spherical or cylindrical, also called converging geometry.

These configurations were investigated by Bell (1951) and Plesset (1954) for inviscid potential flow and by Chandrasekhar (1955) who considered the effect of viscosity. They found that, in this situation, the perturbation growth is modified by pure geometrical effects, independent of the density of the fluid.

1.1.3 Modelling

All the fundamental studies using experiment or high fidelity numerical simulation are usually performed to understand the phenomena involved in RT and RM. The objective of the studies is to find the main ingredients of these buoyancy-driven flows and create meaningful models for real-life problems, where the range of spatial scales exceeds the current numerical capabilities. Multiple models with different levels of complexity have been proposed during the years. The first and most simple is the buoyancy-drag model [Zhou 2017a], which computes the evolution of the amplitudes of the mixing region. It is essentially an equation of motion that balances the inertia, buoyancy, and drag forces.

The Reynolds-Averaged Navier-Stokes (RANS) models are the second step in complexity. They are a class of method which attempt to analyze and characterize flows at high Reynolds number, with well-developed turbulence, which constitutes one of the shortcomings of RANS modeling for mix calculations in RT and RM. They are not designed to compute the production of turbulence from instabilities (Zhou (2017b) in his review discusses different RANS models with corresponding merits and shortcomings).

Multiple models have been proposed during the years, $K - \epsilon$, Besnard-Harlow-Rauenzahn (BHR), Reynolds stresses, multifluid, spectral with an increasing capability to reproduce the complex phenomena of the mixing.

All the proposed models have some free parameters that have to be fixed. The problem that arises at this point is that usually, they are calibrated to reproduce self-similar states. However, nothing ensures that they can reproduce the transient phase, which is more important from an engineering viewpoint since the self-similar state is never reached in real applications. For instance, Gréa et al. (2016a) demonstrated for different initial conditions, how different mixing models are capable of getting the self-similar state but behave very badly and differently in the transient period.

1.1.4 Why is buoyancy-driven mixing important ?

Concerning the hydrodynamic instabilities that we have discussed, the main reason that has driven the efforts over the years has been the quest to understand the role of turbulent mixing in Inertial Confinement Fusion (ICF) implosions.

For many years this has been identified as having a detrimental effect on inertial confinement fusion target. The inward acceleration, coupled with the fact that the density increases with the radius, is the basic context for the onset of baroclinic instability. Moreover, these instabilities are only a part of the phenomena involved in an ICF implosion, where plasma, radiation, and kinetic effects play significant roles. Furthermore, the fact that this is a context of high energy density (HED) physics makes experimental studies to understand the driving mechanisms even more complicated. Besides, numerical simulations used in the context of ICF are costly in terms of computational resources and usually take into account all physical phenomena that occur during an implosion. This makes it difficult to understand the role of hydrodynamics in this context. That is why, in this thesis, we propose to study mixing in a simplified framework, where we consider the effect of transport coefficients variation in an idealized ICF target and the effect of variable density in the homogeneous context.

The remainder of this chapter is organized as follows : After an introduction to the inertial confinement fusion in section 1.2, we discuss the radiation hydrodynamics simulation used to investigate ICF implosion and the assumption made to arrive at the idealized cases studied in this thesis. After this discussion, the following two sections are dedicated to the review of variable viscosity and variable density turbulence, the two main effects that are conserved in the idealized case. Finally, we discuss the plan of the thesis.

1.2 Inertial confinement fusion : an introduction

The idea behind ICF [Atzeni and Meyer-ter Vehn 2004b] is to compress a fuel usually composed by a mixture of hydrogen isotopes deuterium, D, and tritium, T, to incredible pressures, around $\sim 100\,Gbar$, densities $\sim 50\,gcm^{-1}$, and temperature $\sim 10\,keV$. Then the objective is to burn the fuel in a short time, $\sim 50\,ps$, in which inertia keeps the fuel confined. High power radiation, usually provided via multiple high-intensity lasers, is the external source that provides the energy that drives the compression.

In the "direct drive" approach [Betti and Hurricane 2016], the lasers are focused directly on the spherical target. The rapid heating causes vaporization of the shell materials and a consequent inward implosion, compressing the fuel. Moreover, it creates a shock wave, which further increases the fuel temperature and pressure and results in a self-sustaining burn.

Another approach, currently employed at the National Ignition Facility (NIF) and Laser Megajoule (LMJ), is the "indirect drive" method [Lindl 1995], in which the lasers heat the inner walls of a gold cavity containing the target, which is uniformly irradiated by X-rays. This radiation heats the outer surface of the spherical shell, causing a high-speed ablation and consequent implosion of the capsule in the same way as in the "direct drive." These two approaches are schematically represented in Figure 1.4.

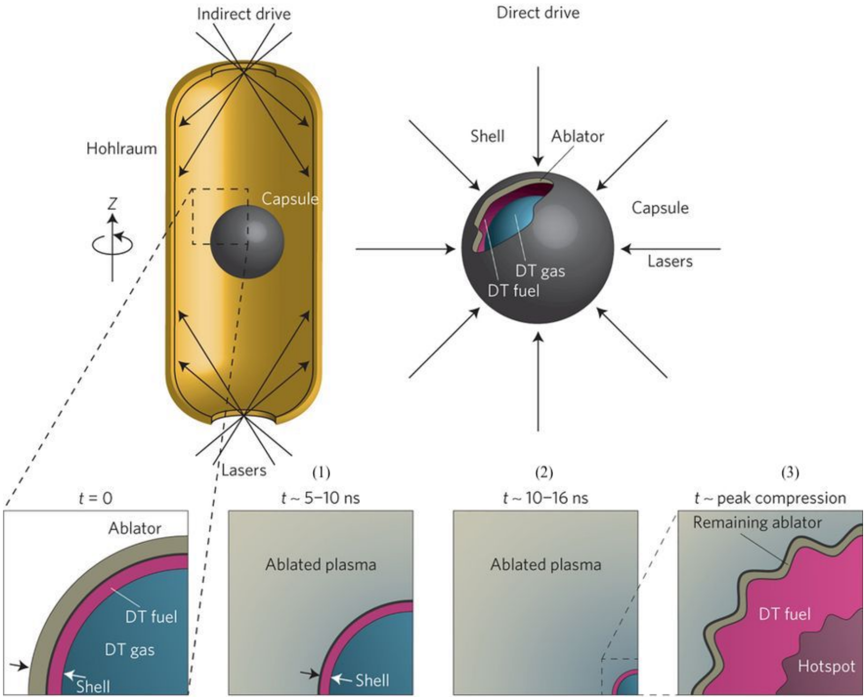

FIGURE 1.4 – Schematic of the indirect drive (upper left) and direct drive (upper right) approaches in inertial confinement fusion experiments. The four images at the bottom describe schematically different stages in the implosion. In the last image on the right, the effects of hydrodynamics instability are evidenced. From Betti and Hurricane (2016)

Following Atzeni and Meyer-ter Vehn (2004b) we can schematically divide the implosion in three phases :

1. Deposition of the energy by laser beams and ablation of the outer materials.

2. Implosion of the capsule that reaches the extreme thermodynamic condition required for the fusion.
3. Ignition of the fuel and hot spot generation.

The numbers correspond to those of the images at the bottom of Figure 1.4.

Once the laser has deposited the energy via direct or indirect drive, the outer surface of the ablator starts to vaporize and expand outwards, forcing the inner part of the capsule shell to move inwards, starting the compression. The pressure that is acting on the ablator/fuel interface at this stage is around 100 Mbar, with an implosion velocity of 300 km/s. At the same time, as the inwards implosion of the ablator, a strong shock intensified by the spherical convergence propagates towards the center of the capsule. When it reaches the center, the shock is reflected and starts to travel outwards, when at some point encounters the inwards moving shell, the shell is decelerated. It is at this point that a significant part of the kinetic energy is transformed in internal energy, and the density increases considerably. At the same time, the sequence of shock and the compression heat the gas to a very high temperature, that is, a hot spot has formed. The hot-spot temperature is around 10 keV with a pressure of the order of 100 Gbar and density around 50 g/cm^3 . At this point, one expects a sudden, around 50 ps, rise in temperature up to 100 keV that would signal the ignition.

During the compression, perturbation to this idealized configuration may alter the dynamics of the implosion, modifying the desired energy output or preventing the fusion at all. These perturbations, which may develop at the ablator/fuel interface, see 1.4(c), are amplified by the Rayleigh-Taylor instability and may lead to the mixing of cold, dense material in the hot-spot plasma, de facto decreasing the possible yield of the fusion.

1.3 ICF hydrodynamic simulations

ICF implosions are usually modeled using radiation hydrodynamics codes, that are capable of accounting for effects coming from all the sources involved in the compression processes from the laser deposition to radiation effects [Marinak et al. 2001]. From the hydrodynamic point of view, since they deal with highly compressible materials, these codes usually employ Arbitrary Lagrangian Eulerian (ALE) scheme with artificial viscosity to stabilize shock, or other compressible hydrodynamic formulations [Cabot and Cook 2006], and they can solve 1D [Vold et al. 2015], 2D [Gittings et al. 2008] or 3D [Marinak et al. 2013] problems. In the case where the fuel reaches temperatures such as the mean free path of the ions become comparable to the size of the hot-spot, a kinetic description has to be used [Hoffman et al. 2015].

The parameter that determines if one can use the continuum mechanics approach to investigate a particular fluid problem is the Knudsen number, Kn, the ratio between the mean free path of the fluid constituents and the characteristic size of the problem. Usually, large imploding targets as the one used at the NIF, kinetic effect seems to be negligible. For instance, this can be verified using the expression given by Molvig et al. (2012), that gives Knudsen numbers of $\sim 10^{-2}$ at bang time, so that the continuum assumption is wholly justified. This assumption would not be verified in other ICF implosions, for instance, is smaller capsules such as the ones used in OMEGA experiments [Rinderknecht et al. 2014b].

Another question that has to be addressed is related to the Magnetohydrodynamics (MHD) effects. There exists the possibility of self-generating magnetic field during the compression due to the asymmetry of the implosion [Igumenshchev et al. 2014]. These fields can have intensity up to 10^4 Tesla, in the last phases of the implosion [Walsh et al. 2017]. The magnetic energy density is

$$E_B = \frac{B^2}{\mu_0} \sim 10^{14} \frac{\text{kg}}{\text{m s}^2}.$$

This value has to be compared with typical kinetic energy density for an ICF implosion that is :

$$E_{kin} = \frac{1}{2}\rho v^2 \sim 10^{17} \frac{\text{kg}}{\text{m s}^2}.$$

The ratio between magnetic and kinetic energy density is $\sim 10^{-3}$ so that MHD effect can be neglected.

ICF simulations are performed mainly to reproduce implosion experiments in order to explain different than expected behaviors and also to suggest possible improvements in the quest to obtain nuclear fusion with desired yields. In recent years, computations mostly concentrated on understanding the impact of various perturbation sources on the evolution of the spherical compressed flow. The investigation considered both low-foot and high-foot implosions, which are differentiated by the shape of the driving laser pulses. In particular low foot implosion have low compression velocities ($320 - 330$ kms^{-1}) but higher convergence ratios, the ratio between the initial and final diameter of the target, ($40 - 45$), compared to the high foot case where compression velocity can reach 380 kms^{-1} but with low convergence ratios of ~ 35. In Figure 1.5, the effects of the various perturbations sources are apparent. From the tent perturbation at the capsule poles to fill tube defects and the roughness of the ablation front that grows during compression. While the results for the two cases are different, it is evident the presence of denser colder matter that reaches the center at the bang time in the two simulations. This is mainly caused by the tent perturbation growth and the hydrodynamic instabilities due to shocks and the strong inward acceleration.

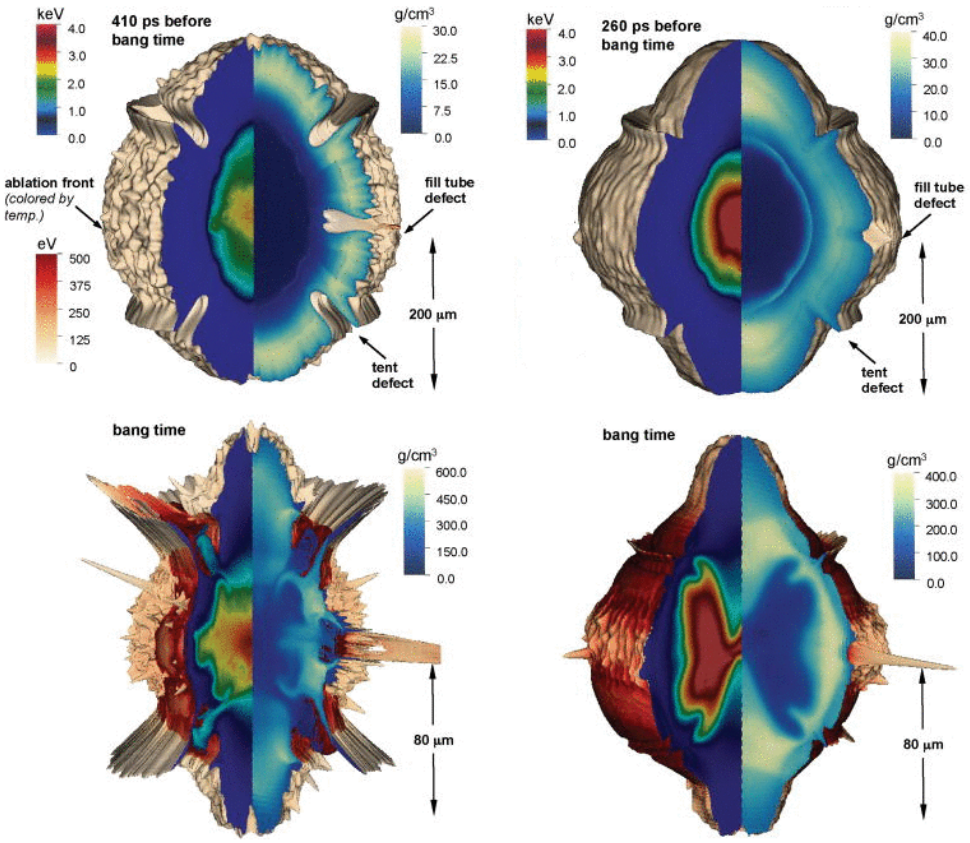

FIGURE 1.5 – Temperature and density contours of low-foot (left) and high-foot (right) implosions simulation of an indirect drive inertial confinement fusion target using the radiation hydrodynamic code HYDRA [Marinak et al. 2001]. The top images show the computational results for a radius of $200\mu m$ while the bottom images the contours of temperature and density at the bang time. Figure adapted from Clark et al. (2016).

1.4 From ICF radiative hydrodynamics simulation to idealized simulation framework

At the moment, many results of ICF implosions simulation exist [Clark et al. 2015; 2016, Weber et al. 2014a; 2017]. They have been used to study multiple aspects of actual ICF experiments. These simulations take into account all the physical phenomena that are important in an ICF context (radiation, alpha heating, alpha burn). However, usually, they did not take into account transport coefficients, although recently Weber et al. (2014a) have shown how important it is to take into consideration viscosity to have a realistic representation of the small scale behavior of the flow in the hot-spot. Clark et al. (2016) in the simulations presented in section 1.3 take into consideration the viscosity, but they do not consider the effect of molecular diffusivity.

The different physical mechanisms in action during an ICF compression are challenging to disentangle if one uses the full simulations just described. A solution is to employ idealized theoretical frameworks allowing to isolate one phenomenon from the others, and in that way, have a deeper comprehension of the involved physics. As an example, in Figure 1.6, we show different levels of idealization for an inertial confinement fusion implosion. For instance, one can discard all the nuclear physics effects and radiative effects, leaving a problem of a spherical mixing zone between a heavy and light material under compression. Furthermore, one can make the hypotheses that locally, the spherical mixing zone could be approximated by a plane mixing layer under the effect of vertical acceleration, leaving with a Rayleigh- Taylor problem. The last step would be to consider the center of the planar mixing zone where inhomogeneous effects are negligible so that one can study homogeneous problems.

In this thesis, we have chosen to study two of the three idealized configurations depicted in Figure 1.6. In particular, we choose to study the compression of spherical turbulent mixing zones composed by Deuterium-Tritium (DT) and Carbon-Hydrogen (CH) in the plasma state, taking into consideration plasma transport coefficients. At the same time, we have used homogeneous turbulence simulations whereby we investigated compressed turbulent plasma and the unstably stratified homogeneous turbulence using the variable density approximation.

The next two sections are dedicated to introducing the two main subjects of this thesis, namely : variable viscosity effects in turbulent flows and variable density turbulence.

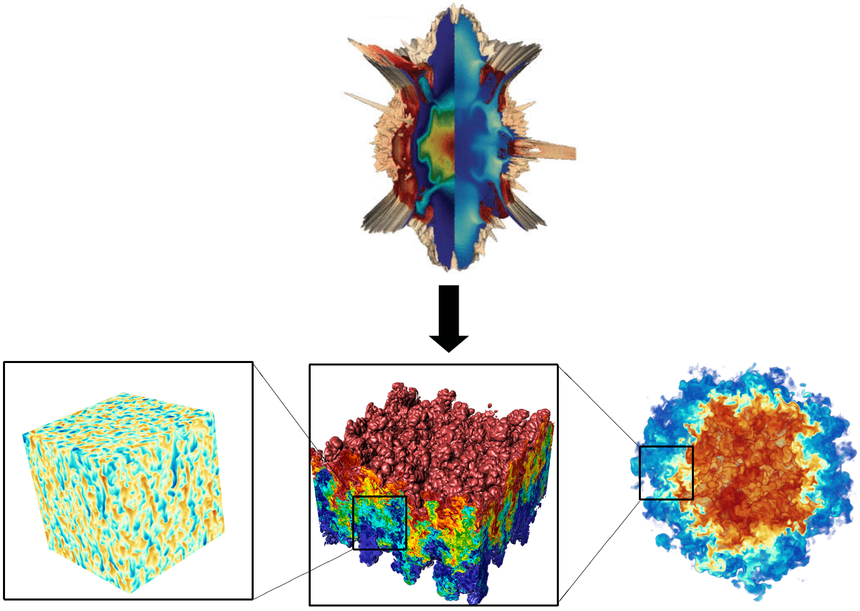

FIGURE 1.6 – Different levels of idealization to study inertial confinement fusion implosion.

1.5 Variable viscosity flows

Variable viscosity flows, are not specific of the ICF context, but on the contrary represent an important part of real-life flow. From geophysics [Turner and Campbell 1986, Christensen and Harder 1991] to Magnetohydrodynamics (MHD) [Pantokratoras 2008, Makinde et al. 2016], from re-entry vehicle aerodynamics [K. Reddy and Sinha 2009] to blood vessel simulation [Layek et al. 2009], from oil industry applications [Joseph et al. 1997] to rising plumes [Carey and Mollendorf 1980].

Viscosity variations, in many real cases due to viscosity stratification, play an essential role in the stability of parallel flows. For instance, Govindarajan and Sahu (2014) have reviewed these effects. They highlight the importance of viscosity variations even at high Reynolds numbers, which can alter the stability of the flow.

Most of the cited works are either theoretical or numerical. One of the first experimental investigations on the nature of flows with different viscosities is due to Campbell and Turner (1985). They studied the injection of a fluid of low viscosity ν_1 in a host fluid with a higher viscosity ν_2 and higher density. When the ratio ν_2/ν_1 is close to one, classical turbulent mixing phenomenology is found, while when this viscosity ratio increases, at fixed Reynolds number, the mixing is less and less effective until a critical viscosity ratio when it is inhibited.

Talbot (2009) conducted an experimental study using a propane jet issuing into an air/neon mix. This setting was chosen because of the lower viscosity of propane with respect to the air/neon mix. Moreover, it allows the author to investigate the effects of viscosity variations in fluid with almost similar densities. These results were then confronted with ones obtained for a case where the jet and the host fluid have identical viscosity, air into air. Talbot (2009) proves that the efficacy of the mixing, is higher for the jet with variable viscosity with respect to the constant viscosity case, with the same initial momentum. Moreover, he shows how viscosity variations influence velocity signals, shown in Figure 1.7 for the two jets, at a position with the same local Reynolds number. In particular, from Figure 1.7, we can see that the turbulence developed by the variable viscosity jet has higher frequency fluctuations, suggesting the presence of finer structure with respect to the constant viscosity jet.

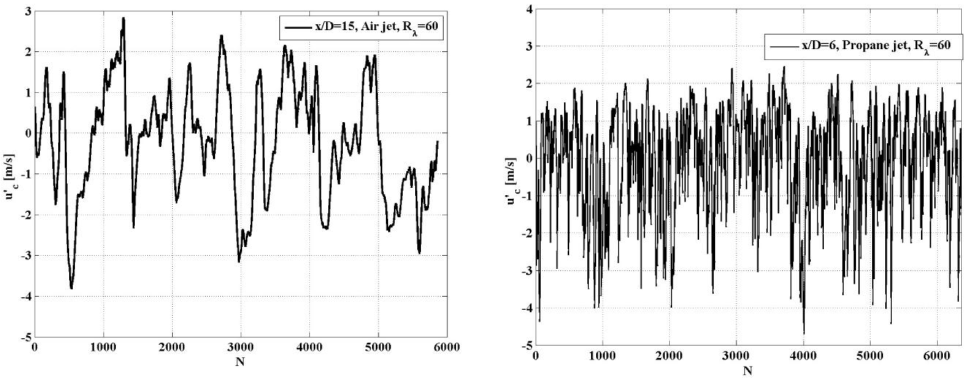

FIGURE 1.7 – Instantaneous velocity signals on the axis of : (Left) a jet with the same viscosity of the issuing fluid, (right) jet with lower viscosity of the issuing fluid. From Talbot (2009)

Concerning more fundamental aspects of variable viscosity turbulence, most of the investigations were concentrated on the Homogeneous Isotropic Turbulence (HIT) decay. One of the first works by Lee et al. (2008) used direct numerical simulation of mixing of two fluids with different viscosities showing that the Taylor postulate, independence of dissipation from viscosity, is still valid in this type of fluid mixtures. Gréa et al. (2014) using DNSs and the Eddy Damped Quasi-Normal Markovian (EDQNM) spectral model show that in the case where viscosity depends linearly on a scalar field, the effective viscosity is proportional to the viscosity fluctuations variance and it is lower than the mean viscosity. A recent investigation by Gauding et al. (2018) confirmed the results of Lee et al. (2008), and they show how in variable viscosity HIT there is an increased level of small scales intermittency due to the presence of smaller scales in the low viscosity region of the flow. Moreover, they demonstrate the presence of an inverse energy cascade contribution, from small to large scales, due to the viscosity gradients. The possible effects of viscosity on the large scales of turbulence is evidenced by Voivenel et al. (2017), who investigated the entrainment of a jet issuing in a more viscous ambient fluid, found that variable viscosity affects the dynamics of the flow at all scales. Moreover, Danaila et al. (2017) using the same experience as Voivenel et al. (2017) showed how the similarity assumption for the jet is valid in regions where the viscosity is uniform but is not valid anymore in regions where the flow has intense viscosity gradients.

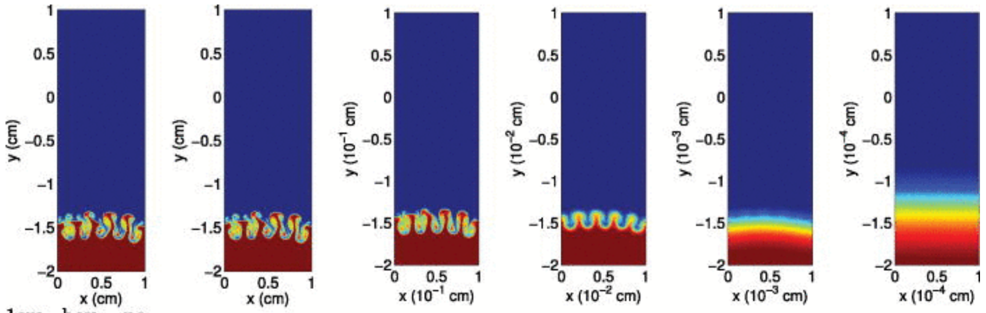

1cm box, no plasma transport, $t = 50$ns

1cm box, $t = 50$ns

0.1cm box, $t = 5$ns

0.01cm box, $t = 0.5$ns

0.001cm box, $t = 0.05$ns

0.0001cm box, $t = 0.005$ns

FIGURE 1.8 – Concentration plots of the two dimensional Rayleigh-Taylor computation, for different characteristic domain sizes. The leftmost results was obtained without plasma transport coefficients, the others corresponds to the spacial scales indicated just below every plot. From Haines et al. (2014b)

Unlike in the works mentioned above, viscosity in ICF increases during the compression due to the growth of temperature, and its effect become more and more important as compression progresses. Weber et al. (2014a) show that thanks to the viscosity growth into the capsule hot-spot, small scale fluctuations are entirely suppressed. On the same subject, Haines et al. (2014b) provided examples of plasma viscous effects on instability growth. The authors performed two-dimensional hydrodynamic simulations of Rayleigh-Taylor and Kelvin-Helmholtz instabilities with plasma transport coefficients, at a fixed temperature of 1 keV. They found that if the characteristic length of the instability is small enough, around $\sim 100\mu m$, viscosity effects become noticeable, and they are dominant at smaller scales, around $\sim 1\mu m$.

1.6 Variable density turbulence

The usual approximation in the fundamentals studies on buoyancy-driven mixing is the Boussinesq approximation [Boffetta and Mazzino 2017], which assumes incompressible flows and small variation in the density. However, in most of the applications, these assumptions may become limiting. Density variation may become important in certain types of flows, and consequently, their effects have to be carefully taken into account. Moreover, the Boussinesq approximation assumes symmetry in the mixing ; it does not differentiate the mixing of a heavy in a light material or the inverse. A famous example was given by Miller et al. (2005), and it is shown in Figure 1.9.

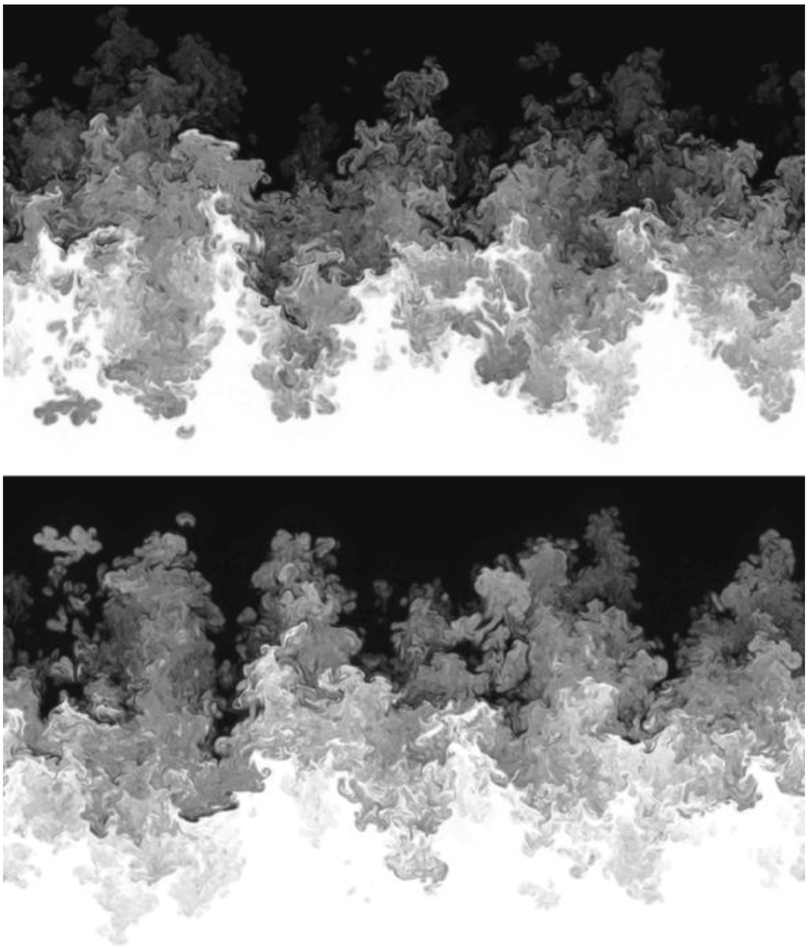

Figure 1.9 – Vertical slices of a Rayleigh-Taylor simulation at Atwood number of 0.5, one of which is upside down. From Miller et al. (2005)

Sandoval (1995), in his thesis, introduced the theoretical framework of the variable density turbulence. His work was based on the evidence, provided by Joseph and Renardy (1993), that the mix of two incompressible flows, *i.e.* flows in which the velocity field, $\mathbf{u}$, is solenoidal $\nabla \cdot \mathbf{u} = 0$, is no longer incompressible and the divergence of the velocity field depends on the density, ρ, and the diffusion coefficient, $\mathcal{D}$, variations *i.e.*

$$\nabla \cdot \mathbf{u} = -\nabla \cdot \left(\frac{\mathcal{D}}{\rho} \nabla \rho \right).$$

Within this approximation, acoustic phenomena are decoupled from the problem, and the density is not dependent on pressure, meaning that with this assumption, only low Mach number (the ratio between the flow velocity and the speed of sound) flows can be studied. Sandoval used this approximation to investigate the turbulent mixing generated by buoyancy effects, with the idea to improve one and two-point turbulence models. He used direct numerical simulations of the Navier-Stokes equations to study the decay of homogeneous isotropic and buoyancy generated turbulence with variable density effects. In both cases, Boussinesq approximation was not applicable, because the ratio between the initial rms value of the density fluctuations and the initial mean density was higher than 0.1.

Livescu and Ristorcelli (2007; 2008) have performed direct numerical simulations of buoyancy-driven turbulence, with different initial conditions. They evidenced that the pure light fluid mixes more rapidly than the pure dense fluid and that when the density contrast grows, one of the limiting factors from a numerical resolution point of view is the sharp gradients in the density field. Rao et al. (2017) studied the L^2-spatial average of the density gradient, evidencing the intense mixing of density field at small scales in buoyancy-driven turbulence and, also, the possible blow-up of density gradient in a finite time.

From an experimental point of view Prestridge (2018) provided a review of the experimental efforts in the investigation of variable density mixing. For instance, the author evidenced that, there are peculiarities in variable density mixing related only to density effect, but independent on the way mixing has started. On the same note, Gerashchenko and Prestridge (2015) evidenced how the same non-Boussinesq mechanism, that modifies the mixing in a high-density jet issuing in a low-density ambient fluid is the same that was identified in homogeneous buoyancy-driven turbulence by Livescu and Ristorcelli (2007) and in Rayleigh-Taylor mixing layer by Livescu et al. (2010). In particular, they found that buoyancy has a considerable impact on turbulent quantities such as velocity fluctuations, turbulent kinetic energy, and Reynolds stresses and that the higher is the Atwood number of the jet, the slower is the mixing. In a following investigation on the same experimental set-up Charonko and Prestridge (2017) found a negative turbulent kinetic energy production near the center of the dense jet, *i.e.* the mean flow receive energy from the fluctuations. To better understand this phenomenon, Lai et al. (2018) derived a Karman-Howarth-Monin equation for variable density turbulence to investigate the energy scale-by-scale budget in the jet. They identified the total inter-scale energy transfer rate across a scale r, as the sum of a linear Π_U and nonlinear contribution Π. The linear contributions take into account vortex stretching and other effects from the mean flow gradient, while the nonlinear term is the classical energy cascade. These transfers are depicted in Figure 1.10. The overall net inter-scale transfer is similar for the two jets, but in the Boussinesq jet, the two terms Π, and Π_U have the same sign, and both contribute to the forward cascade from large to smaller scales. In the non-Boussinesq case, the linear term has a positive sign, indicating an inverse cascade from small to larger scales.

As an example of the difference between variable density and Boussinesq approximation, we show the results of a spherical mixing zone compression. In this

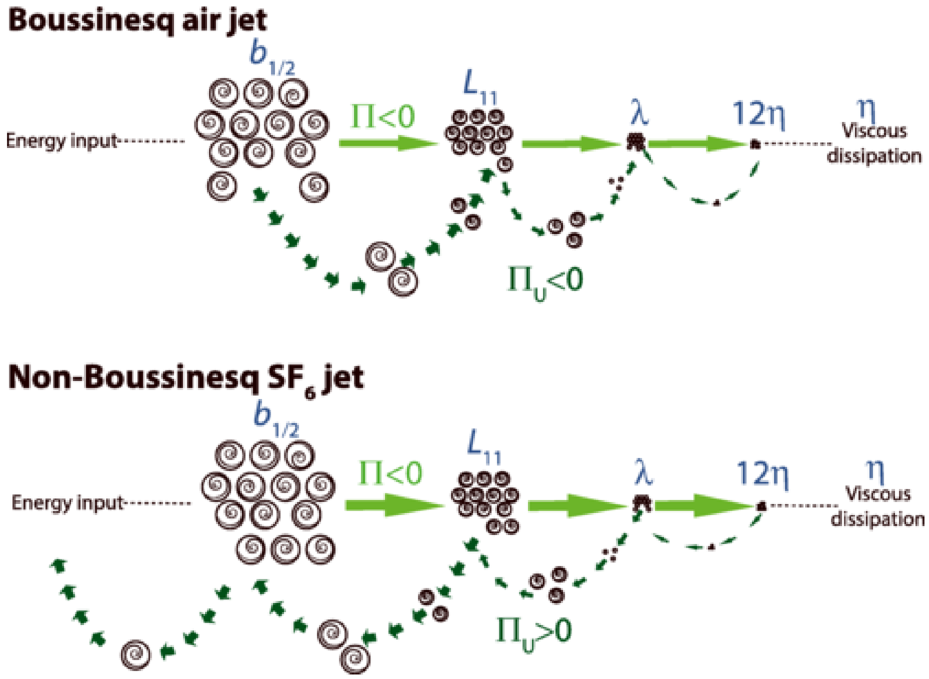

FIGURE 1.10 – Energy transfer mechanism in Boussinesq top and non-Boussinesq jets. From Prestridge (2018)

simulation, the mixing zone is composed of a heavy material that surrounds a light material, with Atwood number equal to 0.7. The compression forces accelerate the mixing layer towards the center of the spherical shell, leading to a Rayleigh-Taylor flow in spherical geometry. In Figure 1.11 are plotted the contours of θ, a density related quantity (the definition of θ, is given in chapter 2). These results are computed using the codes described in chapter 2 and 3. From the same initial condition in (I), the two simulations at the instant (II) show a different flow topology. In the Boussinesq computation, the light/heavy and the heavy/light sides of the mixing zone have the same flow structure, as already pointed out in Figure 1.9. On the other hand, if we observe the variable density results, we find a difference between the flow that is developing in the light material and the one in the heavy material. At the center of the capsule, we observe spikes of heavy materials penetrating, without the typical mushroom topology, that, on the contrary, we observe in the Boussinesq case. This is due to the higher inertia of the heavy material that avoids the development of the Kelvin-Helmholtz instability that causes the mushroom shape. The higher inertia is also the cause of the slow mixing of the heavy fluid with respect to the lighter fluid, as observed by Livescu and Ristorcelli (2007; 2008).

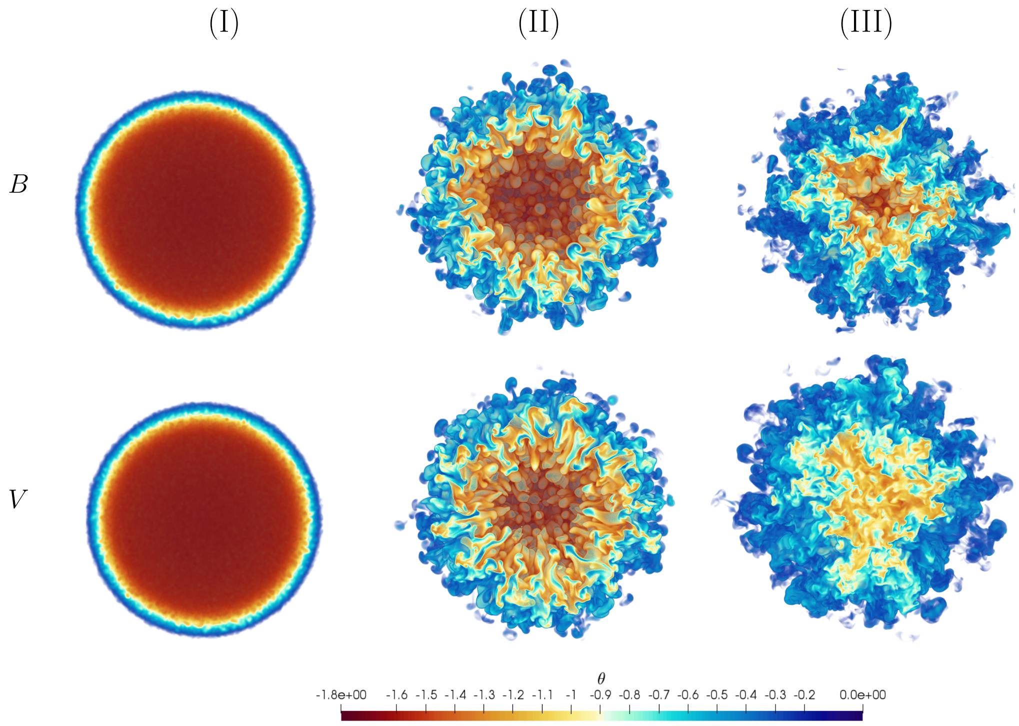

FIGURE 1.11 – Contours of θ, a density related quantity, at three instants during the compression of a spherical mixing zone. (Top) Results obtained using the Boussinesq approximation. (Bottom) Results obtained with the variable density approximation

1.7 Plan of the thesis

The plan of the thesis is the following :

In chapter 2, we present the theoretical developments that allow us to investigate the different topics covered in this thesis, the compressed turbulence, the spherical turbulent mixing zone, and the unstably stratified homogeneous turbulence. In chapter 3, we give an overview of the numerical methods used to solve the equation derived in 2 together with the validation steps for the new code developed.

In chapter 4, we consider a weakly coupled plasma of hydrogen under compression and we investigate the possible influence of initial condition on the sudden dissipation effect, knowing that classically, turbulence has a dependence on initial conditions. To this end, we use the direct numerical simulations of the equation derived in chapter 2 together with a spectral model, knowing that the DNS code cannot explore high Reynolds number flows. We use the eddy damped quasi normal markovian (EDQNM) closure, knowing that the classical version is capable of simulating the decay of homogeneous isotropic turbulence for high Reynolds number. With this model, we perform a parametric study of the compression as a function of the initial Reynolds number and compression number to understand the sensitivity of the sudden dissipation effect to the initial conditions. We establish, theoretically, the connection between initial condition and the statistical proprieties of the flow during compression, to have analytical relations between initial and final states. Furthermore, we extend our analysis to an inhomogeneous spherical configuration.

However, the analysis of chapter 4 does not take into consideration the density field, that is why we introduce the Unstably Stratified Homogeneous Turbulence (USHT) approximation in chapter 5. In this chapter, with constant viscosity and diffusivity, with the help of direct numerical simulations, we investigate the effects of the intensity of the initial density field variance on the self-similar states of USHT, confronting the results of simulations with both variable density and Boussinesq approximations. Moreover, using Implicit Large Eddy Simulations (ILES), we investigate how different initial conditions affect the self-similar behavior of the flow.

Finally, in chapter 6, we analyze the influence of the molecular and turbulent diffusivity on the evolution of the fuel/ablator mixing zone and the hot spot contamination. To pursue this analysis, we have derived the equation for a spherical mixing zone under compression with the variable density approximations. In order to be able to simulate the DT/CH mixtures, we have integrated into the direct numerical simulation code, a plasma physics model capable of predicting the transport coefficient values in a plasma mixture for different thermodynamic conditions.

Chapitre 2
Theory

Contents

In this chapter, we introduce the different theoretical frameworks that have been used through this work. In section 2.1, we introduce the subject of compressed turbulence and the change of reference frame, a useful tool in this study. The problem of mixing in variable density unsteady stratified homogeneous turbulence is discussed in section 2.2. Section 2.3 is focused on spherical compression, with a summary of the literature findings and the theoretical framework that we have developed for this work. Finally, section 3.4 is devoted to the discussion on how to generate initial conditions for the different cases discussed.

2.1 Compressed turbulence

The problem of compressed turbulence has drawn much attention for several years. From reciprocating engines to astrophysics and inertial fusion applications, the interaction between turbulence and the mean compressing field is a fundamental aspect to understand. The relative importance between the effect of the mean field and the nonlinear interactions can be quantified by the time scale associated with the mean field t_M and to the turbulence t_F [Hamlington and Ihme 2014], and their ratio

$$C_M = \frac{t_F}{t_M}$$

When $C_M \gg 1$, the turbulence dynamic is mainly influenced by the mean flow, and the nonlinear transfer and viscous dissipation can be neglected. In this regime, numerous authors have used the Rapid Distortion Theory (RDT) [Hunt and Carruthers

1990] to obtain theoretical results and improve existing turbulence models. The RDT demonstrates, even if in a limit case, how the compression affects turbulence and provides theoretical solutions against which turbulence models can be tested [Cambon et al. 1992, Coleman and Mansour 1993, Blaisdell et al. 1996, Durbin and Zeman 1992, Hamlington and Ihme 2014].

When compression and turbulence have similar time scales, *i.e.* $C_M \sim 1$, RDT hypotheses are no longer valid and Direct Numerical Simulation (DNS) of the Navier-Stokes equations become useful to investigate the physics of this problem. Rogallo (1981) and Wu et al. (1985) performed DNS of compressed turbulence and applied their results to improve turbulence models. In particular, they have studied a case where compressibility does not affect the fluctuating field, *i.e.* the turbulent Mach number $M_T = \frac{u_{rms}}{c}$ is close to zero (here u_{rms} is the rms velocity of the turbulent fluctuations and c the speed of sound). In his paper, Rogallo (1981) proposed a mean velocity field together with a coordinate system that moves with the mean flow, that have been employed in most of the works on isotropic compression [Cambon et al. 1992, Coleman and Mansour 1993, Blaisdell 1991, Davidovits and Fisch 2016a]. The extension to compressible turbulence has been done by Blaisdell (1991), who removed the low Mach number hypothesis and performed a direct numerical simulation.

In this work, we use the same method as in Rogallo (1981). We start from Navier-Stokes and mass conservation equations with constant dynamic viscosity μ

$$\partial_t(\rho U_i) + \partial_j(\rho U_j U_j) = -\partial_i P + \mu \partial^2_{jj} U_i \tag{2.1}$$

$$\partial_t \rho + \partial_j(\rho U_j) = 0 \tag{2.2}$$

in a stationary Cartesian reference frame with space coordinates x_i and time t.

The density ρ, pressure P and velocity U_i are decomposed into base and fluctuation :

$$\rho = \rho^B + \rho' \tag{2.3}$$

$$P = P^B + p \tag{2.4}$$

$$U_i = U_i^B + u_i \tag{2.5}$$

and density fluctuations, ρ', are neglected using the low Mach number hypothesis. The assumption $\rho' \ll \rho$ holds during an isotropic compression while it is not necessarily true for non-isotropic compression, as shown by Coleman and Mansour (1993) and reference therein. If we consider homogeneous velocity fluctuations u_i, the base flow velocity in Eq. (2.5) must have uniform spatial gradient [Sagaut and Cambon 2008]. This requires that the base velocity $\mathbf{U}_B(\mathbf{x}, t)$ be a linear function of position x_i and time t

$$U_i^B(\mathbf{x}, t) = -\mathcal{S}_{ij} x_j, \tag{2.6}$$

where the tensor deformation S_{ij} depends only on time ; in isotropic compressions its expression simplifies as $S_{ij} = \mathcal{S}(t)\delta_{ij}$, allowing us to define the compression rate $\mathcal{S}(t)$. The assumption in this type of compression is to consider uniform base density,

$$\rho^B = \rho^B(t).$$

Together with the base velocity expression (2.6) and the continuity equation (2.2), this gives the time evolution of the base density :

$$\rho^B = \rho^B_0 \exp\left(3\int_0^t \mathcal{S}(s)ds\right), \tag{2.7}$$

where ρ^B_0 is the base density at initial time $t = 0$.

If we consider a cubic domain with edge length $R(t)$ we can define the compression parameter Λ as the normalized size of the domain, $\Lambda = \frac{R(t)}{R_0}$, and we observe that both $R(t)$ and Λ decrease in time.

The volume of the cubic domain is $V(t) = R(t)^3$, which implies that the base density can be written as a function of the compression parameter $\rho^B(t) = \rho_0\Lambda(t)^{-3}$.

Using Eq. (2.7) we find the relation between the compression time rate and the compression parameter

$$\Lambda = \exp\left(-\int_0^t \mathcal{S}(s)ds\right) \text{ or } \mathcal{S}(t) = -\frac{1}{\Lambda}\frac{d\Lambda}{dt} \tag{2.8}$$

and we rewrite the time evolution of the base density as

$$\rho^B = \rho^B_0\Lambda^{-3}. \tag{2.9}$$

Injecting the base/fluctuations decomposition from Eqs. (2.3), (2.4), (2.5) for U_i, P, ρ in Eq. (2.1), and applying the volume average operator $\langle * \rangle$, we obtain an equation for the base flow

$$\partial_t U^B_i + U^B_j \partial_j U^B_i = -\frac{\partial_i P^B}{\rho^B} - \partial_j\langle u_i u_j\rangle, \tag{2.10}$$

and $\partial_j\langle u_i u_j\rangle$ is zero for spatial homogeneity. If needed we can use (2.10) to obtain the base pressure P^B, from the knowledge of the base velocity.
The equation for the perturbation

$$\partial_t u_i + U^B_j \partial_j u_i + u_j\partial_j U^B_i + u_j\partial_j u_i = -\frac{\partial_i p}{\rho^B} + \frac{\mu}{\rho^B}\partial^2_{jj}u_i \tag{2.11}$$

using the expression for the base velocity becomes

$$\partial_t u_i + u_j\partial_j u_i - S(t)x_j\partial_j u_i - S(t)u_j = -\frac{\partial_i p}{\rho^B} + \frac{\mu}{\rho^B}\partial^2_{jj}u_i. \tag{2.12}$$

The inhomogeneous term can be eliminated using a change of reference frame [Rogallo 1981] :

$$\tilde{x}_i = \Lambda^{-1}(t) x_j \tag{2.13}$$

The detailed computation that shows how to choose the particular transformation is developed in appendix A. Using (2.13) and (2.9) in the perturbation momentum equation (2.12) we obtain

$$\partial_t u_i + \frac{1}{\Lambda} u_j \partial_j u_i - \mathcal{S}(t) u_i = -\Lambda^2 \partial_i p + \Lambda \frac{\mu}{\rho_0^B} \partial^2_{jj} u_i. \tag{2.14}$$

At this point we have two possibilities to further simplify this equation :

- We can eliminate the forcing term $-\mathcal{S}(t)u_j$.
- We can eliminate the time dependence due to Λ in front of the viscous term.

In the first case the rescalings of the variables are [Cambon et al. 1992, Viciconte et al. 2018]

$$\tilde{u_i}(\tilde{\mathbf{x}}, \tilde{t}) = u_i(\mathbf{x}, t)\Lambda(t), \quad \tilde{t} = \textstyle\int_0^t \Lambda^{-2}(s) ds, \quad \tilde{p}(\tilde{\mathbf{x}}, \tilde{t}) = p(\mathbf{x}, t)\Lambda^5(t) \tag{2.15}$$

and the corresponding equation is

$$\partial_{\tilde{t}} \tilde{u}_i + \tilde{u}_j \partial_j \tilde{u}_i = -\partial_i \tilde{p} + \Lambda^3(t) \frac{\mu}{\rho_0^B} \partial^2_{jj} \tilde{u}_i \tag{2.16}$$

In the second case [Davidovits and Fisch 2016a]

$$\tilde{u_i}(\tilde{\mathbf{x}}, \tilde{t}) = u_i(\mathbf{x}, t)\Lambda^{-2}(t), \quad \tilde{t} = \textstyle\int_0^t \Lambda(s) ds, \quad \tilde{p}(\tilde{\mathbf{x}}, \tilde{t}) = p(\mathbf{x}, t)\Lambda^{-1}(t) \tag{2.17}$$

and the corresponding equation becomes

$$\partial_{\tilde{t}} \tilde{u}_i + \tilde{u}_j \partial_j \tilde{u}_i + 3\frac{\mathcal{S}(t)}{\Lambda} u_i = -\partial_i \tilde{p} + \frac{\mu}{\rho_0^B} \partial^2_{jj} \tilde{u}_i. \tag{2.18}$$

In equations (2.14), (2.16) and (2.18) the spatial operators are to be considered in the moving frame, depending on $\tilde{x}_i$.

2.2 Unstably stratified homogeneous turbulence

Turbulent mixing driven by buoyancy forces is an important phenomenon common to different fields, from astrophysics to inertial confinement fusion. In these contexts, to investigate the fundamental properties of the turbulence generated by baroclinic instabilities, the homogeneous approximation is an alternative to the full inhomogenous simulation of mixing zones.

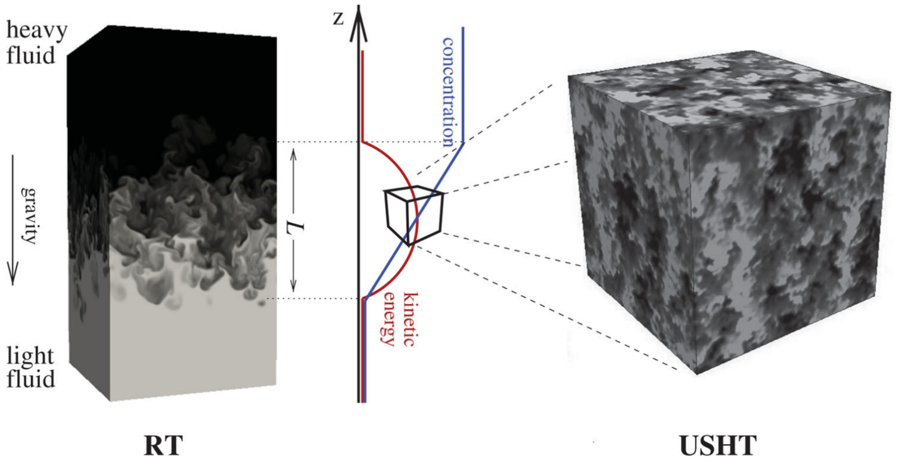

FIGURE 2.1 – Unstably stratified homogeneous turbulence approximation with respect to a Rayleigh-Taylor simulation. (From Griffond et al. (2015a)).

This approximation, called Unstably Stratified Homogeneous Turbulence (USHT) [Griffond et al. 2014], applies at the center of a fully developed mixing zone, as depicted in Figure2.1, where the separation between the mean density gradient and the integral scale of the turbulence allows the decoupling between the mean inhomogenous flow and the homogeneous fluctuations. With respect to the complete configuration of full Rayleigh-Taylor mixing, the USHT approximation removes inhomogeneity and transport mechanisms but conserves the similar properties regarding buoyancy production, nonlinear transfers, and dissipation.

Most investigations on USHT [Burlot et al. 2015a, Gréa et al. 2016b] have used the Boussinesq approximation, which is only adapted when the density fluctuations are small compared to the mean value. To extend the homogeneous approximation to more general cases, we derive the unstably stratified homogeneous turbulence equations using the variable density approximation. As explained in section 1.6, this approximation was introduced by Sandoval (1995) to study the decay homogeneous turbulence with buoyancy effects, generated by the mixing between light and dense fluids.

In this section, we will reformulate the theoretical framework for variable density buoyancy-driven turbulence decay to obtain a non-decaying flow sustained by buoyancy forces *i.e.* USHT flow.

We consider the mixing of two materials with different densities but with the same dynamic viscosity μ and diffusivity $\mathcal{D}$. We start from the conservation equations for momentum ρU_i, mass ρ, species ρY_α, where U_i are the velocity components and Y_α

is the mass fraction of the material $\alpha = 1, 2$:

$$\partial_t \rho U_i + \partial_j \rho U_i U_j = -\partial_i P + \partial_j \tau_{ij} + \rho g \delta_{i3} \tag{2.19}$$
$$\partial_t \rho + \partial_j \rho U_j = 0 \tag{2.20}$$
$$\partial_t \rho Y_\alpha + \partial_j \rho U_j Y_\alpha = \mathcal{D} \partial_j (\rho \partial_j Y_\alpha) \tag{2.21}$$

where g is the gravity acceleration and τ_{ij} is the viscous tensor defined by

$$\tau_{ij} = \mu \Big(\partial_j U_i + \partial_i U_j - \frac{2}{3} \partial_k U_k \delta_{ij} \Big).$$

We add to the system a mixing law :

$$\frac{1}{\rho} = \frac{Y_1}{\rho_1} + \frac{Y_2}{\rho_2} \tag{2.22}$$

where ρ_1 and ρ_2 are the local microscopic densities of each species, assumed constants and not equal to one another.

Using the same approach as Sandoval (1995) and Livescu and Ristorcelli (2007), we start from equation (2.21) for the conservation of species, that, using the conservation of mass (2.20), reduces to

$$\partial_t Y_1 + U_j \partial_j Y_1 = \frac{1}{\rho} \mathcal{D} \partial_j (\rho \partial_j Y_1), \tag{2.23}$$

where without loss of generality we have chosen $\alpha = 1$. The mixing law (2.22) is rearranged to express Y_1 as a function of the density ρ

$$Y_1 = \frac{A}{\rho} - B \quad \text{with} \quad A = \frac{\rho_1 \rho_2}{\rho_2 - \rho_1} \quad \text{and} \quad B = \frac{\rho_1}{\rho_2 - \rho_1}. \tag{2.24}$$

Injecting (2.24) in equation (2.23) we have

$$\partial_t \rho + U_j \partial_j \rho = \rho \mathcal{D} \partial_j \left(\frac{\partial_j \rho}{\rho} \right). \tag{2.25}$$

The comparison of (2.25) with the equation for conservation of mass leads to the following

$$\partial_j U_j = -\mathcal{D} \partial_j \left(\frac{\partial_j \rho}{\rho} \right), \tag{2.26}$$

that is, a relation expressing the dependence of the velocity field compressibility on the mixture density.

We use Eqs (2.25) and (2.26) together with the conservation of momentum (2.19) to have a closed system of equation in the variable density approximation

$$\begin{aligned} \partial_t U_i + U_j \partial_j U_i = & - \partial_i \Pi - \Pi \partial_i \Theta + g \delta_{i3} + \nu \partial_j \left[(\partial_j U_i + \partial_i U_j) \right] \\ & + \nu \left(\partial_j U_i + \partial_i U_j \right) \partial_j \Theta, \end{aligned} \tag{2.27}$$

$$\partial_t \Theta + U_j \partial_j \Theta = \mathcal{D} \partial^2_{jj} \Theta, \tag{2.28}$$

$$\partial_j U_j = -\mathcal{D} \partial^2_{jj} \Theta. \tag{2.29}$$

Π is the reduced pressure $\frac{P}{\rho}$ and Θ is a new scalar value defined as a $\Theta = \log\left(\frac{\rho}{\rho_0}\right)$, where ρ_0 is a reference density. At this point we use the Reynolds decomposition :

$$U_i = \langle U \rangle_i + u_i \tag{2.30}$$

$$\Theta = \langle \Theta \rangle + \theta \tag{2.31}$$

and we assume homogeneity, in order to obtain the equations for the fluctuating quantities, *i.e.* their statistical properties do not vary with position in space. One of the hypotheses of the USHT approximation is that $\langle U \rangle_3$ and $\partial_3 \langle \Theta \rangle$ are uniform, together with $\langle U \rangle_1 = 0$ and $\langle U \rangle_2 = 0$.

Using Eq. (2.29), with the previous assumptions, we obtain for the mean and fluctuations :

$$\begin{aligned}
&\partial_3 \langle U \rangle_3 = -\mathcal{D} \partial^2_{33} \langle \Theta \rangle \;\Rightarrow \langle U \rangle_3 = -\mathcal{D} \partial_3 \langle \Theta \rangle + f(t) \\
&\partial_j u_j = -\mathcal{D} \partial^2_{jj} \theta.
\end{aligned}$$

Furthermore, we impose the function $f(t)$, such that $\langle U \rangle_3 = 0$.

2.2.1 Equations for the scalar Θ

Starting from Eq. (2.28) and decompositions (2.30) and (2.31), we obtain the following equation for the mean $\langle \Theta \rangle$

$$\partial_t \langle \Theta \rangle + \langle u_j \partial_j \theta \rangle = \mathcal{D} \partial^2_{jj} \langle \Theta \rangle \tag{2.32}$$

and the fluctuation θ

$$\partial_t \theta + u_j \partial_j \theta - \langle u_j \partial_j \theta \rangle + u_j \partial_j \langle \Theta \rangle = \mathcal{D} \partial^2_{jj} \theta$$

but $\partial_j \langle \Theta \rangle = \partial_3 \langle \Theta \rangle$ so that

$$\partial_t \theta + u_j \partial_j \theta - \langle u_j \partial_j \theta \rangle + u_3 \partial_3 \langle \Theta \rangle = \mathcal{D} \partial^2_{jj} \theta. \tag{2.33}$$

2.2.1.1 Equations for u_i

The same reasoning can be applied to the momentum equation (2.27). With the decomposition of the reduced pressure $\Pi = \langle \Pi \rangle + \pi$, the mean momentum equation is

$$\begin{aligned}\partial_t\langle U\rangle_i + \langle U\rangle_j\partial_j\langle U\rangle_i + \langle u_j\partial_j u_i\rangle + \langle\Pi\rangle\partial_i\langle\Theta\rangle - \langle\pi\partial_i\theta\rangle =& - \partial_i\langle\Pi\rangle + g\delta_{i3} + \nu\partial^2_{jj}\langle U\rangle_i +\\ &+ \nu\left(\partial_j\langle U\rangle_i + \partial_i\langle U\rangle_j\right)\partial_j\langle\Theta\rangle\\ &+ \nu\partial_i\left(\partial_j\langle U\rangle_j\right)\end{aligned}$$

and knowing that $\langle U\rangle_i = 0$ we have

$$\langle u_j\partial_j u_i\rangle + \langle\Pi\rangle\partial_i\langle\Theta\rangle - \langle\pi\partial_i\theta\rangle = -\partial_i\langle\Pi\rangle + g\delta_{i3}. \tag{2.34}$$

The equation for the fluctuating part is

$$\begin{aligned}\partial_t u_i + u_j\partial_j u_i - \langle u_j\partial_j u_i\rangle + \pi\partial_i\theta - \langle\pi\partial_i\theta\rangle =& - \partial_i\pi - \langle\Pi\rangle\partial_i\theta - \pi\partial_3\langle\Theta\rangle\delta_{i3} + \nu\partial^2_{jj}u_i\\ &+ \nu\partial_i\left(\partial_j u_j\right) + \nu\left(\partial_j u_i + \partial_i u_j\right)\partial_j\theta\\ &+ \nu\left(\partial_3 u_i + \partial_i u_3\right)\partial_3\langle\Theta\rangle.\end{aligned} \tag{2.35}$$

The homogeneity required for the fluctuations imposes that $\langle\Pi\rangle$ does not depend on space. The same condition holds for $\partial_3\langle\Theta\rangle$. From the mean velocity equations (2.34), that assuming turbulent quantities are small enough, there is a relation between two mean quantities $\langle\Pi\rangle$ and $\langle\Theta\rangle$: in fact we have $\langle\Pi\rangle\partial_3\langle\Theta\rangle = g$. The gradient of $\langle\Theta\rangle$ is related to the mixing zone size L via

$$\partial_3\langle\Theta\rangle = \frac{1}{L} \tag{2.36}$$

so that Eq. (2.33) and (2.35) become

$$\begin{aligned}\partial_t u_i + u_j\partial_j u_i + \pi\partial_i\theta =& - \partial_i\pi - gL\partial_i\theta - \frac{1}{L}\pi\delta_{i3} + \nu\partial^2_{jj}u_i\\ &+ \nu\partial_i\left(\partial_j u_j\right) + \nu\left(\partial_j u_i + \partial_i u_j\right)\partial_j\theta\\ &+ \frac{\nu}{L}\left(\partial_3 u_i + \partial_i u_3\right)\end{aligned} \tag{2.37}$$

$$\partial_t\theta + u_j\partial_j\theta = \mathcal{D}\partial^2_{jj}\theta - \frac{1}{L}u_3 \tag{2.38}$$

$$\partial_j u_j = -\mathcal{D}\partial^2_{jj}\theta. \tag{2.39}$$

Assuming small fluctuations for θ, we can write the equations for the Boussinesq case :

$$\partial_t u_i + u_j\partial_j u_i = -\partial_i\pi + g\theta\delta_{i3} + \nu\partial^2_{jj}u_i \tag{2.40}$$

$$\partial_t\theta + u_j\partial_j\theta = \mathcal{D}\partial^2_{jj}\theta - \frac{1}{L}u_3 \tag{2.41}$$

$$\partial_j u_j = 0. \tag{2.42}$$

For both variable density and Boussinesq approximations, we introduce the buoyancy frequency

$$N = \sqrt{\frac{g}{L}}. \tag{2.43}$$

2.3 Spherical compressions

In section 2.1, we have discussed the isotropic compression of homogeneous isotropic turbulence. In this section, we discuss the same isotropic compression, but in the case of a spherical mixing zone. A sketch representing the two configurations is shown in Figure 2.2. We make the hypothesis that the mixing layer is generated by the implosion of a capsule of plastic containing a mix of deuterium and tritium, a configuration of interest for inertial confinement fusion application.

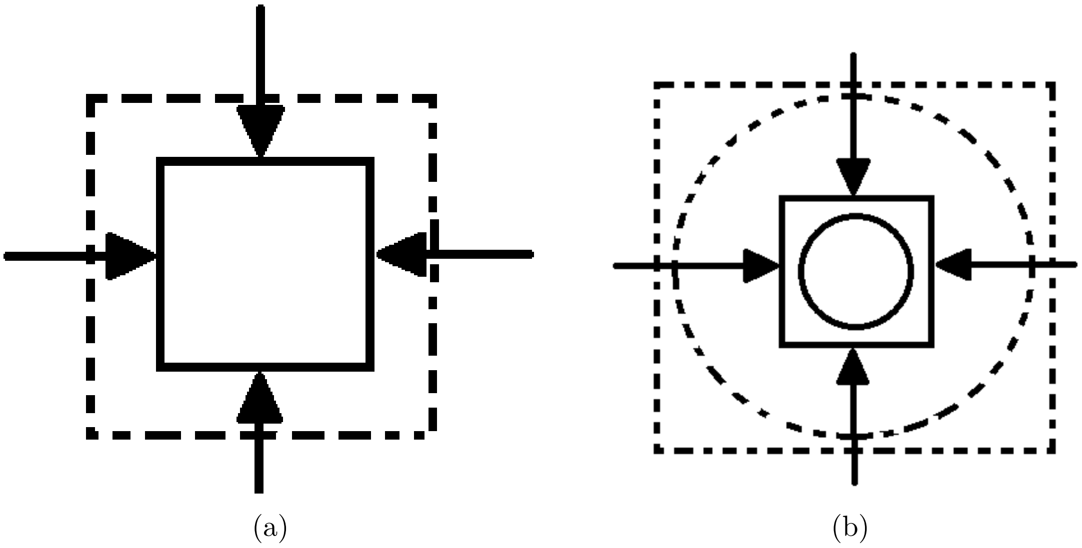

FIGURE 2.2 – Sketches of the isotropic compressions for the (a) homogeneous isotropic case of section 2.1 (b) spherical compression case of section 2.3. The dashed line represents the initial condition while the solid line represents a later time during the compression.

The investigations of mixing in converging spherical geometry have been concentrated mostly on the curvature effect on the baroclinic instability that may develop at the interface.

The first investigations are due to Bell (1951) and Plesset (1954). They used a potential flow approach to study the stability of an accelerated interface between two incompressible fluids. They found a geometric influence that has a major role in the development of instabilities, especially in case of compressions with a large ratio between the initial and final radii. Further investigation by Chandrasekhar (1955) showed the role of viscosity, in particular on the selection of the most unstable modes during the compression.

The following works by Mikaelian (1990) and Amendt (2006) were dedicated to extending the investigation on Rayleigh-Taylor instability in spherical geometry with the objective of developing a model for inertial confinement fusion application. Other works by Prosperetti (1977) and Lin et al. (2002) concentrated on the application of bubbles collapse. Sakagami and Nishihara (1990) presented the first direct numerical simulation of the three-dimensional problem. In this paper, they were able to investigate both linear and nonlinear regimes of the spherical perturbation growth, and they found a good agreement for the linear evolution, between theoretical prediction and simulation results.

Youngs and Williams (2008) proposed an implosion problem and investigated the role of the mesh refinement and dissipation on turbulent statistics. Lombardini et al. (2014a) using a Large Eddy Simulations (LES) studied the Richtmyer-Meshkov driven mixing in low convergence ratio spherical implosion. They evidenced how Bell-Plesset effect has little impact on the dynamics of the imploding mixing layer. In particular, they show how the mean flow is dominated by baroclinic instabilities (Richtmyer-Meshkov, Rayleigh-Taylor) and the turbulent fluctuation inertial subrange approaches the same behavior that is obtained in planar geometry.

In the present study, we suppose that a shock wave has already deposited the vorticity at the interface between the external ablator and the fuel and that the spherical mixing zone at this instant has radius R.

2.3.1 Navier-Stokes for binary mixtures

We use the same conservation equations (2.19)-(2.21), where the variables depend on time t and position $\mathbf{x}$ relative to a cartesian stationary reference frame and we recall that Y_α is the mass fraction of the material $\alpha = 1, 2$. Moreover, we add an equation for the temperature T, as well the ideal gas law, which, in the regimes considered is good approximation for the equation of state (see for instance Vold et al. (2015)).

$$\partial_t \rho U_i + \partial_j \rho U_i U_j = -\partial_i P + \partial_j \tau_{ij}, \tag{2.44}$$

$$\partial_t \rho + \partial_j \rho U_j = 0, \tag{2.45}$$

$$\partial_t \rho Y_\alpha + \partial_j \rho U_j Y_\alpha = \partial_j \phi_{j,\alpha}, \tag{2.46}$$

$$\frac{n k_B}{\gamma - 1}(\partial_t T + U_j \partial_j T) = -P \partial_j U_j + \partial_j (\kappa \partial_j T) + \partial_i U_j \tau_{ij}, \tag{2.47}$$

$$P = n k_B T. \tag{2.48}$$

$$\tag{2.49}$$

where P is the pressure, n is the number density of particles, $\gamma = 5/3$, k_B is the Boltzmann constant, and κ the temperature diffusion coefficient. The viscous stress tensor is modelled with a Newtonian constitutive law and the diffusive flux with a

Fickian law :

$$\tau_{ij} = \mu(\mathbf{x},t)\Big(\partial_j U_i + \partial_i U_j - \frac{2}{3}\partial_k U_k \delta_{ij}\Big)$$
$$\phi_{j,\alpha} = \rho\mathcal{D}(\mathbf{x},t)\partial_j Y_\alpha,$$

and we consider that transport coefficients ν and $\mathcal{D}$ are functions of space x_i and time t. In order to close the system we provide the mixture law for a general two-component mixture with elements 1 and 2 :

$$\frac{1}{\rho} = \frac{Y_1}{\rho_1} + \frac{Y_2}{\rho_2} \text{ with } \rho_1 = \frac{nM_1}{1+Z_1} \text{ and } \rho_2 = \frac{nM_2}{1+Z_2} \tag{2.50}$$

with Z_α and M_α the ionization number and the atomic mass of species $\alpha = 1, 2$.

2.3.2 Base flow and perturbation

In the following we will consider the solution of the previous equations (2.44)-(2.48) as a superposition of a baseflow and a perturbation, that is, if $F(\mathbf{x},t)$ is one of the unknowns of the problem, we can write it as

$$F(\mathbf{x},t) = F^B(\mathbf{x},t) + f(\mathbf{x},t). \tag{2.51}$$

2.3.2.1 Base Flow

In this part we propose to characterize the base flow. In section 2.1 we have already chosen the base component of the velocity field in 2.6. Due to the spherical symmetry of the problem, we propose to derive the base components depending only on the radius r.

First the base velocity is rewritten as

$$U_i^B(r,t) = -\mathcal{S}(t)x_i. \tag{2.52}$$

From the density equation in spherical coordinates

$$\partial_t \rho^B + \frac{1}{r^2}\partial_r\Big(r^2\rho^B\mathbf{U}^B\Big) = 0 \tag{2.53}$$

and substituting the expression (2.52) for $\mathbf{U}^B(r,t)$, we obtain an equation for the base density ρ^B :

$$\partial_t\rho^B - r\mathcal{S}(t)\partial_r\rho^B = 3\mathcal{S}(t)\rho^B \tag{2.54}$$

that admits self-similar solution in the form

$$\rho^B(r,t) = \rho_0\Lambda(t)^{-3}G\Big(\frac{r}{\Lambda}\Big). \tag{2.55}$$

The base temperature equation, neglecting thermal diffusion, reduces to a form that resembles (2.54) :

$$\partial_t T^B - r\mathcal{S}(t)\partial_r T^B = 3(\gamma-1)\mathcal{S}(t)T^B \tag{2.56}$$

with a solution :

$$T^B(r,t) = T_0\Lambda(t)^{-3(\gamma-1)}\mathcal{H}\Big(\frac{r}{\Lambda}\Big). \tag{2.57}$$

To obtain the equation for the base number density of particle n^B, we use the mixing law (2.50)

$$\rho Y_1 = An + B\rho \tag{2.58}$$

$$A = \frac{M_1M_2}{M_2(1+Z_1) - M_1(1+Z_2)} \tag{2.59}$$

$$B = \frac{M_1(1+Z_2)}{M_2(1+Z_1) - M_1(1+Z_2)} \tag{2.60}$$

together with Eq. (2.46). Neglecting the diffusive term, we get

$$\partial_t n^B + \frac{1}{r^2}\partial_r\Big(r^2 n^B U_j^B\Big) = 0 \tag{2.61}$$

that has a self similar solution

$$n^B(r,t) = n_0\Lambda(t)^{-3}G\Big(\frac{r}{\Lambda}\Big). \tag{2.62}$$

From the equation of state we deduce that the base pressure

$$P^B(r,t) = P_0\Lambda(t)^{-3\gamma}G\Big(\frac{r}{\Lambda}\Big)\mathcal{H}\Big(\frac{r}{\Lambda}\Big) \tag{2.63}$$

and the reduced base pressure

$$\Pi^B(r,t) = \frac{P^B}{\rho^B} = \Pi_0\Lambda(t)^{-3(\gamma-1)}\mathcal{H}\Big(\frac{r}{\Lambda}\Big) \tag{2.64}$$

We assume that $G(0) = G_0 = \mathcal{H}(0) = \mathcal{H}_0 = 1$. This means that the subscript 0 corresponds to the initial value at the center of the capsule.

Let us consider the case where $G\big(\frac{r}{\Lambda}\big) = 1$, corresponding to a uniform base density. Using the momentum equation, (2.44) for the base component and neglecting viscous effect we obtain

$$\Big(-\frac{d\mathcal{S}(t)}{dt} + \mathcal{S}(t)^2\Big)r = -\partial_r\Pi^B(r). \tag{2.65}$$

This equation has a solution if Π^B is a quadratic function of the radius r. This requirement determines the expression of the self similar function $\mathcal{H}\left(\frac{r}{\Lambda}\right)$:

$$\mathcal{H}(r,t) = 1 - \frac{r^2}{\eta^2\Lambda(t)^2} \text{ and } \Pi^B(r,t) = \Pi_0\Lambda(t)^{-3(\gamma-1)}\left(1 - \frac{r^2}{\eta^2\Lambda(t)^2}\right) \tag{2.66}$$

where η is the characteristic scale of the temperature gradient. With this choice of Π^B, Eq. (2.65) reduces to

$$-\frac{d\mathcal{S}(t)}{dt} + \mathcal{S}(t)^2 = -2\frac{\Pi_0}{\eta^2}\Lambda(t)^{-3\gamma+1} \tag{2.67}$$

that can be rewritten using the relation between the compression parameter and the compression rate (2.8) :

$$\frac{d^2\Lambda(t)}{dt^2} + \Omega_0^2\Lambda(t)^{-3\gamma+2} = 0 \text{ with } \Omega_0 = \sqrt{2\frac{\Pi_0}{\eta^2}}. \tag{2.68}$$

This equation is solved with initial conditions

$$\Lambda(0) = 1 \text{ and } \frac{d\Lambda}{dt}(0) = \mathcal{S}_0$$

and $\gamma = 5/3$ (monoatomic gas). Finally the evolution of Λ with time is

$$\Lambda(t) = \sqrt{1 - 2\mathcal{S}_0 t + (\mathcal{S}_0^2 + \Omega_0^2)t^2} \tag{2.69}$$

where $\mathcal{S}_0 = \mathcal{S}(0)$, *i.e.* the compression rate at the beginning of the simulation. The value of Ω_0 is specified by fixing $\mathcal{S}_0$ and assigning the minimum value of Λ :

$$\Lambda_{min} = \frac{\Omega_0}{\sqrt{\Omega_0^2 + \mathcal{S}_0^2}} \text{ so that } \Omega_0 = \sqrt{\frac{\mathcal{S}_0^2\Lambda_{min}^2}{1 - \Lambda_{min}^2}}. \tag{2.70}$$

The choice of Λ_{min}, imposes the convergence ratio, that is defined as the ratio between the initial, R_0, and final radius R_{end}, $C_R = \frac{R_0}{R_{end}}$, so that is the inverse of Λ_{min}. These choices are also important because Ω_0 is linked to the characteristic scale of the temperature gradient h, through the relation (2.68). Therefore it is worth exploring how the choices of $\mathcal{S}_0$ and Λ_{min} influence the time evolution of the compression parameter Λ and the radial evolution of the self-similar function $\mathcal{H}(r,t)$.

We plot Λ as function of time in Figure 2.3. In Figure2.3a we consider a constant $\mathcal{S}_0$ but different values Λ_{min}. If Λ_{min} is sufficiently small, the compression parameter curves are similar, only with different values at $t = 1\,ns$. The other effect illustrated in Figure 2.3 is a difference in the time of the minimum of Λ, in particular,

$$t_{\min(\Lambda)} = \frac{1 - \Lambda_{min}^2}{\mathcal{S}_0} \tag{2.71}$$

if in this equation Λ_{min} is sufficiently small, the compression time $t_{\min(\Lambda)}$ depends only on $\mathcal{S}_0$. We explore the compression parameter dependence on the initial compression rate $\mathcal{S}_0$ at fixed Λ_{min} (or fixed convergence ratio) in Figure2.3b. We observe how the increase of $\mathcal{S}_0$ leads to a decrease in the compression time, although with a similar evolution of Λ. For instance, Figure2.3b shows that when $\mathcal{S}_0$ increases from $500\mu s^{-1}$ to $1000\mu s^{-1}$, the minimum of Λ is reached in half the time, from $2\,ns$ to $1\,ns$.

Concerning the self-similar function $\mathcal{H}$ in (2.66), once Π_0 is fixed, *i.e.* once the thermodynamic condition at the center of the capsule are defined, h depends only on $\mathcal{S}_0$ and Λ_{min}. An example of this dependence is plotted in Figure2.4. As for the compression parameter, we show in 2.4a how $\mathcal{H}(r)$ depends on the inverse of convergence ratio and in Figure2.4b its dependence on initial compression rate $\mathcal{S}_0$.

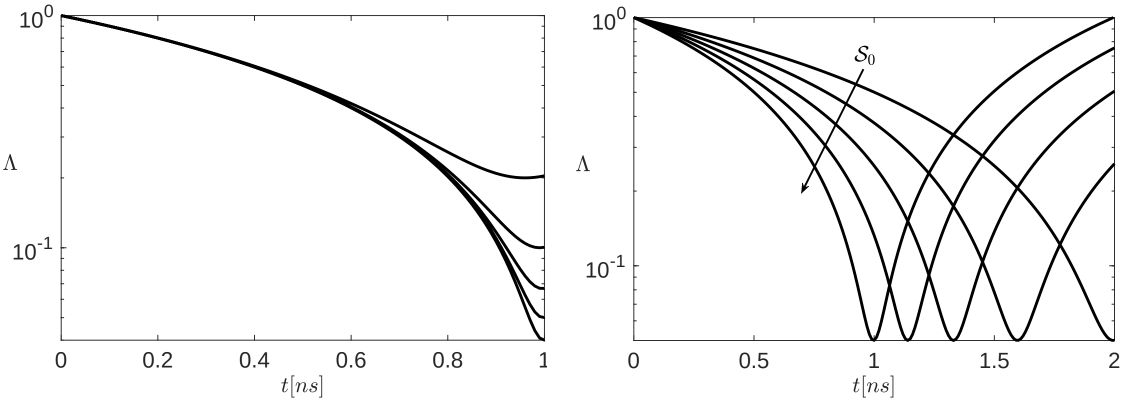

(a)

(b)

FIGURE 2.3 – (a) Time evolution of the compression parameter Λ for different value of Λ_{min} with $S_0 = 1000$. (b) Time evolution of the compression parameter Λ for different value of $\mathcal{S}_0$ ($\mathcal{S}_0 = 500, 625, 750, 875, 1000\,\mu s^{-1}$, increases in the direction of the arrow), with $\Lambda_{min} = 0.05$

At this point, we have all the elements to describe the base flow completely :

$$\mathbf{U}^B(\mathbf{x}, t) = -\mathbf{x} \cdot \frac{\dot{\Lambda}}{\Lambda(t)} \tag{2.72}$$

$$\rho^B(t) = \rho_0 \Lambda(t)^{-3} \tag{2.73}$$

$$\Theta^B(t) = -3 \log \Lambda(t) \tag{2.74}$$

$$n^B(t) = n_0 \Lambda(t)^{-3} \tag{2.75}$$

$$Y^B = 1 \tag{2.76}$$

$$T^B(r, t) = T_0 \Lambda(t)^{-3(\gamma-1)} \left(1 - \frac{1}{\eta^2} \frac{r^2}{\Lambda(t)^2}\right) \tag{2.77}$$

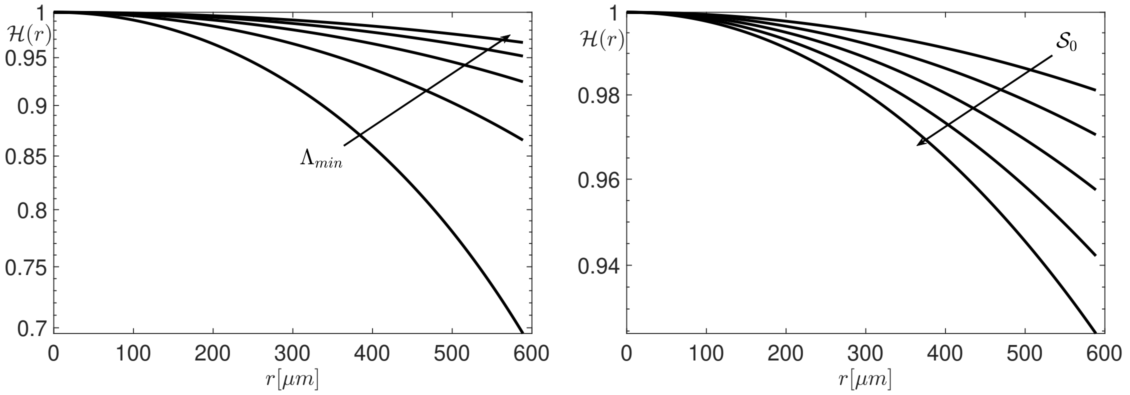

(a) (b)

FIGURE 2.4 – Radial profile of the parabolic function $\mathcal{H}$, in Eq. (2.66), at the beginning of the simulation ($\Lambda = 1$) with fixed value of Π_0. (a) Plot for different values of Λ_{min}, which increases in the direction of the arrow, with $S_0 = 1000$. (b) Plot for different value of $\mathcal{S}_0$ ($\mathcal{S}_0 = 500, 625, 750, 875, 1000\ \mu s^{-1}$ increases in the direction of the arrow), with $\Lambda_{min} = 0.05$

$$P^B(r,t) = P_0 \Lambda(t)^{-3\gamma} \left(1 - \frac{1}{\eta^2} \frac{r^2}{\Lambda(t)^2}\right) \tag{2.78}$$

$$\Pi^B(r,t) = \Pi_0 \Lambda(t)^{-3(\gamma-1)} \left(1 - \frac{r^2}{\eta^2 \Lambda(t)^2}\right) \tag{2.79}$$

2.3.2.2 Perturbations

The perturbations equations follow from the system of equations (2.44) - (2.49) and the base flow expressions determined in section 2.3.2.1 :

$$\begin{aligned} \partial_t u_i + u_j \partial_j u_i - \mathcal{S}(t) x_j \partial_j u_i - \mathcal{S}(t) u_i &= -\partial_i \pi - \pi \partial_i \theta - \Pi^B(\mathbf{x},t) \partial_i \theta \\ + \partial_j \left[\nu \left(\partial_j u_i + \partial_i u_j - \frac{2}{3} \partial_k u_k \delta_{ij}\right)\right] &+ \nu \left(\partial_j u_i + \partial_i u_j - \frac{2}{3} \partial_k u_k \delta_{ij}\right) \partial_j \theta \qquad (2.80) \\ \partial_t \theta + (u_j - \mathcal{S}(t) x_j) \partial_j \theta &= \partial_j u_j \qquad (2.81) \\ \partial_t n + \partial_j n u_j + \partial_j (n^B u_j) + \partial_j (n U_j^B) &= \partial_j \left(\mathcal{D} \partial_j n\right) - \partial_j \left((n + n^B) \mathcal{D} \partial_j \theta\right) \qquad (2.82) \end{aligned}$$

Equations (2.80), (2.81), (2.82) can be simplified with the hypothesis that the fluctuations of the density number of particle are small with respect to its base value, $\frac{n}{n^B} \ll 1$. With this assumption we get the following system of equations :

$$\begin{aligned}
\partial_t u_i + u_j\partial_j u_i - \mathcal{S}(t)x_j\partial_j u_i - \mathcal{S}(t)u_i = -\partial_i\pi - \pi\partial_i\theta - \Pi^B(\mathbf{x},t)\partial_i\theta \\
+\partial_j[\nu(\partial_j u_i + \partial_i u_j)] + \nu(\partial_j u_i + \partial_i u_j)\partial_j\theta \qquad (2.83) \\
\partial_t\theta + (u_j - \mathcal{S}(t)x_j)\partial_j\theta = \partial_j u_j \qquad (2.84) \\
\partial_j u_j = -\partial_j(\mathcal{D}\partial_j\theta) \qquad (2.85)
\end{aligned}$$

The main difference with the classic incompressible approximation is that the divergence of the velocity field is no longer equal to zero but is connected to the scalar field θ. In this approximation we decouple the energy equation from the problem and compressibility effects are only a result of the mixing.

2.3.3 Change of reference frame and rescaling

Equations (2.83)-(2.84) have inhomogeneous and forcing terms representing the base flow effects on the velocity and scalar perturbations. To eliminate these terms we use the change of reference frame (2.13) and the rescaling (2.15) defined in section 2.1. We obtain the following equations for the perturbation in the non-inertial frame :

$$\begin{aligned}
\partial_t\tilde{u}_i + \tilde{u}_j\partial_j\tilde{u}_i =& - \partial_i\tilde{\pi} - \tilde{\pi}\partial_i\tilde{\theta} - \Lambda^2\Pi^B(\tilde{\mathbf{x}},\tilde{t})\partial_i\tilde{\theta} + \partial_j\left[\nu\left(\partial_j\tilde{u}_i + \partial_i\tilde{u}_j\right)\right] \\
&+ \nu\left(\partial_j\tilde{u}_i + \partial_i\tilde{u}_j\right)\partial_j\tilde{\theta} \qquad (2.86) \\
\partial_t\tilde{\theta} + \tilde{u}_j\partial_j\tilde{\theta} =& \partial_j\left(\mathcal{D}\partial_j\tilde{\theta}\right) \qquad (2.87) \\
\partial_j\tilde{u}_j =& - \partial_j\left(\mathcal{D}\partial_j\tilde{\theta}\right) \qquad (2.88)
\end{aligned}$$

Chapitre 3

Numerical methods

Contents

The objective of this chapter is to present shortly the numerical methods used in this thesis. At first, we introduce the Fourier pseudo-spectral method and the third-order Runge-Kutta Strong Stability Preserving (SSP) time advancement scheme . We focus on the solution of the pressure Poisson equation in the incompressible and variable density cases. In particular, for the latter case, we present the Generalized Minimal Residual (GMRES) iterative solver, employed to solve the non-local elliptic equation. In section 3.2.4, we discuss the case of variable transport coefficients and the implicit solution of the diffusive part of the equations.

Finally, we discuss the convergence of the iterative GMRES scheme and the different steps used to validate the code.

3.1 Equations

The equations derived in chapter 2 are not in conservative form. So that during computation, conservation properties may not be assured [Canuto et al. 2012]. The use of the following vector calculus identity

$$(\mathbf{u}\nabla)\mathbf{u} = \omega \times \mathbf{u} + \frac{1}{2}\nabla \mathbf{u}^2 \text{ where } \omega = \nabla \times \mathbf{u}, \tag{3.1}$$

semi-conserves kinetic energy (at least for inviscid flow), and assures numerical stability, which is not granted if we use the standard formulation. Using this substitution, we redefine the pressure to include an additional kinetic energy contribution, into a new variable π^*, as

$$\pi^* = \pi + \frac{1}{2}\mathbf{u}^2. \tag{3.2}$$

The resulting formulation of the equation is called rotation formulation.

Here we rewrite equations in a more compact form that is common to the two studies of this thesis, spherical compression, and USHT, with incompressible and variable density approximations.

- The incompressible approximation yields

$$\partial_t u_i + \underbrace{\mathcal{N}_\omega}_{1} = -\partial_i \pi^* + \partial_j\left(\nu \partial_j u_i\right) + \underbrace{\mathcal{F}_\theta}_{6} \tag{3.3}$$

$$\partial_t \theta + \underbrace{\mathcal{N}_u(\theta)}_{2} = +\partial_j\left(\mathcal{D}\partial_j \theta\right) + \underbrace{\mathcal{F}_L}_{7} \tag{3.4}$$

$$\partial_j u_j = 0. \tag{3.5}$$

- The variable density approximation yields

$$\partial_t u_i + \underbrace{\mathcal{N}_\omega}_{1} + \pi^* \partial_i \theta - \underbrace{\mathcal{N}_\theta(u_i,\theta)}_{3} - \underbrace{\mathcal{N}_\nu(u_i,\theta)}_{4} = -\partial_i \pi^* + \underbrace{\mathcal{F}(x_i,\theta)}_{5} + \partial_j\left(\nu \partial_j u_i\right) + \underbrace{\mathcal{F}_\pi}_{8} \tag{3.6}$$

$$\partial_t \theta + \underbrace{\mathcal{N}_u(\theta)}_{2} - \partial_j\left(\mathcal{D}\partial_j \theta\right) = \underbrace{\mathcal{F}_L}_{7} \tag{3.7}$$

$$\partial_j u_j = -\partial_j\left(\mathcal{D}\partial_j \theta\right) \tag{3.8}$$

In the previous equations, we have used the following short notation :

1. $$\mathcal{N}_\omega = \omega \times \mathbf{u}$$

   This term, also called the Lamb vector $\mathbf{l}$, comes from the reformulation of the nonlinear term to have better energy conservation and stability properties.

2. $$\mathcal{N}_u(\theta) = u_j \partial_j \theta$$

   This is the nonlinear advection term in the scalar θ equation.

3. $$\mathcal{N}_\theta = \frac{u_k u_k}{2} \partial_i \theta$$

   This terms appears when we use the identity (3.1) to introduce the rotation formulation, in order to redefine the pressure as in Eq. (3.2).

4. $$\mathcal{N}_\nu(u_i, \theta) = \partial_j \left(\nu \partial_i u_j\right) + \nu \left(\partial_j u_i + \partial_i u_j\right) \partial_j \theta$$

   This term contains nonlinear viscous contributions. They are among the new nonlinearity introduced by the variable density approximation.

In addition to the above terms which are always present, the following ones may appear, depending on the problem which is specifically studied. In the spherical compression case

5. $$\mathcal{F}(x_i, \theta) = -\Lambda^2 \Pi^B(x_i, t) \partial_i \theta$$

   This is a forcing term due to the base pressure gradient. In this case we do not have other forcing terms, so that

6. $$\mathcal{F}_\theta = 0$$

7. $$\mathcal{F}_L = 0$$

8. $$\mathcal{F}_\pi = 0$$

In the USHT study :

5. $$\mathcal{F}(x_i, \theta) = \mathcal{F}(\theta) = -gL\partial_i \theta$$

   This forcing term comes from the mean homogeneous pressure.

6. $$\mathcal{F}_\theta = g\theta$$

   This term corresponds to the linear approximation of the forcing from the mean pressure.

7. $$\mathcal{F}_L = -\frac{1}{L} u_3$$

   This forcing term comes from the mean θ gradient in the scalar equation.

8.
$$\mathcal{F}_\pi = -\frac{1}{L}\pi^*\delta_{i3}$$
This forcing term comes from the mean θ gradient in the momentum equation.

3.2 Direct numerical simulations

Spectral methods are well-established tools in fundamental studies in fluid mechanics [Canuto et al. 2012] because they are among the highest precision methods. When the solution is smooth, the decay of the error is exponential, as we increase the resolution. Since spectral methods are a particular case of methods of weighted residuals [Canuto et al. 2012], the choice of test and trial functions characterizes different types of spectral methods. In particular, in this discretization, these functions have global support that coincides with the domain of the problem under consideration. Trial functions are used as basis functions for the series expansion of the solution, while the test functions ensure that the differential equation is satisfied as close as possible by the approximation series.

The choice of the trial function depends mostly on the boundary conditions of the problem. There are three classes of polynomials that are widely employed : Fourier, Chebyshev, and Legendre. For the test functions, there are usually three alternatives :

1. If one chooses to have the same as trial functions we have Galerkin spectral scheme ;
2. If one selects translated Dirac delta functions centered on the mesh points, the scheme is called collocation or pseudo-spectral ;
3. If one instead wants the same trial and test functions which do not satisfy boundary conditions, we have the tau spectral scheme ;

In this work, we use a Fourier pseudo-spectral (collocation) scheme as it has been already proven very effective in fluid dynamics problem [Orszag and Patterson 1972].

3.2.1 Pseudo-spectral computation using FFT

One of the advantages of using the Fourier spectral method is that there are libraries that implement the discrete Fourier transform algorithm very effectively. All the most famous implementations are based on the Fast Fourier Transform (FFT), an algorithm of Cooley and Tukey (1965). One of the most famous is the Fastest Fourier Transform in the West (FFTW) library developed at MIT by Frigo and Johnson (2005). In pseudo-spectral methods, the derivatives are calculated in the Fourier space since they reduce to the multiplication of Fourier coefficients by the wavenumbers. All products are instead done in physical space.

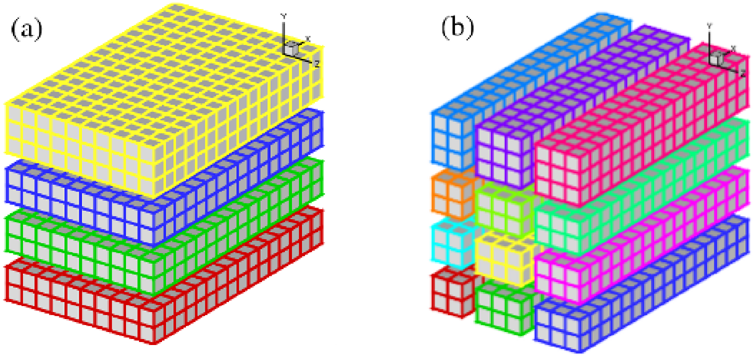

FIGURE 3.1 – From the site http ://www.2decomp.org

In this thesis, we have developed a DNS code based on the Parallel Three-Dimensional Fast Fourier Transforms (PDFFT++), a library for large-scale computer simulations on parallel platforms, developed by Pekurovsky (2012). This library allows the two-dimensional or "pencil" decomposition of the computational domain depicted in Figure 3.1(b), whereas the old version of the DNS code used a one dimensional or "slab" decomposition 3.1(a). If one has a three-dimensional problem where the domain dimensions are $N_x \times N_y \times N_z$, where x, y, and z are the three spacial dimensions, the 1D decomposition allows dividing the domain into planes which are distributed on the available processors N_P. Once the direction of the decomposition is chosen, here we chose z, every processor receives a slab of dimension $N_x \times N_y \times \frac{N_z}{N_P}$. With this decomposition, one can, at most, use the number of processors equal to the size of the domain. For instance, in this case, $N_P = N_z$ is the maximum possible number of processors.

The two-dimensional decomposition allows to have "pencils" or "columns" instead of planes. If we consider the same domain as before, the new sub-domains distributed on every processor have dimension $N_x \times \frac{N_y}{N_{P1}} \times \frac{N_z}{N_{P2}}$. Now the number of the processors that can be potentially used for the domain decomposition is $N_P = N_{P1} \times N_{P2}$. If we consider the maximums of N_{P1} and N_{P2}, we have $N_P = N_y \times N_z$.

If all the dimensions are equal, $N_x = N_y = N_z = N$, 1D, and 2D decomposition allows using respectively at most N and N^2 processors, making it clear why it is interesting to develop a new code based on the 2D decomposition.

The scaling properties of the new direct numerical simulation code, whose numerical details are detailed in the following section, are presented in Figure 3.2. The set-up used for the speed-up calculation is a 1024^3 decay of homogeneous isotropic turbulence, with the resulting time-averaged over 50 time steps. The speed-up is defined as

$$\text{Speed-up} = \frac{\text{Iteration time with N cores}}{\text{Iteration time with 256 cores}}. \tag{3.9}$$

This quantity, which is usually defined with respect to the serial iteration time, in

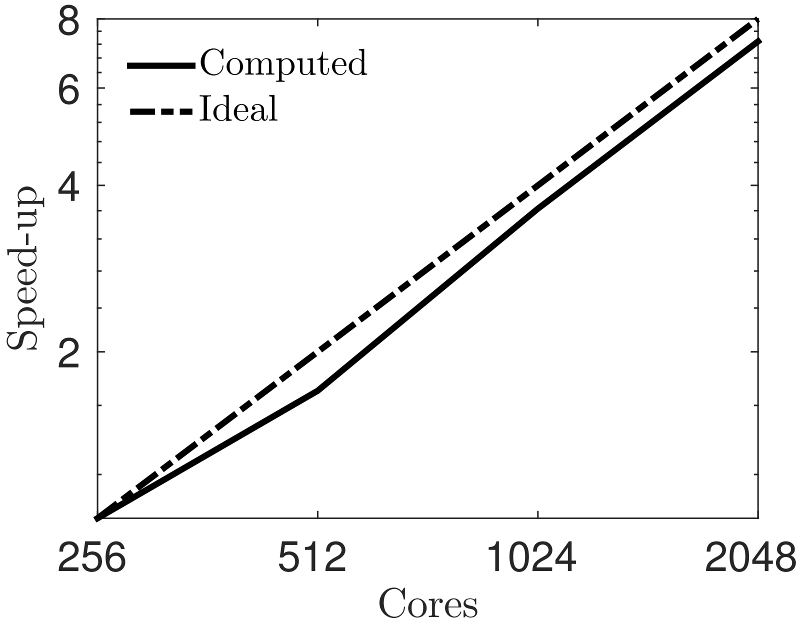

FIGURE 3.2 – Speed up of the code

this case, due to the memory requirements, is defined using the iteration time with 256 cores.

3.2.2 Time advancement scheme

The time advancement is done in Fourier space so that Fourier coefficients are the dependent variables. The numerical scheme chosen is a third-order Runge-Kutta SSP [Gottlieb et al. 2001]. Consider the following dynamical system

$$\frac{dF}{dt} = \mathcal{L}(F,t). \tag{3.10}$$

The time advancement between t_n and t_{n+1} is done using the following three steps

$$F^1 = F(t_n) + \Delta t \mathcal{L}(F(t_n),t), \tag{3.11}$$

$$F^2 = \frac{3}{4}F(t_n) + \frac{1}{4}\Big(F^1 + \Delta t L(F^1, t+\Delta t)\Big), \tag{3.12}$$

$$F(t_{n+1}) = \frac{1}{3}F(t_n) + \frac{2}{3}\left(F^2 + \Delta t L\left(F^2, t + \frac{\Delta t}{2}\right)\right). \tag{3.13}$$

The sub-steps of the scheme are different if one considers either the incompressible approximations or the variable density one, as detailed hereafter.

3.2.2.1 Sub-steps for incompressible computation

One of the advantages of doing the time advancement in Fourier space, is that we can compute implicitly the viscous contribution. For that, one can define a new variable v as

$$v_i = u_i \exp\left[\nu k^2 (t - t_0)\right] \tag{3.14}$$

such that, in wave-number space, the equation for v_i does not have any explicit viscous term. After this substitution, we use the classical projection method of Chorin (1968). Starting at time t^n,

- Compute an intermediate velocity v_i^*

$$v_i^* = v_i^n - \Delta t FT(\mathcal{N}_\omega) \exp\left[\nu k^2 (t - t_0)\right]. \tag{3.15}$$

- Using the incompressibility condition we can derive a Poisson equation for π^*

$$\partial_{ii}^2 \pi^V = \frac{\partial_i v_i^*}{\Delta t}. \tag{3.16}$$

  solving this equation is straightforward in Fourier space.
- We obtain the velocity at time t^{n+1} from

$$v_i^{n+1} = v_i^* - \Delta t \partial_i \pi^*. \tag{3.17}$$

Here we have used the symbol π^V instead of π. The use of the exponential factor to take into account the viscous effects modifies the pressure terms as :

$$\pi^V = \pi \exp\left[\nu k^2 (t - t_0)\right].$$

3.2.2.2 Sub-steps for variable density computation

In this case, the time-advancement steps are a bit more complicated. At time t^n

- Compute intermediate variables u_i^* (without taking into account π^*) and θ^*. In this step, we compute explicitly only a part of the viscous contribution :

$$\begin{aligned} u_i^* = u_i^n + \Delta t [&\mathcal{N}_\omega(u_i^n) + \mathcal{N}_\theta(u_i^n, \theta^n) \\ &+ \mathcal{F}(x_i, \theta^n) + \mathcal{N}_\nu(u_i^n, \theta^n)], \end{aligned} \tag{3.18}$$

$$\theta^{n+1} = \theta^n - \Delta t \mathcal{N}_u(\theta^n). \tag{3.19}$$

- The updated velocity u^{n+1} is obtained by taking into account π

$$u_i^{n+1} = u_i^* + \Delta t(-\partial_i \pi^* - \pi^* \partial_i \theta^n - \mathcal{F}_{\pi^*}). \tag{3.20}$$

— Applying the divergence operator to Eq. (3.20) we obtain the Poisson equation

$$\partial^2_{ii}\pi^* + \pi^*\partial^2_{ii}\theta^n + \partial_i\pi^*\partial_i\theta^n + (\mathcal{F}_\pi)_3 = \frac{1}{\Delta t}\left(-\partial_i u_i^{n+1} + \partial_i u_i^*\right). \tag{3.21}$$

At this point we use the expression for the divergence of u_i^{n+1} given by the variable density approximation $\partial_i u_i^{n+1} = -\partial_j(\mathcal{D}\partial_j\theta^{n+1})$ and we obtain

$$\partial^2_{ii}\pi^* + \pi^*\partial^2_{ii}\theta^n + \partial_i\pi^*\partial_i\theta^n + (\mathcal{F}_\pi)_3 = \frac{1}{\Delta t}\left(\partial_j\left(\mathcal{D}\partial_j\theta^{n+1}\right) + \partial_i u_i^*\right). \tag{3.22}$$

This is a non local Poisson equation that has to be solved with an iterative method. Once π^* is computed, we can finally use Eq. (3.20) to obtain the velocity at time t^{n+1}.

3.2.3 Solution of the Poisson equation

It is worth devoting here a detailed description to the solution method for the Poisson equation, since this task has proven to present difficulties, especially in the variable density case, and has required a dedicated implementation of the original method proposed by Di Pierro (2017). In the incompressible calculations, the Poisson equation in Fourier space has a straightforward solution. We start from the Fourier transform of equation (3.16)

$$k^2\hat{\pi}^* = \frac{k_i\hat{v}_i^*}{\Delta t},$$

where k is the module of the wavevector, whose solution is straightforward :

$$\hat{\pi} = \frac{k_i\hat{v}_i^*}{k^2\Delta t}.$$

In the algorithm for the variable density solution, the equation is more complicated given the non-locality of $\hat{\pi}^*$ in Fourier space :

$$k^2\hat{\pi} + FT\left[\pi\partial^2_{ii}\theta^n\right] + FT[\partial_i\pi\partial_i\theta^n] = \frac{1}{\Delta t}\left(FT\left[\partial_j\left(\mathcal{D}\partial_j\theta^{n+1}\right)\right] + k_i\hat{u}_i^*\right). \tag{3.23}$$

Di Pierro (2017), using $1D$ differentiation matrices, showed that the operator on the left-hand side of the Eq. (3.23) is ill-conditioned. To improve the convergence, he proposes to use the constant density operator as a preconditioner and to introduce a new variable ϕ, such that

$$\pi = e^{-\theta^n/2}\phi.$$

The resulting equation for ϕ is written in physical space as

$$\partial^2_{ii}\phi + \frac{\phi}{2}\partial^2_{ii}\theta^n - \frac{\phi}{4}||\partial_i\theta^n||^2 = \frac{e^{\theta^{n+1/2}}}{\Delta t}\left(\partial_j\left(\mathcal{D}\partial_j\theta^{n+1}\right) + \partial_i u_i^*\right). \tag{3.24}$$

The benefit of this choice is not only connected to the decrease of the condition number but it saves us the computation of the scalar product $\partial_i \pi \partial_i \theta^n$. We can rewrite this equation in condensed form, calling L the operator acting on ϕ and b the right-hand side of the equation :

$$L\phi = b. \tag{3.25}$$

The simplest iterative method for solving Eq. (3.24) is the fixed point iteration method [Di Pierro and Abid 2013]. One of the main disadvantages is the slow convergence of the method when compared with other iterative solvers, and the dependence of the convergence on the mesh size. With this method, the convergence is obtained if

$$\max\left(|\partial_i \theta|\right) < k \tag{3.26}$$

where k is the biggest resolved wavenumber allowed by the mesh. More explicitly, characteristic scales of θ gradients must be of the same size as the grid discretization. See Di Pierro and Abid (2013), Di Pierro (2012) for details. In our work, we would like to achieve relative rapid convergence without such constraints on the grid-$\partial_i \theta$ relation. The quest to find the best all-purpose iterative method is a rather difficult one. In particular, it has been shown by Nachtigal et al. (1992) that the best iterative solver in one case may perform poorly in other situations. In his work, Di Pierro (2017) tested four iterative schemes to solve a non-local Poisson equation. They tested conjugated gradient (CG), Richardson minimal residual (RMR), and the generalized minimal residual methods (GMRES). They find that the GMRES method is the best option, even if it has a higher cost per iteration, and it is more complex to implement. In light of these results, we have decided to implement this algorithm to solve Eq. (3.24). Details of the implementation are given in section 3.2.3.1.

3.2.3.1 Generalized Minimal Residual (GMRES) algorithm

The generalized minimum residual (GMRES) is an iterative method to solve linear systems proposed by Saad and Schultz (1986). It is part of a class of iterative solvers based on Krylov spaces. The methods in this class are among the best iterative methods available to solve problems involving non-symmetric matrices and operators. Such methods are conjugated gradient, bi-conjugated gradient, and the GMRES. The idea behind this approach is to converge to the exact solution of the system (3.25), using the sequence of approximate solutions

$$\phi_n \in \phi_0 + K^n(r_0, L) \tag{3.27}$$

where $K^n(r_0, L)$ is the Krylov subspace generated by the discretized operator L and the starting vector $r_0 = b - L\phi_0$

$$K^n(r_0, L) = \{r_0, Lr_0, L^2 r_0 ... L^{n-1} r_0\} \tag{3.28}$$

where ϕ_0 is an initial choice of ϕ.

The main feature of the GMRES is that the sequence (3.27) is built to minimize the residuals $r = \|b - L\phi\|_2$. It can be shown [Stoer and Bulirsch 2013] that the solution of the problem $L\phi = b$ lies in the affine spaces created by $\phi_n \in \phi_0 + K^n(r_0, L)$, that is, the solution ϕ can be decomposed in this new basis $\phi^n = K^n g$ for some vector g.

The problem with the definition (3.28) is that when n increases, the vectors in the base become more and more linearly dependent so that the method becomes unstable. Instead, the alternative is to construct a new orthonormal basis for K^n using Arnoldi iterations [Stoer and Bulirsch 2013]. The corresponding algorithm is as follows :

- Choose first guess x_0, and the size of the basis m.
- Compute $r_0 = b - L\phi_0$, $\beta = \|r_0\|_2$ and $q_1 = r_0/\beta$.
- To compute the orthonormal base we use the Gram-Schmidt process :
  For $j = 1, .., m$ do
  - Compute $w = Lq_j$. w is the vector that we would have in the Krylov base using the classic power iteration.
  - For w to be orthonormal to the other vectors in the basis we perform the following operation :
    For $i = 1, .., j$ do
    - $h_{i,j} = (w, q_i)$, where $(,)$ is the inner product $(w, q_i) = w^T q_i$
    - $w = w - h_{i,j} q_i$
  - Compute $h_{j+1,j} = \|w\|_2$ and $q_{j+1} = w/h_{j+1,j}$
- At the end we have the orthonormal basis Q_m defined by $Q_m = [q_1, ...q_m]$

In this new basis, ϕ^n is decomposed as

$$\phi_n = Q_n y_n \tag{3.29}$$

The previous Arnoldi process produces the coefficient $h_{i,j}$ that are the coefficients of an upper Hessenberg matrix [Stoer and Bulirsch 2013] H_n that satisfies the following equality

$$LQ_n = Q_{n+1} H_n. \tag{3.30}$$

Recall that the objective of the method is to minimize the norm of the residual $\|r_n\|_2 = \|b - L\phi\|_2$, knowing that the updated solution at each step is $\phi = \phi_0 + \phi_n$. Thus we can rewrite the minimization as

$$\min \|r_n\|_2 = \min \|b - L(\phi_0 + \phi_n)\|_2 = \min \|r_0 - L\phi_n\|_2 . \tag{3.31}$$

Using relations (3.29) and (3.30) we can rewrite the problem as

$$\min \left\| Q_{n+1}^T r_0 - H_n y \right\|_2 . \tag{3.32}$$

In this equation the matrix Q_{n+1} contains the orthonormal vector computed during the Arnoldi iterations. That is the matrix-vector product is zeros for all but one column and Eq. (3.32) simplifies to

$$\min \|\beta e_1 - H_n y\|_2 \,, \tag{3.33}$$

where $\beta = \|r_0\|_2$ and e_1 is the n-dimensional vector $e_1 = [1, 0..., 0]$. Equation (3.33) is a least square problem, that we solve using Givens rotations [Stoer and Bulirsch 2013]. Once y is computed the solution is

$$\phi = \phi_0 + Q_n y.$$

To sum up the steps for the GMRES algorithm, they are presented in a concise form in Algorithm 1 :

Algorithm 1 GMRES

```
 1: Choose the dimension of the Krylov subspaces $m$, the initial guess $\phi_0$.
 2: Compute the initial residual $r_0 = b - L\phi_0$, $\beta = \|r_0\|_2$ and $q_1 = r_0/\beta$
 3: for $j = 1, ...m$ do
 4:     Compute $w = Lq_j$
 5:     for $j = 1, ...m$ do
 6:         $h_{i,j} = (w, q_i)$
 7:         $w = w - h_{i,j}q_i$
 8:     end for
 9:     Compute $h_{j+1,j} = \|w\|_2$ and $q_{j+1} = w/h_{j+1,j}$
10: end for
11: Define the matrix $Q_m = [q_1, ...q_m]$
12: Compute $\phi = \phi_0 + Q_n y_m$ where $y_m = \min \|\beta e_1 - H_n y_m\|_2$
13: If satisfied with the results stop, else set $\phi_0 = \phi_m$ and go to 3
```

3.2.4 Non uniform transport coefficients

In this work, we will consider the compression of weakly coupled plasma mixtures. In these computations, transport coefficients vary considerably in time and space, reaching considerably large values, so that an explicit treatment may require a very stringent restriction on the time step, to satisfy numerical stability constraints. That is why we use an implicit treatment of diffusive terms in the momentum and scalar equation. This method has already be employed in the case of variable viscosity by Gréa et al. (2014), using finite differences in physical space to solve the implicit problem. In the present work, we choose to use the GMRES solver already presented in the previous section.

The following sub-steps are performed before the projection algorithm presented the section 3.2.2.2

- The values of transport coefficients ν and $\mathcal{D}$ depend on mass fraction, temperature, and θ. Therefore the first step is to compute their values at time t^n.

$$\nu^n = \nu(Y^n, T^n, \theta^n) \qquad \text{and} \qquad \mathcal{D}^n = \mathcal{D}(Y^n, T^n, \theta^n).$$

- Ferziger and Peric (2012) argue that the main diffusive contributions that need implicit treatment are the terms

$$\partial_j \left(\nu \partial_j u_i\right) \qquad \text{and} \qquad \partial_j \left(\mathcal{D} \partial_j \theta\right).$$

  While the other viscous nonlinear viscous contribution $\mathcal{N}_\nu(u_i, \theta)$ can be computed explicitly. Furthermore we make the hypothesis that $\mathcal{D}^{n+1/2} = \mathcal{D}^n$ and $\nu^{n+1/2} = \nu^n$, so that

$$\theta^{n+1/2} = \theta^n + \Delta t \partial_j (\mathcal{D}^{n+1/2} \partial_j \theta^{n+1/2}), \tag{3.34}$$

$$u_i^{n+1/2} = u_i^n + \Delta t \partial_j (\nu^{n+1/2} \partial_j u_i^{n+1/2}). \tag{3.35}$$

- At this stage we modify the intermediate variable u^* using $u^{n+1/2}$ (and not u^n) adding the nonlinear effect of the viscous contribution computed explicitly :

$$u_i^* = u_i^{n+1/2} + \Delta t [\mathcal{N}_\omega \left(u_i^{n+1/2}\right) + \mathcal{N}_\theta \left(u_i^{n+1/2}, \theta^{n+1/2}\right) \tag{3.36}$$

$$+ \mathcal{F}\left(x_i, \theta^{n+1/2}\right) + \mathcal{N}_\nu \left(u_i^{n+1/2}, \theta^{n+1/2}\right)]. \tag{3.37}$$

3.2.5 Preconditioning and initial guesses

In this chapter we have presented three equations that have to be solved using iterative methods (3.34), (3.35), (3.24). In all three cases, we have decided to use preconditioning to improve the performance of the GMRES algorithm. In general, preconditioning is employed for ill-conditioned problems to lower the condition number of the operator and obtain better performances from the iterative method, *i.e* accelerate the rate of convergence.

The modifications of algorithm 1 are described in algorithm 2, where the operator M is the preconditioner.

The next question is the choice of M. Di Pierro (2017) demonstrates that the constant density operator is very effective as a preconditioner for the solution of the Poisson equation. Using the same argument, we propose the implicit constant viscous operator for the variable viscosity and diffusivity computations. In particular the constant preconditionings are

Algorithm 2 GMRES with preconditioning

```
1:  Choose the dimension of the Krylov subspaces $m$, the initial guess $\phi_0$.
2:  Compute the initial residual $r_0 = b - L\phi_0$, $\beta = \|r_0\|_2$ and $q_1 = r_0/\beta$
3:  for $j = 1, ...m$ do
4:      Compute $z_j = M^{-1}q_j$
5:      Compute $w = Lz_j$
6:      for $j = 1, ...m$ do
7:          $h_{i,j} = (w, q_i)$
8:          $w = w - h_{i,j}q_i$
9:      end for
10:     Compute $h_{j+1,j} = \|w\|_2$ and $q_{j+1} = w/h_{j+1,j}$
11: end for
12: Define the matrix $Q_m = [q_1, ...q_m]$.
13: Compute $\phi = \phi_0 + M^{-1}Q_n y_m$ where $y_m = \min \|\beta e_1 - H_n y_m\|_2$
14: If satisfied with the results stop, else set $\phi_0 = \phi_m$ and go to 3
```

1. $M_\nu = \frac{1}{1+\nu\Delta t k^2}$
2. $M_\mathcal{D} = \frac{1}{1+\mathcal{D}\Delta t k^2}$
3. $M_\pi = -\frac{1}{k^2}$

where M_ν and $M_\mathcal{D}$ are the preconditioner for the variable viscosity and variable diffusivity substeps (3.34), (3.35) and M_π is the preconditioning matrix for the Poisson equation (3.24).

The last choice to make is to decide the initial guesses to start the algorithm. In our computation they are

1. $u_0^{n+1/2} = \frac{u^n}{1+\nu\Delta t k^2}$
2. $\theta_0^{n+1/2} = \frac{\theta^n}{1+\mathcal{D}\Delta t k^2}$
3. $\phi_0 = \frac{k_i \hat{u}_i^*}{k^2 \Delta t} e^{\theta/2}$

where $u_0^{n+1/2}$ and $\theta_0^{n+1/2}$ are the initial guesses for the variable transport coefficients substeps. They are also the solution that we would have in case of constant viscosity and diffusivity. ϕ_0 is the initial guess for the GMRES algorithm applied to the Poisson equation and it corresponds to the ϕ that we obtain in the solution of the incompressible case.

3.3 Convergence and validation

In this section, we describe the convergence criteria for the GMRES iterative schemes together with the validation steps for the new direct numerical simulation code. We start with the incompressible decay of homogeneous isotropic turbulence (HIT), to validate the computations of the nonlinear convective terms. We move on to the decay of HIT with variable viscosity to validate the GMRES algorithm for the computation of the diffusive terms. The first step toward the validation of the GMRES algorithm for the pressure Poisson equation concerns a case of unstably stratified homogeneous turbulence with low non-Boussinesq effects, such that variable density and Boussinesq approximations should have the same results.

3.3.1 Convergence of the iterative GMRES algorithm

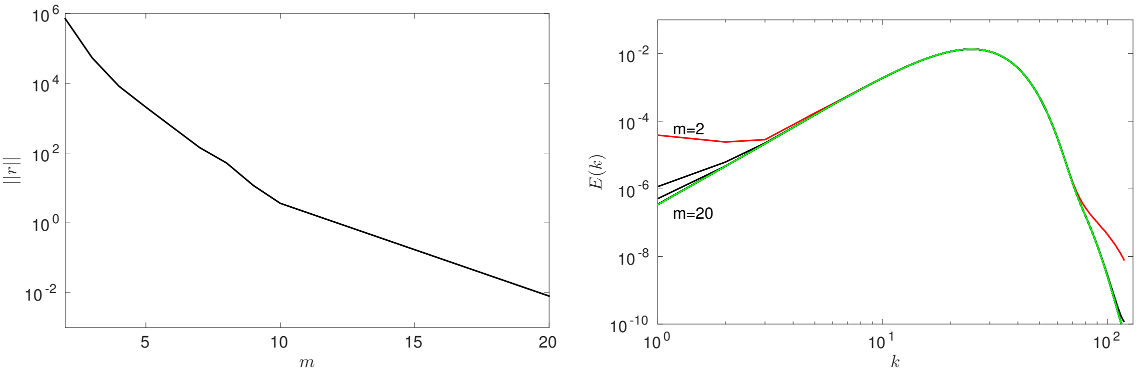

(a) (b)

FIGURE 3.3 – (a) Evolution of GMRES algorithm residuals for the pressure Poisson equation as a function of the Krylov subspaces dimension m (b) Kinetic energy spectra of an unstably stratified homogeneous turbulence simulation, computed at the same time with different Krylov subspaces dimension m.

When one deals with an iterative algorithm to solve linear systems, it is useful to have an idea of what are the conditions under which the iterative scheme can be considered converged. In particular, the GMRES algorithm has a free parameter, the size of the Krylov subspace m, which should be carefully tuned. The more m grows, the more efficient the GMRES method becomes, but at the same time, it became computationally more expensive. Hence, for our computations, a trade-off has to be decided between the increased precision and the increased costs.

Numerical experiments show that a good compromise for the most challenging cases, with mesh sizes of 1024^3 and increasing density contrast, a Krylov base of $m = 20$ have good conservation and convergence properties.

In Figure 3.3, we show an example of the effects of m on the convergence of the GMRES for a 256^3 USHT computation. The decrease of the residuals is plotted in Figure 3.3a, while the consequences of the converged/un-converged iterative algorithm on the kinetic energy spectrum are shown in 3.3b. This convergence analysis, as a function of m, considers only one time step. To further validate the DNS code, we evaluated the conservation of mass of the numerical method, during the computations.

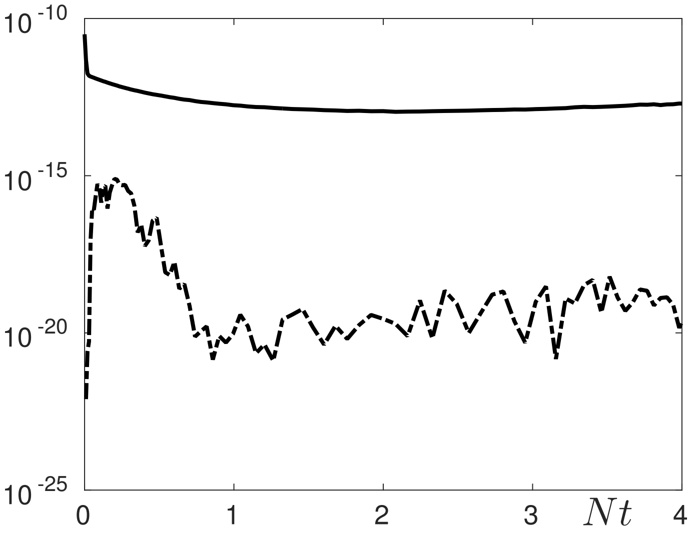

FIGURE 3.4 – Evolution of the variable density condition (dashed line) and norms of the residual (solid line) during an 256^3 USHT computation with $N = 1.4$ and no initial scalar fluctuations.

The equation expresses the mass conservation for the variable density computation

$$\partial_j u_j = -\mathcal{D}\partial^2_{jj}\theta, \tag{3.38}$$

which, if we separate the solenoidal u^S_j, $\partial_j u^S_j = 0$, and dilatational u^D_j, $\partial_j u^D_j \neq 0$, velocity contributions, becomes

$$\partial_j u^D_j = -\mathcal{D}\partial^2_{jj}\theta. \tag{3.39}$$

Therefore, to check the conservativity, during the simulation we compute the quantity

$$V^D = ||\partial_j u^D_j + \mathcal{D}\partial^2_{jj}\theta||. \tag{3.40}$$

An example of the values of V^D during an USHT simulation is given in Figure 3.4, together with the norm of the GMRES residuals at the same time.

3.3.2 Validation : Decay of incompressible homogeneous isotropic turbulence

The first step in validating the new direct numerical simulation code is to compute the time evolution of the isotropic homogeneous turbulence (HIT) decay. The results

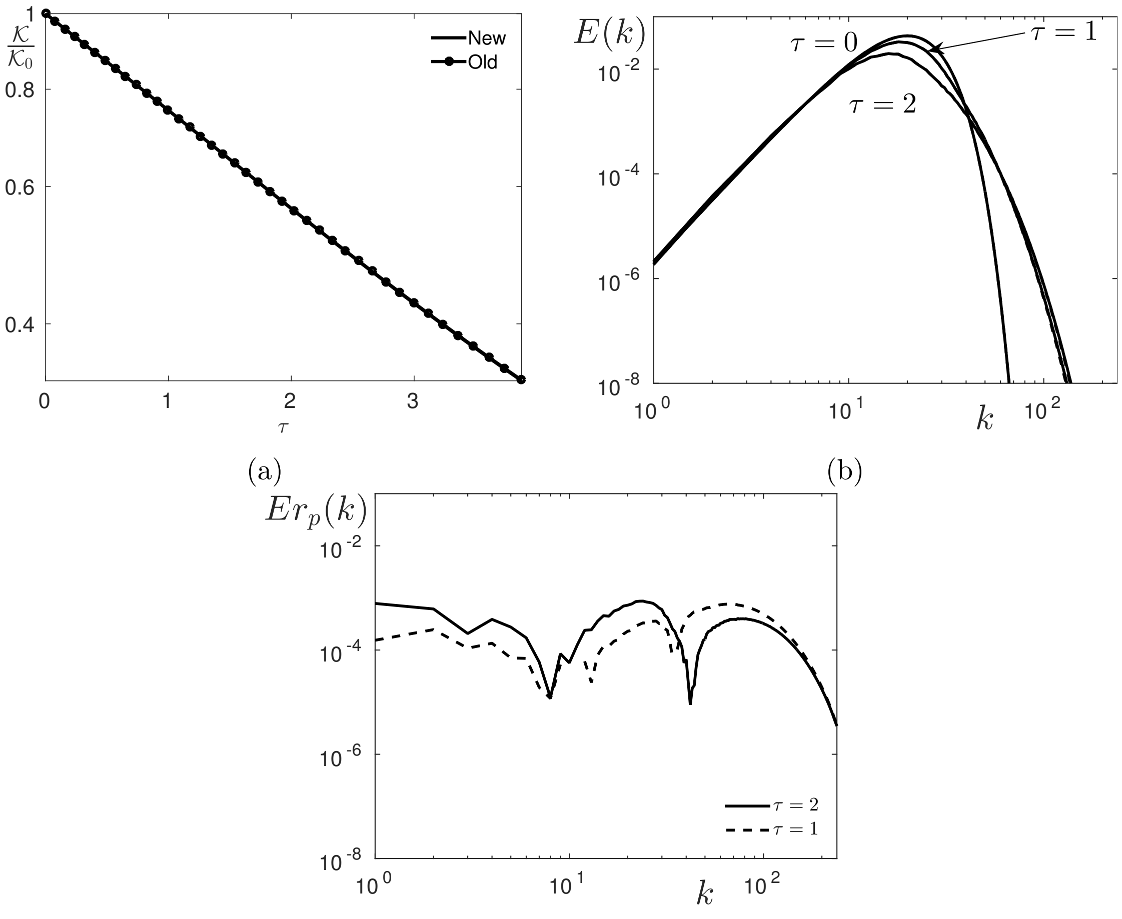

(a) (b)

(c)

FIGURE 3.5 – (a) Evolution of the turbulent kinetic energy, normalized with its initial value, as a function of the non-dimensional time τ. (b) Kinetic energy spectra at three times during the decay. Solid lines indicate results using the new code while dashed line the ones from the previous version. (c) Relative error Er_p between the old and new code.

are compared with the previous version of the DNS code parallelized in slab, described in Griffond et al. (2014).

We consider the case of a HIT with a resolution of 512^3 with an initial Reynolds number of $Re_0 = \frac{\mathcal{K}(0)^2}{\nu\epsilon(0)} = 30$, where ϵ is the turbulence dissipation, $\mathcal{K}$ the integrated turbulent kinetic energy and ν the kinematic viscosity.

The results of the simulations are shown in Figures 3.5 and 3.6. The evolution of the kinetic energy is plotted in 3.5a, as a function of the dimensionless time τ, defined as the time of the simulation divided by the eddy turnover time $t_E = \frac{1}{\mathcal{K}^{1/2(0)}k_p}$, where k_p is the peak of the energy spectrum at $t = 0$. We observe the excellent agreement between the two simulations, on the one-point statistics. Subsequently, the spectra, in Figure 3.5b, show how also the spatial dependencies are similar between the two simulations. In Figure 3.5b, the two results are superimposed, so that we cannot evaluate the differences between the two simulations. That is why in Figure 3.5c we show the relative error between the two spectra, computed as follow

$$Er_p(k) = \frac{E_N(k) - E_O(k)}{E_O(k)} \tag{3.41}$$

where $E_N(k)$ and $E_O(k)$ are respectively the resulting spectra of new and old code. Lastly, the qualitative comparison between the speed fields in Figure 3.6 confirms the similarity between the two results.

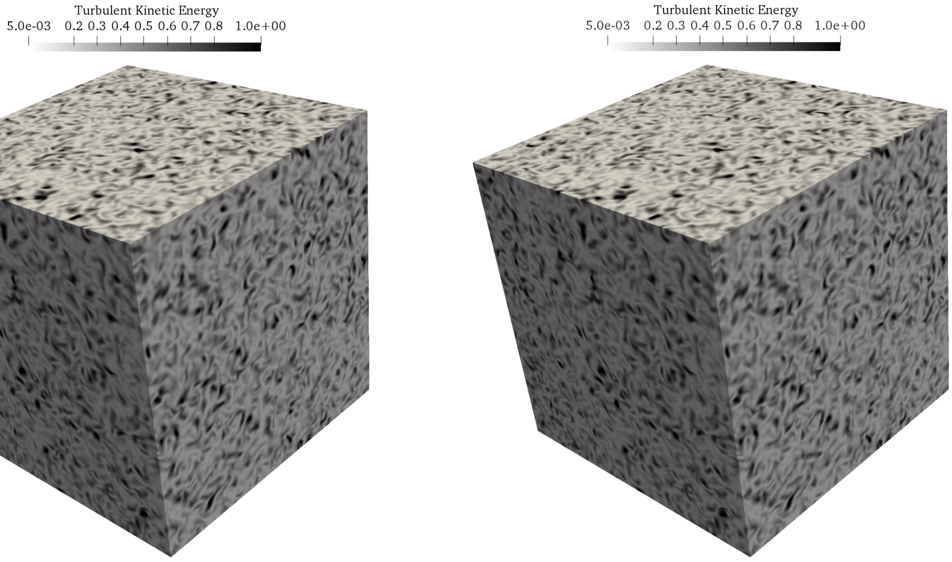

(a) (b)

FIGURE 3.6 – Contours of turbulent kinetic energy at $\tau = 2$ computed with (a) the previous version and with (b) the new version of the DNS code.

3.3.3 Validation : Decay of incompressible homogeneous isotropic turbulence with variable viscosity

To validate the GMRES algorithm for the variable transport coefficients, we compute a case of homogeneous isotropic turbulence with variable viscosity. Gréa et al. (2014) has investigated this problem using spectral direct numerical simulations where viscous effects are accounted for using an implicit finite difference scheme for equation 3.35. The viscosity has a linear relation with the scalar, θ

$$\nu = \nu_A + \mathcal{V}\theta \tag{3.42}$$

In this set up $\theta \in [-1, 1]$ and its averaged value on the volume is zero $\langle \theta \rangle = 0$, so that the mean value of viscosity is $\langle \nu \rangle = \nu_A$.

We compute the decay of homogeneous isotropic turbulence with a resolution of 256^3 with an average viscosity of $\nu_A = 0.5$. It has a maximum equal to 0.99 and a minimum of 0.01. The diffusivity is constant and equal to the minimum of viscosity, $\mathcal{D} = \nu_A$, such that the Schmidt number based on the averaged values is $Sc = \frac{\nu_A}{\mathcal{D}} = 50$.

In Figure 3.7a, we present the comparison of the turbulent kinetic energy as a function of the dimensionless time τ defined in section 3.3.2.

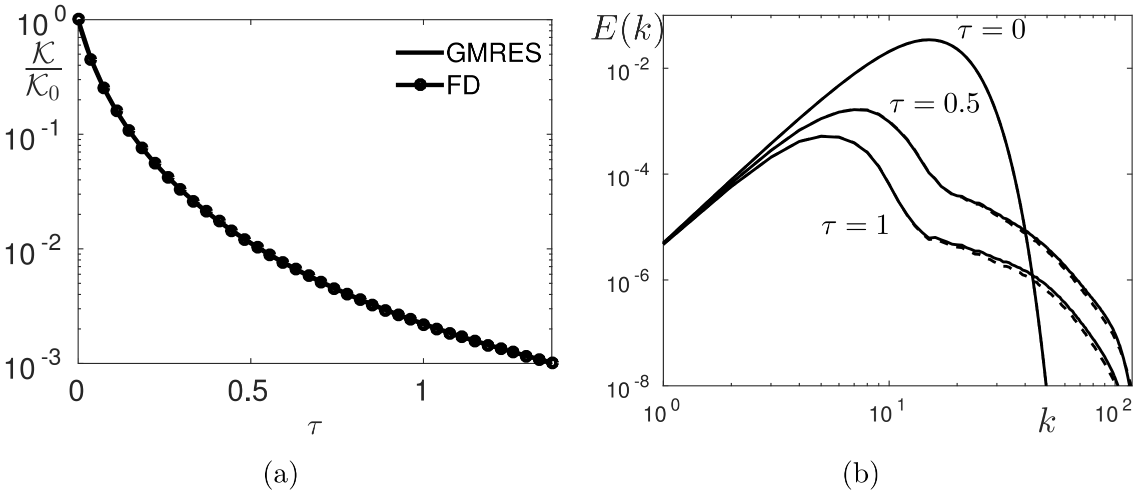

(a) (b)

FIGURE 3.7 – (a) Evolution of the turbulent kinetic energy, normalized with its initial value, as a function of the non-dimensional time τ (b) Kinetic energy spectra at three times during the decay. Solid lines indicate GMRES results while dashed line the finite differences ones.

The evolution of the integrated kinetic energies shows good agreement between the two simulations, and the two curves are superimposed. On the contrary, we observe some differences in the kinetic energy spectra. While at large scales, the two simulations have a good agreement, they show some differences when we look at smaller scales, with the finite difference computation that has a higher dissipation with a lower value of the spectrum at higher k. The difference is caused by the two numerical methods used to solve the variable viscosity step of the computation. The finite difference schemes have a higher numerical dissipation, confronted with the iterative spectral GMRES.

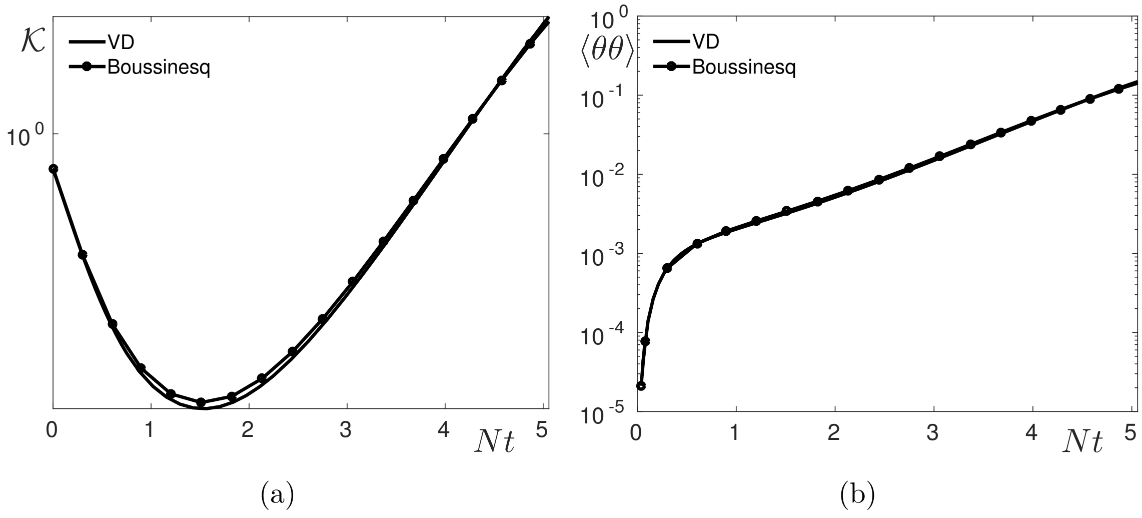

(a) (b)

FIGURE 3.8 – (a) Evolution of the turbulent kinetic energy and (b) scalar variance, as a function of the non-dimensional time Nt. Solid lines : Variable density computations. Solid lines with circles : Boussinesq results.

3.3.4 Validation : Variable density results with small non-Boussinesq effects.

To validate the GMRES algorithm for the Poisson equation, we use unstably stratified homogeneous turbulence (USHT) results with little effects coming from the density field, that is, a case where the small fluctuations approximation is valid.

In this configuration, we confront USHT results from computations using the Boussinesq and the variable density approximations. The 1024^3 simulations, are initialized with velocity fluctuations but without scalar fluctuations. The evolution of kinetic energy $\mathcal{K}$, and the scalar variance $\langle\theta\theta\rangle$ are reported in Figure 3.8.

The variance, in Figure 3.8b, shows a very good agreement between the two simulations, while for the kinetic energy, in Figure 3.8a, a little difference is observed during the decay phase, which is due to the different development of the turbulent energy cascade. The two integral quantities are plotted as a function of the dimensionless quantity Nt, where t is the simulation time and N is the stratification frequency defined, for the USHT computations, as $N = \sqrt{g/L}$, with g and L introduced in section 2.2.

The analogies and differences between the two simulations can be further evidenced by the kinetic energy, Figure 3.9a, and variance spectra, Figure 3.9b.

From the same initial condition at $Nt = 0$, the two simulations continue to have similar results on both spectra at $Nt = 2.5$, after the minimum of the decay. Eventually, at $Nt = 5$, the non-Boussinesq effects, explained in chapter 6, start to affect both large and small scales beginning to drive the two results apart.

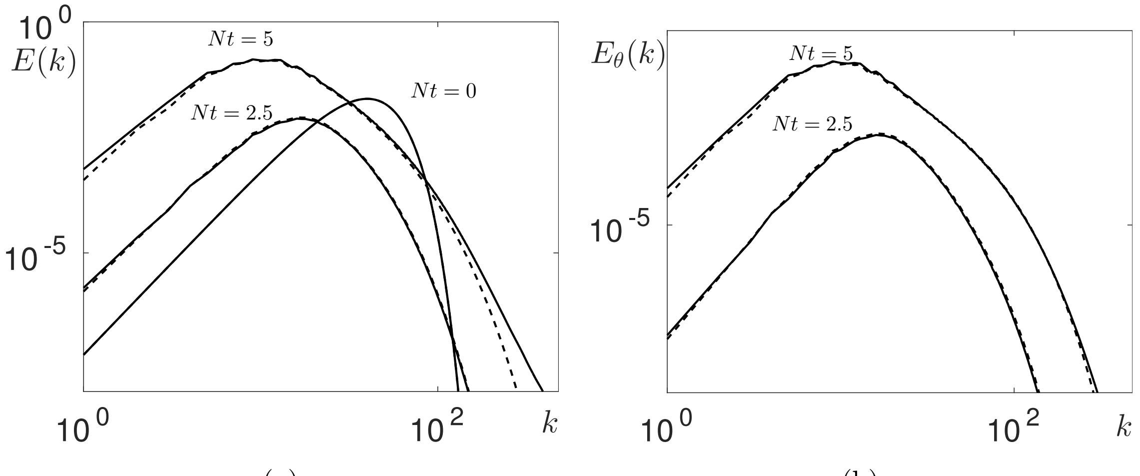

(a) (b)

FIGURE 3.9 – (a) Kinetic energy and (b) Scalar variance spectra at three times during the USH turbulence computations. Solid lines : Variable density computations. Dashed lines : Boussinesq results.

The similarity between the two approximations is confirmed qualitatively by the contours of the scalar θ in Figure 3.10. We observe the formation of the characteristic structures of USHT turbulence, with the light fluid moving upwards and the heavy downwards.

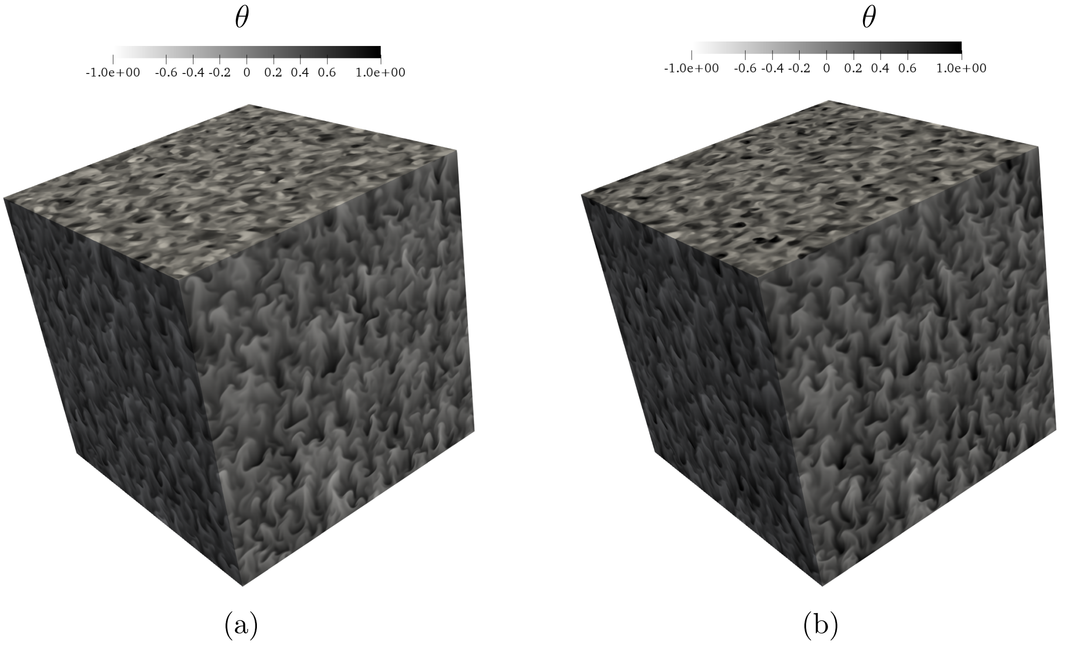

FIGURE 3.10 – Contours of the scalar θ at $Nt = 2.5$ computed with (a) the Boussinesq and (b) the new variable density approximations.

3.4 Initial conditions

In this section, we describe the method used to generate the initial conditions for the resolution of the dynamical equations. The initializing procedure for the homogeneous case is presented in section 3.4.1, while the initialization steps for the spherical compression case are resumed in section 3.4.2.

3.4.1 Homogeneous isotropic turbulence

Initial conditions for homogeneous isotropic turbulence are created in Fourier space, using the following kinetic energy spectrum

$$E(k) = A\left(\frac{k}{k_l}\right)^s \exp\left(-\frac{s}{2}\left(\frac{k}{k_l}\right)^2\right) \tag{3.43}$$

and random phases for the Fourier components. In Eq. (3.43), k_l is the peak wavenumber, s is the infrared slope, and A is a constant parameter used to adjust the amplitude of the spectrum such that it matches a specified initial total kinetic energy $\mathcal{K}(t = 0)$, via the relation

$$\mathcal{K}(t = 0) = \int_0^\infty E(k)dk \tag{3.44}$$

For the initialisation of the scalar field we use the same expression as (3.43) and a relation similar to (3.44) to achieve the desired initial scalar variance. Once the initial velocity and scalar fields are generated, there is a difference between the incompressible and variable density initializations.

For the incompressible case, we have to enforce the solenoidal constraint on the velocity field u_i. This requirement reduces in Fourier space to impose the velocity perpendicular to the wavevector :

$$u_i k_i = 0.$$

The initial condition for variable density computations requires an additional step. In fact for this case we know that velocity and the scalar θ have to satisfy the relation :

$$\partial_j u_{jVD} = -\mathcal{D}\partial^2_{jj}\theta. \tag{3.45}$$

In order to obtain consistent initial conditions we follow the same steps as Sandoval (1995). Using the Helmholtz theorem we can decompose the initial velocity field $\mathbf{u}$ into sum of solenoidal ($\nabla \times \mathbf{H}$) and irrotational ($\nabla\psi$) parts :

$$\mathbf{u}_{VD} = -\nabla\psi + \nabla \times \mathbf{H}. \tag{3.46}$$

We replace the divergence-free vector $\nabla \times \mathbf{H}$ with the incompressible initialization u_i :

$$u_{iVD} = -\partial_i\psi + u_i. \tag{3.47}$$

When we compute the divergence of (3.47), we have

$$\partial_i u_{iVD} = -\partial^2_{ii}\psi. \tag{3.48}$$

If we compare this relation with (3.45), the scalar field ψ is determined by $\psi = \mathcal{D}\theta$. So that the initial velocity fields for the variable density simulations are computed by

$$u_{iVD} = -\mathcal{D}\partial_i\theta + u_i \tag{3.49}$$

3.4.2 Spherical compressions

In section 2.3, we have described how, for the spherical compressions computations, we decompose the velocity and scalar fields as a superposition of base flow and perturbations, and we have discussed how the former is defined and imposed via analytical relations. In this part, we describe the initialization of the perturbations field. First, we use the Reynolds decomposition to separate the mean part of the velocity and the scalar fields from the fluctuations :

$$\theta = \overline{\theta} + \theta' \tag{3.50}$$

$$u_i = \overline{u}_i + u'_i. \tag{3.51}$$

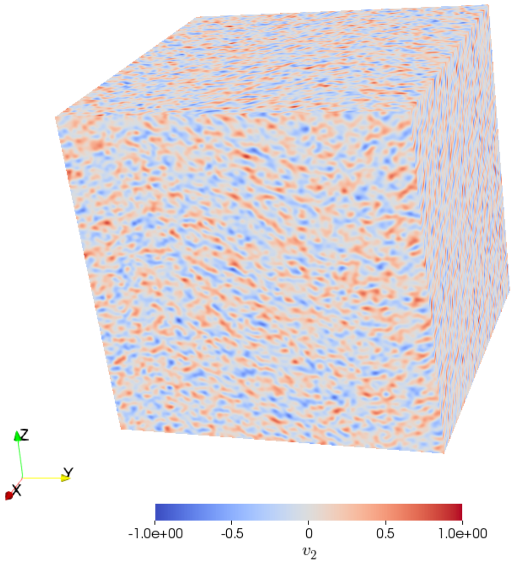

FIGURE 3.11 – Example of initial condition for the component v_2 of the velocity field, with $k_l = 30$ and $\mathcal{K} = 0.2$.

For this problem the mean is defined as a tangential average on the spherical angular variables ψ and ζ :

$$\overline{Q}(r) = \int_0^{2\pi} \int_0^{\pi} Q(t, r, \zeta, \psi) r^2 \sin(\zeta) d\psi d\zeta$$

where Q could be u_i or θ.

3.4.2.1 Initialization of velocity

In all the cases considered, the initial value of mean velocity field $\overline{u}_i$ is always zero. Thus we have to provide only the fluctuating velocity in the spherical layer. We proceed as follows :

1. An homogeneous isotropic velocity field is initialized as described in subsection 3.4.1, with prescribed kinetic energy and peak wavenumber.
2. We compute the vorticity $\omega = \nabla \times \mathbf{u}$ in physical space to which we apply a filter function $F(\mathbf{x})$, which detail are given in the coming subsection 3.4.3, to obtain the filtered vorticity $\omega^{\mathbf{F}}$.
3. Once the filtered vorticity is computed, it is transformed back to Fourier space (the $\hat{}$ indicates variables in Fourier space). At this point we use the vector calculus identity

$$i\mathbf{k} \times (i\mathbf{k} \times \hat{\mathbf{u}}) = i\mathbf{k}(i\mathbf{k}.\hat{\mathbf{u}}) - \hat{\mathbf{u}}(i\mathbf{k}.i\mathbf{k})$$

that can be rewritten as

$$\hat{\mathbf{u}}^F = \frac{i\mathbf{k} \times \hat{\omega}^F - i\mathbf{k}(i\mathbf{k}.\hat{\mathbf{u}}^F)}{\|\mathbf{k}\|_2^2}. \tag{3.52}$$

From (3.52) we see that there is the second term $-i\mathbf{k}(i\mathbf{k}.\hat{\mathbf{u}}^F)$, *i.e.* the gradient of the divergence of the filtered velocity field, that depends on the type of computation that we want to perform. In fact :

— For incompressible initial condition this term is zero, and the filtered velocity is

$$\hat{\mathbf{u}}^F = \frac{i\mathbf{k} \times \hat{\omega}^F}{\|\mathbf{k}\|_2^2}. \tag{3.53}$$

— While in the variable density case we use the relation (3.45) to obtain

$$\hat{\mathbf{u}}^F = \frac{i\mathbf{k} \times \hat{\omega}^F - i\mathbf{k}(\mathcal{D}\, \|\mathbf{k}\|_2^2\, \hat{\theta})}{\|\mathbf{k}\|_2^2}. \tag{3.54}$$

3.4.2.2 Initialization of the scalar θ

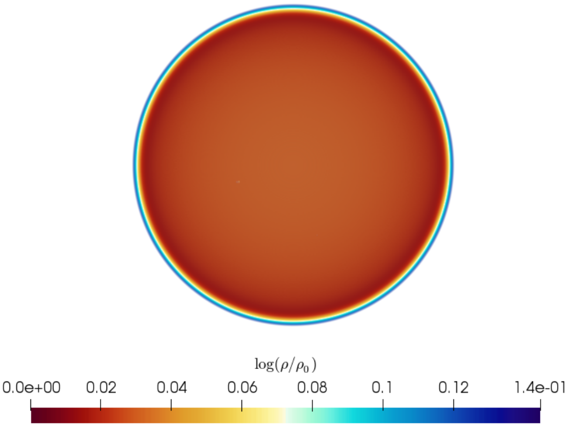

FIGURE 3.12 – Example of initial condition for the scalar field for the spherical compression computations. Here the Atwood number is0.07

The initial condition for the scalar θ is defined through the mean profile, with no fluctuations. In particular we use an analytical function of the radius r.

$$\theta_M(\mathbf{r}) = \frac{1}{2}\log\left(\frac{1-At}{1+At}\right)\left[2 - \tanh\left(\frac{1}{d}\Big(\frac{r-2R_0}{R_0}\Big)\right) + \tanh\left(\frac{1}{d}\Big(\frac{r+2R_0}{R_0}\Big)\right)\right] \tag{3.55}$$

where $At = \frac{\rho_{max}-\rho_{min}}{\rho_{max}+\rho_{min}} = \frac{\exp(\theta_{max})-1}{\exp(\theta_{max})+1}$ is the Atwood number. d is a parameter that is defined as :

$$d = \frac{2}{R_0\theta_{max}} \int_0^\infty \theta_M(1-\theta_M)dr \tag{3.56}$$

The integral in (3.56) is usually employed in the definition of the a mixing zone width [Andrews and Spalding 1990, Gréa 2013]. So that the specification of d directly imposes the initial width of the spherical mixing layer. The influence of the Atwood number and d on the radial profile of scalar is plotted in Figure 3.13. We observe on both figures 3.13a and 3.13b that the scalar gradient is steeper the smaller the d the larger the At. An example of the three dimensional contours for the scalar θ is shown in Figure 3.12.

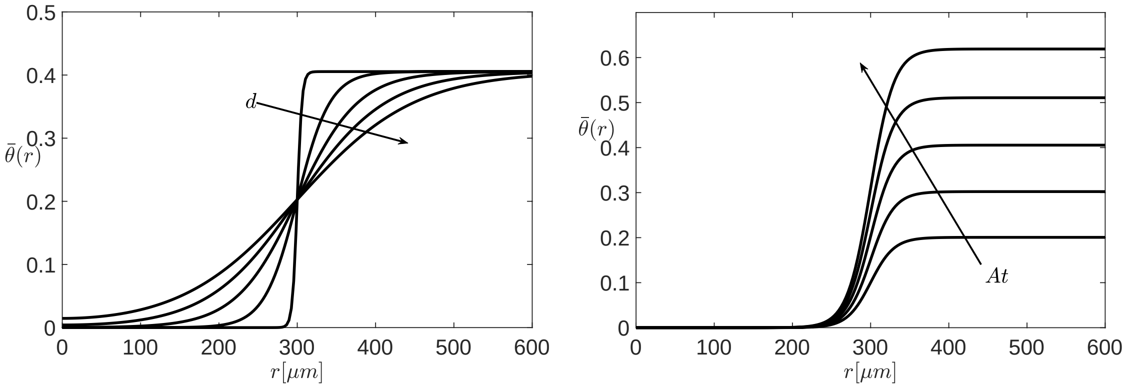

(a)

(b)

FIGURE 3.13 – Initial radial profile of the mean component of the scalar field $\bar{\theta}$. (a) Plot with constant Atwood number $At = 0.2$ and different values of the parameter $d = 0.01, 0.05, 0.10, 0.15, 0.2$, which increase in the direction of the arrow. (b) Plot with constant $d = 0.05$ and different values of the Atwood number,$\mathcal{A}_t = 0.1, 0.15, 0.2, 0.25, 0.3$, which increase in the direction of the arrow.

3.4.3 Filter

In the procedure of section 3.4.2.1, for the initial velocity field, we use a filter function to limit the fluctuation inside a defined spherical shell. The filter $F_s(\mathbf{x})$, is a smoothed square wave, initialized with the characteristic of the spherical layer, such as inner (r_m) and outer (r_M) radii :

$$F_s(\mathbf{x}) = 1 \text{ for } r_m \leq |\mathbf{x}| \leq r_M, \qquad \text{and } F_s(\mathbf{x}) = 0 \text{ elsewhere.} \tag{3.57}$$

The two values r_m and r_M depend on the mean radial profile θ_M defined in the previous section 3.4.2.2. We define r_m and r_M, respectively, such as the radial positions for which $\theta_M = 0.01$ and $\theta_M = 0.99\theta_{max}$

The definition of the filter function, as a discontinuous function in Eq. (3.57), can create numerical oscillations due to the Gibbs phenomenon. One way to avoid this numerical problem is to smooth out high wavenumbers oscillation using a convolution with a smoothing function,

$$S(k) = \exp\left(C_s \frac{k_1^2 + k_2^2 + k_3^2}{N^2}\right)$$

in Fourier space. In the previous equation, N is the grid resolution and $C_s = 128$ is a parameter used to determine the size of the transition zone (see Jause-Labert (2012) for details). Once the function $\hat{F}(k) = \hat{F}_s S(k)$ is transformed back to physical space to obtain $F(\mathbf{x})$, the step 2 of the section 3.4.2.1 procedure can continue. In Figure 3.14, we plot the filter function after the smoothing and the corresponding profile of θ_M.

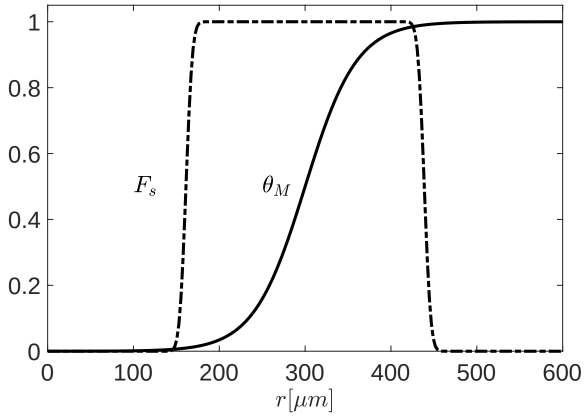

FIGURE 3.14 – Solid line : mean radial profile of the scalar θ for an Atwood number of 0.46. Dashed dotted line : the corresponding filter function F_s after the application of the smoothing function.

Chapitre 4

Sudden dissipation effect : spectral model and direct numerical simulations

---

Contents

In inertial confinement fusion application, the extreme temperatures involved imply that the fusion plasmas are in a weakly coupled regime. In this regime, the kinetic effects are dominant with respect to potential interaction, and the plasma coupling parameter is small compared to 1. In a weakly-coupled plasma, the viscosity μ has a strong dependence on temperature, in particular for light elements it has been shown [Braginskii 1995] that

$$\mu \sim T^{\frac{5}{2}}. \tag{4.1}$$

For heavier material the dependence is different and less intense. As an example Ticknor et al. (2016) showed that silver (Ag) dynamic viscosity evolves following

$$\mu \sim T^{\frac{3}{2}}. \tag{4.2}$$

The theoretical framework for compressed turbulence, introduced in section 2.1, has been applied to plasma compression by Davidovits and Fisch (2016a). They studied an adiabatic compression of Homogeneous Isotropic Turbulence (HIT) in the low Mach number limit, taking into consideration viscosity variations due to the mean temperature increase, as in Eq. (4.1). Besides, the turbulence production is impulsed solely by the compression terms coming from the mean velocity field, while other production sources such as shear or density gradient are neglected. Despite being crude, this framework has already proven an interesting starting point to explore important mechanisms at work during the compression, namely turbulence production and dissipation, but also nonlinear transfer. In particular, they evidenced how, during the compression, there is a moment when viscosity effects begin to dominate the dynamics of the flow until the turbulent kinetic energy is dissipated. In this context, the dissipation is rapid with respect to the compression duration, so they called this phenomenon *sudden dissipation*. In the following paper, Davidovits and Fisch (2016b) take into account the ionization state of the compressed plasma as a phenomenon that modifies the viscosity dependence to the temperature. In particular they consider $\mu \sim T^{\beta}$ where the exponent β is ionization dependent. They find that there is no sudden dissipation for $\beta < 1$.

In a recent paper, Campos and Morgan (2019) have investigated the same phenomenon without the low Mach number approximation, allowing the direct study of the turbulent kinetic energy dissipation on the temperature of the system. These simulations show how the sudden dissipation effect acts on the solenoidal as well as the dilatational part of the kinetic energy. Furthermore, their examination of the internal energy source terms shows that the adiabatic compression term dominates the viscous dissipation. They conclude that, at least for the cases studied, the proposed self-consistent mechanism to increase the local temperature in compressed plasma has a minimal impact ; in particular, the adiabatic contribution is two or three orders of magnitude higher than the frictional viscous heating.

Meanwhile, the initial conditions and particularly the large scale asymmetries of the capsule, due for instance to the support tent or the fill tube [Clark et al. 2015], play a determining role by having a strong imprint on the turbulent mixing. Still, how initial conditions influence the balance between the stirring processes and the microscopic dissipation remains unclear in ICF imploding capsules.

Concerning turbulence, it is known since the work of Batchelor [Batchelor 1949; 1953] followed by George (1992) that the large-scale structures or big eddies play an essential part in the dynamics of turbulent flows. This role has been identified, for instance, through different self-similar solutions, corresponding to the turbulent and final decays of HIT, showing a dependence on the initial distribution of energy at large scales. These solutions have been investigated in particular by spectral models based on Eddy Damped Quasi-Normal Markovian (EDQNM) closures [Orszag 1977, Lesieur 2008] allowing a systematic exploration of the influence of initial conditions at very high Reynolds number [Lesieur and Ossia 2000, Meldi and Sagaut 2012, Mons et al. 2014]. Note that this method has been similarly generalized to other problems such as Rayleigh-Taylor and unstably stratified turbulence [Soulard et al. 2014, Burlot et al. 2015b, Soulard et al. 2015].

In this chapter, we identify different regimes of turbulence in plasma under compression by exploiting the similarity properties of the system and the possibility of finding self-similar solutions in the moving frame corresponding to the coordinate transformation. Back in the laboratory frame, this gives information about the importance of initial conditions. To achieve this goal, we use DNS and spectral models based on classical EDQNM closures. The two methods are complementary : DNS provides the details of the turbulent fields in space, and their time evolution ; while, by construction, the EDQNM model directly predicts the time-evolving turbulent spectra of two-point correlations, and allows exhaustive parametric studies as well as the exploration of high Reynolds number regimes, due to its low computational cost. To extend our analysis to a less academic geometry and an inhomogeneous flow, we also consider a spherical turbulent layer with parameters relevant to ICF, as a paradigm of the hot spot contamination by turbulence.

4.1 Equation for plasma compression

In chapter 2 in section 2.1 we have derived the equation describing the dynamics of the velocity field for a neutral gas under compression. We recall that for a velocity field $\tilde{u}_i$ in the moving frame, moving with the mean compressing flow, we have two possibilities :

$$\partial_{\tilde{t}}\tilde{u}_i + \tilde{u}_j\partial_j\tilde{u}_i = -\partial_i\tilde{p} + \Lambda^3(t)\frac{\mu}{\rho_0^B}\partial^2_{jj}\tilde{u}_i \tag{4.3}$$

and

$$\partial_{\tilde{t}}\tilde{u}_i + \tilde{u}_j\partial_j\tilde{u}_i + 3\frac{\mathcal{S}(t)}{\Lambda}\tilde{u}_i = -\partial_i\tilde{p} + \frac{\mu}{\rho_0^B}\partial^2_{jj}\tilde{u}_i \tag{4.4}$$

depending if one wants to take into account compression effects by having a time dependent viscosity or a forcing term. In this chapter we consider the following time dependence for the compression parameter Λ :

$$\Lambda = 1 - \mathcal{S}_0 t \tag{4.5}$$

The dynamic viscosity in plasmas does not behave as in neutral gases. As already pointed out in the introduction of this chapter, it grows with temperature. In this work we will consider an adiabatic compression and with this hypothesis the mean temperature T has the following dependence on the compression parameter Λ :

$$T(t) = T_0\Lambda(t)^{-2} \tag{4.6}$$

where T_0 is the initial temperature. Using relation (4.6) together with the Braginskii (1995) law in (4.1) we deduce that the dynamic viscosity for a weakly coupled plasma under adiabatic compression is

$$\mu = \mu_0 \Lambda(t)^{-5}. \tag{4.7}$$

If we inject this expression of the dynamic viscosity μ in (4.3) and (4.4) we have

$$\partial_{\tilde{t}} \tilde{u}_i + \tilde{u}_j \partial_j \tilde{u}_i = -\partial_i \tilde{p} + \nu_0 \Lambda^{-2} \partial^2_{jj} \tilde{u}_i \tag{4.8}$$

and

$$\partial_{\tilde{t}} \tilde{u}_i + \tilde{u}_j \partial_j \tilde{u}_i + 3\frac{\mathcal{S}(t)}{\Lambda} \tilde{u}_i = -\partial_i \tilde{p} + \nu_0 \Lambda^{-5} \partial^2_{jj} \tilde{u}_i, \tag{4.9}$$

where $\nu_0 = \mu_0 / \rho_0^B$ is the kinematic viscosity. In Eq. (4.9) there is a new time dependence in front of the viscous term, so that the previous proposed rescaling (2.17) has to be modified [Davidovits and Fisch 2016a] :

$$\tilde{u}_i(\tilde{\mathbf{x}}, \tilde{t}) = u_i(\mathbf{x}, t)\Lambda^3(t), \quad \tilde{t} = \textstyle\int_0^t \Lambda^{-4}(s) ds, \quad \tilde{p}(\tilde{\mathbf{x}}, \tilde{t}) = p(\mathbf{x}, t)\Lambda^9(t) \tag{4.10}$$

and consequently Eq. (2.18) is modified as

$$\partial_{\tilde{t}} \tilde{u}_i + u_j \partial_j \tilde{u}_i + 2\mathcal{S}\Lambda^4 \tilde{u}_i = -\partial_i \tilde{p} + \nu_0 \partial^2_{jj} \tilde{u}_i. \tag{4.11}$$

In the moving frame, an initially homogeneous turbulence remains homogeneous during the compression. So that in this frame we are left with the problem of the decay of HIT with time-varying viscosity or with a new forcing term. These two different choices provide two different equations that model the same phenomenon. In section 4.2, we derive the EDQNM model for both cases, while the direct numerical simulations are performed only for Eq. (4.8).

To fully characterize the flow regime we use two nondimensional numbers : the Reynolds number Re and the compression number Cp, defined at the initial time as

$$\mathrm{Re} = \frac{u_0 \ell_0}{\nu_0}, \quad \text{and} \quad \mathrm{Cp} = \frac{u_0}{\ell_0 \mathcal{S}_0}, \tag{4.12}$$

where u_0 and ℓ_0 are characteristic velocity and length scales of the initial turbulent flow. Re measures the ratio between turbulent and physical viscosity, and Cp the ratio between the turbulent frequency to the compression rate. They give information about the initial conditions of the system and help to determine which physical phenomenon can become dominant during different phases of compression.

4.1.1 Modification to the time integration scheme for the DNS with time-varying viscosity

The DNSs are performed using the methods described in chapter 3 in section 3.2.2.1 for incompressible computations, with the only modification due to time-dependent viscosity. In particular for the step that concerns the implicit treatment of viscosity. In section 3.2.2.1 for the constant viscosity case, after transforming to Fourier space, we use the change of variable

$$v_i = u_i \exp\Big[\nu k^2 (t - t_0)\Big]. \tag{4.13}$$

When the viscosity is a function of time this substitution is no longer adequate. As an alternative we propose to use

$$v_i = u_i \exp\Big[\nu_0 k^2 N(\tilde{t} - \tilde{t}_0))\Big] \tag{4.14}$$

where $N(\tilde{t})$ is

$$N(\tilde{t}) = \int \Lambda(\tilde{t})^{-2} d\tilde{t} = \frac{\Lambda^3}{3\mathcal{S}_0} \tag{4.15}$$

where the compression parameter dependence on the rescaled time $\tilde{t}$, defined in Eq.(2.15), is $\Lambda(\tilde{t}) = 1/(1 + \mathcal{S}_0 \tilde{t})$.

This step is particularly crucial in these DNSs because the viscosity increases considerably during the simulation, causing numerical instability if it is treated explicitly.

4.2 Statistical approach : EDQNM Model

The Eddy Damped Quasi-Normal Markovian (EDQNM) closure has proven an efficient closure for different types of turbulent flows. The first EDQNM model concerned isotropic turbulence, in which a damping timescale $(\Theta_{kpq})^{-1}$ was used to adjust non linear decorrelation of the third-order cumulants generating the exchange of energy between three wavenumbers k, p, q (see *e.g.* Orszag (1977), Lesieur and Ossia (2000)). More or less sophisticated extensions of the EDQNM model were proposed to account for additional distortions to turbulence : mean velocity gradients, buoyancy force for stratified flows, Lorentz-Laplace force in magnetohydrodynamics, Coriolis force for rotating flows [Sagaut and Cambon 2008]. In short, when accounting for such additional forcing in the Navier-Stokes equation, one can account for the corresponding linear term at different levels of the closure (namely, choosing to retain its influence on increasingly higher-order statistics, *e.g.* second- or third-order statistical moments). Since we deal with a rather strong effect of the additional linear terms arising in equations (4.11) and (4.8), we anticipate that its direct impact on non linear transfers will be second-order in amplitude with respect to its direct effect on energy spectra, and we retain a simple version of the EDQNM closure, in which spectral energy transfers $T(k)$ will be closed with the same rationale as for isotropic turbulence. We shall see in section 4.2.3 that the resulting model compares very well with DNS.

Therefore, in the following, we derive the EDQNM closure for the compressed turbulence with plasma effect, for each of the two options mentioned above for behavior equations.

4.2.1 First case : Time-dependent viscosity

In the moving frame the Navier-Stokes equation with time-dependent viscosity is

$$\partial_{\tilde{t}}\tilde{u}_i + \tilde{u}_j\partial_j\tilde{u}_i = -\partial_i\tilde{p} + \nu_0\Lambda^{-2}\partial^2_{jj}\tilde{u}_i \tag{4.16}$$

It is then clear that, when $\tilde{t}$ goes to infinity, the dissipation term in Eq. (4.16) tends to infinity as well, thus causing the sudden dissipation of kinetic energy. As done for the classical Navier-Stokes equation, one can derive the two-point velocity correlation evolution equation from Eq. (4.16), and derive the evolution equation for the two-point velocity spectrum and then obtain the Lin equation for the kinetic energy spectrum $E(k)$. In the present case, the corresponding dynamical equation for the kinetic energy spectrum is

$$\partial_{\tilde{t}}E(k,\tilde{t}) + 2\nu_0(1+\mathcal{S}_0\tilde{t})^2k^2E(k,\tilde{t}) = T(k,\tilde{t}) \tag{4.17}$$

where the energy transfer term $T(k,\tilde{t})$ is closed using the classical EDQNM closure

$$T(k,\tilde{t}) = \iint_{\Delta_k}\Theta_{kpq}\frac{k}{pq}E(q,\tilde{t})b(k,p,q)\left(k^2E(p,\tilde{t}) - p^2E(k,\tilde{t})\right)\mathrm{d}p\mathrm{d}q\ . \tag{4.18}$$

$b(k,p,q)$ is the classical geometrical coefficient related to the geometry of the triad [Sagaut and Cambon 2008] and Θ_{kpq} is the characteristic time appearing during the combined markovianization and eddy-damping process. Its expression is thus provided by

$$\Theta_{kpq}(\tilde{t}) = \frac{1 - e^{\mu_{kpq}\tilde{t}+(1+2\mathcal{S}_0\tilde{t})^2\nu_0(k^2+p^2+q^2)}\tilde{t}}{\mu_{kpq} + (1+2\mathcal{S}_0\tilde{t})^2\nu_0(k^2+p^2+q^2)} \tag{4.19}$$

$$\text{with } \mu_{kpq} = \nu_k + \nu_p + \nu_q \text{ and } \nu_k = 0.36\left(\int_0^k p^2E(p)dp\right)^{1/2}\ .$$

4.2.2 Second case : Forcing term

If one wants to use the compression equation with the forcing term

$$\partial_{\tilde{t}}\tilde{u}_i + u_j\partial_j\tilde{u}_i + 2\mathcal{S}\Lambda^4\tilde{u}_i = -\partial_i\tilde{p} + \nu_0\partial^2_{jj}\tilde{u}_i \tag{4.20}$$

with $\Lambda(\tilde{t}) = 1/\sqrt[3]{1+3\mathcal{S}_0\tilde{t}}$. The corresponding Lin equation for this case reads

$$\left(\partial_{\tilde{t}} + 2\nu_0k^2\right)E(k,\tilde{t}) = T(k,\tilde{t}) - D(\tilde{t})E(k,\tilde{t}) \tag{4.21}$$

where $D(\tilde{t}) = 2\mathcal{S}\Lambda^4 = 2\mathcal{S}_0/(1+\mathcal{S}_0\tilde{t})$. The energy transfer term $T(k,\tilde{t})$ is the same as in the previous case, with the only difference in the detailed expression of Θ_{kpq} :

$$\Theta_{kpq}(\tilde{t}) = \frac{1 - e^{\mu_{kpq}\tilde{t}+\nu_0(k^2+p^2+q^2)}\tilde{t}}{\mu_{kpq} + \nu_0(k^2+p^2+q^2)}\ . \tag{4.22}$$

where μ_{kpq} has the same expression as in (4.19).

4.2.3 Validation

We now present comparisons between EDQNM and DNS results. We use DNS data from Davidovits and Fisch (2016a) from simulations using 128^3 grid points, and from our simulations using 256^3 grid points. A close comparison permits to validate the closure and confirms that the statistical approach can be used for an extensive parametric study. Besides, comparing the different DNS data allows evaluating the influence of a modification of numerical parameters on DNS statistics.

The numerical integration of EDQNM model Equations (4.17) or (4.21) is done using a simple trapezoidal integration quadrature as regards the integral appearing in the transfer $T(k)$. Time-marching is done using the third-order strong stability preserving Runge-Kutta method presented in section 3.2.2, a treatment that we believe is original for solving these Lin-type equations. This scheme improve the numerical stability of the time integration process, permitting the use of a larger time step with respect to the first-order Euler time-integration method used in previous works.

Whereas statistics obtained in DNS is but a by-product of the velocity field for a particular realization, obtained by averaging over the computational domain, the resolution of EDQNM equations directly provides the two-point statistics that can be integrated to obtain one-point statistics such as total kinetic energy. These statistics stand for the ensemble averaging that should be done if many DNS realizations could be afforded. Therefore, when comparing DNS and EDQNM, one needs to bear in mind these differences between the two approaches. Also, initial conditions in DNS use fields that are δ-correlated, thus with zero third-order correlations. This is not the case in EDQNM in which energy transfers are immediately triggered at the beginning of the computation, and therefore have non zero values from the start.

Comparison with DNS of Davidovits *et al.* The time evolution of kinetic energy is shown in Figure 4.1 as a function of Λ, at different compression rates $\mathcal{S}_0$. The figure presents results from the EDQNM model and from DNS by Davidovits and Fisch (2016a). The initial kinetic energy is set to unity, and the time evolution goes from right to left, starting at the domain size $\Lambda = 1$.

The figure shows that kinetic energy evolution initially increases for compression rate $\mathcal{S}_0$ larger than 1, and decreases for $\mathcal{S}_0 < 1$. It then undergoes a sudden drop, triggered at a value of Λ increasing with $\mathcal{S}_0$. This drop is not observed for $\mathcal{S}_0 = 0.1$ since kinetic energy decays too fast from the beginning.

Figure 4.1 also shows that EDQNM results agree very well with DNS data for $\mathcal{S}_0 > 1$. When $\mathcal{S}_0 \leq 1$, the curves depart slightly, but the overall trend is rather good. Such differences can be due to various factors :

1. slight differences in initial conditions (that are not fully detailed in Davidovits and Fisch (2016a)) ;

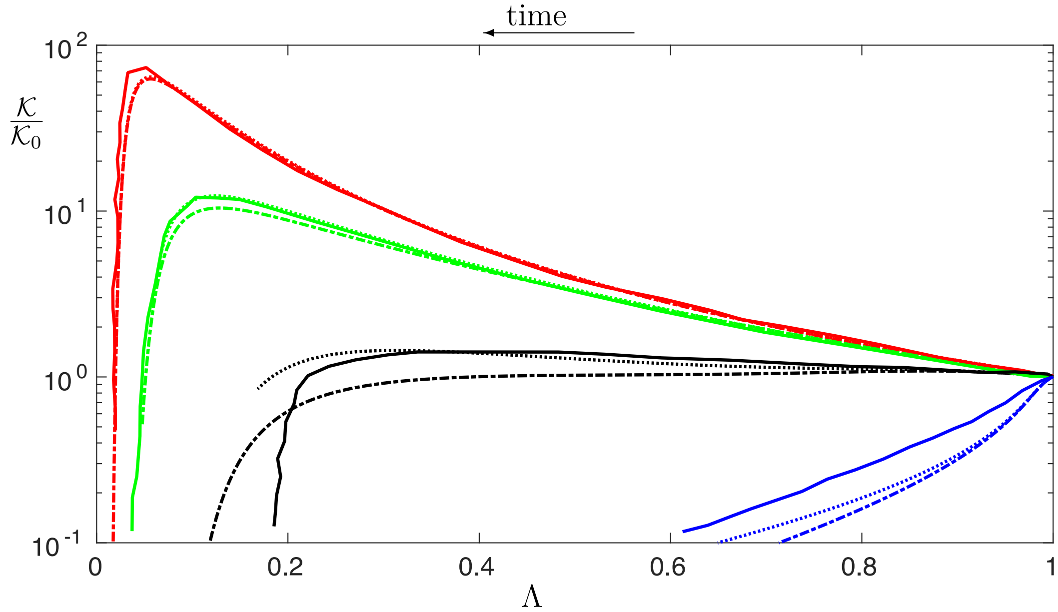

FIGURE 4.1 – Turbulent kinetic energy evolution as a function of the compression parameter Λ. Solid lines : DNS results from Davidovits and Fisch (2016a). Dotted lines : EDQNM forcing term closure. Dash-dotted lines : EDQNM time-dependent viscosity closure. Different colors for decreasing compression rates : red : $\mathcal{S}_0 = 100$; green : $\mathcal{S}_0 = 10$; black : $\mathcal{S}_0 = 1$; blue : $\mathcal{S}_0 = 0.1$.

2. the effect of confinement at low-wave number, when the computational domain is too small in DNS, so that DNS simulation over a 128^3 grid is under-resolved initially, although this resolution rapidly becomes adequate when viscosity increases ;
3. there are differences between the two formulations of the model, based either on the time-dependent viscosity closure or on the forcing term closure. Although the two formulations should be formally equivalent, their numerical implementation can induce departures, as observed on the figure.

Comparison with new DNS data To have better control over the parameters of the simulation, we perform new Direct Numerical Simulations with known initial conditions and an increased resolution of 256^3. This permits further validation and comparison of the EDQNM model results with those of our DNS data, shown in Figure 4.2.

The initial conditions are generated using the method described in section 3.4.1, using the spectrum (3.43) with $s = 4$.

For the large compression rates $\mathcal{S}_0 \geq 10$, Figure 4.2 shows an almost perfect agreement between EDQNM and DNS kinetic energy evolution, better than in Figure 4.1. Also, the agreement is much improved for the lesser compression rates $\mathcal{S}_0$. This is the

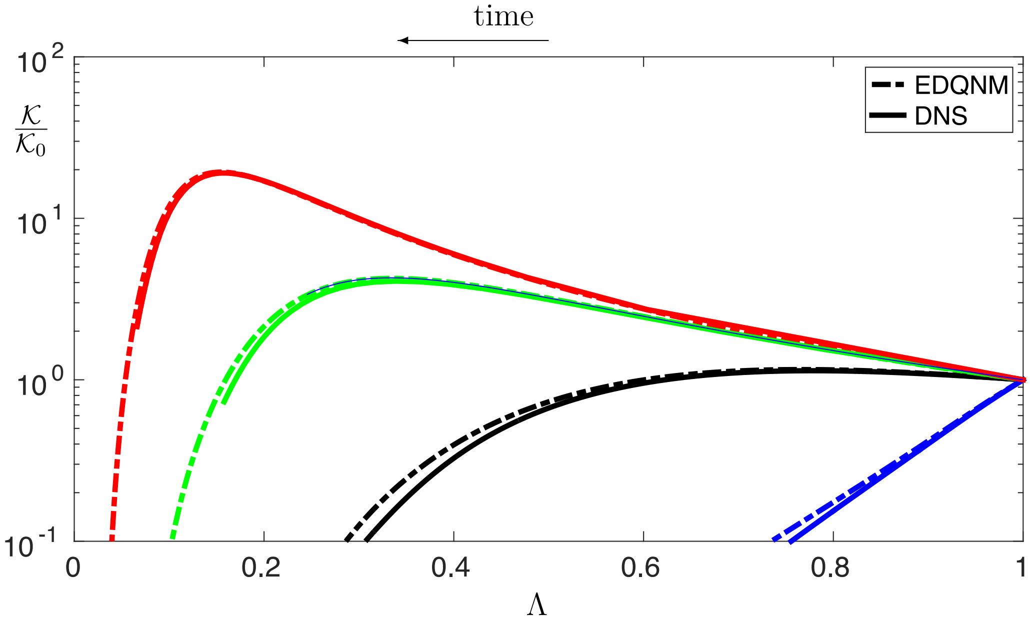

FIGURE 4.2 – Turbulent kinetic energy evolution as a function of the compression parameter Λ. Solid lines : our DNS results. Dash-dotted line : EDQNM time-dependent viscosity closure. Different colors for different compression rates : red : $\mathcal{S}_0 = 100$; green : $\mathcal{S}_0 = 10$; black : $\mathcal{S}_0 = 1$; blue : $\mathcal{S}_0 = 0.1$. Viscosity coefficient $\nu_0 = 5 \times 10^{-2}$ in all simulations.

result of the increase of resolution in the DNS, and better controlled initial conditions as well.

4.3 Direct Numerical Simulations and EDQNM results with increased resolution

To quantify and analyze the different phenomena involved in the flow dynamics, and in particular, to illustrate the competition between turbulence production and viscous dissipation, we present results from DNS with increased resolution along with predictions by the spectral EDQNM model.

We illustrate this in Figures 4.3 an 4.4, with results obtained using an initial kinetic energy spectrum of the Batchelor form $E_0(k) \sim k^4 \exp\left(-2(k/k_{\text{peak}})^2\right)$, where k_{peak} corresponds to the maximum of E_0. The initial Reynolds number is $\text{Re}_0 = 250$ and the compression number $\text{Cp}_0 = 0.1$, based on $\ell_0 = 1/k_{\text{peak}}$ and $u_0 = \mathcal{K}^{1/2}$. Turbulence is therefore relatively weak in this example, while the compression is rapid compared to the turbulent timescale.

In Figure 4.3, we show the evolution of turbulent kinetic energy $\mathcal{K} = \int_0^{+\infty} E(k)dk$ as a function of the compression parameter $\Lambda(t)$. We observe a very good agreement

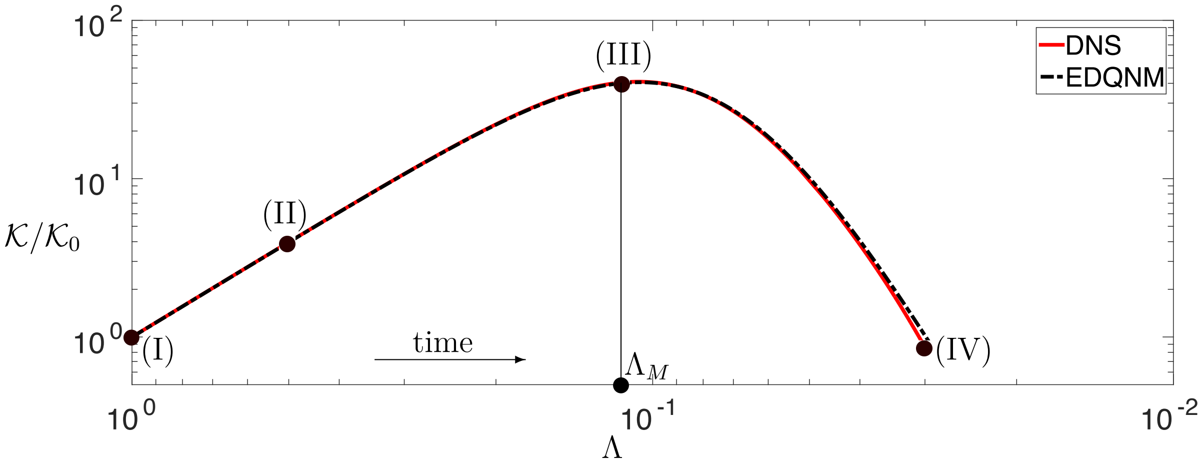

FIGURE 4.3 – Evolution of turbulent kinetic energy $\mathcal{K}$, normalized by its value at $t = 0$, as a function of the compression parameter Λ for both DNS at resolution 512^3 and EDQNM simulations of a HIT compression case with $\mathrm{Re}_0 = 250$ and $\mathrm{Cp}_0 = 0.1$. The critical compression parameter Λ_M corresponds to the kinetic energy maximum before the beginning of the viscous phase.

between simulations of 512^3 grid-point DNS and the EDQNM model during all the phases of the kinetic energy evolution. Moreover, the spectral distribution of energy at four instants plotted in Figure 4.4 (bottom row), show an excellent agreement between DNS and EDQNM at all scales. This supports the relevance of the closure as a model for compressed turbulence.

The case presented in Figures 4.3 and 4.4 is typical of the regime extensively discussed in Davidovits and Fisch (2016a). At the beginning ($\Lambda(t)$ from 1 to $O(10^{-1})$), the dynamic of the flow is dominated by the compression effects leading to the increase of kinetic energy. Progressively, viscosity grows and dissipates energy in the small scales and eventually at larger scales, as indicated by the spectra. This counterbalances the turbulence production mechanisms and finally triggers the sudden viscous dissipation effect. These mechanisms are qualitatively observed in Figure 4.4 (top row), which shows the spatial distribution of kinetic energy in the DNS domain at the same four instants as the presented spectra. One particularly observes the intensification of kinetic energy, especially at the instant (III) corresponding to the peak of kinetic energy in Figure 4.3, and the substantial reduction of energy levels at (IV), along with a smoothing of the field due to the damping of small-scale fluctuations.

The critical value Λ_M of the compression parameter corresponds to the maximum of kinetic energy in Figure 4.3. It indicates how much the turbulence can be compressed before the appearance of the sudden viscous dissipation effect. We have therefore computed the evolution of Λ_M with the two relevant nondimensional pa-

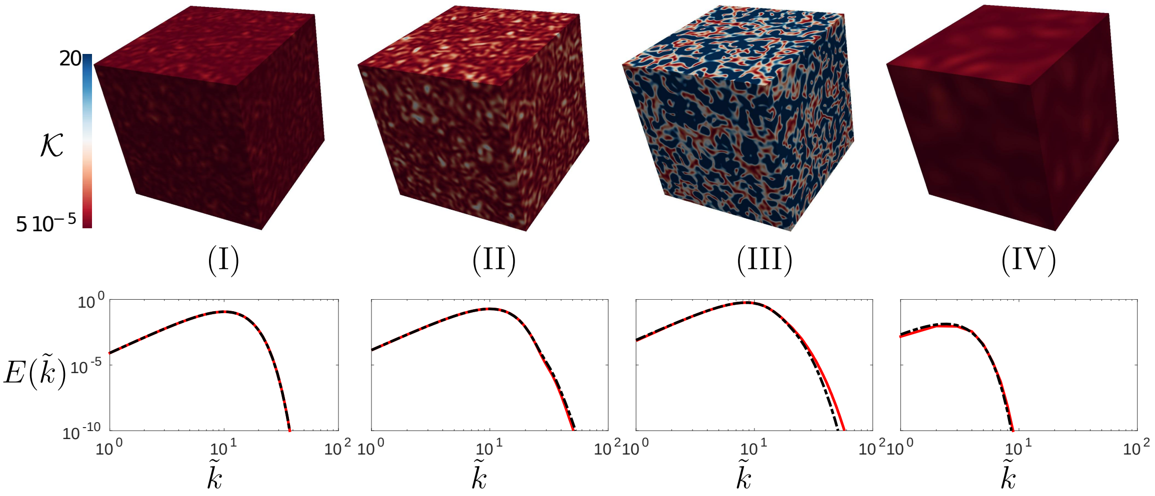

Figure 4.4 – Top row : distribution of turbulent kinetic energy $\mathcal{K}$ in the DNS at four instants of the evolution, indicated in the kinetic energy curve of Figure 4.3. The scaling of the box corresponds to the moving frame of reference. Bottom row : Associated energy spectra $E(\tilde{k})$ for both DNS and EDQNM simulations, at the same instants.

rameters, Reynolds and compression numbers, the initial spectrum remaining of the Batchelor form. The corresponding map of Λ_M in the (Re, Cp) coordinates is shown in Figure 4.5.

This parametric study was permitted by the EDQNM model, which allows exploring six decades of initial Reynolds numbers Re_0 and three decades of initial compression number Cp_0. It required as many as 10000 EDQNM simulations, which would not be possible using DNS due to its high computational cost.

As expected, Figure 4.5 shows two general trends. First, when the initial Reynolds number increases, Λ_M decreases since the viscosity coefficient needs to grow enough to impact the main energetic scales. Second, for decreasing values of the compression number Cp_0, the critical compression parameter Λ_M also becomes smaller since turbulent production is stronger and needs more time before being balanced by dissipation.

Upon closer inspection, the isolines of Λ_M in Figure 4.5 permit to identify two additional kinds of dynamics different from that presented in Figure 4.3, wherein turbulent production dominance is followed by that of viscous dissipation as Λ decreases. The first additional regime occurs at small initial Re_0 and large Cp_0. It is also observed in Davidovits and Fisch (2016a) : dissipation immediately prevails from the very beginning of the compression phase, and yields a decay of turbulent kinetic energy, and a narrow energy spectrum limited to large scales, as in Figure 4.6, case (A).

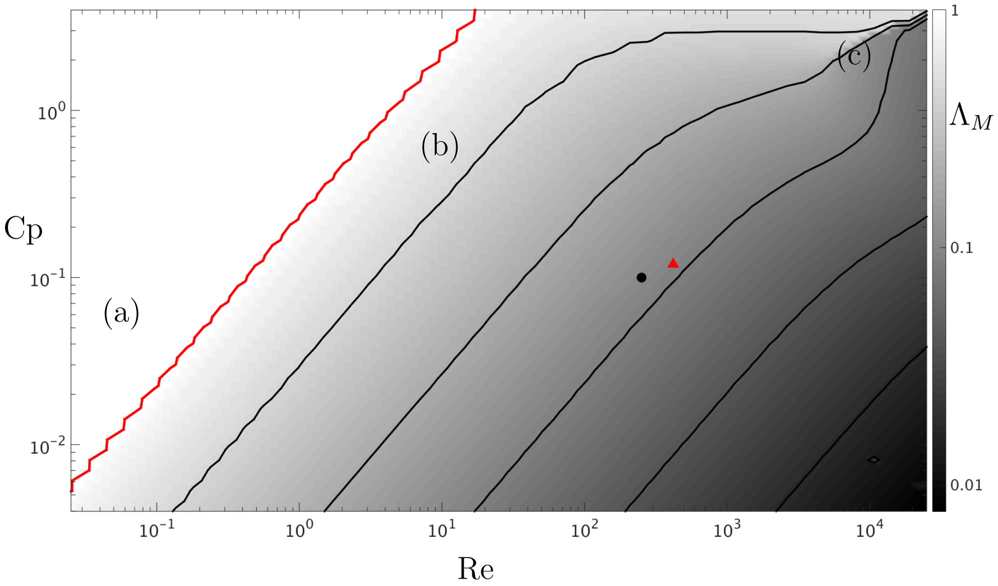

FIGURE 4.5 – Iso-contour map of the critical compression parameter Λ_M corresponding to maximum of kinetic energy, as a function of the initial Reynolds number Re_0 and the compression number Cp_0. Results from EDQNM simulations. The black circle corresponds to the parameters used in Figures 4.3 and 4.4, and the red triangle to that of Figure 4.10. The red line is the contour line at $\Lambda_M = 1$.

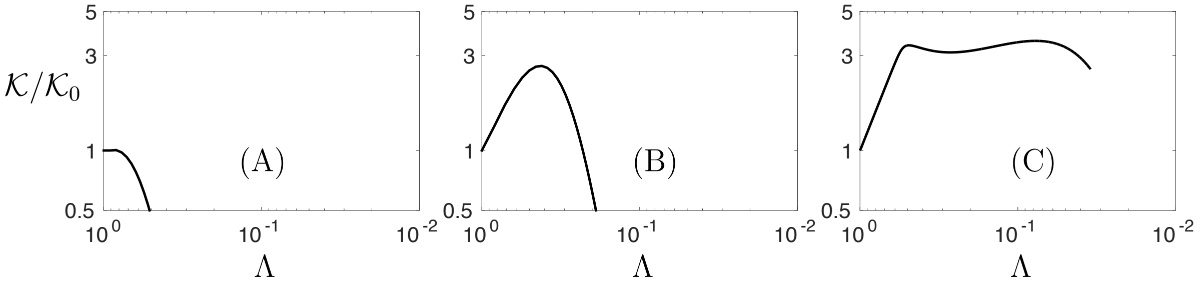

FIGURE 4.6 – Evolution of kinetic energy $\mathcal{K}$ normalized by its initial value as a function of the compression parameter Λ for the three typical cases indicated on the parametric map of Figure 4.5. The spectrum in region (A) illustrates the immediate decay regime, that of region (B) the intermediate regime, and region (C) shows the cascade regime.

The second additional regime appears at large values of Re_0, and Cp_0. It corresponds to the presence of important nonlinear energy transfers. In this new regime, two values of the compression parameter, corresponding to two kinetic energy maxima, may exist. This generates a discontinuity observed in Figure 4.5 (top-right corner, at large Re and Cp, where the label (C) appears), which can be explained by considering the following concurrent phenomena. First, kinetic energy grows as Λ^{-2}, which means it remains constant in the moving frame. In the meantime, energy is transferred to small scales by nonlinear effects. It is then suddenly dissipated when reaching the viscous scales, in the classical mechanism of enstrophy blow up well known in HIT decay. This sudden energy loss can counterbalance the growth of kinetic energy if the Reynolds number is not large enough, leading to the first maximum of $\mathcal{K}(\Lambda)$. Meanwhile, large scales keep gaining energy due to the compression until dissipated by the sudden growth of the viscosity coefficient, resulting in the second maximum shown in the spectrum in Figure 4.6, case (C).

In summary, we have explored the influence of initial nondimensional parameters on the dynamics of turbulent plasma under compression by combining the results of DNS and EDQNM simulations. This has permitted to identify the importance of the various physical mechanisms involved during the compression. In particular, we have shown that nonlinear energy transfer can have a decisive role at high Reynolds numbers. In the following section, we propose theoretical arguments in support of these conclusions.

4.4 Self-similar solutions in plasmas under compression

The main goal of this part is to derive the different self-similar solutions for turbulent plasma under compression. These solutions are first expressed in the moving frame and then transformed back in the laboratory frame using Eq. (2.15). As already stated, we stress that this derivation is limited to a restricted scenario, where a part of the phenomena typically involved are not considered (e.g., shear and buoyancy effects). But again, this kind of analysis may be useful, although not conclusive, to understand the different mechanisms involved in the evolution of turbulence in plasma under compression. Section 4.4.1 is dedicated to the theoretical analysis, and in Section 4.4.2 we show the actual existence of these regimes using DNS and EDQNM simulations.

4.4.1 Self-similar scaling

Three self-similar solutions are found, corresponding to the rapid compression regime, the cascade regime, and the viscous regime. They are listed hereafter, and for convenience, the corresponding scaling laws are gathered in Table 4.1

4.4.1.1 Rapid compression regime

The rapid compression (RC) regime, historically referred to as Rapid Distorsion Theory — called RDT in Cambon et al. (1993), although unlike in sheared turbulence, wavenumbers are not distorted—, is the simplest self-similar solution which can be obtained. Assuming that the turbulent timescale is much larger than the compression time, such that Cp $\ll 1$, turbulence can be considered frozen in the moving frame, leading to the following energy spectrum :

$$\tilde{E}(\tilde{k},\tilde{t}) = E_0(\tilde{k}), \text{ or } E(k,t) = E_0(\Lambda(t)k) \times \Lambda(t)^{-1}, \tag{4.23}$$

whence the evolution of kinetic energy and of the integral length scale ℓ_I :

$$\begin{aligned}\mathcal{K}(t) &= \int_0^{+\infty} E(k,t)dk \sim \Lambda^{-2}(t),\\ \ell_I(t) &= \frac{3\pi}{4}\frac{\int_0^{+\infty} k^{-1}E(k,t)dk}{\int_0^{+\infty} E(k,t)dk} \sim \Lambda(t).\end{aligned}$$

This self-similarity of spectrum $\tilde{E}(\tilde{k},\tilde{t})$ is of course only strictly valid for wavenumbers unaffected by viscosity. It is clear that the RC regime can only last for a limited duration, due to the Λ^{-2} growth of the viscosity and to the non-linear transfer in the moving frame. Note also that $\mathcal{K} \sim \Lambda^{-2}$ does not necessary imply a RC phase. For instance, redistribution of energy by non linear transfers can modify the shape of spectra and the value of integral length scale $\tilde{\ell}_I$, while still conserving the total kinetic energy.

4.4.1.2 Cascade regime

The decay of HIT is extensively discussed in most turbulence books, as for instance in [Batchelor 1953, Lesieur 2008, Sagaut and Cambon 2008]. According to these monographs, the decay rate of energy depends on the cascading process governed by large scales of turbulence, but not on the value of the viscosity coefficient. For compressed turbulence, although the viscosity coefficient varies in the moving frame, one can expect similarly that the dynamics at large Reynolds number is driven only by the turbulent energy flux from large to small scales. Considering a self-similar evolution of kinetic energy as $\tilde{\mathcal{K}} \sim \tilde{t}^{-n_c}$, the integral length scale evolves as $\tilde{\ell}_I \sim \tilde{t}^{1-n_c/2}$. Assuming the permanence of big eddies [Batchelor 1949, Lesieur and Ossia 2000], which can be expressed by $\lim_{\tilde{k}\to 0} \tilde{E}(\tilde{k},\tilde{t}) = \tilde{k}^s$ (s being the infra-red spectral slope), we deduce from self-similarity :

$$n_c = \frac{2(s+1)}{s-3}. \tag{4.25}$$

This provides the classical decay exponent generally encountered in turbulence : $n_c = 10/7 \simeq 1.43$ for Batchelor spectrum ($s = 4$) and $n_c = 6/5 = 1.2$ for Saffman spectrum ($s = 2$). Note that the permanence of big eddies is relatively well observed for $s \leq 3$ while not entirely true for $s = 4$ due to backscatter effects transferring energy from small to large scales.

Returning to the laboratory frame using Eq. (2.15) and the expression for $\Lambda(t)$, this leads to the kinetic energy evolution as $\Lambda \to 0$ for the cascade regime :

$$\mathcal{K} \sim \Lambda^{n_c - 2} \quad \text{and} \quad \ell_I(t) \sim \Lambda^{n_c/2}, \tag{4.26}$$

leading in particular to a growth of kinetic energy and decrease of integral scale as $\mathcal{K} \sim \Lambda^{-4/5}, \ell_I \sim \Lambda$ for Saffman turbulence and as $\mathcal{K} \sim \Lambda^{-4/7}, \ell_I \sim \Lambda^2$ for Batchelor turbulence.

4.4.1.3 Viscous regime

The last regime is closely related to the sudden viscous dissipation effect occurring in a turbulent plasma under compression, discussed in Davidovits and Fisch (2016a). When the Reynolds number becomes small enough, the decay of HIT enters a final regime, which is driven by dissipation and in which the nonlinear turbulent transfer is negligible. This phase exhibits a self-similar solution known as the final decay regime of HIT when the viscosity coefficient is constant [Batchelor 1953]. We propose here a generalization for the time-varying viscosity case corresponding to a weakly-coupled plasma.

As for the turbulent decay presented in Section 4.4.1.2, we consider a self-similar evolution in the moving frame of the form $\tilde{\mathcal{K}} \sim \tilde{t}^{-n_v}$. The scaling for the integral scale can be obtained from the self-similar evolution of the turbulent time $\sim \tilde{t}$ and the viscosity coefficient $\tilde{\nu}(\tilde{t})$, yielding $\tilde{\ell}_I \sim \left(\tilde{\nu}(\tilde{t})\tilde{t}\right)^{1/2}$. Assuming again $\lim_{\tilde{k}\to 0} \tilde{E}(\tilde{k},\tilde{t}) = \tilde{k}^s$ as large scales remain unaffected by viscosity, we obtain, for $\tilde{\Lambda} \to 0$:

$$n_v = \frac{3}{2}(s+1). \tag{4.27}$$

Similarly to the cascade phase, we deduce the scaling laws for the kinetic energy and integral scale in the laboratory frame for the viscous phase,

$$\mathcal{K} \sim \Lambda^{n_v - 2} \text{ and } \ell_I(t) \sim \Lambda^{-1/2}, \tag{4.28}$$

leading in particular to a sudden viscous dissipation of the form $\mathcal{K} \sim \Lambda^{5/2}$ in Saffman turbulence and $\mathcal{K} \sim \Lambda^{11/2}$ for Batchelor turbulence. Therefore, the viscous regime corresponding to the sudden dissipation effect clearly induces an important sensitivity to initial conditions, contrary to the cascade regime, for instance, where the variations of the growth exponent are smaller. Notably in the viscous regime, the integral scale of turbulence grows despite the compression and is not dependent on initial conditions.

	RC regime	Cascade regime	Viscous regime
$\mathcal{K}$	$\sim \Lambda^{-2}$	$\sim \Lambda^{n_c-2}$	$\sim \Lambda^{n_v-2}$
ℓ_I	$\sim \Lambda$	$\sim \Lambda^{n_c/2}$	$\sim \Lambda^{-1/2}$
Re	$\sim \Lambda^{2}$	$\sim \Lambda^{n_c+1}$	$\sim \Lambda^{(n_v+1)/2}$
Cp	$\sim \Lambda^{-1}$	$\sim \Lambda^{0}$	$\sim \Lambda^{(n_v+1)/2}$

TABLE 4.1 – Scaling laws corresponding to the different self-similar regimes for the different turbulent quantities and non dimensional numbers. The coefficients n_c and n_v are given by Eqs. (4.25) and (4.27) as a function of the infrared spectral slope s.

4.4.2 Simulations of self-similar regimes

We now confirm the actual appearance, in simulations, of the different self-similar solutions analytically found in the theoretical study of Section 4.4.1. We consider two types of initial conditions, as representative of many encountered situations : Saffman turbulence ($s = 2$) corresponding to equipartition of energy at large scale among the different wave-vectors, and Batchelor turbulence ($s = 4$) generated by backscatter effects from small scale perturbations. In Section 4.4.2.1, we consider the case of high Reynolds number turbulence, and for this, we use the EDQNM model. In Section 4.4.2.2, we model the compression of a spherical turbulent layer using both DNS and EDQNM.

4.4.2.1 High Reynolds number compressed turbulence with EDQNM simulations

The Reynolds number $\mathrm{Re} = u\ell/\nu$ for a weakly-coupled turbulent plasma under compression is expected to decrease, as assessed by the scaling laws for $u = \mathcal{K}^{1/2}$ and $\ell = \ell_I$ in either the rapid compression, the cascade or the viscous regime. Thus, we use the EDQNM model to reach a very high initial Reynolds number, beyond the possibilities of DNS, to obtain the different self-similar solutions derived in Section 4.4.1.

We choose initial spectra in the von Karman type $E_0(k) \sim k^s \exp\left[-s/2(k/k_{\mathrm{peak}})^2\right]$, both for the Saffman ($s = 2$) or the Batchelor ($s = 4$) case. We set the Reynolds number at $\mathrm{Re}_0 = 10^7$ and the compression number $\mathrm{Cp}_0 = 0.47$. Accordingly, this corresponds to a flow with high intensity turbulent fluctuations and fast compression.

Figure 4.7 shows the evolutions of the kinetic energy $\mathcal{K}$ and of the integral length scale ℓ_I, and Figure 4.8 that of the Reynolds number Re and of the compression number Cp. The corresponding spectra $E(k)$ at different stages of the evolution are given in Figure 4.9.

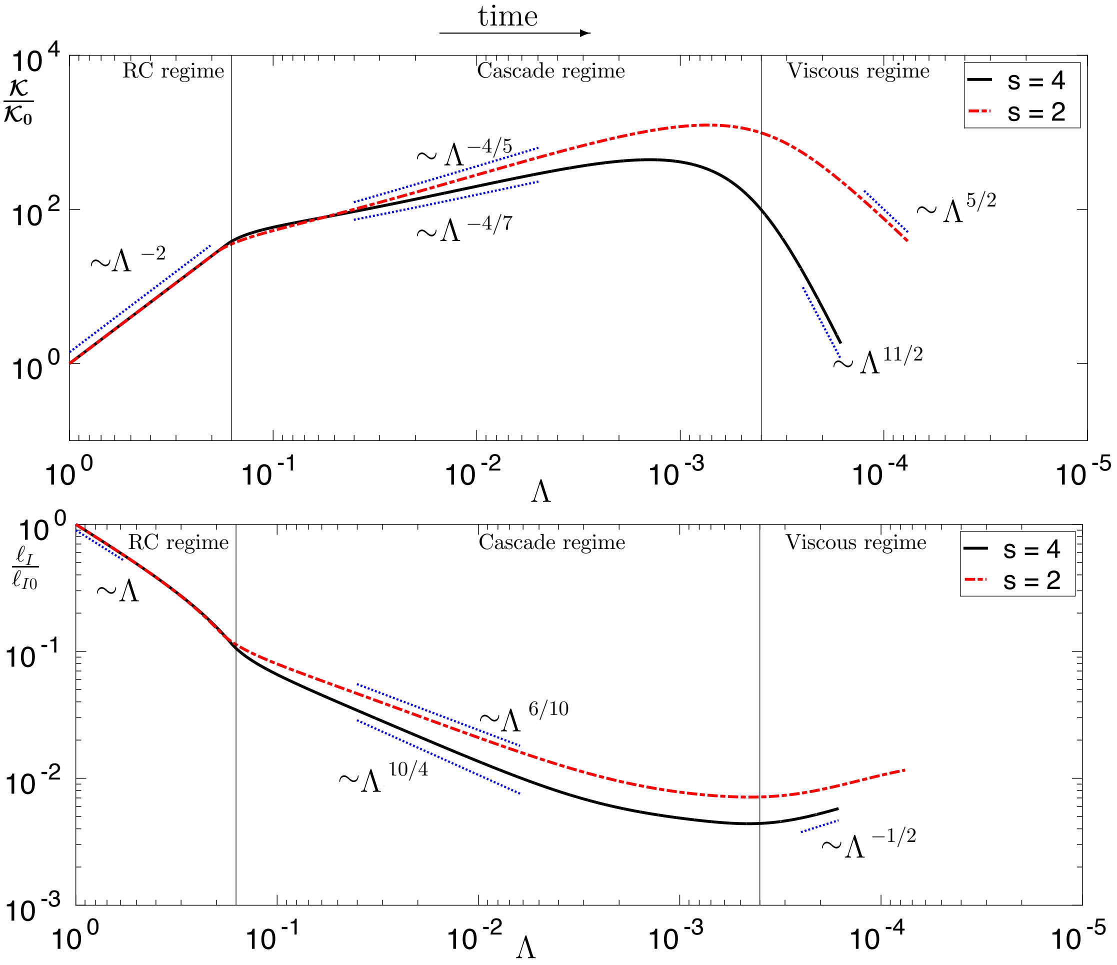

FIGURE 4.7 – Evolution of (Top) the kinetic energy $\mathcal{K}$ and (Bottom) the integral scale ℓ_I as a function of the compression parameter Λ using EDQNM simulations. Solid line : Batchelor initial condition ($s = 4$). Dashed line : Saffman initial condition ($s = 2$). The scaling laws corresponding to the self-similar solutions derived in Sec. 4.4.1 are also shown.

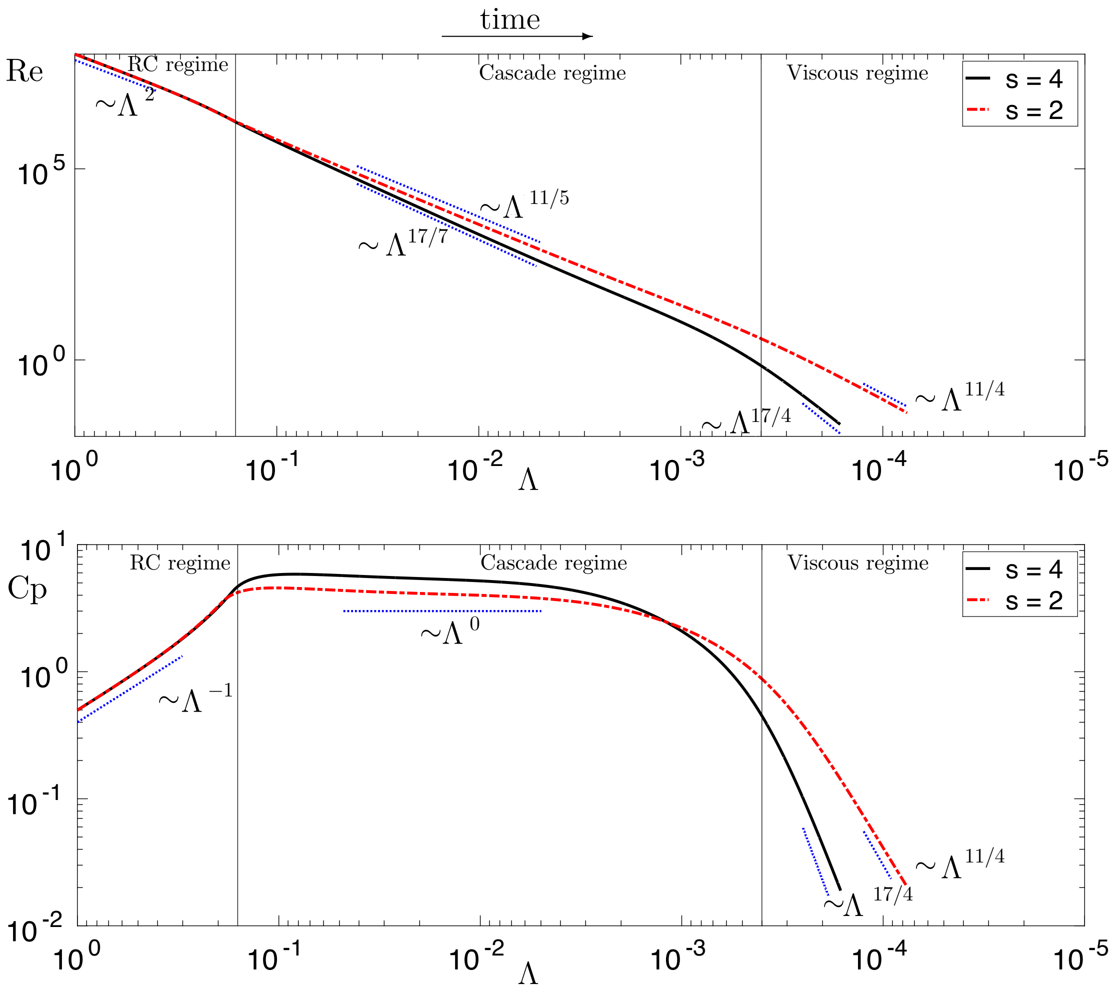

Figure 4.8 – Evolution of (Top) the Reynolds number Re and (Bottom) the compression number Cp as a function of the compression parameter Λ using EDQNM simulations. Solid line : Batchelor initial condition ($s = 4$). Dashed line : Saffman initial condition ($s = 2$). The different scaling laws corresponding to the self-similar solutions derived in Sec. 4.4.1 are also shown.

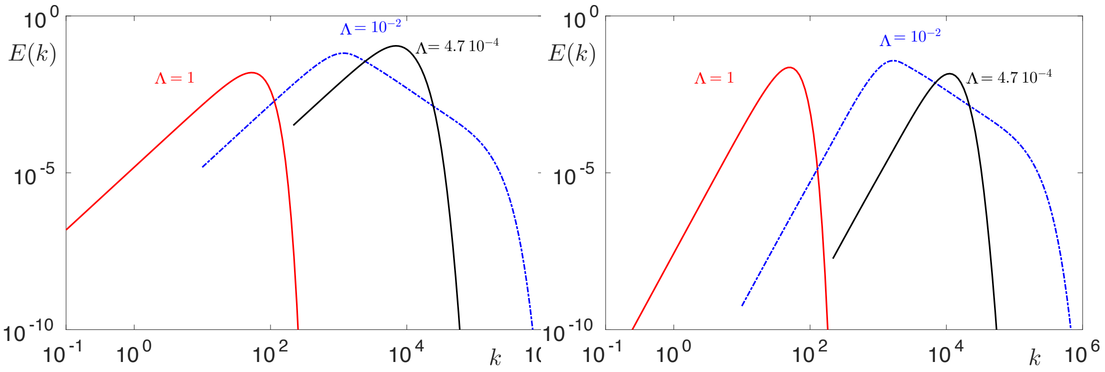

Figure 4.9 – Kinetic energy spectra $E(k)$, corresponding to EDQNM simulations of Figures 4.7 and 4.8, taken at different values of the compression parameter Λ. Left : Saffman initial condition ($s = 2$). Right : Batchelor initial condition ($s = 4$).

Figures 4.7 and 4.8-bottom exhibit very clearly the three different regimes that can be identified by the evolution changes in K, ℓ_I, and Cp when Λ decreases. The dynamical changes in the evolution of Re (Figure 4.8-top) are less evident due to transitions between similar powerlaws, especially the RC to cascade one, but are still present. For all curves, the self-similar scaling laws proposed in Sec. 4.4.1 fit the results of simulations adequately. The succession of rapid compression, cascade, and viscous regimes is clear, and the values of Λ at which the RC-cascade transition occurs seem to be similar for Batchelor and Saffman turbulences.

In Figure 4.7, we observe, for the turbulent kinetic energy evolution, a greater sensitivity to initial conditions in the viscous regime. Still, the integral length scale increase in this regime is similar for both Saffman and Batchelor cases. We conclude that differences in the integral scale ℓ_I dynamics are only due to the cascade phase, thus demonstrating the imprint of nonlinear mechanisms.

The Reynolds number decrease observed in Figure 4.8-top is mainly due to the growth of viscosity, while initial conditions have relatively low influence except during the viscous phase. The compression number Cp (Figure 4.8-bottom) increases from its initial low value of $\mathrm{Cp} = 0.47$ during the RC phase and reaches a plateau at about ten times this value during the cascade phase.

The fact that simulations agree well with the scaling laws proposed in Sec. 4.4.1 is a consequence of the fact that the distribution of energy at large scales remains constant during the compression. This constancy is verified in Figure 4.9, for both Saffman and Batchelor turbulences, in which the infrared slopes of turbulent kinetic spectra are maintained over three decades of k. In particular, energy backscatter usually alters the slope in Batchelor turbulence, but this seems of little influence here. Besides, the presence of nonlinear transfer over a few decades of scales during the cascade regime is attested by the observed Kolmogorov scaling $k^{-5/3}$ in spectra $E(k)$ at $\Lambda = 10^{-2}$ in Figure 4.9. On the contrary, the absence of inertial subrange shows that, during the sudden viscous dissipation phase, energy is systematically dissipated from small to large scales.

In summary, we have evidenced in this section the existence of the self-similar regimes using EDQNM simulations at high Reynolds number with long evolution times, thus reaching very small compression parameter Λ. This demonstrates the influence of the initial distribution of energy at large scales, in particular during the viscous dissipation phase. In the following, we show that these results still apply in configurations more relevant to ICF, *i.e* when the Reynolds number is smaller and in the presence of inhomogeneities.

4.4.2.2 Spherical turbulent layer

An essential question in ICF is how the turbulent ablator/fuel interface eventually contaminates the hot spot at the center of the spherical capsule. We, therefore, consider here a spherical turbulent layer configuration, more relevant to the ICF problem than homogeneous turbulence. Of course, this case is still simplified, for it discards important physical phenomena that are present in ICF, for instance, density effects and the stagnation shock in the fuel, which has to be taken into account before the bang time. Nonetheless, it is progress towards more realistic predictions. Therefore, in this section, we investigate the self-similar solutions and the influence of large scale perturbations in the case of a spherical turbulent layer under compression using both DNS and EDQNM.

Although some estimates of physical parameters of experimental ICF are very difficult to make, we choose initial conditions that can be relevant to actual flow situations. We evaluate the Reynolds and compression numbers based on the ICF simulations corresponding to the NIF shot N120205 presented in Weber et al. (2014a). During the phase considered just before the bang time, the ablator/fuel interface passes from a radius of $340\,\mu m$ to $54\,\mu m$ in $1\,ns$ giving $\mathcal{S}_0 \sim 10^9\,s^{-1}$. The initial fuel viscosity is around $\nu \sim 10\,cm^2 s^{-1}$ for $\rho \sim 10\,g\,cm^{-3}$ and $T \sim 500\ eV$ corresponding to a plasma coupling parameter $\Gamma \sim 0.1$ for the deuterium-tritium fuel. The integral scale and fluctuating velocity are respectively $\ell_0 \sim 10^{-2}\,cm$ and $u_0 \sim 10^6\,cm\,s^{-1}$, leading to $\mathrm{Re}_0 \sim 10^3$ and $\mathrm{Cp}_0 \sim 10^{-1}$. In our simulations, we therefore choose $\mathrm{Re}_0 = 450$ and $\mathrm{Cp}_0 = 0.1$, figures that are relevant to ICF configurations.

The initial spectra are of von Karman type already introduced in Section 4.4.2, $E_0(k) \sim k^s \exp\left[-s/2(k/k_{\mathrm{peak}})^2\right]$. These conditions are sufficient to initialize the EDQNM model, which assumes homogeneity and isotropy of turbulence. Its predictions will be used to compare to the DNS results. The initialization of the DNS fluctuating velocity field is performed using the procedure described in section 3.4.2.1

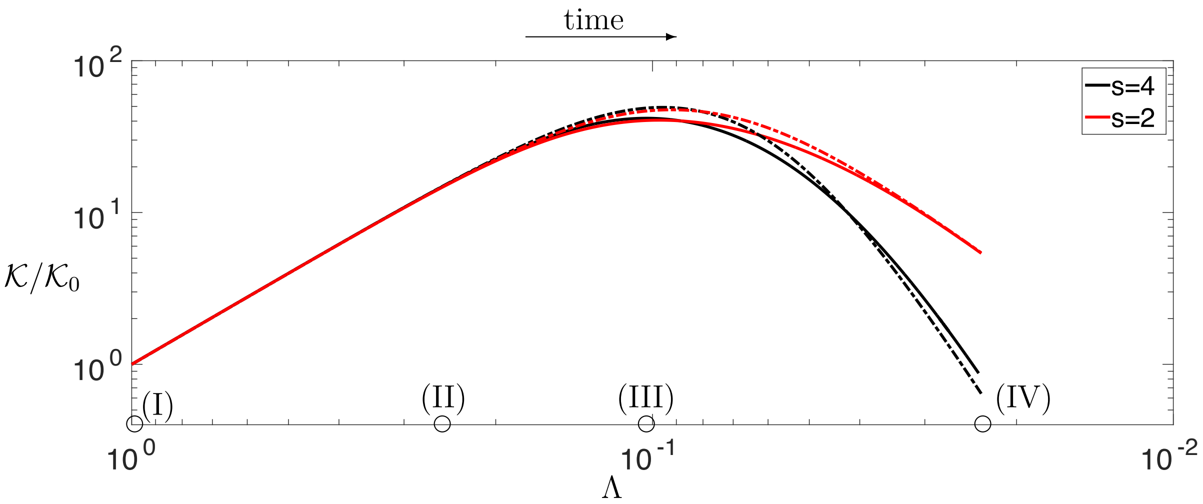

FIGURE 4.10 – Evolution of turbulent kinetic energy $\mathcal{K}$ as a function of the compression parameter Λ for both 1024^3 DNS and EDQNM simulations corresponding to the case of the spherical turbulent layer. Solid line : DNS ; Dashed line : EDQNM simulation. Saffman and Bachelor initial conditions with respectively ($s = 2$) and ($s = 4$) are used, as indicated in the legend.

for the incompressible velocity field in a spherical layer.

The DNSs are done in a three-dimensional 2π-periodic domain so that it is important to ensure minimal interaction between adjacent spherical turbulent layers. Therefore, we choose an outer radius r_M small enough compared to the size of the domain $H = 2\pi$, so that the velocity decreases sufficiently between the layers. We have experienced that $r_M/H = 1/\pi$ is adequate for that, and we also choose an inner radius such that $(r_M - r_m)/H = 1/(2\pi)$. The thickness of the turbulent spherical layer ℓ_{MZ} is determined on the spherically integrated kinetic energy profiles and corresponds to the region where $\mathcal{K} \geq 0.1 \max_r \mathcal{K}(r)$. The integral length scale ℓ_I has to be smaller than ℓ_{MZ} to avoid a fast turbulent diffusion of the layer during the compression. In consequence, we choose $\ell_{I0}/\ell_{\mathrm{MZ0}} \sim 0.07$. This scale separation, together with the constraint of resolving all the scales of turbulence, calls for 1024^3 DNS grid points.

Figure 4.10 shows the evolution of kinetic energy from DNS and EDQNM, and Figure 4.11 visualizations of the kinetic energy field extracted from DNS at different stages of the compression. The Reynolds and compression numbers Re and Cp, the integral scales ℓ_I and the turbulent layer size ℓ_{MZ} are plotted in Figures 4.12 and 4.13 respectively. Energy spectra at the same compression stages as the kinetic energy distribution in Figure 4.10 are plotted in Figure 4.14. The kinetic energy radial profiles averaged over spherical shells in physical space are shown in Figure 4.15.

The kinetic energy evolution in Figure 4.10 exhibits two self-similar phases corresponding to rapid compression followed by the viscous dissipation regimes. As ex-

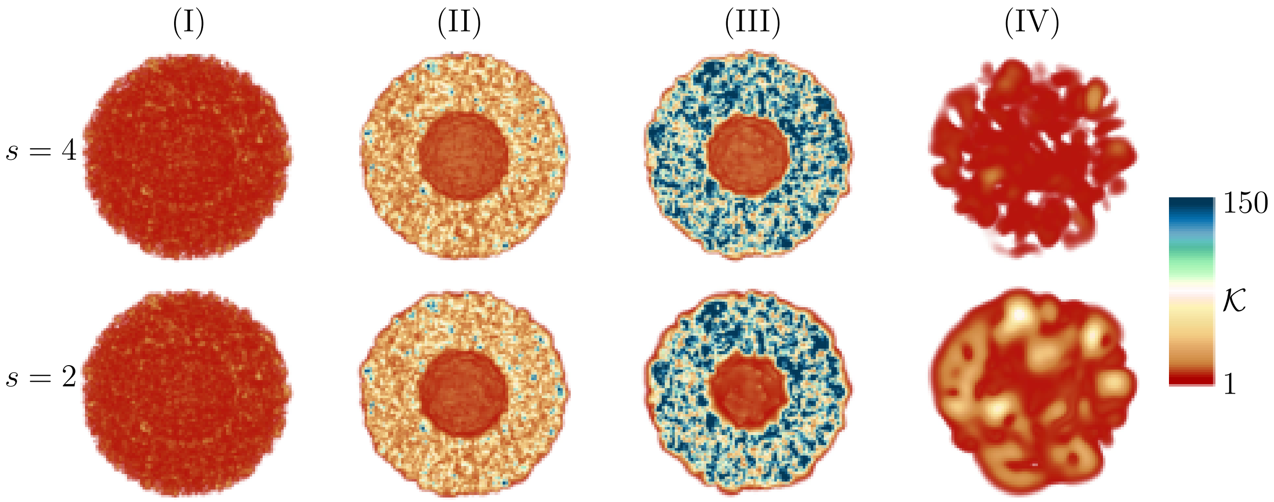

FIGURE 4.11 – Distribution in a plane cut of turbulent kinetic energy $\frac{u_i^2}{2}$ in the DNS at different instants indicated in Figure 4.10. Top row : the Batchelor case ($s = 4$) ; and bottom row : the Saffman case (s=2). The scaling corresponds to that of the moving frame.

pected, the intermediate cascade phase is not observed due to the low value of the initial Reynolds number.

As for the simulations presented previously, DNS and EDQNM agree very well if one considers the non dimensional parameters (Figure 4.12) and the one-point statistics $\mathcal{K}$, ℓ_I (Figure 4.13), but it is also true for the kinetic energy spectra (Figure 4.14). This may appear surprising in the sense that EDQNM is a model for homogeneous isotropic turbulence, whereas the spherical turbulent layer is spatially inhomogeneous. This can be explained by the fact that turbulence lengthscales remain smaller than the size of the turbulent layer throughout the compression, as shown in Figure 4.13. Thus the evolution of turbulent structures is not influenced by the large-scale inhomogeneity, and the flow remains quasi-homogeneous as regards its statistics.

The different scaling laws derived in Sec. 4.4.1 are also recovered in the spherical turbulent layer simulations confirming in particular that viscous dissipation is more important in the Batchelor case compared to the Saffman case, as shown in Figure 4.11. One, however, remarks in Figure 4.13 That the integral length scale ℓ_I is larger in Saffman turbulence than in the Batchelor case. This can be explained by non-negligible nonlinear turbulent transfer around Λ_M, since, during the compression phase, ℓ_I always evolves as Λ^2 in the rapid compression regime, while it scales as Λ^{-1} in the viscous regime.

It is interesting to look at the ℓ_{MZ} evolution during the compression in Figure 4.13

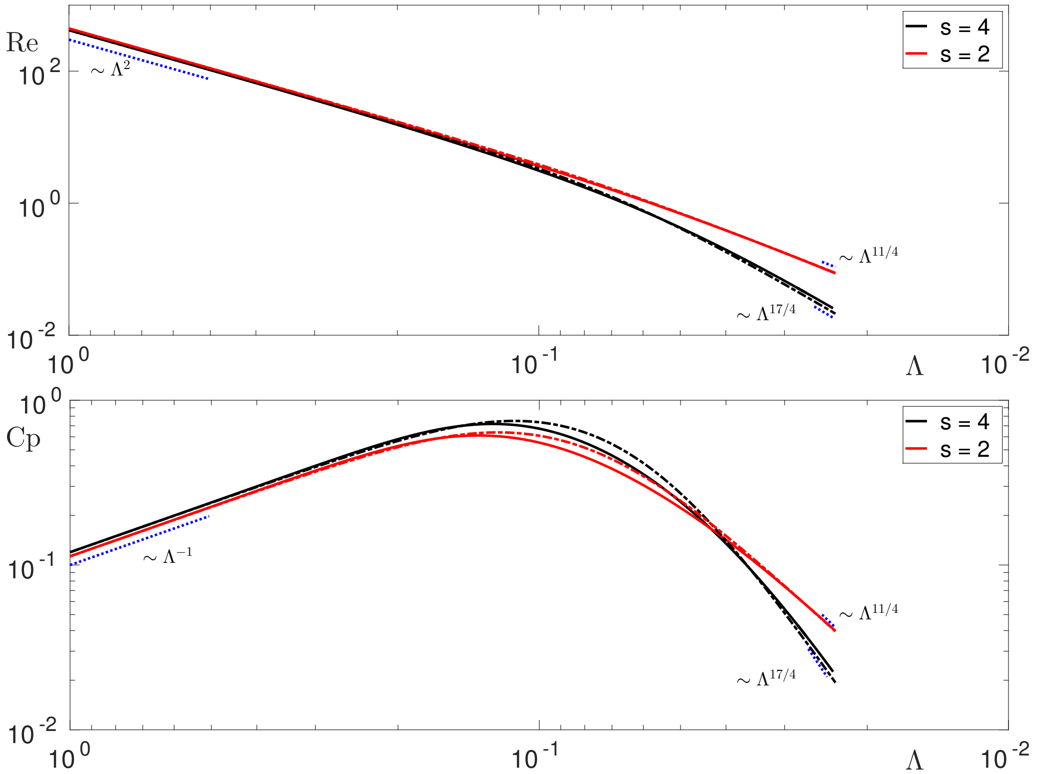

FIGURE 4.12 – Evolution of (Top) the Reynolds number Re and (Bottom) the compression number Cp as a function of the compression parameter Λ for the spherical turbulent layer case extracted from DNS (solid line) and EDQNM (dashed line) simulations. Black lines : Batchelor initial condition ($s = 4$). Red lines : Saffman initial condition ($s = 2$).

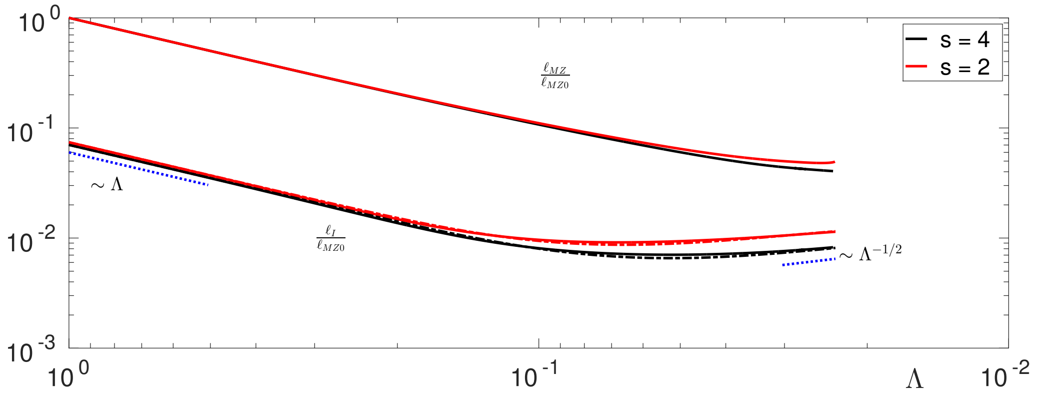

FIGURE 4.13 – Evolution of the integral scale ℓ_I (DNS and EDQNM) and the turbulent layer size ℓ_{MZ} (DNS) as a function of the compression parameter Λ corresponding to the case of the spherical turbulent layer with (red lines) Saffman and (black lines) Batchelor initial conditions.

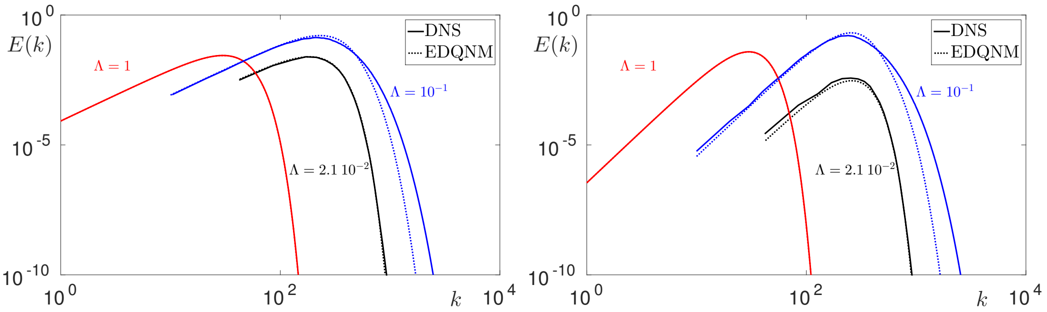

FIGURE 4.14 – Energy spectra as a function of wavenumber, $E(k)$, corresponding to the spherical turbulent layer case both in DNS (Plain line) and EDQNM (Dashed line) and taken at different values of the compression parameter Λ. (Right) Batchelor initial condition ($s = 4$). (Left) Saffman initial condition ($s = 2$).

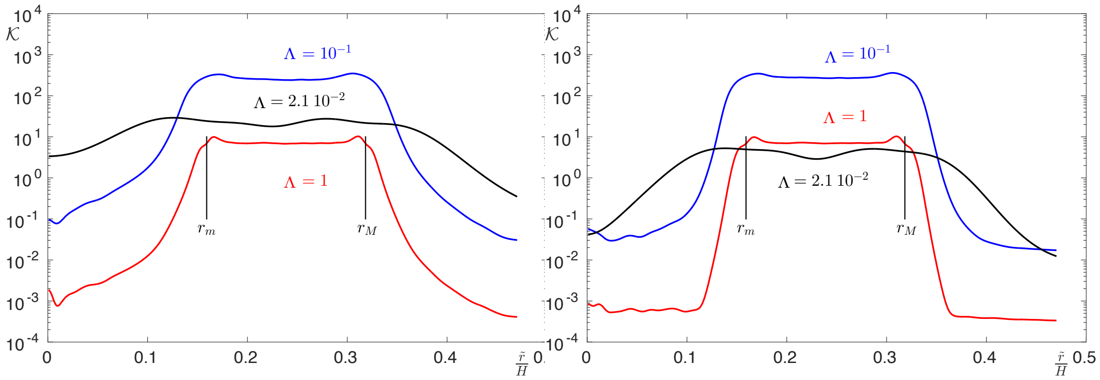

FIGURE 4.15 – Spherically integrated kinetic energy profile extracted from DNS as a function of radius $\tilde{r}$ and taken at different values of the compression parameter Λ. (Left) Saffman initial condition ($s = 2$) (Right) Batchelor initial condition ($s = 4$).

and at the different kinetic energy profiles in Figure 4.15 which, in the ICF context would correspond to studying the contamination of the hot spot by the turbulence. In the beginning, for $\Lambda \leq \Lambda_M$, the evolution of the turbulent fronts of the turbulent layer is slow and $\ell_{\text{MZ}} \sim \Lambda^2$. However, the dynamics of ℓ_{MZ} changes when entering the viscous phase, which corresponds to a diffusive increase of turbulent kinetic energy towards the center, as seen in the radial profiles in Figure 4.15. This phase also is sensitive to initial conditions since kinetic energy in the center in the Saffman case is higher than in the Batchelor case.

In summary, our simulations show that the sudden viscous phase not only dissipates the turbulent kinetic energy but also enhances its transport, possibly leading in the context of ICF to the contamination of the hot spot. Accordingly, it seems particularly important to predict the time at which the viscous phase occurs, especially if it is before the bang time. From the data of the simulations of Weber et al. (2014a), one can obtain a quantitative estimate of the order of the corresponding timescales. Although some physical phenomena are overlooked and there remain uncertainties concerning their relative magnitude, it seems that the bang time appears before the viscous phase, hence possibly explaining why the contamination of the hot spot is not very important (by bang time the fuel-ablator interface has converged from $340\mu m$ to $54\mu m$ giving $\Lambda_{bang} \sim 0.16 > \Lambda_M$). However, it seems possible to consider different initial perturbations in which the viscous phase may appear earlier than the bang time. This would clearly result in important modifications of the turbulent mixing in the fuel.

4.5 Conclusion

In this chapter, we have investigated compressed turbulence in a weakly-coupled plasma by identifying the different regimes resulting from the competition between turbulence production, nonlinear energy transfer, and viscous dissipation. Depending on the relative importance of these terms, three self-similar regimes can appear, namely rapid compression, cascade and viscous phases. All three are clearly observed in our DNS and EDQNM simulations. While the rapid compression and viscous phases have been discussed in Davidovits and Fisch (2016a), the cascade phase is precisely characterized for the first time thanks to the EDQNM model that permits to explore very high Reynolds number configurations. Besides, this new model has proven its efficiency at lower Reynolds numbers, by matching DNS results regarding one-point statistics and two-point correlation spectra.

For sufficiently large initial Reynolds numbers and small initial compression numbers, weakly-coupled plasmas under compression experience growth of kinetic energy due to a rapid compression or cascade phase. However, the viscous phase always prevails at the end of the compression leading to the sudden dissipation phenomenon. By performing a parametric study with the EDQNM model, we have been able to explore the phase space of nondimensional numbers, Re and Cp, and to locate the values of the critical compression parameter at the maximum of kinetic energy corresponding to the beginning of the viscous phase. This also reveals the complex interplay between turbulence production, transfer, and dissipation, leading to some configurations to two successive growth/decay phases of kinetic energy in place of one during the compression.

The scaling laws for the different self-similar regimes have been derived from a theoretical analysis and recovered in DNS and EDQNM simulations. As in other classical turbulence problems, it demonstrates the dependence of the flow dynamics on the initial distribution of energy at large scales. This appears particularly crucial during the viscous phase since it can change the decay exponents of kinetic energy drastically. Consequently, a much higher amount of turbulent fluctuations remain at the end of compression when initial kinetic energy is concentrated at large scales.

Thanks to these results about the refined stages of the flow dynamics and the conditions of their appearance, we were able to extend our study to the case of an inhomogeneous spherical turbulent layer under compression, using parameters representative of ICF capsules. While recovering the different phases already identified in the homogeneous configurations, the simulations permit us to observe the diffusion of the layer towards the center, mimicking the contamination of the hot spot by turbulence. The results show an enhanced enlargement of the layer during the viscous phase, along with great sensitivity to initial conditions. Therefore, it raises the question of whether the sudden viscous phenomenon is favorable to achieve ignition in ICF. On the one hand, viscous dissipation participates in a global temperature increase by converting kinetic energy into internal energy, increasing the fusion reactions. On the other hand, turbulent mixing can be transported into the core, cooling the hot spot. In all cases, the appearance of the viscous phase indicates an important change in the plasma dynamics, and it seems important to figure out when this happens, before or after the bang time for some configurations.

Chapitre 5

Variable density effects in unstably stratified turbulence

Contents

In the introduction, we have presented the problems that are still open in the context of the baroclinic instability. The complexity of this type of flows makes fundamental studies difficult because of the different interacting mechanisms, such as inhomogeneity, anisotropy, and compressibility [Zhou 2017a].

This is the reason why, during the years, some simplified frameworks have been introduced to study the buoyancy generated turbulence.

The first simplified set-up was proposed by Batchelor et al. (1992), who investigated the decay of homogeneous turbulence, with passive scalar and buoyancy effects. They limited their analysis to Boussinesq approximations, that is, cases with small scalar fluctuations that correspond to low Atwood number Rayleigh-Taylor turbulence. They found, using linear analysis of the Navier-Stokes equations together with

DNS, that the history of the motion depends on the large scales of the flow. They also show that similar behavior is still present when the nonlinear terms are taken into account, that is, the self-similar state of the flow at large times depends on the behavior of the spectra near $k = 0$.

Subsequently, studies on a similar problem were carried out by Sandoval (1995) and Livescu and Ristorcelli (2007; 2008), who eliminated the small fluctuation hypothesis using the variable density approximations.

Although they consider buoyancy effects in homogeneous configurations, they limit their investigations to a case of turbulence decay, which is an essential difference with the Rayleigh-Taylor turbulence. One of the features of the latter is the continuous conversion of potential energy into kinetic energy, which increases turbulence intensity.

The closer simplified configuration, which retains most of the Rayleigh-Taylor features together with the idealization of homogeneous turbulence, is the Unstably Stratified Homogeneous Turbulence (USHT).

The USHT was investigated experimentally by Thoroddsen et al. (1998), who studied the effects of an unstable linear density profile on the evolution of homogeneous grid-generated turbulence, in a thermally stratified wind tunnel. They found that, contrary to the stably stratified case, where vertical velocity fluctuations are inhibited, the buoyancy forces feed energy into the vertical motions.

The derivation of the USHT equations and the first numerical simulations were performed by Griffond et al. (2014), Soulard et al. (2014), who identified this idealized framework configuration as a tool to obtain a deeper understanding of buoyancy-driven mixing. The underlying hypothesis of the unstably stratified homogeneous turbulence is the homogeneity. This is justified if the integral scale ℓ of turbulence is small compared to the mixing zone size L. The ratio between these two quantities has been measured by Vladimirova and Chertkov (2009) in incompressible Rayleigh-Taylor mixing layer, where they found $\frac{\ell}{L} \approx 0.2$.

The direct numerical simulation of the USHT equations presents, as usual, for DNS, limitation on the Reynolds number of the flow. That is why Burlot et al. (2015a), proposed a spectral model based on the EDQNM closure to investigate USHT dynamics at large Reynolds number.

They found that for several initial conditions, the late time study of the self-similar states is limited due to confinement effect and that large numerical simulations for both DNS and EDQNM are required to reach these states.

The Rayleigh-Taylor turbulent mixing zone, at late times, presents a self-similar evolution, as discussed in the introduction of this thesis. The unstably stratified homogeneous turbulence maintains the same characteristic.

It has been shown [Griffond et al. 2014, Soulard et al. 2014] that, for the case of constant buoyancy frequency N, the second-order moments grow exponentially with time, for example, the turbulent kinetic energy

$$\langle u_i u_i \rangle = \exp{(\beta N t)}. \tag{5.1}$$

Here the parameter β plays the same role as the α for the Rayleigh-Taylor turbulence.

The value of β can be directly connected to the large scale of the flow and in particular, to the infrared slope of the energy spectrum [Poujade and Peybernes 2010]. In fact, Soulard et al. (2014) show that

$$\beta = \frac{4}{3+s}, \quad \text{for } s \leq 4. \tag{5.2}$$

So that the large scales of the flows are the determinant factor to determine the growth rate of an USHT field second order moments.

5.1 Velocity field induced by an isolated eddy in a variable density field

Here we consider a blob of vorticity located at $\mathbf{x} = 0$ within a domain V [Davidson 2015] with characteristic length ℓ_B. Inside this domain, the density is nonuniform, while outside of V, it is constant. The following developments are based on the work of Soulard et al. (2019).

If we use the approximation that the velocity is still incompressible we can relate it

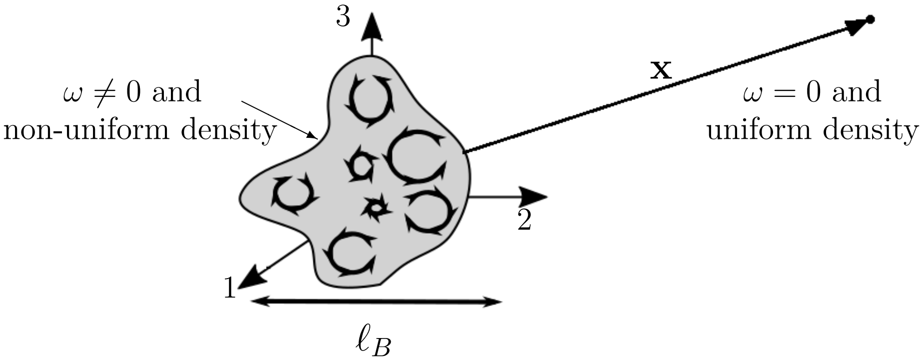

FIGURE 5.1 – Isolated blob of vorticity in a domain with variable density located at $\mathbf{x} = 0$. Figure modified from Soulard et al. (2019).

with the vector potential $\boldsymbol{A}$,

$$\mathbf{u} = \nabla \times \boldsymbol{A} \tag{5.3}$$

which is connected to the vorticity $\boldsymbol{\omega}$ via the Biot-Savart law

$$\boldsymbol{A}(\mathbf{x}) = \frac{1}{4\pi} \int \boldsymbol{\omega}(\mathbf{x}') \frac{d\mathbf{x}'}{|\mathbf{x} - \mathbf{x}'|}, \tag{5.4}$$

where the integral is all over the space. If we consider value of $\mathbf{x} \gg \ell_B$, we can find value of $\boldsymbol{A}$ using the Taylor expansion of the $|\mathbf{x}-\mathbf{x}'|$

$$\frac{1}{|\mathbf{x}-\mathbf{x}'|} = \frac{1}{r} - \partial_i\left(\frac{1}{r}\right)x'_i + \frac{1}{2}\partial^2_{ij}\left(\frac{1}{r}\right)x'_i x'_j + \cdots\,, \tag{5.5}$$

where $r = |\mathbf{x}|$. If one substitutes this expression in Eq (5.4) and after some simplifications one obtains

$$4\pi\boldsymbol{A}(\mathbf{x}) = \partial_i\left(\frac{1}{r}\right) \times \int \frac{\mathbf{x}' \times \boldsymbol{\omega}}{2} d\mathbf{x}' + \frac{1}{2}\partial^2_{ij}\left(\frac{1}{r}\right)\int x'_i x'_j \boldsymbol{\omega}' d\mathbf{x}' + \cdots\,. \tag{5.6}$$

The first integral is a measure of the linear momentum introduced into the fluid by the blob of vorticity and we shall call it *linear impulse* $\mathbf{L}$. To finally obtain the expression for the velocity, We take the curl of (5.6), to finally obtain the expression for the velocity

$$4\pi\mathbf{u}(\mathbf{x}) = (\mathbf{L}\cdot\nabla)\nabla\left(\frac{1}{r}\right) + \nabla\left(\partial^2_{ij}\left(\frac{1}{r}\right)\right) \times \int x'_i x'_j \boldsymbol{\omega}' d\mathbf{x}' + \cdots\,. \tag{5.7}$$

This expression evidences how, if $\mathbf{L} \neq 0$ the velocity in the far field goes like $\mathbf{u}(\mathbf{x}) \sim r^{-3}$ while in the case of $\mathbf{L} = 0$, we have $\mathbf{u}(\mathbf{x}) \sim r^{-4}$. In case of constant density, it has been shown [Davidson 2015] that $\mathbf{L}$ is an integral invariant for the isolated blob of vorticity, so that the far-field decay of the velocity is not modified during the blob evolution.

Taking the divergence of the incompressible Navier-Stokes equation provides a relation between the velocity and the pressure. Which allows expressing the pressure p as a function of the velocity $\mathbf{u}$ using the Biot-Savart law

$$4\pi\frac{p}{\rho} = \int [\nabla\cdot(\mathbf{u}\cdot\nabla\mathbf{u})]' \frac{d\mathbf{x}'}{|\mathbf{x}-\mathbf{x}'|}. \tag{5.8}$$

Again we can expand the integral using the Taylor series (5.5) which after some simplification leads to

$$4\pi\frac{p}{\rho} = \partial^2_{ij}\left(\frac{1}{r}\right)\int u'_i u'_j d\mathbf{x}' + \cdots\,. \tag{5.9}$$

which shows how the pressure field decays as $p \sim r^{-3}$.

However, when the density is not uniform, equation (5.8) is no longer valid. In this case, we start from the incompressible Navier-Stokes equation

$$\partial_t u_i + u_j \partial_j u_i = -\tau\partial_i p + \nu\partial^2_{jj} u_i, \tag{5.10}$$

where the specific volume $\tau = 1/\rho$ is non uniform. Taking the divergence of (5.10) we obtain

$$\partial^2_{ii}(\tau p) - \partial_j(p\partial_j\tau) = -\partial^2_{ij}(u_i u_j). \tag{5.11}$$

This equation cannot be simply inverted to obtain an equation similar to (5.8), however an implicit solution can still be found

$$4\pi\tau p = \int \partial_j[\partial_i(u_iu_j) - p\partial_j\tau)]' \frac{d\mathbf{x}'}{|\mathbf{x}-\mathbf{x}'|} \tag{5.12}$$

which can be expanded, as in the constant density case using the Taylor series

$$4\pi\tau p = -\partial_i\Big(\frac{1}{r}\Big)\int p\partial_j\tau d\mathbf{x} + \partial^2_{ij}\Big(\frac{1}{r}\Big)\Big(\int u'_iu'_jd\mathbf{x}' - \frac{1}{2}\int p(x_i\partial_j\tau + x_j\partial_i\tau)d\mathbf{x}\Big) + \cdots \tag{5.13}$$

From equations (5.9) and (5.13), we observe that in the two cases, the pressure scaling is not the same, due to the additional terms coming from the τ gradients.

Soulard et al. (2019) show that injecting the far-field expansion of the velocity $\mathbf{u}$, Eq (5.7), into the evolution Eq (5.10) and using the scaling obtained from the pressure, one obtains an evolution equation for the linear impulse $\mathbf{L}$:

$$\partial_t L_i = \int p\partial_i\tau d\mathbf{x}. \tag{5.14}$$

In particular, this result shows that linear impulse can be created in the vorticity blob by the correlation of pressure and density gradient, so that in this case the velocity in the far-field

$$\mathbf{u}(\mathbf{x}) \sim r^{-3}. \tag{5.15}$$

In the same paper, the author analyzes the case of homogeneous turbulence with variable density. They show that the permanence of large eddy is not achieved in the case when the infrared slope of the kinetic energy spectra s is greater than 2. This conclusion is, however, only verified if the density fluctuations are sufficiently large; if it is not the case, a kinetic energy spectrum with $s = 4$ will maintain this value during the flow evolution.

5.2 Unstably stratified homogeneous turbulence equations

The equations for the unstably stratified homogeneous turbulence derived in section 2.2 are recalled for both approximations, variable density, and Boussinesq.

These equations are derived for a turbulent mixing zone between two fluids with different densities, in a uniform gravity field. In the following u_i is the velocity, π the reduced pressure, $\theta = \log(\rho/\rho_0)$ is a scalar value connected to the density, g is the acceleration and L is the mixing zone width. ν and $\mathcal{D}$ are the molecular viscosity and diffusivity that in this chapter are considered constant.

$$\begin{aligned}\partial_t u_i + u_j \partial_j u_i + \pi \partial_i \theta = & - \partial_i \pi - gL \partial_i \theta - \frac{1}{L} \pi \delta_{i3} + \nu \partial_{jj}^2 u_i \\ & + \nu \partial_i \left(\partial_j u_j \right) + \nu \left(\partial_j u_i + \partial_i u_j \right) \partial_j \theta \\ & + \frac{\nu}{L} \left(\partial_3 u_i + \partial_i u_3 \right) \end{aligned} \tag{5.16}$$

$$\partial_t \theta + u_j \partial_j \theta = \mathcal{D} \partial_{jj}^2 \theta - \frac{1}{L} u_3 \tag{5.17}$$

$$\partial_j u_j = -\mathcal{D} \partial_{jj}^2 \theta. \tag{5.18}$$

The variable density assumption introduces new nonlinear terms due to the scalar gradients, together with the relation (5.18) connecting the divergence of the velocity field to the Laplacian of the scalar.

If one assumes small fluctuations for θ, equations (5.16), (5.17), (5.18) reduce to the Boussinesq case :

$$\partial_t u_i + u_j \partial_j u_i = -\partial_i \pi + g \theta \delta_{i3} + \nu \partial_{jj}^2 u_i \tag{5.19}$$

$$\partial_t \theta + u_j \partial_j \theta = \mathcal{D} \partial_{jj}^2 \theta - \frac{1}{L} u_3 \tag{5.20}$$

$$\partial_j u_j = 0. \tag{5.21}$$

And we recall the expression of the buoyancy frequency

$$N = \sqrt{\frac{g}{L}}. \tag{5.22}$$

which is maintained constant in time.

The different USHT flows considered in this work are characterized by two non-dimensional numbers : the Reynolds and the Froude numbers which are defined as

$$Re = \frac{u\ell}{\nu}, \quad \text{and} \quad Fr = \frac{u}{\ell N}, \tag{5.23}$$

where u is the characteristic velocity and ℓ is the integral scale, already introduced in chapter 4, defined as

$$\ell = \frac{3\pi}{4} \frac{\int_0^{+\infty} k^{-1} E(k,t) dk}{\int_0^{+\infty} E(k,t) dk} \tag{5.24}$$

where $E(k,t)$ is the kinetic energy spectrum.

The Reynolds number helps to understand the relative importance of inertial over viscous terms, while the Froude number indicates the ratio between inertial and forcing terms.

5.2.1 Numerical methods

We solve equations (5.16)-(5.18) and (5.19)-(5.21) using the pseudo-spectral method and the third-order Runge-Kutta SSP scheme described in chapter 3. We recall that in all the simulations, the velocity and scalar mean values are imposed to be 0.

The solution of both variable density and Boussinesq systems of equations faces, in part, the same numerical challenges due to the properties of the USH turbulence. The growth of the integral scale, together with the decrease of the Kolgomorov length scale, $\eta = (\epsilon/\nu^3)^{-1/4}$, requires a careful choice of the initial conditions and mesh sizes.

On the one hand, one should have a higher k_{peak} (the wavenumber of the energy spectrum peak) possible, knowing that it decreases during the simulation. Pope (2000) estimates that for a DNS free of confinement $k_{peak}/k_{min} \geq 10$. In our cases, we stop our simulations when $k_{peak}/k_{min} \sim 8$, which is a compromise between the minimization of confinement effects and the concurrent need to have long enough simulations to observe the establishment of self-similar states.

On the other hand, the k_{peak} is limited by the mesh size, which imposes the smallest resolved scale. Furthermore, during the simulations, due to the turbulence kinetic energy increase, the Kolgomorov length scale decreases. Consequently, the computations resolution deteriorates.

Pope (2000) proposes the limit $k_{max} \times \eta = 1.5$, where k_{max} is the maximum resolved wavenumber, as a lower limit to satisfy in order to have resolved simulations. For the Boussinesq case at the end of the DNS simulation, we have $k_{max} \times \eta \sim 4$, which satisfies the proposed criterion.

Moreover, we recall that, in addition to the issues mentioned above, for variable-density approximation, the non-locality, in spectral space, of the Poisson equation requires an iterative method to invert the linear system and compute the pressure contribution. We use the generalized minimal residual (GMRES) algorithm described in section 3.2.3.1, which ensures convergence even in cases with significant density fluctuations. Nevertheless, the convergence of this method is one of the variable density USHT critical features. As shown by Di Pierro (2017), in the Poisson equation, the pressure operator conditioning number depends on the density contrast in the computational domain. That is why, in USHT computations, where the scalar variance grows with time, the number of GMRES iteration required to achieve the desired convergences increases as the simulation advances.

The increasing computational cost of the DNSs would not be manageable for a parametric study on the initial conditions, for instance, the direct numerical simulation Ud3, presented in section 5.4, demanded 1000000 CPU hours dispatched on 4196 cores.

For this reason, to explore the influence of initial conditions, we propose to use the implicit large eddy simulation method of Mathew et al. (2006) and referred to as ADM-LES.

The ILES allows us to study the same initial conditions that one would have for the DNS with coarser meshes and reduced computational time.

5.2.1.1 Validation ILES for variable density

The effectiveness of the ADM-LES for USHT computation in Boussinesq approximation has already be proven by Griffond et al. (2015b). Here we show how this simple large eddy simulation method can be useful in variable density computation too. The ADM-LES is based on a low pass filter and an approximate deconvolution [Grinstein et al. 2007]. In this method, as explained in Mathew et al. (2006), the filtering and the deconvolution can be combined into a single step, which reduces to simply filtering the variable at each time step. A comparison between DNS and ILES data for the same case with a domain respectively of 1024^3 and 512^3 mesh points is plotted in Figure 5.2. These cases correspond to the simulation Ud3$_{VD}$ and Ul3$_{VD}$, which details are summarised in table 5.1.

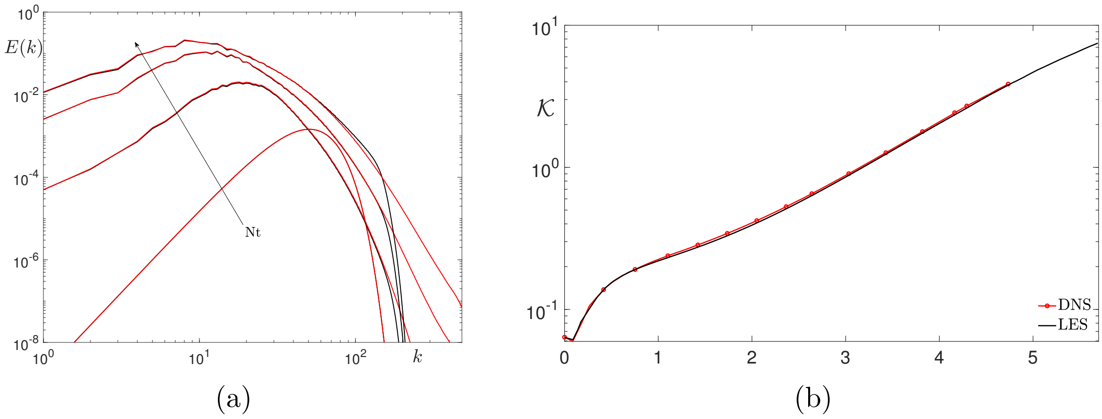

(a)

(b)

FIGURE 5.2 – Comparison of DNS (red) and ILES (black) results. (a) Kinetic energy spectra. (b) Total kinetic energy.

From the comparison of the one point integrated kinetic energy in Figure 5.2b, we observe a very good agreement between the two simulations with the ILES results having the same temporal dependence as the DNS.

The differences between the two methods are evidenced by the kinetic energy spectra of Figure 5.2a. The two spectra are in excellent agreement for all the wave numbers resolved by the ILES method until the sharp cut-off due to the low pass filtering around $k \simeq 200$.

The difference that is limited to the smallest scale of the simulation has to be considered when one discusses ILES results. All in all, the utility of this kind of under resolved simulation is undeniable, as it decreases the computational cost of the parametric study to 150000 CPU hours per simulation, retaining most of the physical properties of the direct numerical simulations.

Name		Type	Mesh size	Re_0	Fr_0	N	$\langle\theta\theta\rangle/\mathcal{K}$	$\mathcal{A}_t$
Ud3	VD	DNS	1024^3	4.92	1.24	4	3	0.98
	B	DNS	1024^3	4.92	1.24	4	3	0.98
Ul3	VD	ILES	512^3	4.92	1.24	4	3	0.98
	B	ILES	512^3	4.92	1.24	4	3	0.98
Ul1	VD	ILES	512^3	4.92	1.24	4	1	0.87
	B	ILES	512^3	4.92	1.24	4	1	0.87
Ul05	VD	ILES	512^3	4.92	1.24	4	0.5	0.74
	B	ILES	512^3	4.92	1.24	4	0.5	0.74
Ul01	VD	ILES	512^3	4.92	1.24	4	0.01	0.4
	B	ILES	512^3	4.92	1.24	4	0.01	0.4
Ul0	VD	ILES	512^3	4.92	1.24	4	0	0
	B	ILES	512^3	4.92	1.24	4	0	0

Table 5.1 – Simulation characteristics in terms of initial Reynolds number, initial Froude number, buoyancy frequency, the ratio between scalar variance and kinetic energy, and initial Atwood number. Type VD corresponds to simulations with variable density approximation while for type B to Boussinesq approximation.

5.2.2 Initial conditions

The initial conditions are generated using the methods described in section 3.4.1, for both variable density and Boussinesq approximations.

A total of 12 simulations are presented in this study, using either the Variable Density (VD) or Boussinesq (B) approximation to study non-Boussinesq effects. The 12 initial conditions have the same initial Reynolds number, Froude number, integral scale, and buoyancy frequency N but with a different ratio between scalar variance and kinetic energy.

5.3 Flow Topology

In this section, we discuss the differences in the flow topology during the time evolution of USHT direct numerical simulation Ud3. In Figure 5.3, we show the contours of the scalar fields resulting from Boussinesq and variable density approximations. We observe that from the same initial condition at $Nt = 0$, the two flows have a similar evolution until $Nt = 1.8$.

The first differences appear on the contours at $Nt = 3.7$, when in the scalar field of the variable density case, we can differentiate between the more spike-like and bubble-like structures, while this differentiation is not evident in the Boussinesq case, which shows a more symmetric behavior.

The different behaviors of the scalar field become more evident as the simulations advance with the last two contours showing striking differences.

The variable density tendency to form spike-like structures reach some extreme, with the presence of thin layers of heavy fluid moving towards the lighter fluid.

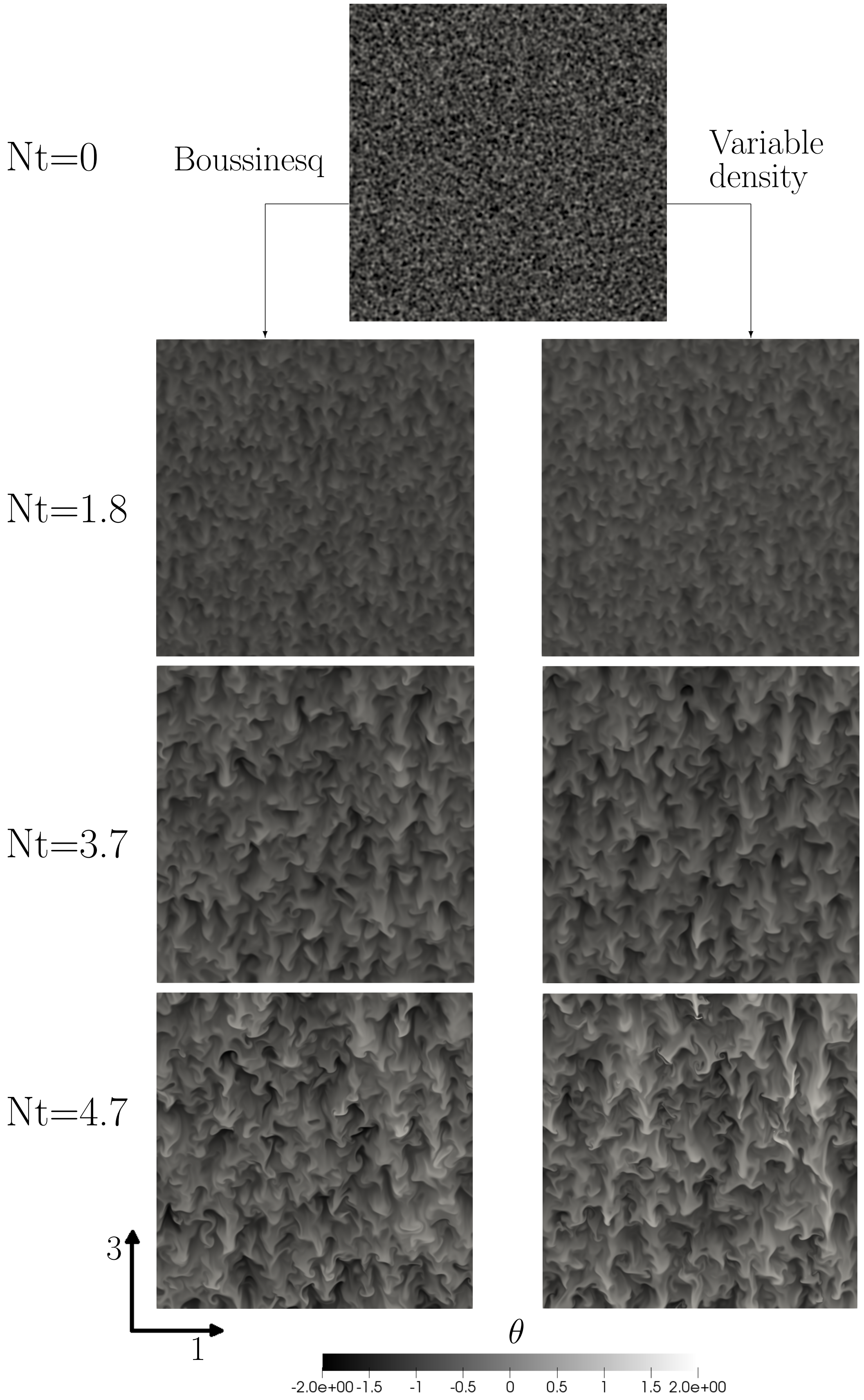

FIGURE 5.3 – Contours of the scalar field θ of simulations $\mathrm{Ud3}_B$ (left) and $\mathrm{Ud3}_{VD}$ (right). At four different times during the flow evolution.

5.4 Results

In this section we confront the results between the two direct numerical simulations Ud3 with Variable Density (VD) and Boussinesq (B) approximations.

5.4.1 Non dimensional numbers

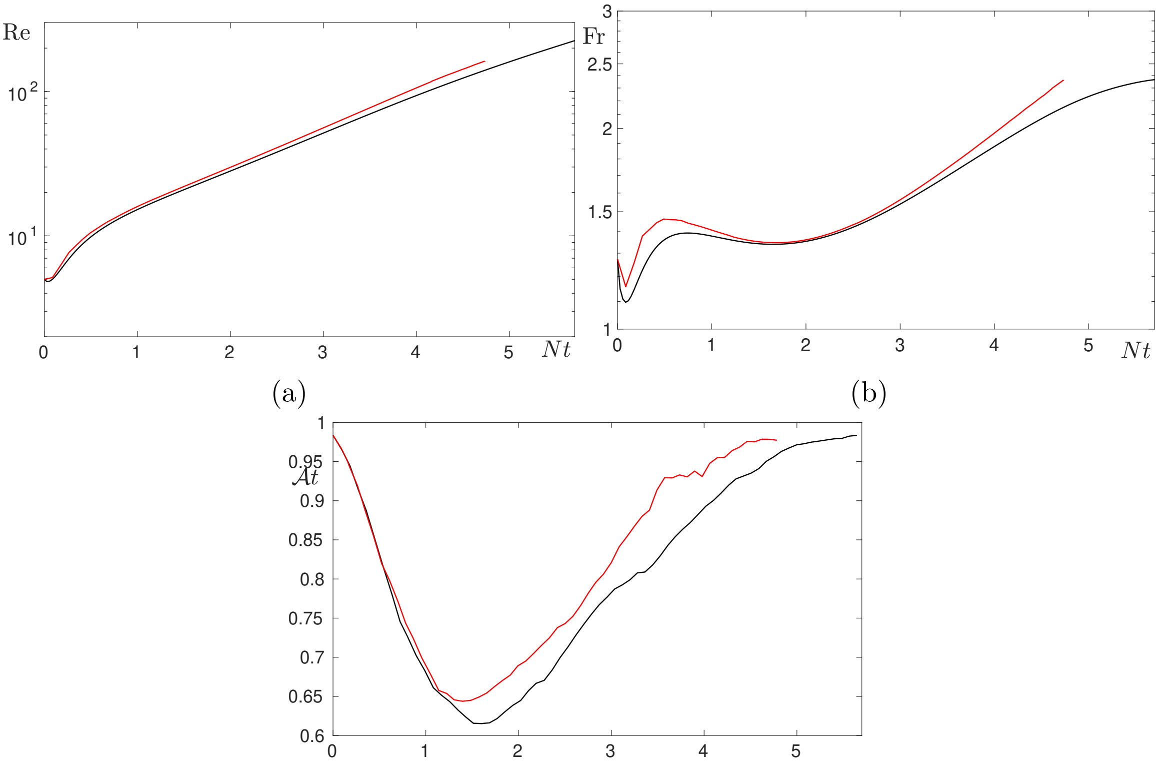

(a) (b)

(c)

FIGURE 5.4 – Temporal evolution of nondimensional quantities of the flow. (a) Reynolds number. (b) Froude number. (c) Atwood number. Red : Variable density. Black : Boussinesq.

Figure 5.4 shows the evolution of the nondimensional number characteristic of the flow. The Reynolds number that, at the beginning, has a value of $\simeq 5$ grows considerably and reaches different values for the variable density and Boussinesq approximations. At the end of the simulations, we have $Re \simeq 287$ for $Ul3_{VD}$ and $Re \simeq 220$ for $Ul3_B$, which is the first indication of different behaviors between the two simulations.

The effective Atwood number computed using the maximum and minimum value of θ, that is found in the computational domain at every time step,

$$\mathcal{A}_t = \frac{\exp(\theta_{max}) - \exp(\theta_{min})}{\exp(\theta_{max}) + \exp(\theta_{min})} \tag{5.25}$$

is plotted in 5.4c. In this figure, we can observe how, at the beginning, there is a phase where the $\mathcal{A}_t$ decays, which corresponds to the decrease in the scalar variance, in Figure 5.5b, discussed in section 5.4.2. After the minimum, reached around $Nt \simeq 1.5$ for the two simulations, the Atwood number increases during the evolution of the flow, reaching values close to 1 at the end. We remark how the values for the VD simulation are always higher than B simulation, suggesting the presence of larger fluctuations of density in the domain.

5.4.2 One-point statistics

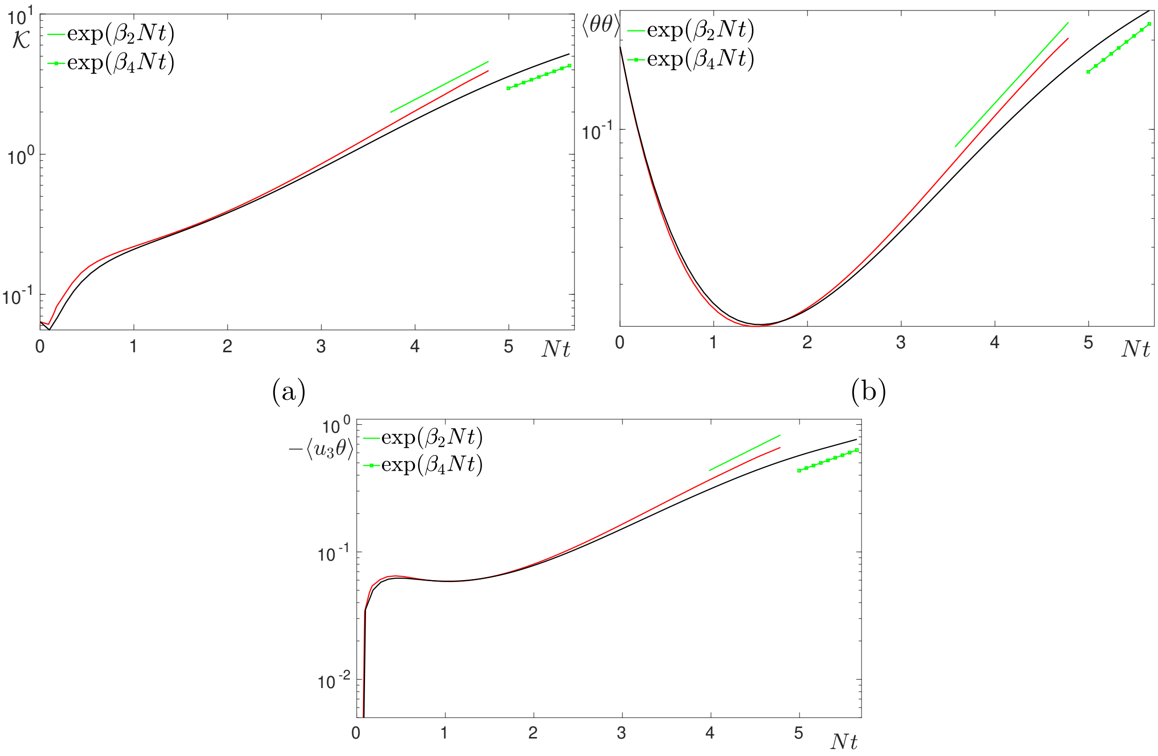

(a) (b)

(c)

FIGURE 5.5 – Temporal evolution of one-point statistics. (a) Turbulent kinetic energy. (b) Variance of the scalar. (c) Vertical flux. Red : Variable density. Black : Boussinesq

The evolution of the one-point statistics is plotted in Figure 5.5. From the evolution of the turbulent kinetic energy in Figure 5.5a, we can observe how the two approximations have analogies and differences.

At the beginning of the simulation, the kinetic energy in the VD approximations grows more rapidly with respect to the Boussinesq case. The different behavior during this first transient phase can be explained by the variable density effects, which are intense enough to modify the large scale of the flow.

During the following phase, from $Nt \simeq 1$, when the nonlinear effects begin to dominate the dynamics, we observe a period where the two approximations have a good agreement. This period is, however, short, and from $Nt \simeq 3$, the kinetic energy of the two simulations shows, again, different temporal dependencies. After this phase, where the nonlinearities become the principal mechanism, we observe the flow entering the self-similar state. As explained in the introduction, in this phase the second-order moments grow exponentially, with the following scaling

$$\mathcal{K} \sim \exp(\beta N t) \quad \langle \theta\theta \rangle \sim \exp(\beta N t) \quad \langle u_3 \theta \rangle \sim \exp(\beta N t) \tag{5.26}$$

where β depends on the infrared part of the spectra.

It is in this phase that the large scale flow modifications due to variable-density effects become evident. In particular, we observe that the kinetic energy of the VD simulation has a growth rate of $\beta_2 = 4/5$ corresponding to $s = 2$, while for the B simulation $\beta_4 = 4/7$ corresponding to $s = 4$. Additionally, we also remark how the infrared slope alteration, not only modifies β, but also the time when the flow enters the self-similar regimes, anticipating it.

The scalar variance $\langle \theta\theta \rangle$ time evolutions for both simulations, plotted in 5.5b, have a decay from $Nt = 0$ to $Nt \simeq 1.5$, followed by phase of growth reaching the self similar state at $Nt \simeq 4$, where the modification of the growth rate is also observed.

As expected, we also find the same behavior in the self-similar phase for the vertical flux $\langle u_3 \theta \rangle$.

5.4.3 Two-point statistics

The kinetic energy $E(k,t)$, the scalar variance $E_\theta(k,t)$, and the vertical flux $E_{\langle u_3 \theta \rangle}$ are presented in Figure 5.6.

From the same initial condition, we observe how the infrared part of the spectra of the three quantities, in the variable density approximation, is not constant and on the contrary, is modified, from a slope of k^4 to k^2. This modification induces the difference already observed on the one point quantities in section 5.4.2. For most of the temporal evolution, the main difference between the two approximations is due to this large scale effects.

However, we observe at $Nt = 3.7$ and more clearly at $Nt = 4.73$, that differences are also present in the nonlinear cascading processes, with small scales differences that are more and more evident, as the simulations proceed.

In the inertial zone of the VD simulation, we start to observe a scaling close to the $k^{-5/3}$, while for the Boussinesq, this dependence is less evident.

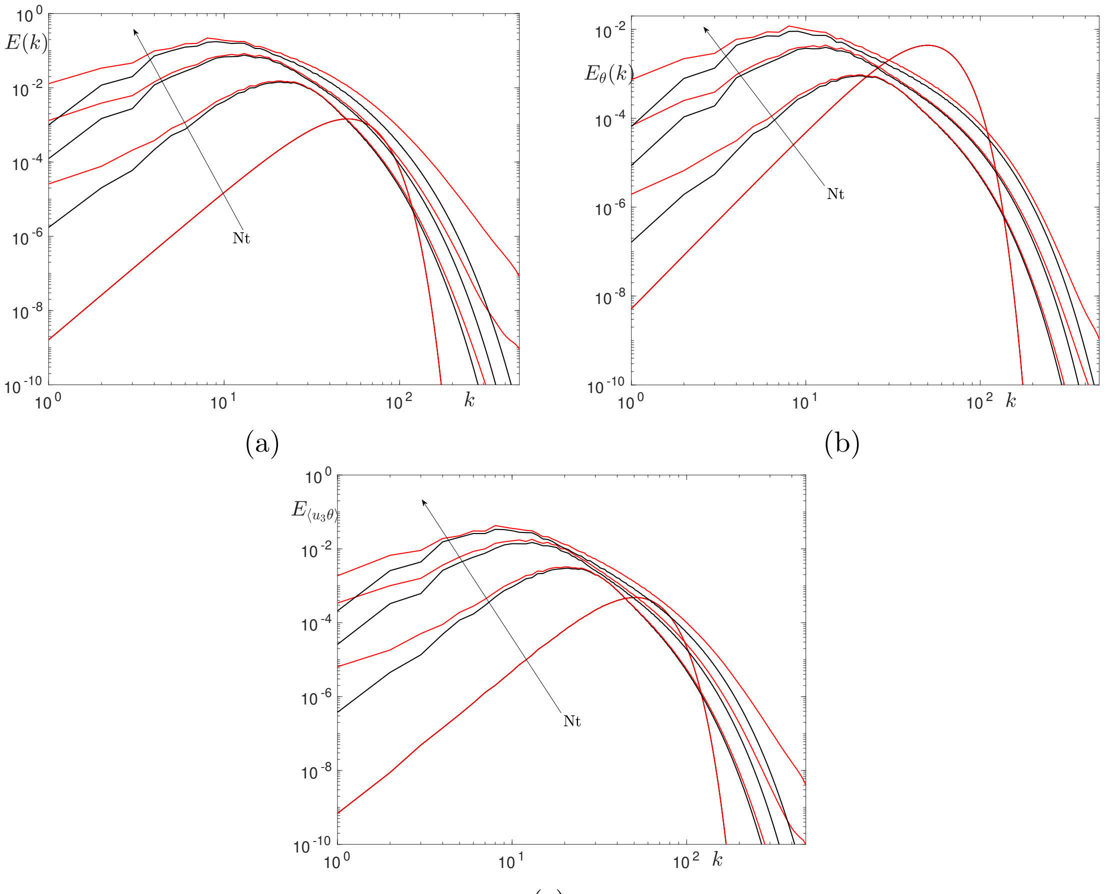

(a)

(b)

(c)

FIGURE 5.6 – Temporal evolution at four instants, $Nt = 0, 1.8, 3.7, 5$ of : (a) Turbulent kinetic energy spectra. (b) Scalar variance spectra. (c) Vertical flux spectra. The time increases in the direction of the arrows. Red : Variable density. Black : Boussinesq

At $Nt = 4.73$, the confinement effects are evident for both cases. This is a known problem for the direct numerical simulations of USHT configuration, which prevents the study of large Reynolds number configurations.

The difference just discussed is observed on the spectra of the three quantities, with the large scale justifying the difference observed for most of the simulations, while towards the end, we can appreciate the increased influence of the nonlinearities and the onset of confinement effects.

5.4.4 Anisotropy

Anisotropy is one of the main characteristics of the unstably stratified homogeneous turbulence, and it is one of the main features of buoyancy-driven flows such as Rayleigh-Taylor.

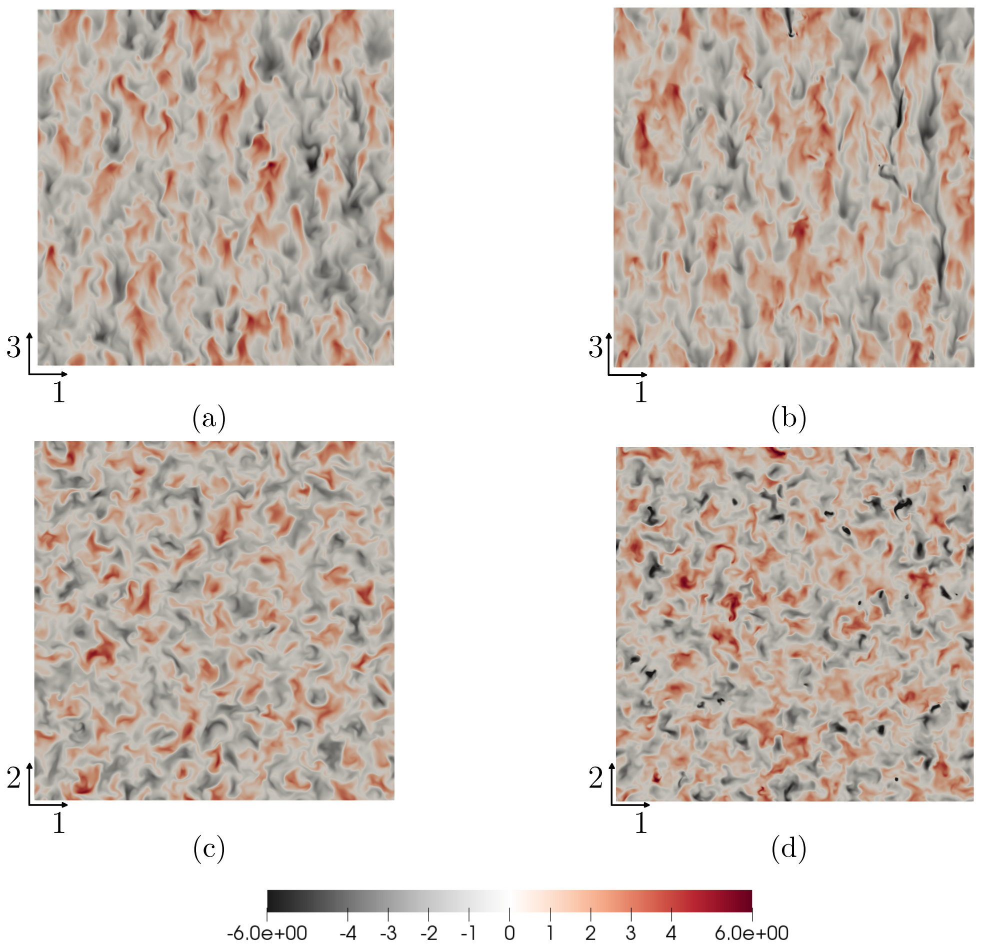

(a) (b) (c) (d)

FIGURE 5.7 – Vertical component of the velocity at $Nt = 4.73$. Top : Contours in a plane parallel to the acceleration. Bottom : Contours in a plane perpendicular to the acceleration. (a) and (c) Boussinesq results (b) and (d) Variable density

The acceleration direction imposes the anisotropy in USHT configuration, and as shown in section 5.3, it is present in both Boussinesq and variable density approximations.

As a further illustration in Figure 5.7 we show the contours of the vertical component of the velocity in a plane parallel 5.7a, 5.7b and perpendicular 5.7c, 5.7d to the vertical direction, for both simulations Ul3. The two figures show a marked anisotropy in the vertical direction, with the variable density case that has higher values.

A more quantitative way of looking at the anisotropy is using the anisotropy coefficient

$$b_{ij} = \frac{\langle u_i u_j \rangle}{\langle u_i u_i \rangle} - \delta_{ij}\frac{1}{3} \tag{5.27}$$

for the case of $i = j$.

This coefficient is a simple but effective way of looking at the anisotropic behavior of a flow. When this value is zero, it means that the kinetic energy is distributed equally among all the components. While if it is different means that the energy distribution is not isotropic, and we have preferential directions.

The evolution of the three anisotropy coefficients is plotted in Figure 5.8. As we already remarked qualitatively, the direction of anisotropy of the flow is the direction 3, following the acceleration. b_{33} is positive with values around 0.4 for most of the simulations, with a slight decrease towards the end. The difference between variable density and Boussinesq results is small and seems to increase from $Nt = 2$ to $Nt = 4$, and then decreases until the end of the simulation.

The difference, observed in the phase where nonlinear effects are important, may be caused by the different redistribution of energy produced by the further nonlinearities of the variable density equation.

Since the primary sources of the anisotropy are the large scales, the confinement effects in the last steps of the simulation may play a role in the final decrease.

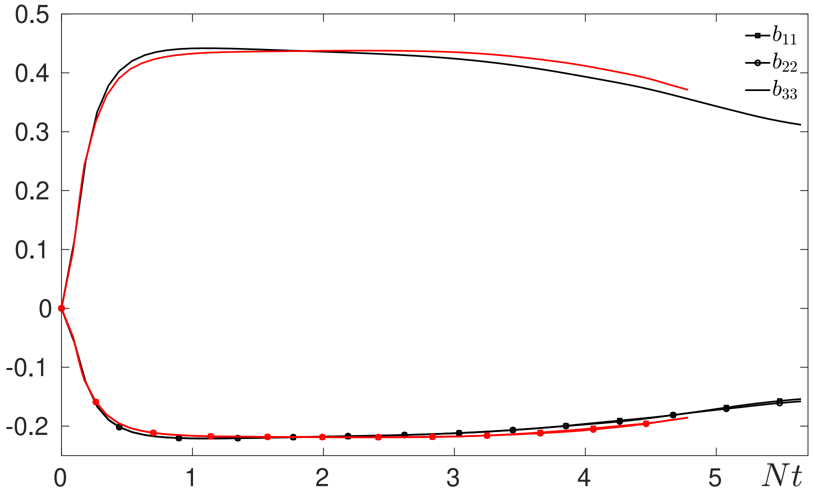

FIGURE 5.8 – Evolution of the anisotropy coefficients.In red variable density and black Boussinesq results.

In Figure 5.9 are reported the kinetic energy spectra of u_2 in 5.9a and u_3 in 5.9b. We observe how the difference between the two velocity components increases during the simulation for both variable density and Boussinesq approximations. The density influence on the infrared spectra is more evident on the vertical than on the horizontal component. The other interesting difference is observed at higher wavenumber, where the difference between the two approximations is higher in the vertical direction than the horizontal.

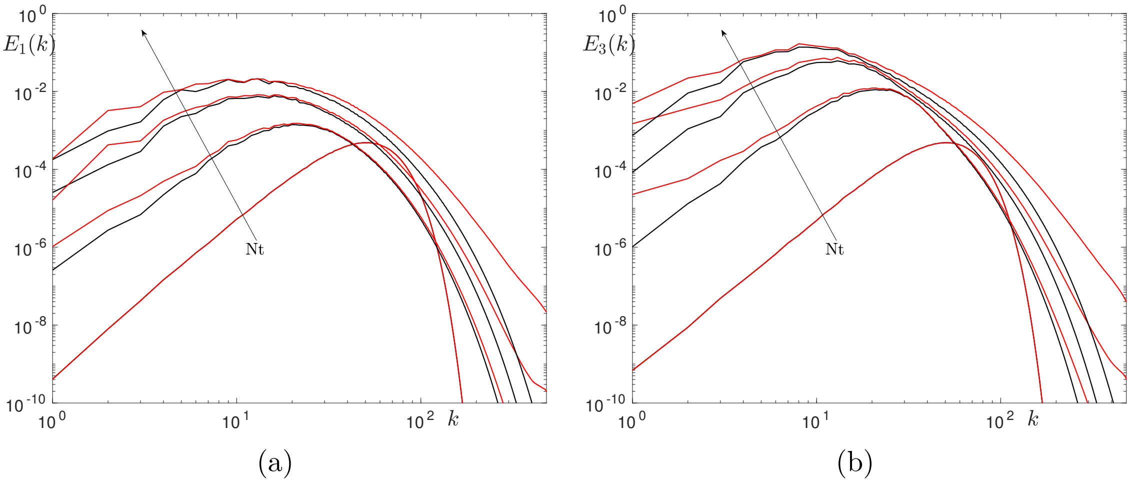

FIGURE 5.9 – Spectral energy spectra at four instants during the flows evolution $Nt = 0, 1.8, 3.7, 4.73$ of :(a) the horizontal component u_2 and (b) vertical component u_3. In red variable density and black Boussinesq results

5.4.5 Probability density functions

In this section, we compute the probability density functions for the scalar θ and two components of its gradient $\partial_3\theta$ and $\partial_1\theta$. The objective is to understand, in the physical space, how the fluctuations of θ are influenced by the variable density effects.

5.4.5.1 Probability density function of θ

The initial condition plotted in Figure 5.10a shows a symmetric distribution of θ around the mean value 0. The probability density functions stay symmetric for both simulations, but the values that θ can take decrease from $Nt = 0$ to $Nt = 1.8$, Figure 5.10b, which is implied by the narrowing of the pdf, which is a decrease of the variance of θ, already observed in section 5.4.2.

Until this point, the two simulations have similar results, with the VD, which already has a small asymmetry between positive and negative values of θ.

At $Nt = 3.7$, while the Boussinesq result is still symmetric, the variable density has a clear asymmetry toward the positive value of θ, which becomes more evident, as the simulation progresses, until becoming striking at $Nt = 4.73$. That is, during the variable density simulation, the heavy material mixes more slowly, so that the probability of finding positive fluctuations of θ of increasing values, grows during the simulations, an effect already evidenced by Livescu and Ristorcelli (2008).

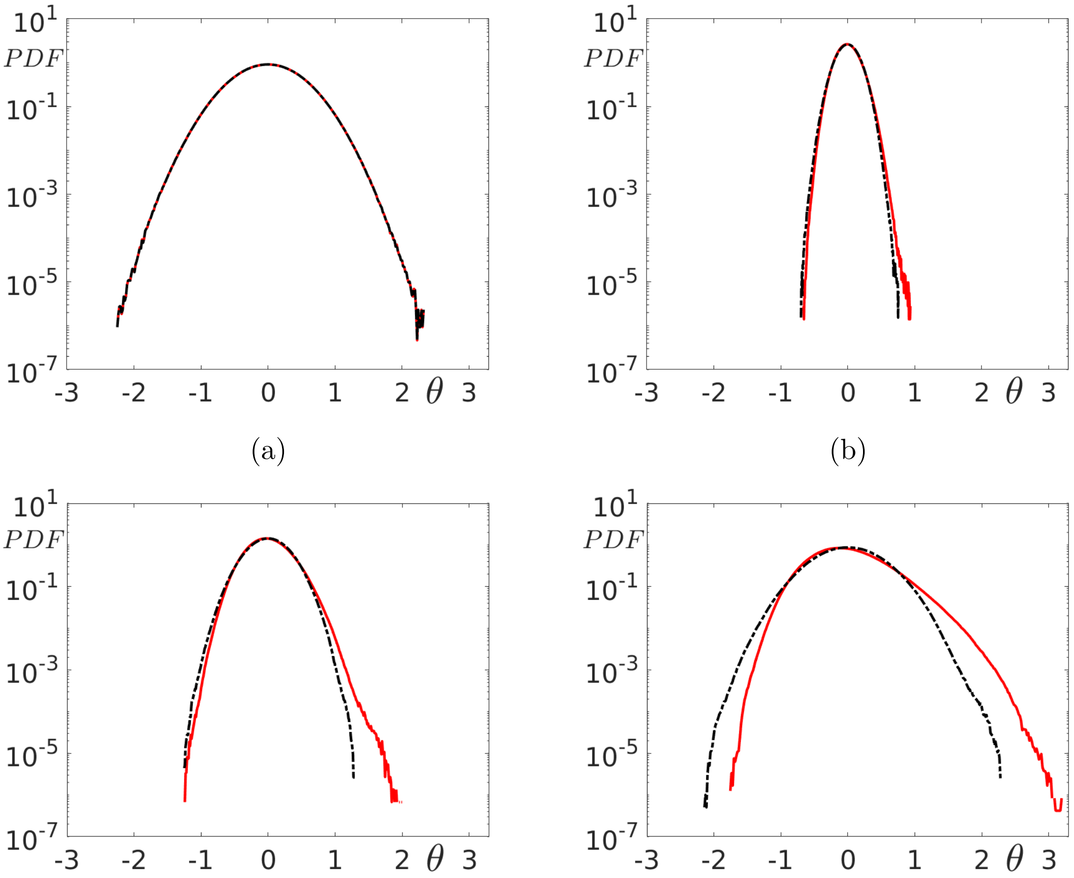

(a) (b) (c) (d)

FIGURE 5.10 – Probability density function of the scalar at four instants during the flows evolution : (a)$Nt = 0$, (b)$Nt = 1.8$, (c) $Nt = 3.7$, (d) $Nt = 4.73$. In red variable density and black Boussinesq results

5.4.5.2 Probability density function of $\partial_1\theta$

As for θ, the initial condition of the gradient $\partial_1\theta$ is plotted in Figure 5.11a, and show symmetry of the values around the mean 0.

After the decrease that we observe until $Nt = 1.8$, Figure 5.11c, we find that at $Nt = 3.8$, the two simulations have still similar probability density functions.

The main difference is obtained towards the end of the simulation at $Nt = 4.73$. In Figure 5.11d, we observe that the tails of the probability density function of the VD simulation are much wider than the Boussinesq. Confirming the observation of Rao et al. (2017), that is, intense variable density effects may be the cause of the existence of sharp and intense gradients in the domain.

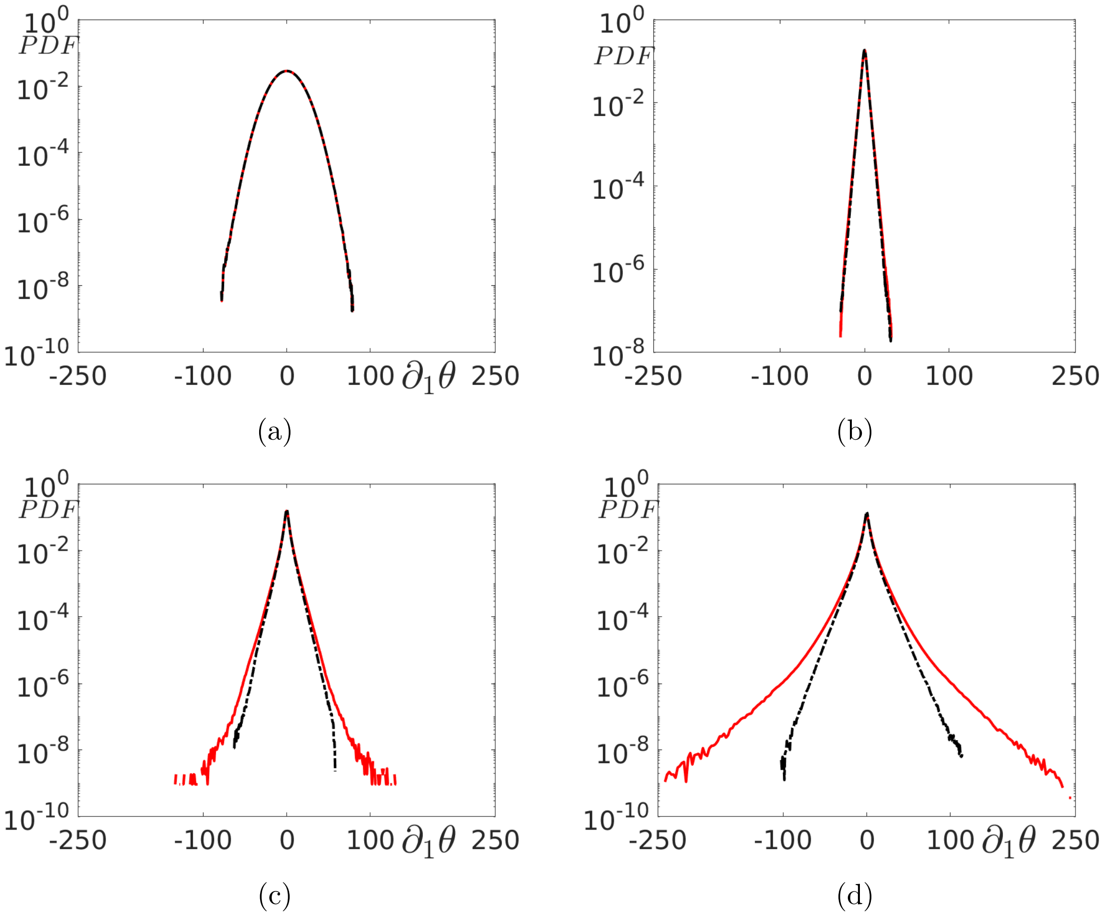

FIGURE 5.11 – Probability density function of one of the scalar gradient horizontal component at four instants during the flows evolution : (a)$Nt = 0$, (b)$Nt = 1.8$, (c) $Nt = 3.7$, (d) $Nt = 4.73$. In red variable density and black Boussinesq results

5.5 Initial condition variation

In this chapter, as already stated in section 5.2.2, the only difference in initial conditions is the initial ratio of the scalar variance and the kinetic energy. Since we want to keep the initial Reynolds number constant, this reduces to varying the scalar variance $\langle\theta\theta\rangle$. The characteristics of the different simulations are reported in table 5.1.

The modification of the initial scalar variance implies a variation of the initial Atwood number of the flow, defined by Eq. (5.25).

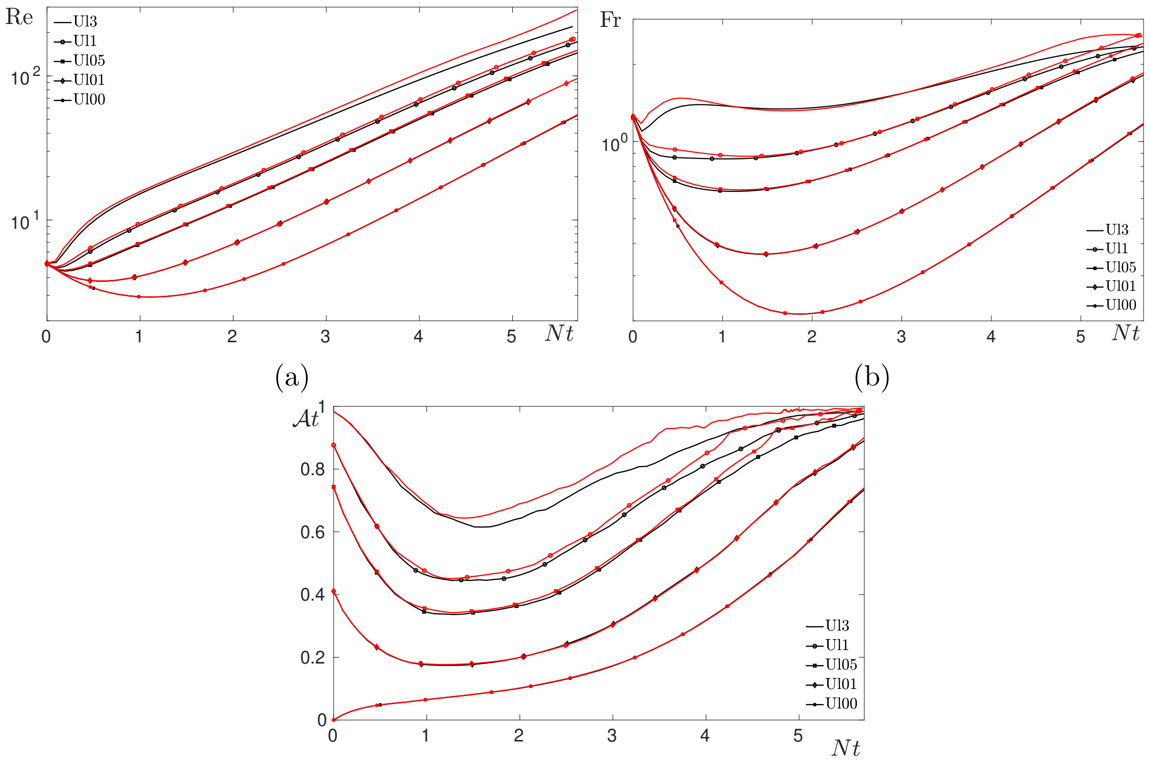

(a) (b)

(c)

Figure 5.12 – Temporal evolution of nondimensional number characteristic of the flows. (a) Reynolds number. (b) Froude number. (c) Atwood number. In red variable density and black Boussinesq results

5.5.1 Non dimensional numbers

The evolution of the nondimensional numbers of the flow is plotted in Figure 5.12, for the 10 LES simulation.

The Reynolds numbers are shown in Figure 5.12a. We observe how, for both variable density and Boussinesq simulations, the strong Reynolds number dependence on the initial value of scalar variance. That is, the production of turbulence is connected to the scalar fluctuations, the stronger they are, the higher the Reynolds number is. On the same figure, we observe how the difference between VD and B simulation decreases when the initial scalar fluctuations are less intense. For instance, for the simulations Ul01 and Ul00, no noticeable difference seems to exist.

The Froude number in Figure 5.12b has a similar dependence on the initial conditions. The difference observed for Ul3 decreases for all the other cases becoming non-existent for the two cases Ul01 and Ul00. The notable difference with respect to the Reynolds number is the tendency for all the 10 simulations to converge to a value of the Froude number $\simeq 2$.

The Atwood number, as explained in the introduction of this section, decreases for all the simulations due to the scalar variance decrease.

5.5.2 One point statistics

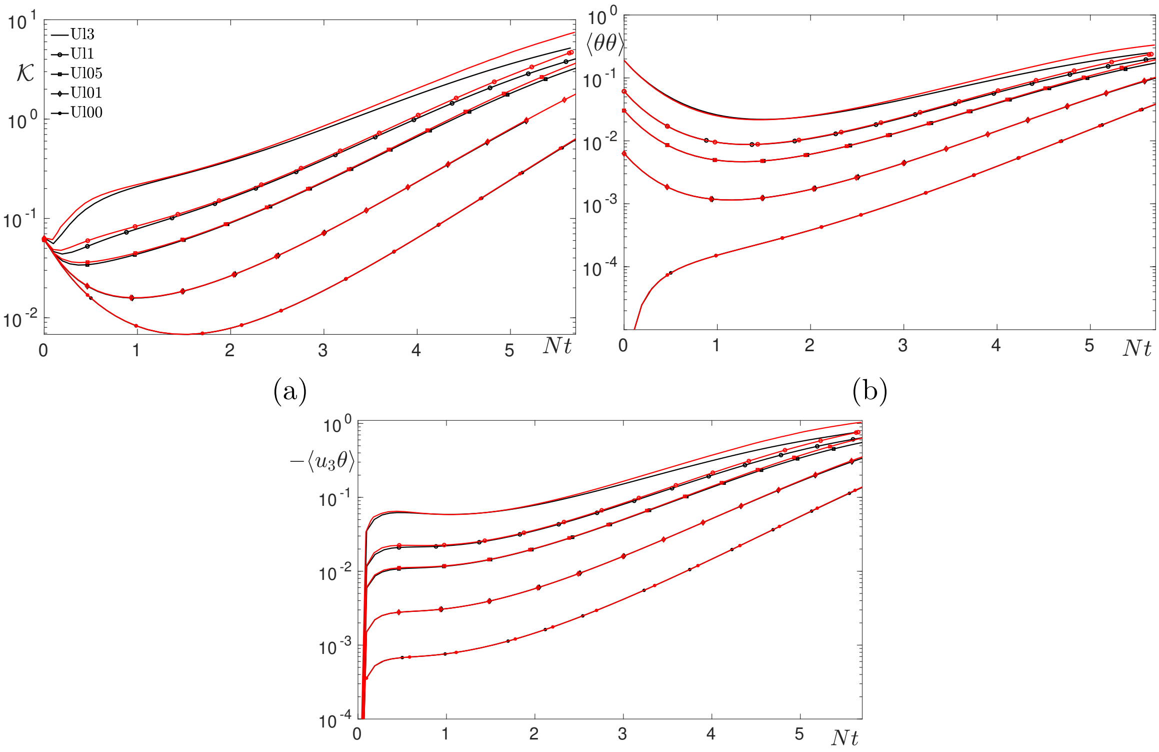

(a) (b)

(c)

FIGURE 5.13 – Temporal evolution of one-point statistics. (a) Turbulent kinetic energy. (b) Variance of the scalar. (c) Vertical flux. In red variable density and black Boussinesq results. The different simulations are indicated in the legend of every figure.

After the non-dimensional numbers, we investigate the influence of the initial conditions on the one-point statistics : integrated kinetic energy, integrated scalar variance, and vertical flux.

The kinetic energy evolution for the 10 LES simulation is plotted in Figure 5.13a. Here we have the same effect observed in the previous section, that is, the difference between variable density and Boussinesq simulation decreases with the decrease of the initial scalar variance. One of the main consequences of the reduction of variable density effects concerns the growth rate of the kinetic energy in the self-similar phase, which becomes the same for Ul01 and Ul00. That is, we expect no modification of the infrared part of the kinetic energy spectra.

Similar behaviors are observed for the other two quantities in Figures 5.13b and 5.13c, where the differences that are evident for the case Ul3 are less and less so as the initial scalar variance decreases.

In particular, the disappearance of variable density effects, observed between Ul05 and Ul01, suggests that the non-Boussinesq limit for the USHT simulations is between these two initial conditions.

5.5.3 Two point statistics

The influence of the initial variance on the spectra is illustrated using as examples simulations Ul1 and Ul05. In Figure 5.14, we show the spectra for the four simulations at the same time instants during the evolution of the flow.

We observe how the effects of variable density, which act on both large and small scales, are more evident for the simulation Ul1, Figure 5.14a, where the scalar fluctuations at the beginning of the simulation are more intense, with respect to Ul05.

In the simulation Ul05, Figure 5.14b, the large scale effects are still visible, but they do not concern the energetic scales near the peak of the four spectra. Even if their influence is still present on the integrated quantity, as shown in Figure 5.13.

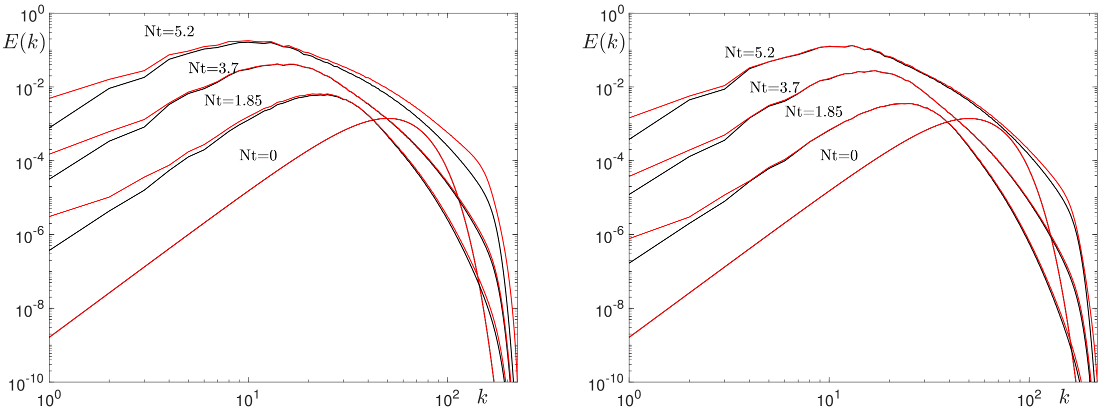

(a)

(b)

FIGURE 5.14 – Temporal evolution of kinetic energy spectra at four instants for : (a) Ul1 simulations. (b) Ul05 simulation. In red variable density and black Boussinesq results.

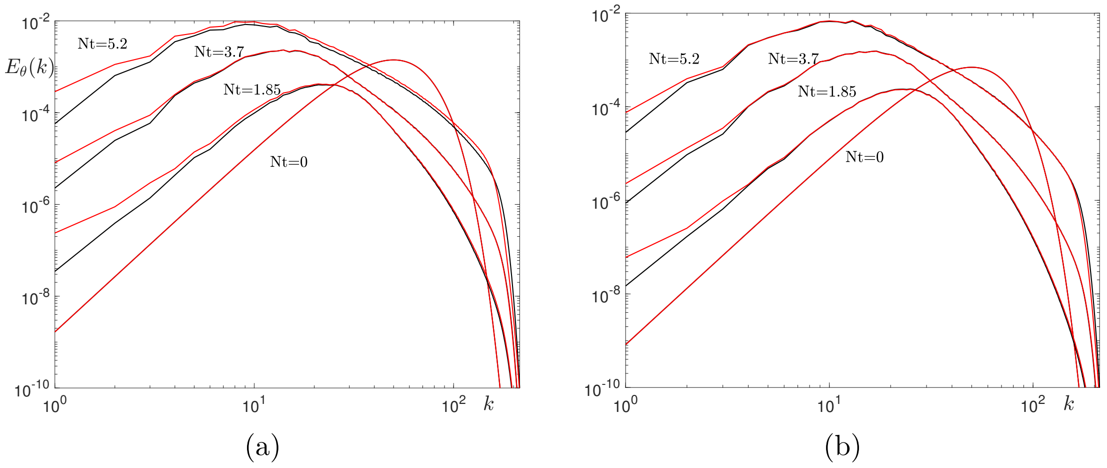

FIGURE 5.15 – Temporal evolution of scalar variance spectra at four instants for : (a) Ul1 simulations. (b) Ul05 simulation. In red variable density and black Boussinesq results.

5.6 Conclusion

This chapter concerns the study of the variable density effects on the unstably stratified homogeneous turbulence (USHT). In particular, following the work of Soulard et al. (2019) on the permanence of large eddies, we are interested in the possible modification of the the self-similar state growth rate β, which is related to the energy distribution at large scales. The investigation is carried out, confronting the results of variable density and Boussinesq direct numerical simulations. Moreover, we report 10 LES simulations with different initial conditions to study in what measure the variance of the initial scalar field θ influences the late time self-similar flow evolution.

The study of USHT configurations is accompanied by the numerical challenges associated with the growing spectral range, which requires adequate numerical discretization. On the one hand, one has to consider the rapid growth of the integral scale, which could cause the confinement of the flow and on the other, the development of the turbulence cascade, which involves more and more small scales.

Furthermore, the variable density approximation requires an iterative method to solve the Poisson equation, which, in this case, is not straightforward to solve. In this work, we propose the GMRES algorithm, which has been used in both direct numerical simulation and large eddy simulations. The latter has been introduced to allow the parametric study on initial conditions, that with the DNS alone, would not have been possible.

From the results of the numerical simulations, we find that in the variable density approximation, the permanence of the large eddies is not verified for initial conditions having an infrared spectrum with $\sim k^4$. In particular, the presence of a scalar field, with sufficiently high variance, causes the modification of the large scales of the flow, reflected by the change of the infrared part of the kinetic energy spectra, which was already reported by Soulard et al. (2019). In unstably stratified homogeneous turbulence, the infrared exponent has a direct influence on the growth rates β of the self-similar state. That is why we observe differences between the β found in Boussinesq and variable density results. These are evident in the time evolution of the integrated quantities : kinetic energy, scalar variance, and vertical flux.

From the analysis of the two-point statistics, in addition to the large scale differences, we observe that the two approximations lead to different nonlinear cascade processes, evidenced by the differences in the inertial and dissipative parts of the spectra. Moreover, the anisotropy of the flow seems to be enhanced in the variable density case, even if the difference with the Boussinesq result is small.

Furthermore, we compute the Probability Density Function (PDF) of the scalar θ. Thanks to the PDF, we show that, during the simulation, in the variable density case, the scalar fluctuations tend to create a longer tail towards large positive values, while in the Boussinesq case, the PDF stays symmetric. That is, in the variable density case, after the initial transient, it is more probable to find heavy fluid particles than light ones. While in the Boussinesq case, the probability is the same during the computation. This result seems to confirm previous observations of Livescu and Ristorcelli (2007).

Likewise, the study of the density gradients shows that during the flow evolution, the variable density PDFs have more extended tails with respect to the Boussinesq's, which indicates an increased probability of sharper interfaces and the possible blow-up of the density gradient proposed by Rao et al. (2017).

Finally, we use the LES simulations to perform a parametric analysis of initial conditions. We chose to vary the initial scalar variance and to observe its effect on spectra and self-similar growth rates. As we expect for the Boussinesq simulation, no dependence on initial condition is observed, while in case of variable density, we find that the decrease of the scalar variance decreases the influence of the scalar field in the dynamics of the flows. In particular we find that the non-Boussinesq behaviour has its onset for a value of $\frac{\langle\theta\theta\rangle}{\mathcal{K}}$ between 0.01 and 0.05. The results presented in this chapter are only the beginning of the analysis of the variable density unstably stratified turbulence. Future studies may go deeper into the investigation of its small scales properties. Or one could push further the studies on the initial conditions dependencies.

Chapitre 6

Sudden diffusion of plasma turbulent mixing layers under compression

Contents

In chapter 4, we have discussed how the weakly coupled plasma produced in inertial confinement fusion compressions experiences a tremendous growth of the dynamic viscosity μ, as the temperature T increases. Considering the small dimensions of a hot spot in ICF devices, $\sim 10-100[\mu m]$, and the temperatures achieved, above $10[keV]$, hydrodynamic instabilities can be partially damped [Haines et al. 2014b] and small scale velocity structures can be significantly dissipated [Weber et al. 2014a]. We have investigated the sudden viscous dissipation effect proposed by Davidovits and Fisch (2016a), which by rapidly converting the kinetic energy of turbulent motions into internal energy, could, in principle, enhance the hot spot temperature, helping the fusion reactions to take place. The different regimes and scaling laws characteristics of compressed turbulent plasmas have been explored theoretically and with spectral EDQNM model, also evidencing an important sensitivity to initial conditions during the sudden viscous dissipation phase due to the distribution of energy fluctuations between scales.

Besides, inhomogeneous simulations of turbulent kinetic energy layers under compression also investigated in chapter 4 have shown an increased transport of turbulence toward the center of the capsule during the implosion. These observations, although not accounting for plasma molecular diffusion, suggest that a new mechanism producing mixing of the heavy elements from the ablator into the DT fuel may take place in ICF. Can sudden viscous dissipation come together with sudden diffusion ? Mixing is indeed an important issue in ICF as having depleting cooling effects on the hot spot [Betti and Hurricane 2016, Ma et al. 2017]. The asymmetry of the implosion [Haines et al. 2016], the presence of defects on the capsule, like fill tube [Hammel et al. 2010, MacPhee et al. 2017] or support tent [Weber et al. 2017] are among the large scale mechanisms known as principally responsible for mixing in ICF targets. Other contributions may come from the fine scale perturbations amplified by hydrodynamic instability [Hammel et al. 2010]. Plasma transport coefficients have been shown to play a role in the mixing zone dynamics (see Vold et al. (2015)). In their paper, Rinderknecht et al. (2014a) present an experiment from the OMEGA facility, having a more than expected ablator-fuel mix prior to the deceleration phase, a period in which hydrodynamic instability effects are expected to be negligible. Post-processing experimental data and using one-dimensional radiation-hydrodynamic calculations, they demonstrated that the main process driving mixing is the molecular diffusion. On the same experimental platform, Zylstra et al. (2018) provide evidence that implosion with a moderate temperature ($< 6keV$) and moderate convergence are dominated by diffusive mix and that any turbulence-related effect is less significant.

Still, the question of how and when nonuniformities and strong temporal variations of plasma transport coefficients due to temperature and mass fraction mixture [Ticknor et al. 2016] act on the mixing zone dynamics is pending.

Here we study the idealized case of the DT/CH mixing layer in spherical compressions representative of ICF. Here the plasma transport coefficients are taken into account using the Pseudo-Ion-in-Jellium (PIJ) model, proposed by Arnault (2013), and further validated in Ticknor et al. (2016). These simulations will be compared to constant viscosity and diffusivity simulations to identify the importance of the transport coefficients on the evolution of the mixing zones.

This chapter is organized as follows : At first, we present the pseudo-ions in jellium model and some results concerning the role of the coupling parameter in plasma mixtures. Then, after recalling the equations derived in chapter 2 for the spherical turbulent layer under compression, we detail the configurations for direct numerical simulations (DNS) of DT/CH mixing layer. We then identify the different regimes corresponding to the dominance of turbulent or molecular diffusion on the mixing from a parametric study on initial conditions.

6.1 Description of the pseudo-ions in jellium (PIJ) model

In this section, we recall the principle of the pseudo-ions in jellium model, whose details can be found in Arnault (2013). The most precise estimates, to compute transport coefficients in a plasma, come from the quantum molecular dynamics simulations. This method is very accurate, although computationally demanding and not of practical use in hydrodynamic simulations, which need the values of viscosity and diffusivity at every mesh point and for every time steps.

We consider a plasma as a gas of ions, atoms which, due to extreme heating, lose part of their electrons, and the free electrons. The ions are composed of the atom nucleus plus, if the elements are not fully ionized, bound electrons.

In the pseudo-ions in jellium model, the jellium is a background of uniform electric density representing the free electrons, in which we place the pseudo ions, *i.e.* a first-order approximation of the real ions accounting for the approximation on the electrons density assumed uniform. One of the most significant quantities in plasma physics, and especially for the PIJ model, is the coupling parameter Γ, the ratio of the Coulomb electrostatic potential energy of nearest neighbors, and the thermal energy. This parameter, in general, can vary from values less than 1 to more than 100 [Piel 2017], identifying plasma regime with different properties.

When $\Gamma \ll 1$, the kinetic energy of the single particles of the plasma exceeds the potential energy of their interaction, this regime is called weakly-coupled plasma, and it is characterized by high temperature and low density. On the contrary, when $\Gamma \geqslant 1$, plasma is in the strongly-coupled regime, which corresponds, usually, to colder and denser plasma with strong interaction between particles.

An example of the different plasma regimes that are present in nature or engineering application is given by Piel (2017) and reported in fig. 6.1.

The coupling parameter is defined as

$$\Gamma = \frac{Z^* e^2}{a k_B T}, \tag{6.1}$$

where e is the electron charge, Z^* is the ionization of the pseudo-ion, or pseudo-

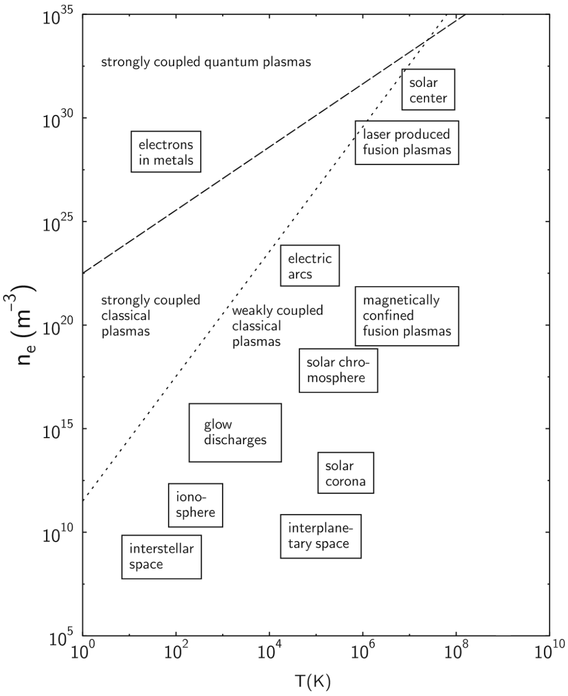

FIGURE 6.1 – Different plasma regimes characterized by the temperature T, measured in Kelvin, and the electron density, i.e., the number of electron for unit volume. On this figure, the dotted lines represent the border between weakly and strongly coupled plasma, defined for a coupling parameter of $\Gamma = \frac{1}{3}$. From Piel (2017).

ionization, T is the temperature, k_B is the Boltzmann constant and a is the Wigner-Seitz radius, the radius of the sphere whose volume is equal to the average volume occupied by one atom. The pseudo ionization Z^* is computed using the scaling law from the Thomas-Fermi approximation, a description of the electronic structure of atoms using only information from electronic density function. Once the value of the coupling parameter Γ is determined, the model uses simple kinematic formulas with collision frequencies and scaling laws to compute viscosity and diffusivity in pure elements as well as in plasma bi-component mixtures.

One of the advantages of this model is that it can predict viscosity and diffusivity for different plasma regimes spanning from the high-temperature low-density weakly-coupled regime to the low-temperature high-density strongly-coupled regime. Figure 6.2 gives an example of the capability of the PIJ model in a plasma mixture of hydrogen and silver, validated against results obtained with a more accurate method [Ticknor et al. 2016].

Two examples of the coupling parameter values in plasma mixture that are of interest for inertial confinement fusion are given in Fig. 6.3. We observe that the values of the coupling parameter are higher in the DT/gold mixture than in the

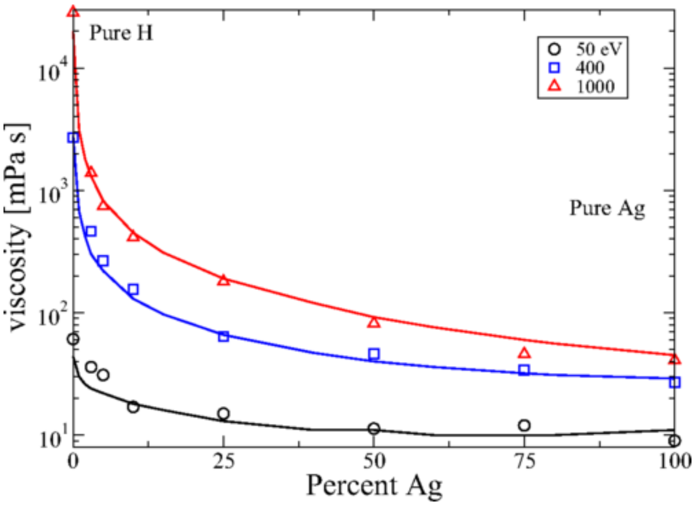

FIGURE 6.2 – Viscosity of a hydrogen (H) silver (Ag) mixture. PIJ simulation (continuous lines) are compared with results from orbital free molecular dynamics simulation (symbols). From Ticknor et al. (2016).

DT/CH mixture, nevertheless for both cases, Γ decreases with temperature and the mass fraction of the heavier element. These demonstrate that plasma mixtures can be weakly or strongly coupled depending on temperature or composition, thus requiring the use of models, like the particle-ion in jellium, for case in which thermodynamic conditions vary significantly during the simulations.

6.1.1 How the PIJ results depend on mass fraction, density and temperature

We have observed how the PIJ model is able to compute the viscosity and diffusivity of plasma mixtures in different thermodynamic conditions. In this section, we show how the results of the model depend on the three quantities that the PIJ routine demands as inputs : mass fraction, density, and temperature. The mixture used as an example is the DT/CH. The results are plotted in Fig. 6.4.

In Fig. 6.4a viscosity and diffusivity show an inverse dependence on the CH mass fraction Y_{CH}, the first decreases while the second increases when Y_{CH} grows. On the contrary, in Fig. 6.4b, we observe that the two transport coefficients have the same dependence on the density : they decrease when the density increases. Finally, Fig. 6.4c shows the temperature dependence of viscosity and diffusivity, in this case, for the pure DT. We observe how the curves, for sufficiently high temperatures, follow the kinematic scaling $\sim T^{5/2}$ [Braginskii 1995].

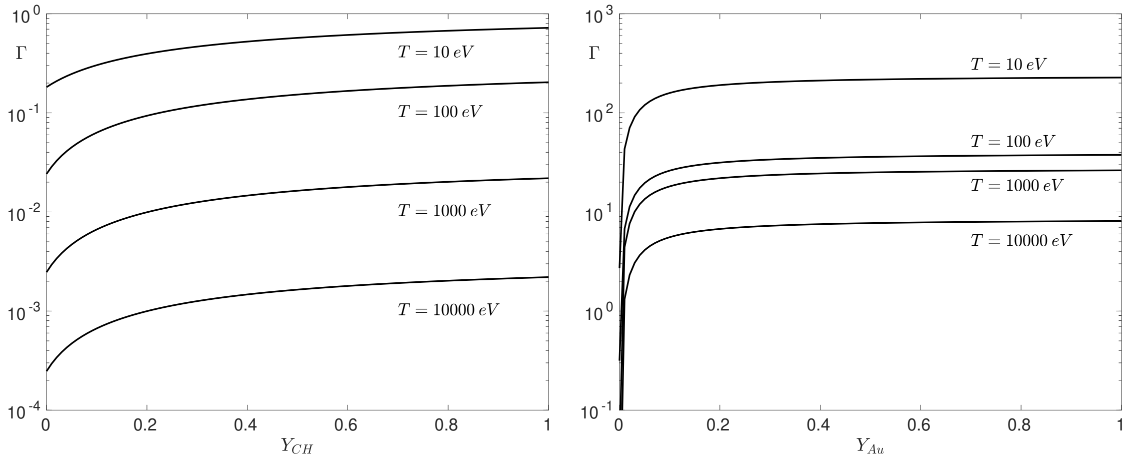

(a) (b)

FIGURE 6.3 – Evolution of the coupling coefficient in plasma mixtures, as a function of the mass fraction of the heavier element, for different temperature and constant density. (Left) : Mixture DT/CH with density $\rho = 5\ 10^{-3} g/cm^3$. (Right) : Mixture DT/ Gold with density $\rho = 20 g/cm^3$

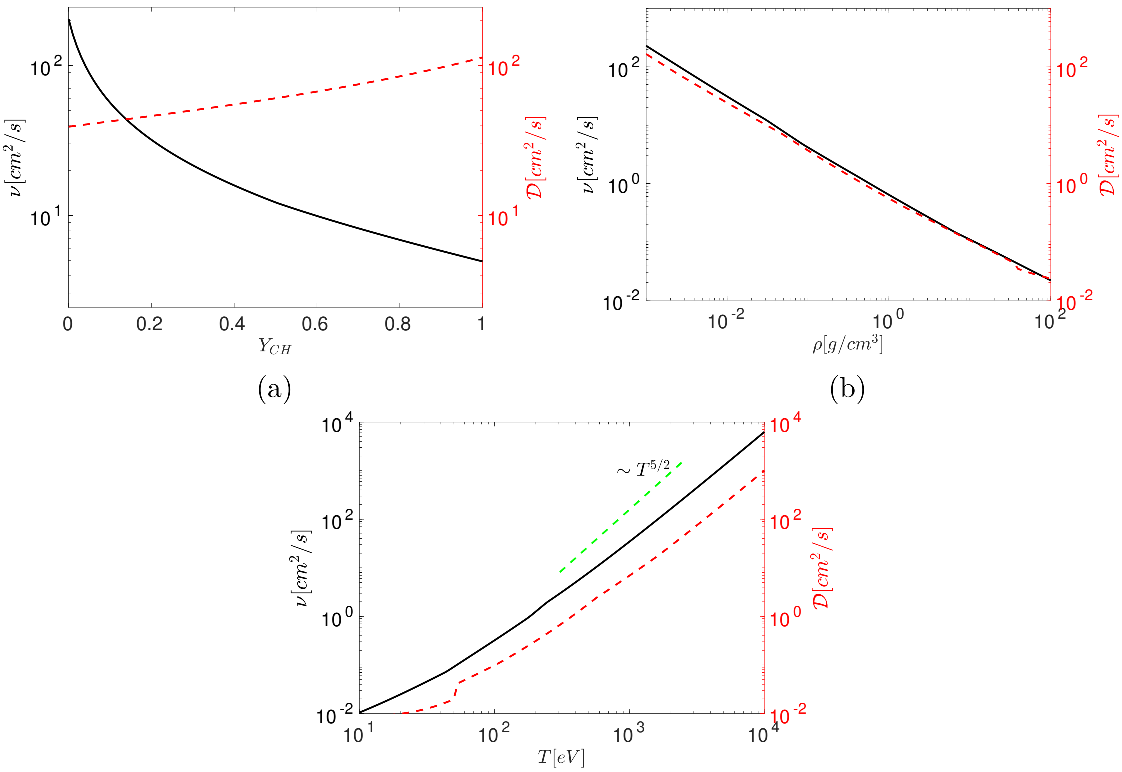

(a) (b)

(c)

FIGURE 6.4 – Transport coefficients variation in a DT/CH mixture, (a) as a function of the CH mass fraction with $T = 100\,eV$ and $\rho = 5\,10^{-3}\,g/cm^3$, (b) as a function of the density of the mixture with $T = 100\,eV$ and $Y_{CH} = 0.1$, (c) as a function of the temperature with $\rho = 5\,10^{-3}\,g/cm^3$ and $Y_{CH} = 0$. Black continuous line : viscosity. Red dashed line : diffusivity.

6.2 Theoretical framework

In this section, we recall the system of equations derived in chapter 2, that describe the evolution of a spherical mixing zone under compression. The flow is decomposed into a base component and a perturbation one. On the one hand, the base flow accounts for the radial velocity and the deuterium-tritium thermodynamics quantities during the adiabatic compression of an idealized ICF target. It can be derived analytically from conservation laws. On the other hand, the fluctuations account for the turbulence and the fuel/ablator mixing zone and are computed from direct numerical simulations.

6.2.1 Equations for DT/CH mixtures

We specialize the equation derived in section 2.3 for the DT fuel/CH ablator mixture. We recall that, in this study, radiative effects and combustion terms due to fusion reactions are not taken into account. In this specific case the mixture law (2.50), becomes for deuterium-tritium (DT) fuel and ablator (CH) :

$$\frac{1}{\rho} = \frac{1-Y}{\rho_{DT}} + \frac{Y}{\rho_{CH}}, \tag{6.2}$$

where ρ_{DT} and ρ_{CH} are respectively the microscopic densities of the light and heavy materials. They are defined as

$$\rho_{DT} = \frac{nM_{DT}}{1+Z_{DT}} \text{ and } \rho_{CH} = \frac{nM_{CH}}{1+Z_{CH}} \tag{6.3}$$

The particularity of plasma is the strong dependence of the kinematic viscosity μ and the molecular diffusion $\mathcal{D}$ coefficients on the temperature T, density ρ, and mass fraction Y of CH.

At this stage, we recall that to solve the problem, it is convenient to decompose the flow quantities into a base flow (noted with suffix ^{B}) and fluctuations (identified by small letters). For instance velocity components are written as $U_i = U_i^B + u_i$.

6.2.2 Base flow

The objective pursued by selecting an arbitrary base flow is twofold. First, we wish to obtain simplified equations for the perturbations when expressed in a non-inertial frame (see section 2.1). Also, the base thermodynamics conditions are selected to represent the hot spot characteristics in ICF capsules. We start by recalling the choice of the radial base velocity field, U_i^B, accounting for the main compression,

$$U_i^B(\mathbf{x}, t) = -\mathcal{S}(t)x_i, \tag{6.4}$$

introducing the uniform compression time rate $\mathcal{S}(t)$, assumed positive for a compression. Any non-distorted length scale evolves proportionality to Λ during the compression. In particular, the radius R corresponding to the fuel/ablator interface, if unperturbed by instabilities, would decreases as $R(t) = R_0\Lambda(t)$. Thereafter, initial values at $t = 0$ are identified with the suffix $_0$.

While the expressions of the other base flow quantities are :

$$\rho^B(t) = \rho_0\Lambda(t)^{-3}, \tag{6.5a}$$

$$n^B(t) = n_0\Lambda(t)^{-3}, \tag{6.5b}$$

$$Y^B(t) = Y_0 = 0. \tag{6.5c}$$

Where the base density ρ^B is taken uniform and the base mass fraction is set to one, $Y^B = 0$, corresponding to pure DT fuel. The base temperature T^B and pressure P^B are derived assuming an adiabatic compression in which viscous and diffusion effect have no impact on the base flow. They are :

$$T^B(r,t) = T_0\Lambda(t)^{-3(\gamma-1)}\left(1 - \frac{1}{h_0^2}\frac{r^2}{\Lambda(t)^2}\right). \tag{6.6}$$

$$P^B(r,t) = P_0\Lambda(t)^{-3\gamma}\left(1 - \frac{1}{h_0^2}\frac{r^2}{\Lambda(t)^2}\right). \tag{6.7}$$

The length scale $h_0 > 0$ expresses the temperature gradient at the beginning of the compression.

The compression parameter $\Lambda(t)$ expression is

$$\Lambda(t) = \sqrt{1 - 2\mathcal{S}_0 t + (\mathcal{S}_0^2 + \Omega_0^2)t^2}, \tag{6.8}$$

with the characteristics frequencies $\mathcal{S}_0 = \mathcal{S}(0)$, the initial compression rate, and $\Omega_0 = \left(\frac{2P_0}{\rho_0 h_0^2}\right)^{1/2}$ expressing pressure gradient effects. The position of the fuel/ablator interface, $R(t) = R_0\Lambda(t)$, is principally driven by the initial impulsion $\mathcal{S}_0$ at the beginning of the compression, and then decelerated by pressure gradient effects, Ω_0, leading to a minimum convergence radius (see Figure 6.5).

The adiabatic compressions studied here differ qualitatively from realistic implosions of ICF capsules, which are driven by shocks. However, it is possible to choose parameters such that the duration and convergence ratio are representative of ICF implosions. Also, we can impose at the minimum convergence ratio the thermodynamics conditions relevant to hot spots in ICF capsules (see Atzeni and Meyer-ter Vehn (2004a)). These conditions are gathered in Tab. 6.1 and in figure 6.5.

We can remark that the initial parameters at $t = 0$ correspond to compressed and heated plasma state where DT and CH are already fully ionized with $Z_{DT} = 1$

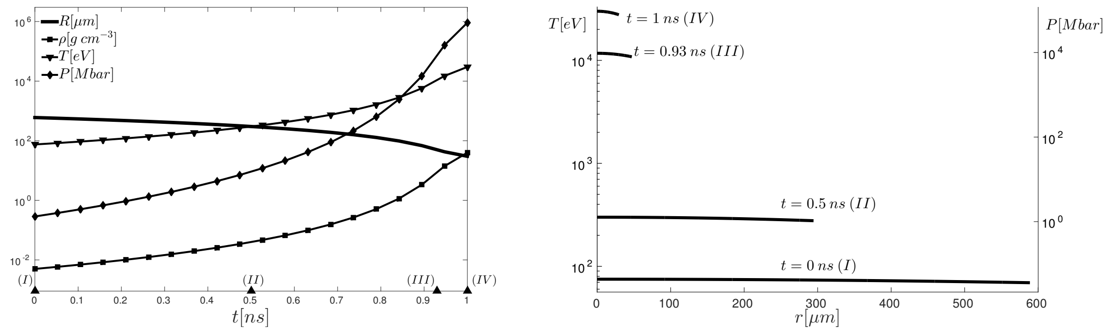

(a) (b)

FIGURE 6.5 – Description of the implosion characteristics studied in the present work. (Left) : Time evolution of the temperature T^B, the pressure P^B and density ρ^B at the center of the domain. The thick solid line represents the radius of the capsule. (Right) : Radial profiles of base temperature and pressure, at four instants during the compression as indicated in the left figure by the black triangles on the time axis.

$t\ [ns]$	$T[eV]$	$P[Mbar]$	$\rho[gcm^{-3}]$	$R[\mu m]$
0	75	2.87×10^{-1}	5×10^{-3}	300
0.5	293	8.7	3.9×10^{-2}	150
0.93	12.8×10^3	1.08×10^5	11.08	24
1	30×10^3	9.14×10^5	40	15

TABLE 6.1 – Temperature T, pressure P and density ρ at the center of the capsule, for different instants. The last column indicates the radius of the unperturbed fuel/ablator interface R.

and $Z_{CH} = 3.5$. The inner radius diameter is $R_0 = 300\ \mu$m, the duration of the compression 1 ns and a convergence ratio of 20 is achieved. The base temperature at the center of the capsule varies from 75 eV to 30 keV, with the base pressure reaching 10^3 Gbar and fuel density 40 gcm^3. In figure 6.5 is plotted the temperature and pressure profiles at different times, revealing the gradients responsible for the deceleration of the capsule radius. It also generates Rayleigh-Taylor instability at the fuel/ablator interface. However, due to the fact that $\Omega_0 = 50\text{ns}^{-1} \ll \mathcal{S}_0$, its effect remains very weak during the implosion.

6.2.3 Perturbation equations

The equations describing the dynamics of the perturbations around the mean flow are derived in section 2.3.2.2. We recall that we work in a non-inertial frame with the new time $\tilde{t}$ and position variable $\tilde{\mathbf{x}}$ corresponding to the reference frame deforming with the base radial velocity :

$$\tilde{t} = \int_0^t \Lambda^{-2}(s)ds, \ \tilde{\mathbf{x}} = \frac{\mathbf{x}}{\Lambda(t)}. \tag{6.9}$$

Moreover, we recall the rescaling that we use in order to eliminate inhomogeneous forcing terms due to base velocity in the velocity equation.

$$\tilde{\mathbf{u}}(\tilde{\mathbf{x}}, \tilde{t}) = \mathbf{u}(\mathbf{x}, t)\Lambda(t), \ \tilde{\pi}(\tilde{\mathbf{x}}, \tilde{t}) = \pi(\mathbf{x}, t)\Lambda^2(t), \ \tilde{\theta}(\tilde{\mathbf{x}}, \tilde{t}) = \theta(\mathbf{x}, t). \tag{6.10}$$

The equations for the perturbation in the non-inertial frame are :

$$\begin{aligned} \partial_t \tilde{u}_i + \tilde{u}_j \partial_j \tilde{u}_i = -\partial_i \tilde{\pi} - \tilde{\pi} \partial_i \tilde{\theta} - \Lambda^2 \Pi^B \partial_i \tilde{\theta} + ... \\ \partial_j \left[\nu \left(\partial_j \tilde{u}_i + \partial_i \tilde{u}_j \right) \right] - \nu \left(\partial_j \tilde{u}_i + \partial_i \tilde{u}_j \right) \partial_j \tilde{\theta}, \end{aligned} \tag{6.11a}$$

$$\partial_t \tilde{\theta} + \tilde{u}_j \partial_j \tilde{\theta} = \partial_j \left(\mathcal{D} \partial_j \tilde{\theta} \right), \tag{6.11b}$$

$$\partial_j \tilde{u}_j = -\partial_j \left(\mathcal{D} \partial_j \tilde{\theta} \right). \tag{6.11c}$$

In Eq. (6.11a) for the velocity perturbation, one inhomogeneous term remains which is proportional to the base reduced pressure, Π^B, and accounts for the buoyancy production. The quantity, $\tilde{\pi}$, expressed in the new coordinate system not only accounts for the reduced pressure fluctuations, but also for the diagonal components of the viscous stress tensor. We emphasize again that for the perturbation, the variable density condition (6.11c) holds. Therefore, compressibility is accounted only for the base flow in this work, while it is neglected for the perturbations.

6.2.4 Numerical methods

The perturbation equations in the non-inertial reference frame are solved using the pseudo-spectral method for variable density turbulence with nonuniform transport coefficients described in chapter 3. In particular, we recall that in the variable density approximation, the non-locality in spectral space requires an iterative method to invert the linear system. We use the generalized minimal residual (GMRES) algorithm described in section 3.2.3.1, which ensures convergence even if density fluctuations are important contrary to fixed point methods.

The strong dependence of the dynamic viscosity μ and the molecular diffusion $\mathcal{D}$ coefficients on the temperature T, density ρ, and mass fraction Y of CH are taken into account using the particle-ion-in-jellium (PIJ) model, described in section 6.1. Viscous and diffusive contributions are taken into account implicitly, also using a GMRES algorithm.

The typical cost of a simulation is roughly 200000 CPU hours dispatched over 2048 cores.

6.2.5 Initial conditions

To define more precisely the initial conditions in the simulations, we introduce the volume average of a quantity $*$ as $\langle * \rangle$. It is also convenient to use $\overline{*}$ as the tangential average of the same quantity (thus depending on r only). The fluctuations around these radial averaged profiles are noted as $*'$. At this stage quantities are expressed by a triple decomposition with for instance the full velocity given by $U_i = U_i^B + u_i = U_i^B + \overline{u_i} + u_i'$.

The initial conditions are generated using the methods described in section 3.4.2. The initial density profile is radial, such that $\theta = \overline{\theta}$. It forms a diffuse spherical interface between fuel and ablator of width $L_0 = 5\mu m$, centered on radius $R_0 = 300\mu m$. Therefore, θ is zero at the center of the capsule, while in the ablator region of pure CH, $\theta = 0.16$. This latter value is obtained from Eq. (6.3) as the density number of particles is constant, $n = n_0$, to ensure the variable density approximation. The Atwood number between DT and CH is then given by $At = \frac{\rho_{CH} - \rho_{DT}}{\rho_{CH} + \rho_{DT}} = 0.08$. Along with the small value of the mean base pressure gradient, this small Atwood number value explains why Rayleigh-Taylor instability remains limited.

Also, zero-mean random velocity perturbations with $\langle u_i \rangle = 0$ are added around the interface, using the filtering procedure described in section 3.4.2.1 and a classical von Karman spectra (3.43) with integral scale, ℓ_0, and rms fluctuations, u_0. Here, the spectra are of Batchelor type, i.e., the distribution of energy at small wavenumber k scales as k^4.

Along with the initial size of the mixing layer L_0, the simulations are characterized by an initial Reynolds number, $\mathrm{Re}_0 = \frac{u_0 \ell_0}{\nu}$, here defined with the DT viscosity at the center of the capsule (see Tab. 6.2). The values range from $\mathrm{Re}_0 = 0$, for simulations without turbulence, to $\mathrm{Re}_0 = 217$, reaching the limits of our available computational resources. In addition, by introducing the compression parameter, $\mathrm{Cp}_0 = \frac{u_0}{\ell_0 \mathcal{S}_0}$, we observe that the compression is relatively rapid compared to turbulence in the simulations. This choice is motivated to avoid the contamination of the whole domain by mixing before the bang time.

At this stage, it is important to assess the validity of the variable density approximation from the initial conditions. For S1 simulations, which have the largest rms velocity $u_0 = 1.73\mathrm{km}s^{-1}$, we find a Mach number value of $M = u_0/c = 0.02$, using the sound speed provided by $c = (\gamma P_0/\rho_0)^{1/2} = 79\mathrm{km}s^{-1}$. This small value ensures the validity of the variable density approximation during the whole simulation. The advantage of using the variable density approximation in our code has to be stressed. Indeed, a fully compressible code would have been very demanding and would have failed to resolve the small scales of turbulence due to the shock-capturing schemes [Thornber and Drikakis 2008]. By contrast, the initial base velocity at interface radius R_0 is $300\mathrm{km}s^{-1}$, which gives a Mach number of $M = 3.8$. This shows that energy contained in the perturbation is small compared to the base component, justifying

Name		Type	Mesh size	Re_0	Cp_0	ℓ_0/R_0	L_0/R_0
$S1$	a	DNS	512^3	217	0.27	0.07	0.016
	b	ILES	1024^3	217	0.27	0.07	0.016
$S2$	a	DNS	512^3	153	0.2	0.07	0.016
	b	ILES	512^3	153	0.2	0.07	0.016
$S3$	a	DNS	512^3	108	0.13	0.07	0.016
	b	DNS	512^3	108	0.13	0.07	0.016
$S4$	a	DNS	256^3	32	0.1	0.05	0.016
	b	DNS	256^3	32	0.1	0.05	0.016
$S5$	a	DNS	256^3	0	0	0	0.016

Table 6.2 – Simulation characteristics in terms of initial Reynolds number, compression number, integral length scale, and mixing layer size. Type a corresponds to simulations with plasma transport coefficients while for type b viscosity and molecular diffusion are kept constant during the computation.

our choice to neglect the feedback of the perturbations on the base flow.

6.2.6 Resolution

A total of 9 simulations are presented in this study, varying the initial Reynolds numbers and using either a plasma model for transport coefficients (type a) or constant ones (type b) to evidence its effects.

The simulations start from an initial computational cubic domain of $1200\mu m$ size. This choice results from a compromise to encompass the fuel/ablator interface to avoid confinement effects, and also to guarantee that the finest turbulent structures are correctly resolved.

Therefore, the mesh size depends on the initial Reynolds number and the simulation type a or b. The most demanding simulations, $S1_b$ and $S2_b$, uses a 1024^3 and 512^3 mesh size respectively and correspond to a constant viscosity and molecular diffusion configuration. The small scales of turbulence are not fully resolved in these simulations, which enter the category of Implicit Large Eddy Simulations (ILES). By contrast, all other simulations can be considered as DNS . In particular, simulations with plasma coefficients (type a) are less demanding as the diffusion and viscosity growths rapidly smooth the small scales of turbulence.

As an illustration, we provide in Figure 6.6 the 3D representations of the density θ field at different instants for $S1_{a,b}$ simulations. This evidences the strong imprint of transport coefficients, which dissipate turbulence during the implosion ($S1_a$). We now quantify this phenomenon in the following section.

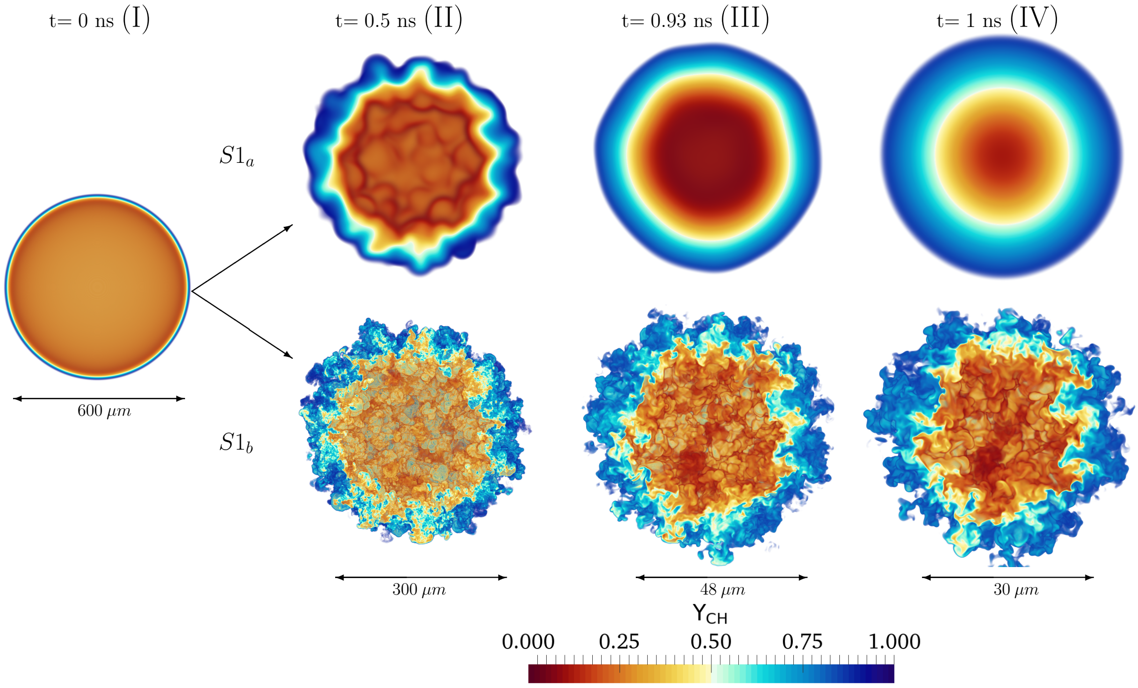

FIGURE 6.6 – Three dimensional contours of mass fraction of CH, Y, using volume rendering at different instants and for simulations with plasma, $S1_a$, and constant, $S1_b$, viscosity and diffusion coefficients. The different times correspond to Figure 6.5.

6.3 One-dimensional evaluation of the transport coefficients effects on the implosion

In section 6.2.5, we have illustrated the implosion characteristics that we use in this chapter and the thermodynamic properties of the base flow at the beginning and during the compression. Nonetheless, in section 6.1.1, we have shown how the transport coefficients have a strong dependence on temperature density and composition.

Hence, the question that arises is how much their effects depend on the characteristics of the implosion or the values of the thermodynamic quantities. A parametric study using DNS simulations is not feasible due to the high computational cost. An alternative is to use a one-dimensional model of the perturbation equations (6.11a)-(6.11c), in spherical coordinates such as

$$\partial_t \tilde{u}_r + \tilde{u}_r \partial_r \tilde{u}_r = -\partial_r \tilde{\pi} - \tilde{\pi} \partial_r \tilde{\theta} - \Lambda^2 \Pi^B \partial_r \tilde{\theta} + \frac{1}{r^2} \partial_r \left[2\nu r^2 \partial_r \tilde{u}_r \right] - 2\nu \partial_r \tilde{u}_r \partial_r \tilde{\theta}, \quad (6.12a)$$

$$\partial_t \tilde{\theta} + \tilde{u}_r \partial_r \tilde{\theta} = \frac{1}{r^2} \partial_r \left(\mathcal{D} r^2 \partial_r \tilde{\theta} \right), \quad (6.12b)$$

$$\partial_r \tilde{u}_r = -\frac{1}{r^2} \partial_r \left(\mathcal{D} r^2 \partial_r \tilde{\theta} \right). \quad (6.12c)$$

together with a one-dimensional initial condition for θ, without velocity perturbations, using the radial profile discussed in section 3.4.

The parameter that we use to investigate to what extent the implosion conditions impact the molecular diffusion in the mixing layer is the mixing layer width L, whose definition is given in section 6.4.2, and whose value is computed at the end of the implosions, $L(\Lambda_{min}) = L_E$.

We perform two parametric studies obtaining the maps, shown in Figure 6.7. In one case, we set the thermodynamic conditions to the ones chosen in section 6.2.2 and vary the initial compression rate and the convergence ratio. In the other, the compression characteristics are constant, and we change the initial temperature and density of the DT at the center of the capsule.

On Figure 6.7a , we observe that the faster the compression, the lower the final value of the mixing zone size, since the diffusion has less time to act. This tendency is observed for every convergence ratio. For the same reason, as the minimum of the compression parameter decreases, *i.e.* the capsule is compressed to a smaller radius, the values of L_E increase.

On the map in Figure 6.7b, the value of the final mixing zone width grows with the increase of the initial temperature, and it has the inverse dependence of the initial density. The first effect is explained by the fact that the higher is the temperature, the greater is the diffusion. The dependence on the density is similar to that observed in Figure 6.4b.

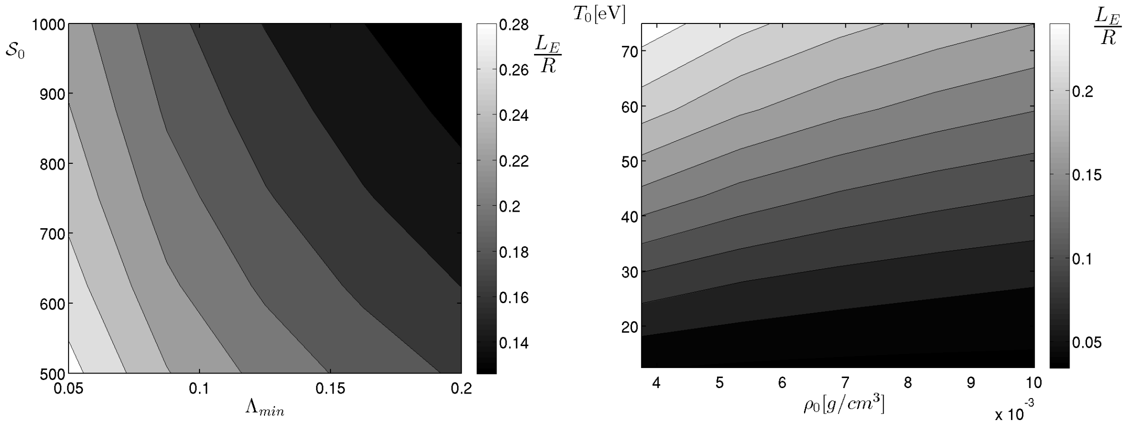

(a) (b)

Figure 6.7 – Dependence of the final size of the mixing zone, on initial compression velocity and final size of the domain (left) and on initial temperature and density of the capsule center (right)

6.4 Results

In this section, we extract the different turbulent quantities from simulations to observe the effects of plasma transport coefficients on the dynamics of turbulent layers.

6.4.1 Global statistics

Figure 6.8 shows the variations of the turbulent kinetic energy, $\langle \mathcal{K} \rangle = \langle u_i' u_i' \rangle / 2$, and of the variance $\langle \theta' \theta' \rangle$ for high Reynolds number simulations $S1_{a,b}$. This comparison shows the role of plasma transport coefficients in the mixing evolution.

For both simulations, the dynamics of the flow is first driven by compression effects, leading to an increase of kinetic energy. This phase, identified as the rapid compression in chapter 4, leads to a Λ^{-2} growth of $\langle \mathcal{K} \rangle$. Simultaneously, the density fluctuations initially at rest and expressed by $\langle \theta' \theta' \rangle$ rise rapidly due to the advection term. After this initial phase, simulations $S1_a$ and $S1_b$ start to differ. On the one hand, for the $S1_a$ simulation, the turbulent kinetic energy growth is progressively slowed down due to the viscosity increase. Then, the sudden viscous dissipation effect occurs [Davidovits and Fisch 2016a], since the turbulent production mainly due to compression cannot balance viscous terms. Note that a scaling $\langle \mathcal{K} \rangle \sim \Lambda^{11/2}$ is expected for the self-similar decay of a Batchelor spectra with constant implosion rate (see chapter 4).

On the other hand, the $S1_b$ simulation goes from rapid compression to a nearly cascade regime dominated by turbulent nonlinear transfers. This phase lasts until

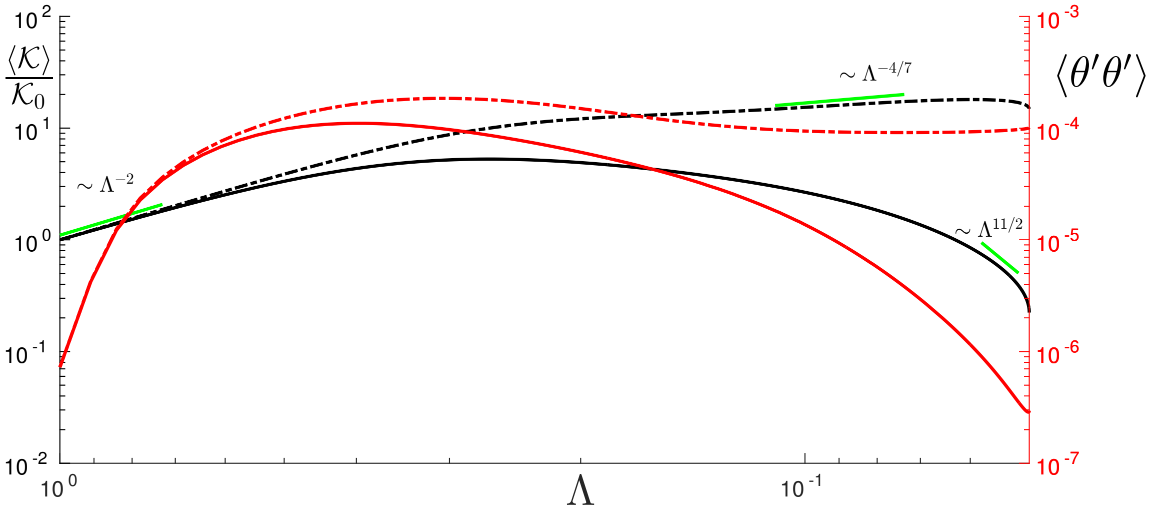

FIGURE 6.8 – Evolution of the turbulent kinetic energy normalized by its initial value (black) and the scalar variance $\langle\theta'\theta'\rangle$ (red), as functions of the compression parameter Λ. The solid lines represent the results of plasma transport coefficients simulation $S1_a$, and the dashed-dotted lines are for $S1_b$ results. Scaling laws corresponding to the self-similar regimes identified in Viciconte et al. (2018) are also plotted.

the end of the compression with scaling close to $\Lambda^{-4/7}$ as expected for a Batchelor spectrum [Viciconte et al. 2018]. A sharp decrease is observed at the end of all the simulations, which can be attributed to the deceleration of the compressed matter.

The smaller values of $\langle\theta'\theta'\rangle$ in $S1_a$ simulations compared to $S1_b$ are the first indication of enhanced mixing due to plasma transport coefficients.

6.4.2 Mixing layer width

We now compare the time evolutions of the size of the mixing layers in Figure 6.9 for high Reynolds simulations $S1_{a,b}$, with or without plasma effects, and also for $S5$ to stress the role of plasma transport coefficients when turbulence is absent.

The mixing layer sizes L can be evaluated in simulations using the following integral function of the radial averaged mass fraction $\overline{Y}(r,t)$ [Andrews and Spalding 1990, Gréa 2013].

$$L(t) = 6\int_0^{+\infty} \overline{Y}(t,r)(1-\overline{Y}(t,r))dr \tag{6.13}$$

During the implosion, the mixing layers in $S1_{a,b}$ simulations first experience growth due to the rapid compression regime identified in section 6.4.1. This growth is slowed due to the dissipation of turbulent energy, either by the cascade process in $S1_b$ or directly by transport coefficient in $S1_a$. This process is very similar to the growth of a mixing layer in the plane Richtmyer-Meshkov instability as the turbulence scales are small compared to the radius of the interface.

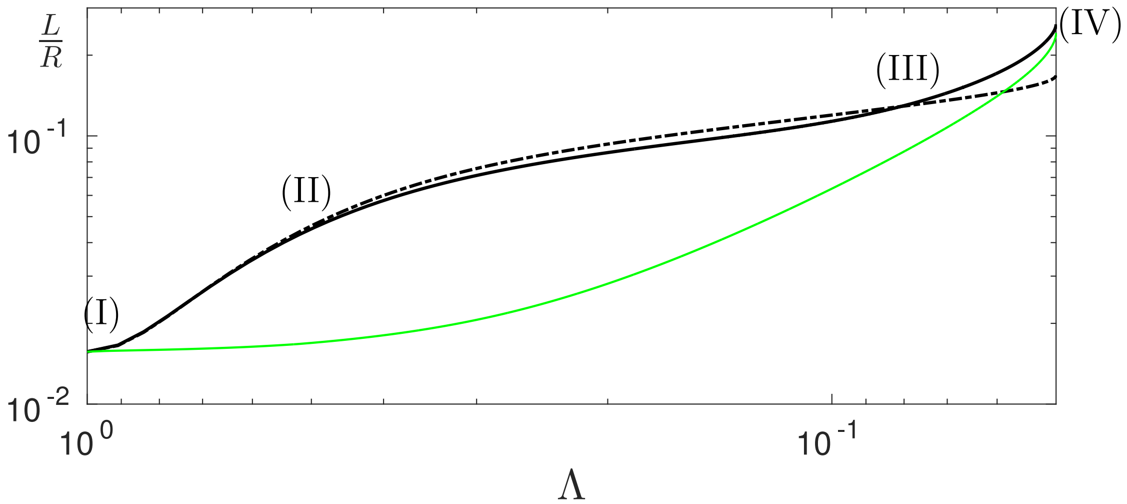

Figure 6.9 – Evolution of the renormalized mixing layer width as a function of the compression parameter Λ. The solid black line for the case of plasma transport coefficients ($S1_a$). The black dashed line is for the constant case ($S1_b$). The solid green line is the reference case with Re $= 0$ ($S5_a$) where the mixing layer is only enlarged by molecular diffusion.

Despite the active role of plasma viscosity in destroying turbulence and relaminarizing the flow, $S1_a$ simulation has only a slightly lower growth rate as $S1_b$ simulation until the time (III) $t = 0.93ns$. This can be explained as the dynamics of a layer is principally driven by the large energetic scales, which are not dissipated by viscous effects acting at smaller scales. The molecular diffusion increase can also compensate for the loss of turbulent diffusion in the $S1_a$ simulation. Eventually, this process completely dominates the turbulence at the end of the simulation leading to a sudden diffusion of the layer also present in $S5$ simulation at $Re = 0$.

It is during this last sudden diffusion phase, that $S1_{a,b}$ simulations become significantly different, with the mixing layer width in $S1_a$ increasing rapidly much above the values obtained in $S1_b$ simulation.

The effect of initial conditions, mainly with varied Reynolds number detailed in Table 6.2, is now investigated in Figure 6.10. For the range of Re investigated, the final sizes of mixing layers are weakly sensitive to the initial level of turbulence in simulations accounting for plasma transport coefficients (Figure 6.10a). The difference between simulations with or without varying plasma transport coefficients mainly occurs during the sudden diffusion phase, appearing earlier in low Reynolds number simulations. Besides, the relaminarization process due to viscosity increase has a low impact on the mixing layer dynamics. The simulations at higher Reynolds number would allow us to determine a critical Re where the sudden diffusion no longer occurs.

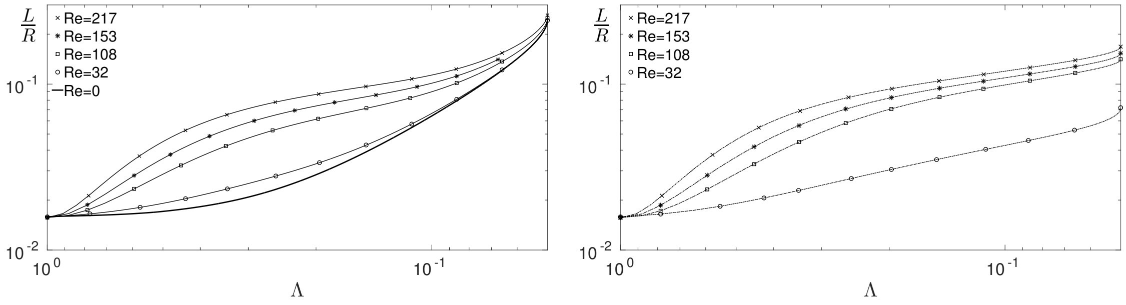

(a) (b)

FIGURE 6.10 – Evolution of the mixing layer width as a function of the compression parameter Λ for the simulations of table 6.2. (a) Simulation with plasma transport coefficients $S1_a - S5_a$. (b) Simulations with constant transport coefficients $S1_b - S4_b$.

Still, these simulations are presently out-of-reach, too computationally demanding.

6.4.3 Radial profiles

In this section, we explore the mean radial structures of mixing zones and compare their evolutions when the relaminarization process occurs due to plasma transport coefficients.

We show in Figure 6.11 the mean mass fraction of ablator, $\overline{Y}$, extracted from $S1_{a,b}$. The selected times correspond to the phases identified in Figure 6.9 in section 6.4.2. Whereas at early times there are small differences between simulations accounting or not for varying transport coefficients, at late times, the sudden diffusion phase in $S1_a$ marks a strongly different behavior. This phenomenon is very effective at contaminating the capsule center with heavy ablator elements.

In parallel, we present the mean profiles of turbulent kinetic energy $\overline{u_i'u_i'}/2$ and variance $\overline{\theta'\theta'}$ in Figure 6.12 also for $S1_{a,b}$ simulations. These profiles are classically maximum at the center of the mixing layers. The relaminarization process due to viscous effects is marked by the dissipation of turbulent variances and occurs very soon, as shown by the differences between the simulations. Interestingly, relaminarization is close to symmetric between the fuel and ablator sides on $\overline{\theta'\theta'}$ radial profile, but, this is not the case on kinetic energy profiles where dissipation seems to occur firstly on the DT side. Finally, only molecular diffusion is responsible for the sudden diffusion of the mixing layer as turbulent quantities are completely quenched at late times in $S1_a$ simulation.

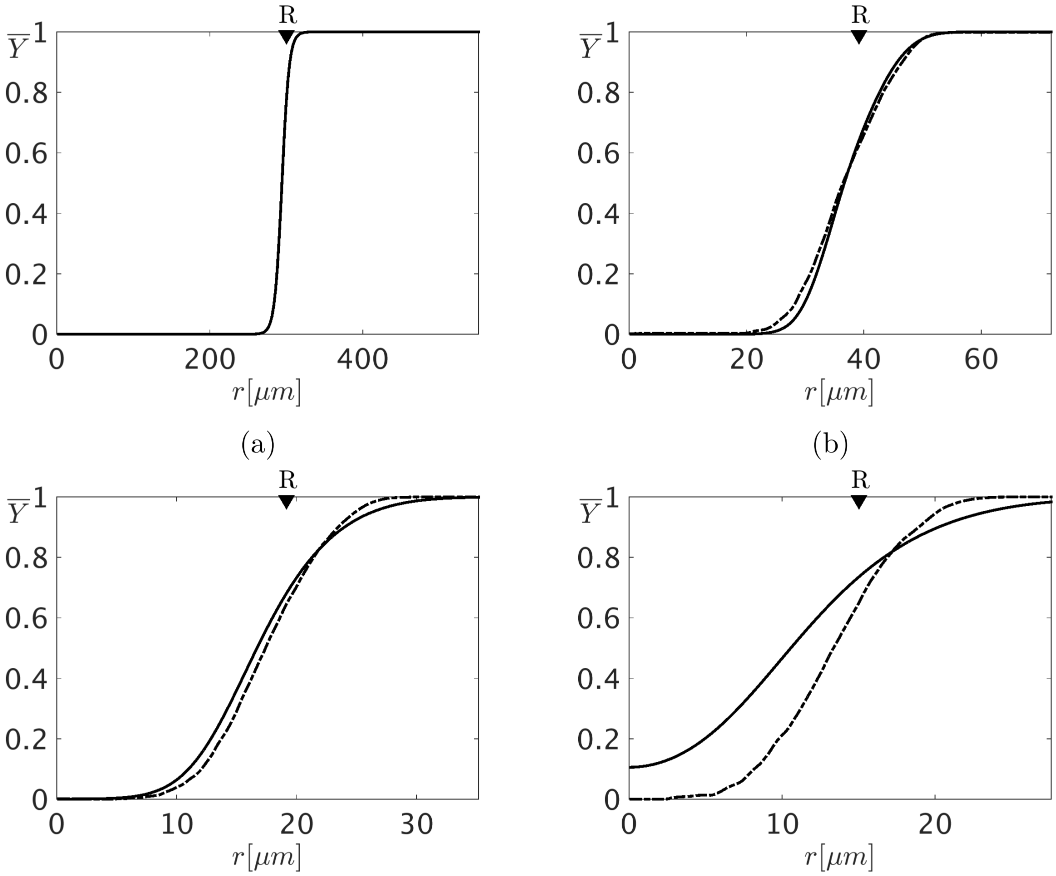

(a) (b)

(c) (d)

FIGURE 6.11 – Ablator (CH) tangential averaged mass fraction Y at four times during compression. (a) Initial condition at $t = 0$ ns and $\Lambda = 1$ (b) (II) $t = 0.5$ ns and $\Lambda = 0.5$ (c) (III) $t = 0.93$ ns and $\Lambda = 0.08$ (d) (IV) $t = 1$ ns and $\Lambda = 0.05$. Solid line for the $S1_a$ simulation, dashed-dotted line for the $S1_b$ simulation. The lagrangian position of the unperturbed fuel/ablator interface is also indicated in the figure.

6.4.4 Mixing parameter

We further shed light on mixing in $S1_{a,b}$ simulations using the molecular mixing parameter $\Xi(r,t)$ defined from the mass fraction of the ablator as (see Youngs (1991)) :

$$\Xi(r,t) = \frac{\overline{Y(1-Y)}}{\overline{Y}(1-\overline{Y})} = 1 - \frac{\overline{Y'Y'}}{\overline{Y}(1-\overline{Y})}. \tag{6.14}$$

The mixing parameter value thus reaches 1 when mixing is completed. This quantity is important in ICF for expressing the ratio between the amount of fusion reactions in the mixing zone and the amount obtained without mass fraction fluctuations [Youngs 1991]. Therefore, molecular mixing reflects to what extent the local mass

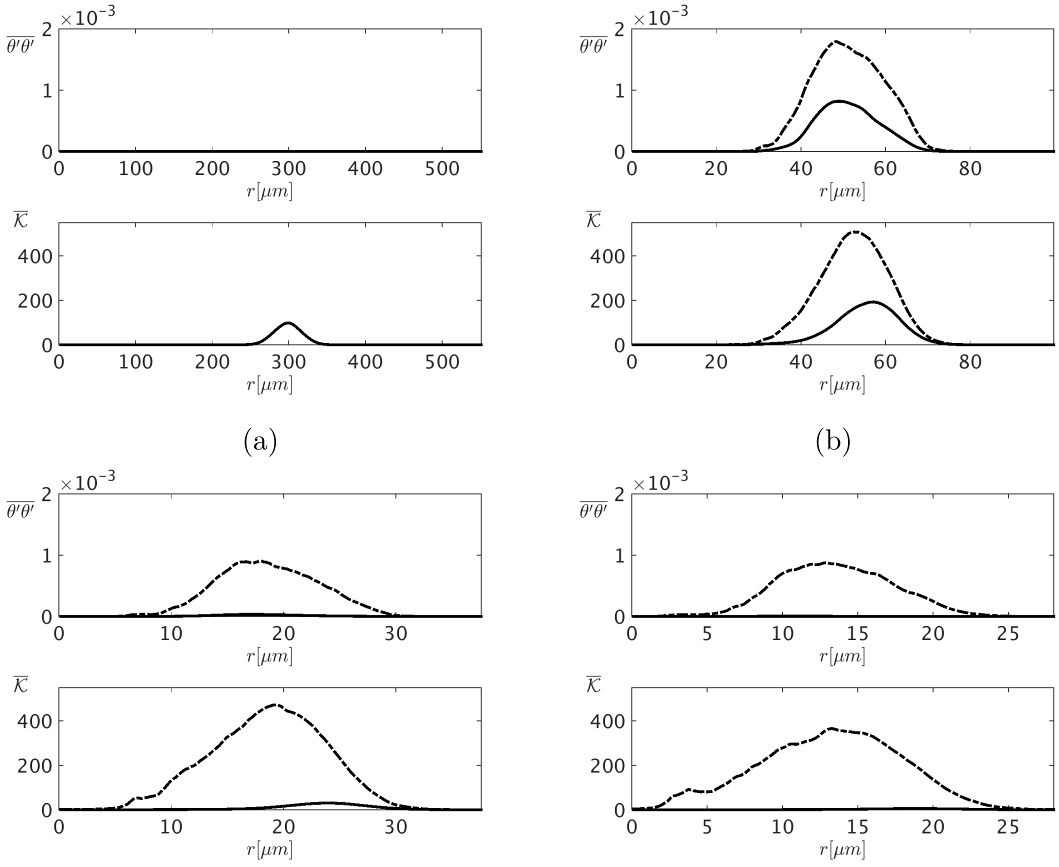

(a)

(b)

(c)

(d)

FIGURE 6.12 – Radial profiles of the variance of θ (top) and kinetic energy $\overline{\mathcal{K}}$ (bottom), at four times during compression. (a) Initial condition at $t = 0$ ns and $\Lambda = 1$ (b) (II) $t = 0.5$ ns and $\Lambda = 0.5$ (c) (III) $t = 0.93$ ns and $\Lambda = 0.08$ (d) (IV) $t = 1$ ns and $\Lambda = 0.05$. Solid line for the $S1_a$ simulation, dashed-dotted line for the $S1_b$ simulation.

fraction departs from the mean but does not give the relative amount of the two species in the mix [Danckwerts 1952].

We compare the temporal evolution of Ξ between $S1_a$ and $S1_b$ simulations in Figure 6.13. Here, the mixing layer width is shown by the specific radii r_{01}, r_{99} where $\overline{Y} = 0.01$ reaches 0.01 and 0.99 respectively. From the time (I) to (II) corresponding to the rapid compression phase, the mixing parameter values are similar, since the process is mainly driven by turbulence.

From the time (II) to (III), although the sizes of the mixing layer are comparable between both simulations, the values of the molecular mixing parameter in $S1_a$ become gradually larger than in $S1_b$, owing to the varying transport coefficients of the plasma. At time (III) and during the sudden diffusion phase, the values of Ξ in $S1_a$

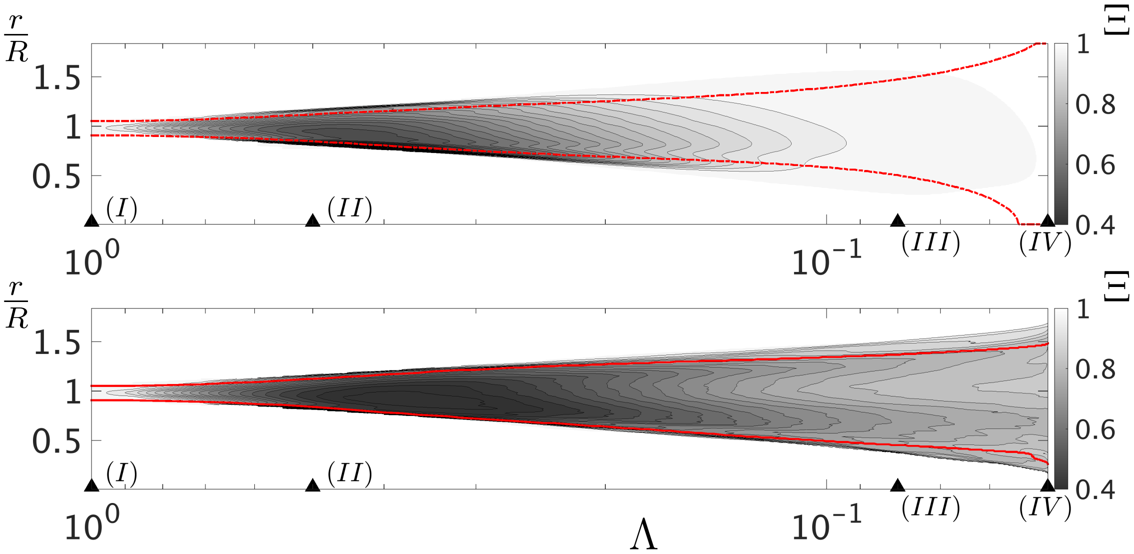

FIGURE 6.13 – Contour maps of the molecular mixing parameter Ξ as a function of the compression parameter Λ and normalized radial position r/R. (Top) $S1_a$ simulation ; (Bottom) $S1_b$ simulation. The red lines show the evolution of the mass fraction dependent radii r_{01}/R and r_{99}/R, corresponding respectively to $\overline{Y} = 0.01$ and $\overline{Y} = 0.99$.

become very close to 1, indicating that the mixing is almost complete. By contrast, in $S1_b$ simulation, the mixing parameter also grows but at a smaller pace, as the mixing is driven by the turbulent cascade.

6.4.5 Transport coefficient evolutions

In this section, we present the temporal and spatial evolutions of plasma transport coefficients evaluated from the PIJ model [Arnault 2013, Ticknor et al. 2016, White et al. 2017]. This model is based on a formulation in terms of collision frequencies with scaling laws to cover the different regimes from weakly to strongly-coupled plasmas and to address binary mixtures with chemical elements of arbitrary atomic number Z. In that respect, it extends the theory limited to kinetic regime of Molvig et al. (2014), Kagan and Tang (2014), and better represent the early time evolution of the simulations that exhibit moderate coupling ($\Gamma = 0.3$).

We show in Figure 6.14 the mean radial profiles of kinematic viscosity $\overline{\nu}(r,t)$ and diffusion $\overline{\mathcal{D}}(r,t)$ at different instants extracted from the $S1_a$ simulation. The temporal evolutions of viscosity and diffusion are also shown for specific radii r_{01} and r_{99}. Several classical features of transport coefficients in plasma are thus recovered. Viscosity and molecular diffusion follow the kinetic scaling laws Braginskii (1995) and thus experience tremendous growth, up to two orders of magnitude, due to

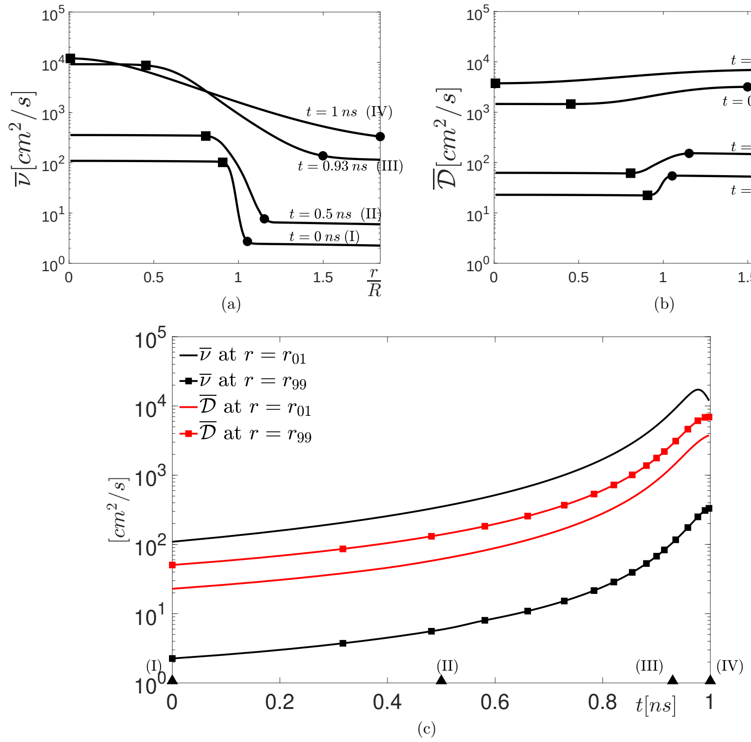

(a)

(b)

(c)

FIGURE 6.14 – Transport coefficient values extracted from $S1_a$ simulation. (a) and (b) : mean radial profiles of viscosity and diffusion at four different instants. (c) : Time evolution of mean viscosity and diffusion at the edges of the mixing layer at r_{01} (solid line) and r_{99} (dashed lines) corresponding to $Y = 0.01$ and 0.99 respectively. At the end of the simulation ($t \lesssim 1$ ns), r_{01} reaches zero as mixing is entirely spread inside the capsule. The mean viscosity and diffusion are then plotted at the center of the capsule, $r = 0$, and therefore decrease since $\overline{Y}$ becomes greater than 0.01 at $r = 0$

temperature increase. The mean radial profiles of ν exhibit a strong dependence on the mixture composition expressed by the mass fraction Y. The presence of heavy CH ions in the pure DT plasma indeed increases the effective plasma coupling parameter, leading to $1 - 2$ orders of magnitude lower viscosity on the ablator side. Here, the plasma coupling parameter indeed evolves from 3×10^{-2} to 2×10^{-3} in pure DT, and from 3×10^{-1} to 10^{-2} in pure CH. Conversely, the molecular diffusion is $2 - 3$ times higher on the ablator side. Indeed, the ion density number on the ablator side is lower than on the DT side, considering that the particle number distribution (ion and electron) n is constant in the mixing layer. However, the spatial variations of $\mathcal{D}$ are less spectacular than for viscosity. Consequently, the Schmidt number $\nu/\mathcal{D}$ varies between 3 and 4 close to the DT side of the mixing layer, while it reaches values of around 0.05 on the CH side.

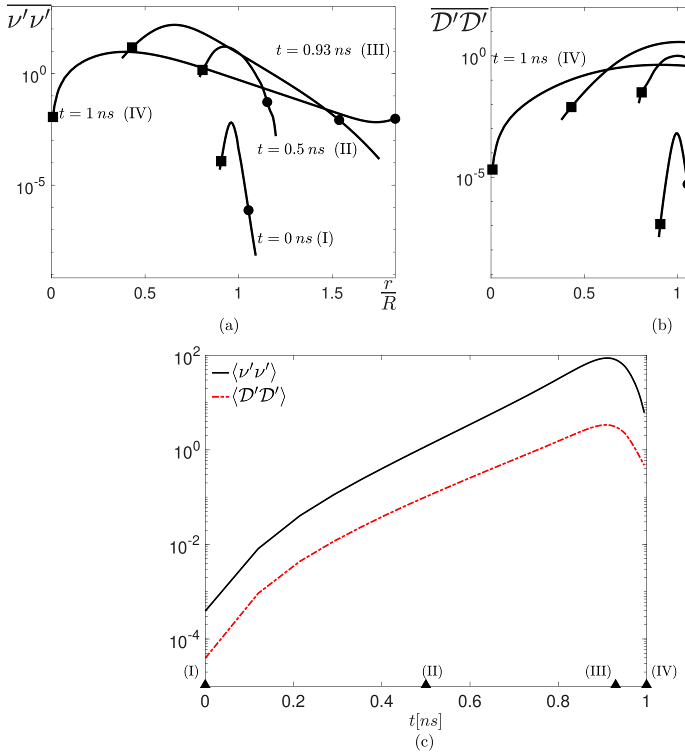

(a) (b)
(c)

FIGURE 6.15 – Transport coefficient variances extracted from $S1_a$ simulation.(Top) mean radial profiles of (a) viscosity, $\overline{\nu'\nu'}$, and (b) diffusion, $\overline{\mathcal{D}'\mathcal{D}'}$, at four different instants. (c) : Time evolution of mean variance of viscosity $\langle\nu'\nu'\rangle$ and diffusion $\langle\mathcal{D}'\mathcal{D}'\rangle$.

The time evolution of the mean variances of viscosity $\langle\nu'\nu'\rangle$ and diffusion, $\langle\mathcal{D}'\mathcal{D}'\rangle$, and their radial profiles, $\overline{\nu'\nu'}$ and $\overline{\mathcal{D}'\mathcal{D}'}$, are plotted at different instants in Figure 6.15. These quantities reveal how fast viscosity and diffusion vary inside the mixing layer justifying the use of implicit iterative methods for numerical simulations. Transport coefficient variances increase during the compression until the decay of turbulence smooths the mass fraction fluctuations. Interestingly, while radial profiles of molecular diffusion variances remain maximum and well-centered around the mixing layer center, $r/R = 1$, viscosity variances shift toward the DT edge where even a small amount of CH drives huge variations of viscosity. This effect has also been observed on kinetic energy, and θ' variance profiles in section 6.4.3.

6.4.6 Bi-dimensional Maps

In this section, we exhibit the instantaneous turbulent fields extracted from $S1_{a,b}$ simulations to better understand how the relaminarization process and sudden diffusion effect induced by plasma transport coefficients operate.

We start by showing the two-dimensional contours of local kinetic energy $\mathcal{K} =$

$u_iu_i/2$ in $S1_{a,b}$ simulations for the three radial positions, r_{01}, r_{50} and r_{99} (defined for $S1_b$) and four times I, II, III IV in Figure 6.16. The contour maps are obtained using

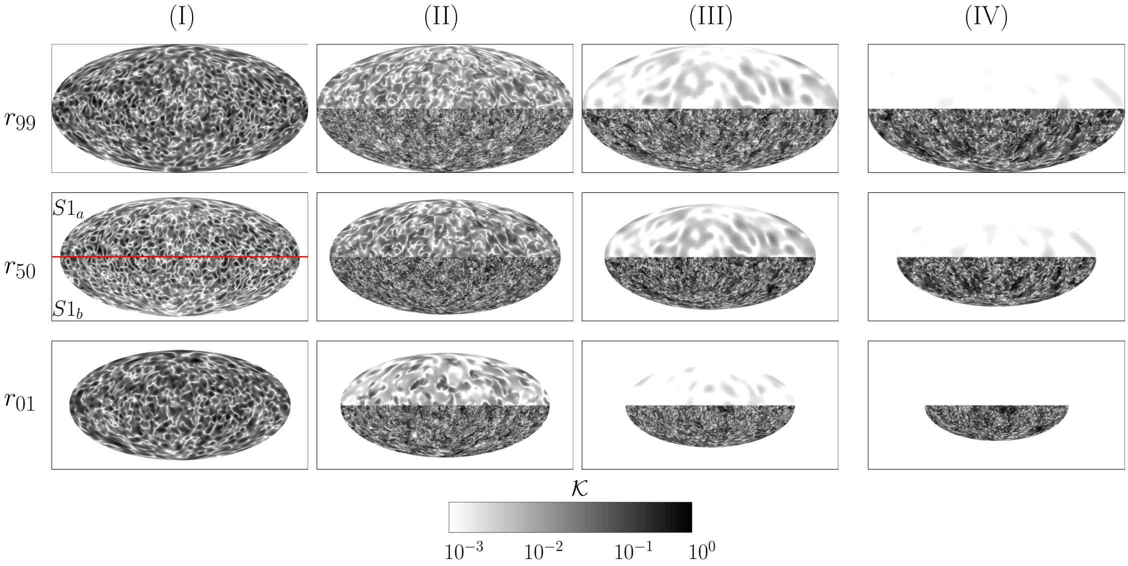

FIGURE 6.16 – Mollweide projection of the local turbulent kinetic energy in the mixing layer. The three rows correspond to the radial positions r_{99}, r_{50}, r_{01} defined in $S1_b$ simulation, at times I, II, III, IV. Top and bottom half contours corresponds respectively to $S1_a$ and $S1_b$ results.

the pseudo-cylindrical or Mollweide projection, as detailed in Appendix C.1.

Figure 6.16 clearly evidences the asymmetric relaminarization process due to the viscosity growth in $S1_a$ simulation. The turbulent kinetic energy is firstly dissipated on the DT side of the mixing layer, following the spatial variations of viscosity, as detailed in section 6.4.5. Also, the fact that turbulent structures are larger in $S1_a$ simulation compared to $S1_b$ shows that dissipation acts at small scales before reaching larger ones during the final phase of the compression. On the contrary, the constant viscosity of $S1_b$ simulation allows the development of small structures by classical nonlinear energy cascade.

We now compare the structure of the θ' variance in Figure 6.17 at the center of the mixing zone, *i.e.* $r = r_{50}$, with kinetic energy contours at the same position. Interestingly, the characteristic sizes of the scalar field $\theta'\theta'$ are larger than for the kinetic energy contours, indicating that the dissipation is more effective for the variance of θ' than for the turbulent kinetic energy, as already seen in Figure 6.8.

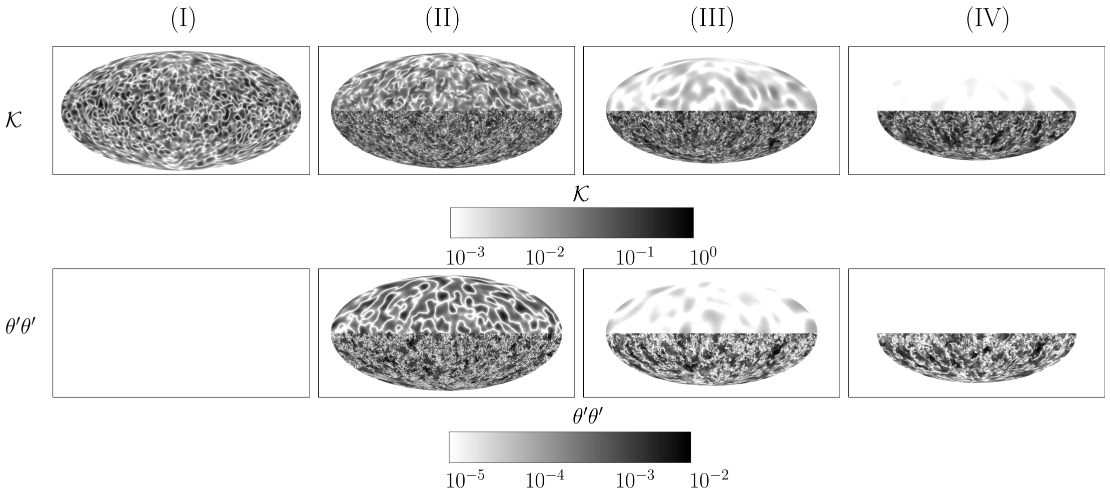

FIGURE 6.17 – Top : Mollweide projection of the kinetic energy. Bottom : Mollweide projection of the scalar variance. The radius of the spheres corresponds to the center of the mixing zone. Top and bottom half contours correspond respectively to $S1_a$ and $S1_b$ results.

6.4.7 Spherical harmonics spectra

The two-dimensional maps offer only a qualitative appreciation of the transport coefficient effects on the turbulence within the mixing layer. To quantify the information given by the maps of section 6.4.6, we use the spectral analysis of fluctuating fields on spherical surfaces proposed by Lombardini et al. (2014b). The natural spectral basis to represent these fields are the spherical harmonics. For instance, a function $f(r_i, \psi, \phi)$ defined on a sphere of radius r_i can be decomposed using the real spherical harmonic basis as

$$f(r_i, \psi, \phi) = \sum_{l=0}^{\infty} \sum_{m=-l}^{l} f_{lm} Y_{lm}(\psi, \phi), \tag{6.15}$$

where $Y_{lm}(\psi, \phi)$ are the real spherical harmonics [Abramowitz and Stegun 1965, Groemer 1996], and f_{lm} are the expansion coefficients (see also Appendix C.2).

Within this basis, it can be shown [Lombardini et al. 2014b] that the angular power spectrum C_l associated with the two-point correlation of the quantity f taken on the sphere of radius r_i (and assumed statistically homogeneous and isotropic on the same sphere) can be computed from the expansion coefficient as

$$C_l = \frac{1}{2l+1} \sum_{m=-l}^{l} f_{lm}^2. \tag{6.16}$$

Considering high l spherical harmonics, corresponds to very small characteristic dimensions with respect to sphere curvature, there is a direct relationship between the angular power spectra C_l and the local one-dimensional planar spectrum $E(\kappa)$, where the “wavenumber" κ is defined as $\kappa^2 = l(l+1)/r_i^2$. In the limit of $l \gg 1$, $\kappa \simeq l/R$ and it can be shown that $lC_l \sim \kappa^{-\alpha}$ [Lombardini et al. 2014b].

We thus compute the angular power spectra, using the field interpolated on spheres with radii r_{01}, r_{50}, and r_{99}. Because of the mixing, these radii vary during the compressions. Therefore, in order to compare the different spectra at different times and radii, we plot lC_l as a function of the non-dimensional wavenumber q_l, that is directly related to the spherical harmonics number l, by the relation $q_l = \frac{R}{r_i}\frac{l}{2\pi}$.

In Figure 6.18, we compare the angular power spectra of kinetic energy $lC_{l,\mathcal{K}}$ and scalar field variance $lC_{l,\theta}$, between the simulations $S1_a$ with varying plasma transport coefficients and $S1_b$ with constant transport coefficients. At the time (I), the kinetic energy spectra of the two initial conditions are superimposed, while, as we explained in section 6.2.5, the initial conditions have no scalar fluctuations. At the time (II), as observed on the bi-dimensional maps of section 6.4.6, in the constant viscosity simulation, nonlinear phenomena produce a turbulent cascade. The inertial range, exhibiting a $l^{-5/3}$ slope of the kinetic energy spectrum, extends up to the maximum resolved q_l. On the contrary, the spectrum of the $S1_a$ simulation shows less energetic scales, with no inertial range due to the increased value of viscosity. At small q_l, which coincides with the most energetic spherical harmonics, the two spectra have a similar energy distribution. This implies that the mixing zone evolution, in both simulations, is still driven by large scale turbulent diffusion, confirming the results of sections 6.4.2 on the mixing zone width. The scalar spectra, $lC_{l,\theta}$, exhibit the same behavior, with the $l^{-5/3}$ scaling recovered for the constant transport coefficient simulations, and the relaminarization effects in the $S1_a$ case. When the simulations reach time (III), the $S1_b$ kinetic energy spectrum maintains an inertial zone at intermediate wavenumber. Still, the $l^{-5/3}$ scaling does not extend to the $q_{l,max}$, and we observe the beginning of a dissipative range. In contrast, for the $S1_a$ case, the energy-containing harmonics, for both kinetic energy and scalar, are reduced to the small q_l, suggesting that at this time, the dynamics of the mixing zone is dominated entirely by viscous and diffusive effects. At the time (IV), the $S1_a$ spectra, for both quantities, show a very limited spherical harmonics range since the transport coefficients dissipate almost all the fluctuations. These results are consistent with the bi-dimensional maps of section 6.4.6, where at the time (IV), minimal fluctuations are visible. On the other hand, the constant coefficient spectra suggest that turbulence is still the primary driving phenomenon of the mixing zone evolution.

The temporal variation of the kinetic energy and scalar spectra of the $S1_a$ simulation, in Figure 6.19, is a further indication of the relaminarization caused by the transport coefficients. This effect smooths velocity and density fluctuations equally, leaving only large scales fluctuations at the end of the implosion.

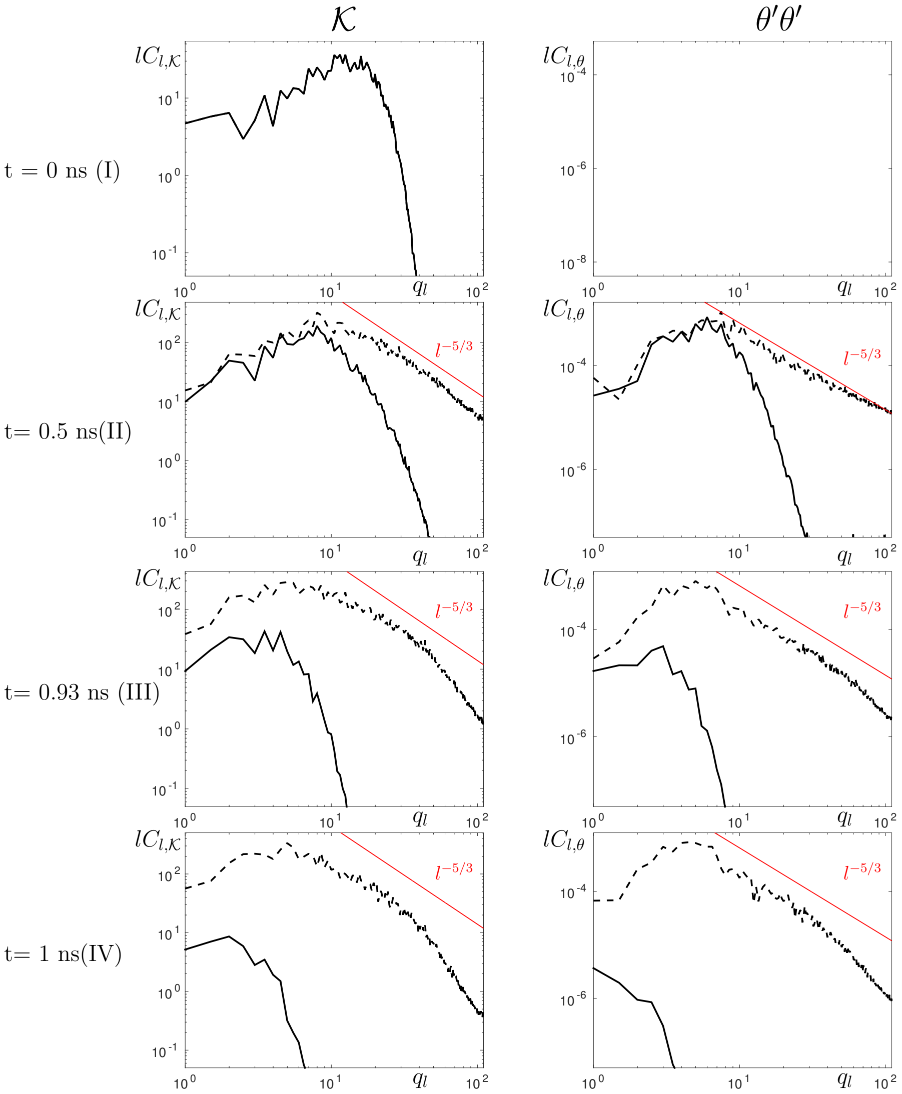

FIGURE 6.18 – Spherical harmonics spectra computed at the center of the mixing zone, r_{50}, at the instants I, II, III, IV. Left : kinetic energy spectra ; right : scalar spectra. The solid black lines correspond to the simulation $S1_a$, the dashed lines to the simulation $S1_b$. The red solid line represents the $l^{-5/3}$ power law.

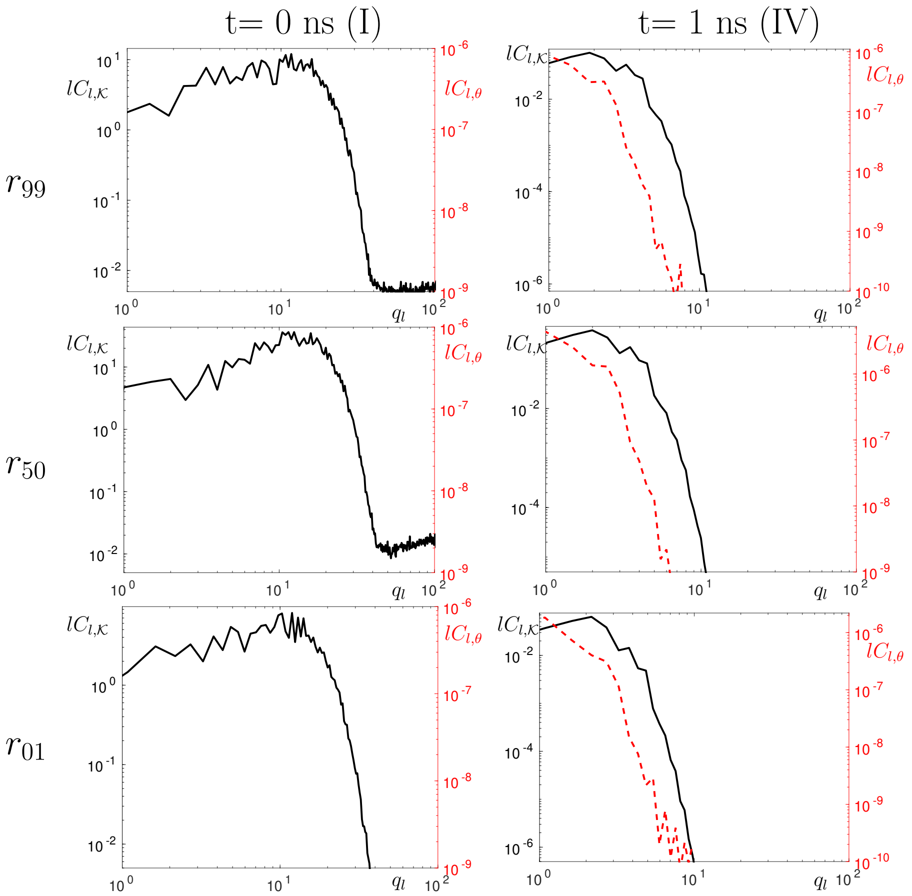

FIGURE 6.19 – Spherical harmonics spectra computed at the beginning (I) and at the end (IV) of the simulation $S1_a$ at three radial positions r_{01}, r_{50}, r_{99}. Black solid lines correspond to kinetic energy spectra. Red dashed lines correspond to scalar spectra.

6.5 Conclusion

This chapter presents numerical simulations of turbulent plasma mixtures under compression using a fluid approach and the PIJ [Arnault 2013, Ticknor et al. 2016, White et al. 2017] modeling of the transport coefficients, which vary with temperature, density, and composition. The parameters are chosen to be representative of adiabatic implosions of DT/CH layers, mimicking the characteristic times and hot spot thermodynamic conditions of an ICF capsule before the bang time. To achieve full resolution of low Mach number turbulent fluctuations, we use a Rogallo non-inertial frame following the compression and the variable density approximation.

Simulations with or without varying plasma coefficients evidence the influence of plasma viscosity and molecular diffusion on the dynamics of mixing layers. This aspect is crucial in the context of ICF as the hot spot contamination by heavy materials has deleterious effects on the capsule yield. A complex relaminarization process has been observed, occurring first on the DT side where viscosity is higher, as shown by radial profiles and angular spectra. Although this phenomenon dissipates the small scales of turbulence and leads to a more homogeneous DT/CH mixing layer, it does not drastically reduce the dynamics of the mixing zone, mainly driven by larger scales. However, we show that during the late time evolution of the compression, the plasma molecular diffusion overcomes the turbulent one, leading to enhanced diffusion of the DT/CH layer anticipated in chapter 4. This sudden diffusion effect comes along with the sudden viscous dissipation of turbulence already observed by Davidovits and Fisch (2016a). This gives credit to the interpretation of mixing due to physical diffusion in recent experiments performed at the Omega facility by Rinderknecht et al. (2014a), Zylstra et al. (2018).

Chapitre 7
Conclusions

Contents

The objective of the works presented in this thesis is to study turbulent mixing in fluid with strong transport coefficients and density variation. We consider both canonical flows like the homogeneous isotropic turbulence and unstably stratified homogeneous turbulence and inhomogeneous configurations like spherical implosions.

The contributions presented in this thesis are, for the most part, based on the analysis of direct numerical simulations of the Navier-Stokes equations with the working hypothesis for every case considered.

In the first part of the thesis, we have presented

- The derivation of model equations for spherical compression and USHT in the variable density approximation.
- The spectral GMRES algorithm employed to solve the Poisson equation in the variable density simulations.
- The development of a massively parallel spectral direct numerical simulation code based on the two-dimensional domain decomposition for both incompressible and variable density case.
- The GMRES algorithm used to compute the viscous and diffusive contribution in turbulent plasma mixtures whose transport coefficients are computed using a plasma physics code interfaced with the DNS code.

In the following chapters, we have used the codes developed to investigate three major topics :

- The sudden dissipation effect of turbulent kinetic energy in plasma under compression in the context of homogeneous isotropic turbulence with time-varying viscosity, for which we have developed a spectral model based on EDQNM closure.

- Then, still in a homogeneous approximation, we study the effect of variable density on the turbulence properties in an unstably stratified configuration.
- Finally, we consider an inhomogeneous configuration of a spherical implosion, with transport coefficients and variable density effects.

7.1 Sudden dissipation effect : spectral modeling and influence of initial conditions

In the context of turbulent weakly-coupled plasma under compression, we have identified three different self-similar regimes resulting from the competition between turbulence production, non-linear energy transfer, and viscous dissipation, which are observed in our DNS and EDQNM simulations.

In the case where turbulence is sufficiently intense and compression sufficiently rapid, we observe that weakly-coupled plasma under compression experiences growth of kinetic energy. However, the viscous effects always prevail at the end of the compression leading to the sudden dissipation phenomenon.

Using the EDQNM model, we have explored the phase space of the non-dimensional numbers, *Re* and **Cp**, initial values thanks to which we have identified the critical values of the compression parameter corresponding to the beginning of the viscous phase.

This analysis has revealed a strong dependence of critical values on the initial conditions and evidenced the complex interplay between turbulence production, transfer, and dissipation, leading for some configurations to two successive growth/decay phases of kinetic energy instead of one during the compression.

We have identified three self-similar regimes during the isotropic compression of a weakly-coupled turbulent plasma. Using a theoretical analysis, we have derived the scaling laws which have been verified using DNS and EDQNM simulations.

The scaling demonstrates the dependence of flow dynamics on the initial distribution of energy at large scales, which becomes crucial during the viscous phase since it changes the decay exponents of kinetic energy drastically.

We further extended our study to the case of an inhomogeneous spherical turbulent layer under compression, using parameters representative of ICF capsules.

In this configuration, we were able to observe the different phases already identified in the homogeneous settings together with the enhanced enlargement of the layer during the viscous phase and high sensitivity to initial conditions.

7.2 Unstably stratified homogeneous turbulence

The other subject of the thesis concerns the study of the variable density effect in the unstably stratified homogeneous turbulence, a canonical flow that retains some of the features of the Rayleigh-Taylor mixing layer.

We consider two approximations, Boussinesq (B) and Variable Density (VD). The objective of the investigation is twofold : to understand in what measure the variance of the initial scalar field influences the late time self-similar flow evolutions, and the limitations of the Boussinesq approximation and the condition of the onset of non-Boussinesq effects.

The numerical solution of the USHT equation with the variable density approximation is considerably challenging in the cases considered due to the high-density contrasts that are already present at the beginning of the simulation. Together with the direct numerical simulation, we have introduced the implicit large-eddy simulations, which are less computationally demanding, thanks to which we can perform a parametric study of initial conditions.

We show that depending on the initial scalar field variance, in VD approximation, contrary to Boussinesq, the large scale of the flow can be modified. In particular, we confirm a recent observation of Soulard et al. (2019) demonstrating how variable density effects modify the infrared slope of the kinetic energy spectrum if the intensity of the scalar fluctuations is sufficiently important.

In particular, we observe that, from an initial condition where the large scales of the flow have a dependence in k^4, during the initial transient, the spectrum changes to k^2, if the initial variance is sufficiently high. This large scale modification is extremely important because of the direct influence of the infrared exponent on the growth rate of the self-similar phase. Furthermore, using the probability density function, we demonstrate other differences between variable density and Boussinesq approximation. The pdfs of the scalar computed from Boussinesq results have a symmetric distribution around the mean value, while the VD cases show an asymmetrization of the probability density functions towards the positive values of θ.

Moreover, the investigation of the scalar gradients shows that in the variable density case, the tails of the probability density functions are much wider than the Boussinesq case implying the presence of sharper interfaces that can be observed qualitatively on the scalar contours too. Finally, performing the parametric study on the initial conditions, we find that the non-Boussinesq effects become important for a scalar variance to kinetic energy ratio between 0.01 and 0.05.

7.3 Sudden diffusion effect in spherical mixing zones of plasma under compression

The last chapter of the thesis presents numerical simulations of turbulent plasma mixtures under compression using a fluid approach and the uses of the PIJ model to compute the transport coefficients, which vary with temperature, density, and composition.

The theoretical framework derived allows for the study of variable-density flow with extreme variations of viscosity and diffusivity, both taken into account thanks to the GMRES iterative scheme.

The parameters of inhomogeneous spherical configuration, together with the thermodynamic variable of the hot spot, are chosen to be representative of adiabatic implosions of DT/CH layers, mimicking the characteristic of an ICF capsule before the bang time. To evidence the effects of plasma transport coefficients, we present two sets of simulations : In the first, viscosity and diffusivity are computed using the PIJ model ; in the second, both transport coefficients are maintained constant. In the two cases, different initial Reynolds numbers are considered.

During the compression, we can identify different phases based on the mixing zone width, which evolution evidence the influence of plasma viscosity and molecular diffusion on the dynamics of mixing layers.

In the first rapid compression phase, both simulations present similar results, and no effects of transport coefficients are observed. In the following period, turbulence is the primary factor influencing the evolution of the mixing zone, and the growth of viscosity comes into play. During this phase, we observe a complex relaminarization process, occurring first on the side closer to the pure DT , where viscosity is higher than the part closer to the ablator, and move outwards towards the CH as the temperature in the capsule increases. This non-homogenous behavior has been demonstrated with both radial profile and angular power spectra. Although this phenomenon dissipates the small scales of turbulence and leads to a more homogeneous DT/CH mixing layer, it does not drastically reduce the dynamics of the mixing zone, mainly driven by larger scales.

In the last phase of the compression, however, we show that plasma molecular diffusion overcomes the turbulent one, leading to enhanced diffusion of the DT/CH layer anticipated in chapter 4. This aspect is crucial in the context of ICF as the hot spot contamination by heavy materials has deleterious effects on the capsule yield. This sudden diffusion effect comes along with the sudden viscous dissipation of turbulence already observed in chapter 4 and can explain some recent experimental results on the Omega laser facility.

7.4 Perspective

The results of this work, together with the code developed, allow different possible future researches. For the spherical implosion with plasma transport coefficients, the first improvement would be to explore other cases of implosion. In particular, one could use thermodynamic paths extracted from real Inertial Confinement Fusion (ICF) experiment or simulation. Moreover, the studies of these idealized implosions could help to include the transport coefficients effects in models used in ICF design.

In the case of variable density unstably stratified turbulence, one could investigate in-depth the small scale properties and their difference with the Boussinesq cases. Furthermore, the parametric study on initial conditions could be widened, including the variation of other quantities such as the Froude number or the buoyancy frequency. Moreover, the USHT problem could be explored in the case of variable acceleration.

Finally, the variable density code with little modification can be adapted to simulate Richtmyer-Meshkov, Rayleigh-Taylor, and Faraday turbulent mixing zones.

7.5 Publications & Conferences

Viciconte, G., Gréa, B. J., and Godeferd, F. S. (2018). *Self-similar regimes of turbulence in weakly coupled plasmas under compression.* Physical Review E, 97(2), 023201.

Viciconte, G., Gréa, B. J. and Godeferd, F. S., Arnault, P. and Clérouin, J (2019). *Sudden diffusion of turbulent mixing layers in weakly-coupled plasmas under compression.* Accepted for publication in Physical Review E.

Viciconte, G., Gréa, B. J. and Godeferd, F. S. (2017) *A spectral model for sudden dissipation effect in turbulent plasma under compression*, Congrès Français de Mecanique, Lille, France

Viciconte, G., Gréa, B. J., Godeferd, F. S., Arnault P., Clérouin J. and Desbiens N. (2018) *Viscous and diffusion effects in weakly-coupled plasma mixtures under compression*, 16th International Workshop on the Physics of Compressible Turbulent Mixing. Marseille, France

Viciconte, G., Gréa, B. J. Godeferd, F. S., Arnault P. and Clérouin J. (2018) *Viscous and diffusion effects in spherical mixing zone under compression*, 12th European Fluid Mechanics Conference. Vienna, Austria

Viciconte, G., Gréa, B. J. Godeferd, F. S, Soulard O. and Griffond J. (2019) *Numerical methods for variable density turbulence*, Turbulent Mixing and Ejecta at Interfaces II. Cambridge, UK

Viciconte, G., Gréa, B. J. and Godeferd, F. S (2019), *Transport Coefficients Effects In Spherical Mixing Zone Under Compression* 11th International Symposium on Turbulence and Shear Flow Phenomena. Southampton, UK

Annexe A
Compression

A.1 Moving frame

Here we sum up the derivation of the relation between frames coordinates , that is found in Rogallo (1981). The moving frame $(\tilde{x}_i)$ has to be linearly related to the fixed frame (x_i)

$$\tilde{x}_i = B_{ij} x_j,$$

where the tensor B_{ij} is derived imposing that the new coordinates moves with the mean flow

$$\frac{D\tilde{x}_i}{Dt} = \left(\frac{dB_{ij}}{dt} + B_{ik} S_{kj} \right) x_j = 0.$$

In this work we will only consider isotropic compression so that $B_{ij} = \delta_{ij} \mathcal{B}(t)$ and $S_{ij} = \delta_{ij} \mathcal{S}(t)$ With this simplification the previous equations reduce to

$$\frac{d\mathcal{B}(t)}{dt} - \mathcal{B}(t) \mathcal{S}(t) = 0.$$

so that we have the following relation

$$\mathcal{S}(t) = \frac{\dot{\mathcal{B}}(t)}{\mathcal{B}(t)}$$

Following other works on isotropic compression [Wu et al. 1985, Cambon et al. 1992], $\mathcal{B}(t)$ can be expressed as a function of a characteristic length R of the compressing domain :

$$\mathcal{B}(t) = \frac{R_0}{R(t)} = \frac{1}{\Lambda(t)}$$

where $R_0 = R(t = 0)$, so that we have the following

$$\mathcal{S}(t) = -\frac{\dot{\Lambda}(t)}{\Lambda(t)}.$$

Considering a particle moving with the base velocity U^B, its distance to the center decreases by a factor $\Lambda(t) = \exp\left(-\int_0^t \mathcal{S}(s) ds \right)$, referred to as the *compression parameter*. So that, finally, we have the following relations

$$\tilde{x}_i = \Lambda(t)^{-1} x_j \tag{A.1}$$

for the change of reference frame.

A.2 Rescaling

Once the reference frame change derived in section A.1 is applied to the inhomogeneous dynamical equations derived in section 2.1, they reduce to an expression without explicit space dependence

$$\partial_t u_i + \frac{1}{\Lambda} u_j \partial_j u_i - \mathcal{S}(t) u_i = -\Lambda^2 \partial_i p + \Lambda \frac{\mu}{\rho_0^B} \partial_{jj}^2 u_i. \tag{A.2}$$

At this point we have Navier-Stokes equation with a time dependent viscosity $\Lambda \frac{\mu}{\rho_0^B}$ and a forcing term $-\mathcal{S}(t)u_i$. We can further simplify Eq. (A.2) choosing to eliminate the forcing term or to eliminate the time dependence before the viscous term.

Since the space variable x_i is rescaled using the compression parameter Λ, we look for the rescaling of velocity u_i, time t and pressure p as a function of Λ :

$$\tilde{u} = \Lambda^{-a} u_i, \tag{A.3}$$

$$\tilde{p} = \Lambda^{-c} p, \tag{A.4}$$

$$d\tilde{t} = \Lambda^e dt. \tag{A.5}$$

When we use Eqs. (A.3), (A.4), (A.5) we obtain, for the time derivative in Eq. (A.2)

$$\partial_t u_i = \frac{\partial(\Lambda^a \tilde{u}_i)}{\partial t} = a\Lambda^{a-1}\dot{\Lambda}\tilde{u}_i + \frac{\partial \tilde{u}_i}{\partial t}\Lambda^a = a\Lambda^{a-1}\dot{\Lambda}\tilde{u}_i + \frac{\partial \tilde{u}_i}{\partial \tilde{t}}\Lambda^{(a+e)}, \tag{A.6}$$

where the time derivatives relation for $\tilde{u}_i$ is

$$\partial_t \tilde{u}_i = \frac{\partial \tilde{u}_i}{\partial \tilde{t}} \frac{d\tilde{t}}{dt} = \Lambda^e \frac{\partial \tilde{u}_i}{\partial \tilde{t}}. \tag{A.7}$$

The full expression of Eq. (A.2) using the rescalings for velocity, pressure and time is

$$a\Lambda^{a-1}\dot{\Lambda}\tilde{u}_i + \frac{\partial \tilde{u}_i}{\partial \tilde{t}}\Lambda^{a+e} + \Lambda^{2a-1}\tilde{u}_j\partial_j\tilde{u}_i + \Lambda^{a-1}\dot{\Lambda}\tilde{u}_i = -\Lambda^{2+c}\partial_i\hat{p} + \frac{\mu}{\rho_0^B}\Lambda^{a+1}\partial_{jj}^2\tilde{u}_i. \tag{A.8}$$

If we group together the forcing terms we have

$$\frac{\partial \tilde{u}_i}{\partial \tilde{t}}\Lambda^{a+e} + \Lambda^{2a-1}\tilde{u}_j\partial_j\tilde{u}_i + \Lambda^{a-1}\dot{\Lambda}\tilde{u}_i(a+1) = -\Lambda^{2+c}\partial_i\hat{p} + \frac{\mu}{\rho_0^B}\Lambda^{a+1}\partial_j^2\tilde{u}_i. \tag{A.9}$$

We want a Navier-Stokes-like equation so the time derivative and the convection term factors have to be equal,

$$\Lambda^{a+e} = \Lambda^{2a-1} \tag{A.10}$$

imposing the equality $e = a - 1$. We can then divide all the terms in Eq. (A.9) by Λ^{2a-1} obtaining :

$$\frac{\partial \tilde{u}_i}{\partial \tilde{t}} + \tilde{u}_j \partial_j \tilde{u}_i + \Lambda^{-a} \dot{\Lambda} \tilde{u}_i (a+1) = -\Lambda^{3+c-2a} \partial_i \hat{p} + \frac{\mu}{\rho_0^B} \Lambda^{2-a} \partial_{jj}^2 \tilde{u}_i, \tag{A.11}$$

and we eliminate the time dependence in front of the pressure taking $3 + c - 2a = 0$. This results in

$$\frac{\partial \tilde{u}_i}{\partial \tilde{t}} + \tilde{u}_j \partial_j \tilde{u}_i + \Lambda^{-a} \dot{\Lambda} \tilde{u}_i (a+1) = -\partial_i \hat{p} + \frac{\mu}{\rho_0^B} \Lambda^{2-a} \partial_{jj}^2 \tilde{u}_i. \tag{A.12}$$

Now we have two choices :

1. We can eliminate the forcing term imposing $a + 1 = 0$ obtaining

$$\tilde{u} = \Lambda u_i, \tag{A.13}$$

$$\tilde{p} = \Lambda^5 p, \tag{A.14}$$

$$d\tilde{t} = \Lambda^{-2} dt. \tag{A.15}$$

2. We can eliminate the time dependence in front of the viscous term imposing $2 - a = 0$

$$\tilde{u} = \Lambda^{-2} u_i, \tag{A.16}$$

$$\tilde{p} = \Lambda^{-1} p, \tag{A.17}$$

$$d\tilde{t} = \Lambda dt. \tag{A.18}$$

Annexe B

EDQNM models

B.1 EDQNM Model for isotropic turbulence

In this first section we derive a spectral equation based on an EDQNM closure for a case of homogeneous isotropic turbulence.

We start from the Navier-Stokes equations for an incompressible flow

$$\partial_t u_i + \partial_j u_i u_j = -\partial_i p + \nu \partial_{jj} u_i, \tag{B.1}$$

together with the continuity equation

$$\partial_i u_i = 0. \tag{B.2}$$

We apply the Fourier transform to B.1 to obtain its spectral counterpart

$$\partial_t \hat{u}_i + \mathrm{i}k_j \int_{\mathbb{R}^3} \hat{u}_i(\mathbf{p})\hat{u}_j(\mathbf{k}-\mathbf{p})d\mathbf{p} = -\mathrm{i}k_i\hat{p} - \nu k^2 \hat{u}_i. \tag{B.3}$$

while the incompressibility condition is simply expressed by

$$k_i u_i = 0. \tag{B.4}$$

The pressure can be eliminated from B.3, using the fact that the velocity field is solenoidal, resulting in

$$\partial_t \hat{u}_i(\mathbf{k}) + \nu k^2 \hat{u}_i(\mathbf{k}) = -\frac{\mathrm{i}}{2} P_{i\alpha\beta}(\mathbf{k}) \int_{\mathbb{R}^3} \hat{u}_\alpha(\mathbf{p})\hat{u}_\beta(\mathbf{k}-\mathbf{p})d\mathbf{p} \tag{B.5}$$

where $P_{i\alpha\beta}(\mathbf{k}) = k_\alpha P_{i\beta}(\mathbf{k}) + k_\beta P_{i\alpha}(\mathbf{k})$ is the Kraichnan projector, and $P_{ij}(\mathbf{k}) = \delta_{ij} - \frac{k_i k_j}{k^2}$.

B.1.1 Double correlation equation

The goal of a spectral model is to derive a closed equation for the two point correlation in spectral space. To this end we use equation (B.5) to derive an equation for the double correlation tensor R_{ij}.

$$\begin{aligned}(\partial_t + 2\nu k^2) R_{ij}(\mathbf{k}) &= -\frac{\mathrm{i}}{2} P_{i\alpha\beta}(\mathbf{k}) \int_{\mathbb{R}^3} S_{j\alpha\beta}(-\mathbf{k},\mathbf{p})d\mathbf{p} \\ &\quad + \frac{\mathrm{i}}{2} P_{j\alpha\beta}(\mathbf{k}) \int_{\mathbb{R}^3} S_{i\alpha\beta}(\mathbf{k},\mathbf{p})d\mathbf{p}.\end{aligned} \tag{B.6}$$

Where we observe how the double correlation R_{ij}, depends on the triple correlation S_{abc}. T

Equation (B.6) is simply obtained taking the product of (B.5) by $\hat{u}_j(\mathbf{k}')$ summed to the (B.5) rewritten for $\hat{u}_j(\mathbf{k}')$ and multiplied by $\hat{u}_i(\mathbf{k}')$, and using an the ensemble average operator $\langle * \rangle$.

The definition of the double R_{ij} and triple $S_{i\alpha\beta}$ correlation tensors are the following

$$\langle \hat{u}_i(\mathbf{k})\hat{u}_j(\mathbf{k}')\rangle = R_{ij}\delta(\mathbf{k}+\mathbf{k}'), \tag{B.7}$$

$$\langle \hat{u}_i(\mathbf{k})\hat{u}_\alpha(\mathbf{p})\hat{u}_\beta(\mathbf{k}'-\mathbf{p})\rangle = S_{i\alpha\beta}(\mathbf{k},\mathbf{p})\delta(\mathbf{k}+\mathbf{k}'), \tag{B.8}$$

$$\langle \hat{u}_j(\mathbf{k}')\hat{u}_\alpha(\mathbf{p})\hat{u}_\beta(\mathbf{k}-\mathbf{p})\rangle = S_{j\alpha\beta}(\mathbf{k}',\mathbf{p})\delta(\mathbf{k}+\mathbf{k}'). \tag{B.9}$$

B.1.2 Triple correlation equation

A similar method is used to derive an equation for the triple correlation tensor $S_{i\alpha\beta}$. If one follows with the computation one finds an equation for $S_{i\alpha\beta}$ that depends on quadruple correlation. Giving an example of the closure problem of turbulence, caused by the intrinsic nonlinear nature of the process .

One solution to close the system is to use a quasi normal hypothesis on the fourth order moment (quadruple correlation), meaning that they can be expressed as a sum of the products between second order moments

$$\begin{aligned}\langle g(x_1)g(x_2)g(x_3)g(x_4)\rangle &= \langle g(x_1)g(x_2)\rangle\langle g(x_3)g(x_4)\rangle \\ &\quad +\langle g(x_1)g(x_3)\rangle\langle g(x_2)g(x_4)\rangle + \langle g(x_1)g(x_4)\rangle\langle g(x_2)g(x_3)\rangle.\end{aligned}$$

This assumption together with some computation allows us to obtain a closed equation for the triple correlation tensor

$$\begin{aligned}(\partial_t + \nu(k^2+k'^2+(k+k')^2))S_{ijh}(\mathbf{k},\mathbf{k}') = &-\mathrm{i}P_{i\alpha\beta}(\mathbf{k})\left(R_{j\alpha}(\mathbf{k}')R_{h\beta}(-\mathbf{k}-\mathbf{k}')\right) \\ &-\mathrm{i}P_{j\alpha\beta}(\mathbf{k}')\left(R_{i\alpha}(\mathbf{k})R_{h\beta}(-\mathbf{k}-\mathbf{k}')\ \right) \\ &-\mathrm{i}P_{h\alpha\beta}(-\mathbf{k}-\mathbf{k}')\left(R_{i\alpha}(\mathbf{k})R_{j\beta}(\mathbf{k}')\right).\end{aligned} \tag{B.10}$$

This equation has a solution, which expresses S_{ijh} as a sum of second order tensors products :

$$S_{ijh}(\mathbf{k},\mathbf{k}') = -\mathrm{i}\int_0^t e^{-\nu(k^2+k'^2+(k+k')^2)(t-s)} \times \begin{pmatrix} P_{i\alpha\beta}(\mathbf{k})R_{j\alpha}(\mathbf{k}')R_{h\beta}(-\mathbf{k}-\mathbf{k}') \\ +P_{j\alpha\beta}(\mathbf{k}')R_{i\alpha}(\mathbf{k})R_{h\beta}(-\mathbf{k}-\mathbf{k}') \\ +P_{h\alpha\beta}(-\mathbf{k}-\mathbf{k}')R_{i\alpha}(\mathbf{k})R_{j\beta}(\mathbf{k}') \end{pmatrix} ds. \tag{B.11}$$

At this point we introduce the markovian hypotheses on the double correlation, we consider that R_{ij} values do not depend on their past, so that they can be taken out of the integral sign

$$S_{ijh}(\mathbf{k},\mathbf{k}') = -\mathrm{i}\begin{pmatrix} P_{i\alpha\beta}(\mathbf{k})R_{j\alpha}(\mathbf{k}')R_{h\beta}(-\mathbf{k}-\mathbf{k}') \\ +P_{j\alpha\beta}(\mathbf{k}')R_{i\alpha}(\mathbf{k})R_{h\beta}(-\mathbf{k}-\mathbf{k}') \\ +P_{h\alpha\beta}(-\mathbf{k}-\mathbf{k}')R_{i\alpha}(\mathbf{k})R_{j\beta}(\mathbf{k}') \end{pmatrix} \times \int_0^t e^{-\nu(k^2+k'^2+(k+k')^2)(t-s)}ds, \tag{B.12}$$

defining the quantity $\overline{\Theta}_{kpq} = \int_0^t e^{-\nu(k^2+k'^2+(k+k')^2)(t-s)}ds$ we can rewrite the expression of the third order correlation tensor

$$S_{ijh}(\mathbf{k},\mathbf{k}') = -\mathrm{i}\overline{\Theta}_{kpq}\begin{pmatrix} P_{i\alpha\beta}(\mathbf{k})R_{j\alpha}(\mathbf{k}')R_{h\beta}(-\mathbf{k}-\mathbf{k}') \\ +P_{j\alpha\beta}(\mathbf{k}')R_{i\alpha}(\mathbf{k})R_{h\beta}(-\mathbf{k}-\mathbf{k}') \\ +P_{h\alpha\beta}(-\mathbf{k}-\mathbf{k}')R_{i\alpha}(\mathbf{k})R_{j\beta}(\mathbf{k}') \end{pmatrix}. \tag{B.13}$$

B.1.3 Lin equation for $E(k)$

At this point we use the derived expression for S_{ijk} in the double correlation equation (B.6), obtaining

$$(\partial_t + 2\nu k^2)R_{ii}(\mathbf{k}) = \int_{\mathbb{R}^3} \overline{\Theta}_{kpq}P_{i\alpha\beta}(\mathbf{k})\begin{pmatrix} P_{ilm}(\mathbf{k})R_{l\alpha}(\mathbf{p})R_{m\beta}(\mathbf{q}) \\ +P_{\alpha lm}(\mathbf{p})R_{il}(\mathbf{k})R_{m\beta}(\mathbf{q}) \\ +P_{\beta lm}(\mathbf{q})R_{il}(\mathbf{k})R_{m\alpha}(\mathbf{p}) \end{pmatrix} d\mathbf{p} \tag{B.14}$$

where we have already imposed the case $i = j$, to consider only the trace of the tensor. However, Ogura (1963) shows that the quasi-normal approximation leads to nonphysical behaviour of the solution, in particular it can lead to negative energies. That is why Orszag (1977) proposes to add to equation (B.10), an eddy-damping term proportional to the third-order correlation tensor

$$\mu_{kpq}(t)S_{ijk} = (\mu_k + \mu_p + \mu_q)S_{ijk} \tag{B.15}$$

where the expression of μ_k is given by Pouquet et al. (1975)

$$\mu_k = a_0\sqrt{\int_0^k pE(p,t)dp} \tag{B.16}$$

where a_0 is a model constant. When we add this new term to equation (B.10) the term $\overline{\Theta}_{kpq}$ is modified and becomes

$$\Theta_{kpq} = \int_0^t e^{-(\mu_{kpq}+\nu(k^2+k'^2+(k+k')^2))(t-s)}ds$$

So that finally

$$(\partial_t + 2\nu k^2)R_{ii}(\mathbf{k}) = \int_{\mathbb{R}^3} \Theta_{kpq} P_{i\alpha\beta}(\mathbf{k}) \begin{pmatrix} P_{ilm}(\mathbf{k})R_{l\alpha}(\mathbf{p})R_{m\beta}(\mathbf{q}) \\ +P_{\alpha lm}(\mathbf{p})R_{il}(\mathbf{k})R_{m\beta}(\mathbf{q}) \\ +P_{\beta lm}(\mathbf{q})R_{il}(\mathbf{k})R_{m\alpha}(\mathbf{p}) \end{pmatrix} d\mathbf{p} \tag{B.17}$$

It can be shown that the integral in the wavenumber space is limited to the triads $\mathbf{k}+\mathbf{p}+\mathbf{q} = 0$. Here we introduce the isotropic spectrum $E(k)$ connected to the trace of the double correlation tensor via

$$R_{ii} = \frac{E(k)}{2\pi k^2} \tag{B.18}$$

After some algebra and geometric consideration on the triads $\mathbf{k}$,$\mathbf{p}$,$\mathbf{q}$ one finally obtains

$$(\partial_t + 2\nu k^2)E(k) = \int \Theta_{kpq} \frac{k}{pq} E(q) b(k,p,q) \left[k^2 E(p) - p^2 E(k)\right] dpdq \tag{B.19}$$

where b is geometric factor depending on the angles of the triad.

At this point if one defines the transfer term

$$T(k,t) = \int \Theta_{kpq} \frac{k}{pq} E(q) b(k,p,q) \left[k^2 E(p) - p^2 E(k)\right] dpdq \tag{B.20}$$

we obtain the following Lin equation

$$(\partial_t + 2\nu k^2)E(k) = T(k,t) \tag{B.21}$$

ANNEXE C

Spherical harmonics and Mollweide projection

C.1 Mollweide Projection

The Mollweide projection is an equal-area, pseudo-cylindrical map projection Snyder (1987). It has been previously used in other application for the projection of spherical results onto a plane such as the cosmic microwave background radiation Bennett et al. (2013).
The first step is to interpolate the field of interest on a sphere of given radius R, to get data as function of the polar angular coordinates (ψ,ϕ). The Mollweide projection establish a relation between these variables and the map coordinates X and Y. They represent respectively the equator and the central meridian.

$$X = R\frac{2\sqrt{2}}{\pi}\psi\cos\lambda \tag{C.1}$$

$$Y = R\sqrt{2}\sin\lambda \tag{C.2}$$

where λ is a parametric angle defined by

$$2\lambda + 2\sin\lambda = \pi\sin\phi \tag{C.3}$$

Equations (C.2), (C.3) have to be solved via an iterative Newton-Raphson method.

C.2 Spherical harmonics

We follow Lombardini et al. (2014b). Here we sum up the principal steps :

1. At time t we have a field in the Cartesian reference frame $f(x, y, z)$. We interpolate it on a sphere of radius R obtaining a $f(R, \theta, \phi)$.
2. Using a discrete spherical harmonics transform we obtain the values f_{lm}. The spherical harmonics are defined by

$$Y_{lm}(\theta,\phi) = \begin{cases} N_{(l,m)}P_l^m(\cos\theta)\cos(m\theta), & \text{if } m \geq 0 \\ N_{(l,|m|)}P_l^{|m|}(\cos\theta)\sin(|m|\theta), & \text{if } m < 0 \end{cases} \tag{C.4}$$

Where P_l^m are the associated Legendre polynomials. The continuous spherical harmonics transform is defined as

$$f_{lm} = \frac{1}{4\pi} \iint_{\Omega} f(R, \theta, \phi) Y_{lm}(\theta, \phi) \, d\Omega \tag{C.5}$$

3. The coefficient of the angular power spectrum can then be now computed

$$C_l = \frac{1}{2l+1} \sum_{m=-l}^{m=+l} |f_{lm}|^2 \tag{C.6}$$

Bibliographie

M. Abramowitz and I. Stegun. *Handbook of Mathematical Functions.* Dover Publications, 1965. (Cited on page 146.)

P. Amendt. Bell-Plesset effects for an accelerating interface with contiguous density gradients. *Physics of Plasmas*, 13(4) :042702, 2006. (Cited on page 35.)

M. J. Andrews and D. B. Spalding. A simple experiment to investigate two-dimensional mixing by Rayleigh-Taylor instability. *Physics of Fluids A : Fluid Dynamics*, 2(6) :922–927, 1990. doi : 10.1063/1.857652. (Cited on pages 67 and 137.)

P. Arnault. Modeling viscosity and diffusion of plasma for pure elements and multicomponent mixtures from weakly to strongly coupled regimes. *High Energy Density Physics*, 9(4) :711–721, 2013. (Cited on pages 122, 123, 142 and 150.)

S. Atzeni and J. Meyer-ter Vehn. *The Physics of inertial fusion.* 01 2004a. ISBN 978-0-19-85624-1. doi : 10.1093/acprof:oso/97801985626641.001.0001. (Cited on page 129.)

S. Atzeni and J. Meyer-ter Vehn. *The physics of inertial fusion : beam plasma interaction, hydrodynamics, hot dense matter*, volume 125. OUP Oxford, 2004b. (Cited on pages 12 and 13.)

A. Baglin. Rotation and mixing in the outer layers of a stars. turbulent mixing due to the meridional circulation velocity field. *Astron. & Astrophys*, 19 :45–50, 1972. (Cited on page 2.)

A. Banerjee and M. J. Andrews. 3d simulations to investigate initial condition effects on the growth of Rayleigh-Taylor mixing. *International Journal of Heat and Mass Transfer*, 52(17-18) :3906–3917, 2009. (Cited on page 9.)

G. K. Batchelor. The role of big eddies in homogeneous turbulence. *Proc. Roy. Soc. London. Series A, Math. & Phys. Sci.*, 195(1043) :513–532, 1949. ISSN 00804630. (Cited on pages 70 and 82.)

G. K. Batchelor. *The Theory of Homogeneous Turbulence.* Cambridge monographs on mechanics and applied mathematics. Cambridge University Press, 1953. ISBN 9780521041171. (Cited on pages 70, 82 and 83.)

G. K. Batchelor, V. M. Canuto, and J. R. Chasnov. Homogeneous buoyancy-generated turbulence. *J. Fluid Mech.*, 235 :349–378, 2 1992. ISSN 1469-7645. doi : 10.1017/S0022112092001149. (Cited on page 95.)

G. I. Bell. Taylor instability on cylinders and spheres in the small amplitude approximation. *Los Alamos Scientific Laboratory, Los Alamos, NM, Technical Report No. LA-1321*, 1951. (Cited on pages 11 and 35.)

C. L. Bennett, D. Larson, J. Weiland, N. Jarosik, G. Hinshaw, N. Odegard, K. Smith, R. Hill, B. Gold, M. Halpern, et al. Nine-year wilkinson microwave anisotropy probe (wmap) observations : final maps and results. *The Astrophysical Journal Supplement Series*, 208(2) :20, 2013. (Cited on page 165.)

R. Betti and O. A. Hurricane. Inertial-confinement fusion with lasers. *Nature Physics*, 12(5) :435, 2016. (Cited on pages 13 and 122.)

G. Blaisdell, G. Coleman, and N. Mansour. Rapid distortion theory for compressible homogeneous turbulence under isotropic mean strain. *Physics of Fluids*, 8(10) : 2692–2705, 1996. (Cited on page 28.)

G. A. Blaisdell. *Numerical simulation of compressible homogeneous turbulence.* PhD thesis, Stanford University, 1991. (Cited on page 28.)

G. Boffetta and A. Mazzino. Incompressible Rayleigh-Taylor turbulence. *Annual Review of Fluid Mechanics*, 49 :119–143, 2017. (Cited on pages 4, 6 and 20.)

S. I. Braginskii. *Rev. Plasma Phys.*, 1 :205, 1995. (Cited on pages 69, 71, 125 and 142.)

M. Brouillette. The Richtmyer-Meshkov instability. *Annual Review of Fluid Mechanics*, 34(1) :445–468, 2002. (Cited on pages 6 and 8.)

J. M. Budzinski, R. F. Benjamin, and J. W. Jacobs. Influence of initial conditions on the flow patterns of a shock-accelerated thin fluid layer. *Physics of Fluids*, 6 (11) :3510–3512, 1994. (Cited on page 9.)

A. Burlot. *Etude et modélisation de la turbulence homogène stratifiée instable.* PhD thesis, Ecully, Ecole centrale de Lyon, 2015. (Cited on page 10.)

A. Burlot, B.-J. Gréa, F. S. Godeferd, C. Cambon, and J. Griffond. Spectral modelling of high Reynolds number unstably stratified homogeneous turbulence. *J. Fluid Mech.*, 765 :17–44, 2015a. (Cited on pages 31 and 96.)

A. Burlot, B.-J. Gréa, F. S. Godeferd, C. Cambon, and O. Soulard. Large Reynolds number self-similar states of unstably stratified homogeneous turbulence. *Physics of Fluids*, 27(6) :065114, 2015b. doi : http://dx.doi.org/10.1063/1.4922817. (Cited on page 71.)

W. H. Cabot and A. W. Cook. Reynolds number effects on Rayleigh-Taylor instability with possible implications for type Ia supernovae. *Nat. Phys.*, 2(8) :562–568, Aug. 2006. ISSN 1745-2473. (Cited on pages 6 and 14.)

C. Cambon, Y. Mao, and D. Jeandel. On the application of time dependent scaling to the modelling of turbulence undergoing compression. *Eur. J. Mech. B-Fluids.*, 11 :683–703, May 1992. (Cited on pages 28, 30 and 157.)

C. Cambon, G. N. Coleman, and N. N. Mansour. Rapid distortion analysis and direct simulation of compressible homogeneous turbulence at finite Mach number. *Journal of Fluid Mechanics*, 257 :641–665, 1993. doi : 10.1017/S0022112093003258. (Cited on page 82.)

I. H. Campbell and J. S. Turner. Turbulent mixing between fluids with different viscosities. *Nature*, 313(5997) :39, 1985. (Cited on page 18.)

A. Campos and B. E. Morgan. Self-consistent feedback mechanism for the sudden viscous dissipation of finite-Mach-number compressing turbulence. *Physical Review E*, 99(1) :013107, 2019. (Cited on page 70.)

C. Canuto, M. Y. Hussaini, A. Quarteroni, and A. Thomas Jr. *Spectral methods in fluid dynamics.* Springer Science & Business Media, 2012. (Cited on pages 44 and 46.)

V. P. Carey and J. C. Mollendorf. Variable viscosity effects in several natural convection flows. *International Journal of Heat and Mass Transfer*, 23(1) :95–109, 1980. (Cited on page 18.)

S. Chandrasekhar. The character of the equilibrium of an incompressible fluid sphere of variable density and viscosity subject to radial acceleration. *The Quarterly Journal of Mechanics and Applied Mathematics*, 8(1) :1–21, 1955. (Cited on pages 11 and 35.)

S. Chandrasekhar. *Hydrodynamic and Hydromagnetic Stability.* The International Series of Monographs on Physics. Dover Publ., 1961. ISBN 9780486640716. (Cited on pages 4 and 11.)

J. J. Charonko and K. Prestridge. Variable-density mixing in turbulent jets with coflow. *Journal of Fluid Mechanics*, 825 :887–921, 2017. (Cited on page 22.)

M. Chertkov, V. Lebedev, and N. Vladimirova. Reactive Rayleigh-Taylor turbulence. *Journal of Fluid Mechanics*, 633 :1–16, 2009. (Cited on page 11.)

A. J. Chorin. Numerical solution of the Navier-Stokes equations. *Mathematics of computation*, 22(104) :745–762, 1968. (Cited on page 49.)

U. Christensen and H. Harder. 3-d convection with variable viscosity. *Geophysical Journal International*, 104(1) :213–226, 1991. (Cited on page 18.)

D. S. Clark, M. M. Marinak, C. R. Weber, D. C. Eder, S. W. Haan, B. A. Hammel, D. E. Hinkel, O. S. Jones, J. L. Milovich, P. K. Patel, H. F. Robey, J. D. Salmonson, S. M. Sepke, and C. A. Thomas. Radiation hydrodynamics modeling of the highest compression inertial confinement fusion ignition experiment from the national ignition campaign. *Physics of Plasmas*, 22(2) :022703, 2015. doi : 10.1063/1.4906897. (Cited on pages 16 and 70.)

D. S. Clark, C. Weber, J. L. Milovich, J. D. Salmonson, A. L. Kritcher, S. W. Haan, B. A. Hammel, D. E. Hinkel, O. A. Hurricane, and O. S. Jones. Three-dimensional simulations of low foot and high foot implosion experiments on the national ignition facility. *Physics of Plasmas*, 23(5) :056302, 2016. (Cited on page 16.)

G. N. Coleman and N. N. Mansour. Simulation and modeling of homogeneous compressible turbulence under isotropic mean compression. In *Turbulent Shear Flows 8*, pages 269–282. Springer, 1993. (Cited on page 28.)

J. W. Cooley and J. W. Tukey. An algorithm for the machine calculation of complex Fourier series. *Mathematics of Computation*, 19(90) :297–301, 1965. (Cited on page 46.)

L. Danaila, L. Voivenel, and E. Varea. Self-similarity criteria in anisotropic flows with viscosity stratification. *Physics of Fluids*, 29(2) :020716, 2017. (Cited on page 19.)

P. Danckwerts. The definition and measurement of some characteristics of mixtures. *Applied Scientific Research, Section A*, 3(4) :279–296, 1952. (Cited on page 141.)

S. Davidovits and N. J. Fisch. Sudden viscous dissipation of compressing turbulence. *Phys. Rev. Lett.*, 116 :105004, Mar 2016a. doi : 10.1103/PhysRevLett.116.105004. (Cited on pages 28, 30, 69, 72, 75, 76, 78, 79, 83, 93, 122, 136 and 150.)

S. Davidovits and N. J. Fisch. Compressing turbulence and sudden viscous dissipation with compression-dependent ionization state. *Physical Review E*, 94(5) :053206, 2016b. (Cited on page 70.)

P. A. Davidson. *Turbulence : an introduction for scientists and engineers*. Oxford University Press, 2015. (Cited on pages 97 and 98.)

B. Di Pierro. *Etude de l'évolution spatio-temporelle d'un jet tournant tridimensionnel à masse volumique variable*. PhD thesis, Aix-Marseille, 2012. (Cited on page 51.)

B. Di Pierro. On a preconditionment for the spectral solution of incompressible variable density flows. 2017. (Cited on pages 50, 51, 54 and 101.)

B. Di Pierro and M. Abid. A projection method for the spectral solution of non-homogeneous and incompressible navier–stokes equations. *International Journal for Numerical Methods in Fluids*, 71(8) :1029–1054, 2013. (Cited on page 51.)

G. Dimonte, D. Youngs, A. Dimits, S. Weber, M. Marinak, S. Wunsch, C. Garasi, A. Robinson, M. Andrews, P. Ramaprabhu, et al. A comparative study of the turbulent rayleigh–taylor instability using high-resolution three-dimensional numerical simulations : the alpha-group collaboration. *Physics of Fluids*, 16(5) : 1668–1693, 2004. (Cited on page 5.)

P. E. Dimotakis. Turbulent mixing. *Annu. Rev. Fluid Mech.*, 37 :329–356, 2005. (Cited on page 2.)

P. Durbin and O. Zeman. Rapid distortion theory for homogeneous compressed turbulence with application to modelling. *Journal of Fluid Mechanics*, 242 :349–370, 1992. (Cited on page 28.)

T. Ebisuzaki, T. Shigeyama, and K. Nomoto. Rayleigh-Taylor instability and mixing in sn 1987a. *The Astrophysical Journal*, 344 :L65–L68, 1989. (Cited on page 10.)

C. Eckart. An analysis of the stirring and mixing processes in compressible fluids. *J Mar Res*, 7(3) :265–275, 1948. (Cited on page 1.)

L. Erwin. Theory of laminar mixing. *Polymer Engineering & Science*, 18(13) :1044–1048, 1978. (Cited on page 2.)

M. Faraday. On the forms and states of fluids on vibrating elastic surfaces. *Phil. Trans. R. Soc. Lond.*, 121 :319–340, 1831. (Cited on page 3.)

H. J. S. Fernando. Turbulent mixing in stratified fluids. *Annual review of fluid mechanics*, 23(1) :455–493, 1991. (Cited on page 3.)

J. H. Ferziger and M. Peric. *Computational methods for fluid dynamics.* Springer Science & Business Media, 2012. (Cited on page 54.)

M. Frigo and S. G. Johnson. The design and implementation of fftw3. *Proceedings of the IEEE*, 93(2) :216–231, 2005. (Cited on page 46.)

M. Gauding, L. Danaila, and E. Varea. One-point and two-point statistics of homogeneous isotropic decaying turbulence with variable viscosity. *International Journal of Heat and Fluid Flow*, 72 :143–150, 2018. (Cited on page 19.)

W. K. George. The decay of homogeneous isotropic turbulence. *Physics of Fluids A : Fluid Dynamics*, 4(7) :1492–1509, 1992. doi : 10.1063/1.858423. (Cited on page 70.)

S. Gerashchenko and K. Prestridge. Density and velocity statistics in variable density turbulent mixing. *Journal of Turbulence*, 16(11) :1011–1035, 2015. (Cited on page 22.)

M. Gittings, R. Weaver, M. Clover, T. Betlach, N. Byrne, R. Coker, E. Dendy, R. Hueckstaedt, K. New, and W. R. Oakes. The RAGE radiation-hydrodynamic code. *Computational Science & Discovery*, 1(1) :015005, 2008. (Cited on page 14.)

S. Gottlieb, C.-W. Shu, and E. Tadmor. Strong stability-preserving high-order time discretization methods. *SIAM review*, 43(1) :89–112, 2001. (Cited on page 48.)

R. Govindarajan and K. C. Sahu. Instabilities in viscosity-stratified flow. *Annual Review of Fluid Mechanics*, 46(1) :331–353, 2014. doi : 10.1146/annurev-fluid-010313-141351. (Cited on page 18.)

B.-J. Gréa. The rapid acceleration model and the growth rate of a turbulent mixing zone induced by Rayleigh-Taylor instability. *Phys. Fluids*, 25(1) :015118, 2013. doi : 10.1063/1.4775379. (Cited on pages 9, 67 and 137.)

B.-J. Gréa and A. E. Adou. What is the final size of turbulent mixing zones driven by the faraday instability ? *Journal of Fluid Mechanics*, 837 :293–319, 2018. (Cited on page 3.)

B.-J. Gréa, J. Griffond, and A. Burlot. The effects of variable viscosity on the decay of homogeneous isotropic turbulence. *Phys. Fluids*, 26(3) :035104, 2014. doi : http://dx.doi.org/10.1063/1.4867893. (Cited on pages 19, 53 and 59.)

B.-J. Gréa, A. Burlot, , J. Griffond, and A. Llor. Challenging mix models on transients to self-similarity of unstably stratified homogeneous turbulence. *ASME. J. Fluids Eng.*, 138 :070904–070904, 2016a. (Cited on page 12.)

B.-J. Gréa, A. Burlot, F. Godeferd, O. Soulard, J. Griffond, and C. Cambon. Dynamics and structure of unstably stratified homogeneous turbulence. *Journal of Turbulence*, 17 :651–663, 2016b. (Cited on pages 9 and 31.)

J. Griffond, B.-J. Gréa, and S. O. Unstably stratified homogeneous turbulence as a tool for turbulent mixing modeling. *J. Fluids Eng.*, 136 :091201, 2014. (Cited on pages 31, 58 and 96.)

J. Griffond, B.-J. Gréa, and O. Soulard. Numerical investigation of self-similar unstably stratified homogeneous turbulence. *J. Turb.*, 16(2) :167–183, 2015a. doi : 10.1080/14685248.2014.979351. (Cited on page 31.)

J. Griffond, B.-J. Gréa, and O. Soulard. Numerical investigation of self-similar unstably stratified homogeneous turbulence. *Journal of Turbulence*, 16(2) :167–183, 2015b. (Cited on page 102.)

F. F. Grinstein, L. G. Margolin, and W. J. Rider. *Implicit large eddy simulation : computing turbulent fluid dynamics*. Cambridge university press, 2007. (Cited on page 102.)

H. Groemer. *Geometric applications of Fourier series and spherical harmonics*, volume 61. Cambridge University Press, 1996. (Cited on page 146.)

B. M. Haines, F. F. Grinstein, and J. R. Fincke. Three-dimensional simulation strategy to determine the effects of turbulent mixing on inertial-confinement-fusion capsule performance. *Physical Review E*, 89(5) :053302, 2014a. (Cited on page 2.)

B. M. Haines, E. L. Vold, K. Molvig, C. Aldrich, and R. Rauenzahn. The effects of plasma diffusion and viscosity on turbulent instability growth. *Physics of Plasmas*, 21(9) :092306, 2014b. (Cited on pages 20 and 122.)

B. M. Haines, G. P. Grim, J. R. Fincke, R. C. Shah, C. J. Forrest, K. Silverstein, F. J. Marshall, M. Boswell, M. M. Fowler, R. A. Gore, et al. Detailed high-resolution three-dimensional simulations of omega separated reactants inertial confinement fusion experiments. *Physics of Plasmas*, 23(7) :072709, 2016. (Cited on page 122.)

P. E. Hamlington and M. Ihme. Modeling of non-equilibrium homogeneous turbulence in rapidly compressed flows. *Flow, turbulence and combustion*, 93(1) :93–124, 2014. (Cited on pages 27 and 28.)

B. A. Hammel, S. W. Haan, D. S. Clark, M. J. Edwards, S. H. Langer, M. M. Marinak, M. V. Patel, J. D. Salmonson, and H. A. Scott. High-mode Rayleigh-Taylor growth in nif ignition capsules. *High energy density physics*, 6(2) :171–178, 2010. (Cited on page 122.)

N. M. Hoffman, G. B. Zimmerman, K. Molvig, H. G. Rinderknecht, M. J. Rosenberg, B. J. Albright, A. N. Simakov, H. Sio, A. B. Zylstra, and M. Gatu Johnson. Approximate models for the ion-kinetic regime in inertial-confinement-fusion capsule implosions. *Physics of Plasmas*, 22(5) :052707, 2015. (Cited on page 14.)

J. C. R. Hunt and D. J. Carruthers. Rapid distortion theory and the problems of turbulence. *J. Fluid Mech.*, 212 :497–532, 2 1990. ISSN 1469-7645. doi : 10.1017/S0022112090002075. (Cited on page 27.)

H. E. Huppert and J. S. Turner. Double-diffusive convection. *Journal of Fluid Mechanics*, 106 :299–329, 1981. (Cited on page 3.)

I. V. Igumenshchev, A. B. Zylstra, C. K. Li, P. M. Nilson, V. N. Goncharov, and R. D. Petrasso. Self-generated magnetic fields in direct-drive implosion experiments. *Physics of Plasmas*, 21(6) :062707, 2014. (Cited on page 15.)

C. Jause-Labert. *Simulation numérique d'écoulements turbulents en rotation, confinement et forçage à l'aide d'une méthode de pénalisation.* PhD thesis, Ecully, Ecole centrale de Lyon, 2012. (Cited on page 68.)

D. D. Joseph and Y. Y. Renardy. Fluid dynamics of two miscible liquids with diffusion and gradient stresses. In *Fundamentals of Two-Fluid Dynamics*, pages 324–395. Springer, 1993. (Cited on page 21.)

D. D. Joseph, R. Bai, K. P. Chen, and Y. Y. Renardy. Core-annular flows. *Annual Review of Fluid Mechanics*, 29(1) :65–90, 1997. (Cited on page 18.)

D. S. K. Reddy and K. Sinha. Hypersonic turbulent flow simulation of fire ii reentry vehicle afterbody. *Journal of Spacecraft and Rockets*, 46(4) :745–757, 2009. (Cited on page 18.)

G. Kagan and X.-Z. Tang. Thermo-diffusion in inertially confined plasmas. *Physics Letters A*, 378(21) :1531 – 1535, 2014. ISSN 0375-9601. doi : https://doi.org/10.1016/j.physleta.2014.04.005. (Cited on page 142.)

H. J. Kull. Theory of the Rayleigh-Taylor instability. *Physics Reports*, 206(5) : 197 – 325, 1991. ISSN 0370-1573. doi : http://dx.doi.org/10.1016/0370-1573(91)90153-D. (Cited on page 4.)

C. C. K. Lai, J. J. Charonko, and K. Prestridge. A Kármán–Howarth–Monin equation for variable-density turbulence. *Journal of Fluid Mechanics*, 843 :382–418, 2018. (Cited on page 22.)

K. G. Lamb. Internal wave breaking and dissipation mechanisms on the continental slope/shelf. *Annual Review of Fluid Mechanics*, 46 :231–254, 2014. (Cited on page 4.)

G. C. Layek, S. Mukhopadhyay, and R. S. R. Gorla. Unsteady viscous flow with variable viscosity in a vascular tube with an overlapping constriction. *International journal of engineering science*, 47(5-6) :649–659, 2009. (Cited on page 18.)

K. Lee, S. S. Girimaji, and J. Kerimo. Validity of Taylor' s dissipation-viscosity independence postulate in variable-viscosity turbulent fluid mixtures. *Physical review letters*, 101(7) :074501, 2008. (Cited on page 19.)

M. Lesieur. *Turbulence in Fluids*. Fluid Mechanics and Its Applications Series. Springer, 2008. ISBN 9781402064357. (Cited on pages 70 and 82.)

M. Lesieur and S. Ossia. 3D isotropic turbulence at very high Reynolds numbers : EDQNM study. *J. Turb.*, 1 :1–25, 2000. doi : 10.1088/1468-5248/1/1/007. (Cited on pages 70, 73 and 82.)

J. M. Lighthill. *Waves in fluids*. Cambridge university press, 2001. (Cited on page 3.)

H. Lin, B. D. Storey, and A. J. Szeri. Rayleigh-Taylor instability of violently collapsing bubbles. *Physics of Fluids*, 14(8) :2925–2928, 2002. (Cited on page 36.)

J. Lindl. Development of the indirect-drive approach to inertial confinement fusion and the target physics basis for ignition and gain. *Physics of Plasmas*, 2(11) : 3933–4024, 1995. (Cited on page 13.)

D. Livescu. Compressibility effects on the Rayleigh-Taylor instability growth between immiscible fluids. *Physics of fluids*, 16(1) :118–127, 2004. (Cited on page 5.)

D. Livescu and J. R. Ristorcelli. Buoyancy-driven variable-density turbulence. *J. Fluid Mech.*, 591 :43–71, 11 2007. ISSN 1469-7645. doi : 10.1017/S0022112007008270. (Cited on pages 22, 23, 32, 96 and 119.)

D. Livescu and J. R. Ristorcelli. Variable-density mixing in buoyancy-driven turbulence. *Journal of Fluid Mechanics*, 605 :145–180, 2008. (Cited on pages 22, 23, 96 and 112.)

D. Livescu, J. Ristorcelli, R. Gore, S. Dean, W. Cabot, and A. Cook. High-reynolds number Rayleigh-Taylor turbulence. *Journal of Turbulence*, (10) :N13, 2009. (Cited on page 9.)

D. Livescu, J. R. Ristorcelli, M. R. Petersen, and R. A. Gore. New phenomena in variable-density rayleigh–taylor turbulence. *Physica Scripta*, 2010(T142) :014015, 2010. (Cited on page 22.)

M. Lombardini, D. I. Pullin, and D. I. Meiron. Transition to turbulence in shock-driven mixing : a mach number study. *Journal of Fluid Mechanics*, 690 :203–226, 2012. (Cited on page 10.)

M. Lombardini, D. I. Pullin, and D. I. Meiron. Turbulent mixing driven by spherical implosions. Part 1. Flow description and mixing-layer growth. *Journal of Fluid Mechanics*, 748 :85–112, 2014a. (Cited on page 36.)

M. Lombardini, D. I. Pullin, and D. I. Meiron. Turbulent mixing driven by spherical implosions. Part 2. Turbulence statistics. *Journal of Fluid Mechanics*, 748 :113–142, 2014b. (Cited on pages 146, 147 and 165.)

T. Ma, P. K. Patel, N. Izumi, P. T. Springer, M. H. Key, L. J. Atherton, M. A. Barrios, L. R. Benedetti, R. Bionta, and E. Bond. The role of hot spot mix in the low-foot and high-foot implosions on the NIF. *Physics of Plasmas*, 24(5) :056311, 2017. (Cited on page 122.)

A. G. MacPhee, D. T. Casey, D. S. Clark, S. Felker, J. E. Field, S. W. Haan, B. A. Hammel, J. Kroll, O. L. Landen, and D. A. Martinez. X-ray shadow imprint of hydrodynamic instabilities on the surface of inertial confinement fusion capsules by the fuel fill tube. *Physical Review E*, 95(3) :031204, 2017. (Cited on page 122.)

O. D. Makinde, W. A. Khan, and J. R. Culham. Mhd variable viscosity reacting flow over a convectively heated plate in a porous medium with thermophoresis and radiative heat transfer. *International Journal of Heat and Mass Transfer*, 93 : 595–604, 2016. (Cited on page 18.)

M. M. Marinak, G. D. Kerbel, N. A. Gentile, O. Jones, D. Munro, S. Pollaine, T. R. Dittrich, and S. W. Haan. Three-dimensional hydra simulations of national ignition facility targets. *Physics of Plasmas*, 8(5) :2275–2280, 2001. (Cited on pages 14 and 16.)

M. M. Marinak, G. D. Kerbel, J. M. Koning, M. V. Patel, S. M. Sepke, M. S. McKinley, M. J. O'Brien, R. J. Procassini, and D. Munro. Advances in hydra and its applications to simulations of inertial confinement fusion targets. In *EPJ Web of Conferences*, volume 59, page 06001. EDP Sciences, 2013. (Cited on page 14.)

A. Mashayek, H. Salehipour, D. Bouffard, C. P. Caulfield, R. Ferrari, M. Nikurashin, W. R. Peltier, and W. D. Smyth. Efficiency of turbulent mixing in the abyssal ocean circulation. *Geophysical Research Letters*, 44(12) :6296–6306, 2017. (Cited on page 2.)

J. Mathew, H. Foysi, and R. Friedrich. A new approach to LES based on explicit filtering. *International journal of heat and fluid flow*, 27(4) :594–602, 2006. (Cited on pages 101 and 102.)

M. Meldi and P. Sagaut. On non-self-similar regimes in homogeneous isotropic turbulence decay. *J. Fluid Mech.*, 711 :364–393, 10 2012. ISSN 1469-7645. doi : 10.1017/jfm.2012.396. (Cited on page 70.)

E. E. Meshkov. Instability of the interface of two gases accelerated by a shock wave. *Fluid Dynamics*, 4(5) :101–104, 1969. (Cited on page 6.)

K. O. Mikaelian. Rayleigh-Taylor and Richtmyer-Meshkov instabilities and mixing in stratified spherical shells. *Physical Review A*, 42(6) :3400, 1990. (Cited on page 35.)

K. O. Mikaelian. Effect of viscosity on Rayleigh-Taylor and Richtmyer-Meshkov instabilities. *Physical Review E*, 47(1) :375, 1993. (Cited on page 6.)

P. L. Miller, W. H. Cabot, and A. W. Cook. Which way is up ? A fluid dynamics riddle. *Physics of Fluids*, 17(9) :091110, 2005. (Cited on pages 20 and 21.)

K. Molvig, N. M. Hoffman, B. J. Albright, E. M. Nelson, and R. B. Webster. Knudsen layer reduction of fusion reactivity. *Physical review letters*, 109(9) :095001, 2012. (Cited on page 15.)

K. Molvig, A. N. Simakov, and E. L. Vold. Classical transport equations for burning gas-metal plasmas. *Physics of Plasmas*, 21(9) :092709, 2014. doi : 10.1063/1.4895666. (Cited on page 142.)

A. S. Monin and A. M. Obukhov. Basic laws of turbulent mixing in the surface layer of the atmosphere. *Contrib. Geophys. Inst. Acad. Sci. USSR*, 151(163) :e187, 1954. (Cited on page 2.)

V. Mons, J.-C. Chassaing, T. Gomez, and P. Sagaut. Is isotropic turbulence decay governed by asymptotic behavior of large scales ? An eddy-damped quasi-normal Markovian-based data assimilation study. *Physics of Fluids*, 26(11) :115105, 2014. doi : 10.1063/1.4901448. (Cited on page 70.)

N. M. Nachtigal, S. C. Reddy, and L. N. Trefethen. How fast are nonsymmetric matrix iterations ? *SIAM Journal on Matrix Analysis and Applications*, 13(3) : 778–795, 1992. (Cited on page 51.)

A. W. Nienow, M. F. Edwards, and N. Harnby. *Mixing in the process industries.* Butterworth-Heinemann, 1997. (Cited on page 2.)

T. Oggian, D. Drikakis, D. L. Youngs, and R. J. R. Williams. Computing multi-mode shock-induced compressible turbulent mixing at late times. *Journal of Fluid Mechanics*, 779 :411–431, 2015. (Cited on page 9.)

Y. Ogura. A consequence of the zero-fourth-cumulant approximation in the decay of isotropic turbulence. *J. Fluid Mech.*, 16 :33–40, 5 1963. ISSN 1469-7645. doi : 10.1017/S0022112063000562. (Cited on page 163.)

G. Orlicz, S. Balasubramanian, and K. Prestridge. Incident shock mach number effects on richtmyer-meshkov mixing in a heavy gas layer. *Physics of Fluids*, 25 (11) :114101, 2013. (Cited on page 7.)

S. A. Orszag. Lectures on the statistical theory of turbulence. In *Les Houches Summer School 1973*, pages 273–374, 1977. (Cited on pages 70, 73 and 163.)

S. A. Orszag and G. S. Patterson. Numerical simulation of three-dimensional homogeneous isotropic turbulence. *Phys. Rev. Lett.*, 28 :76–79, Jan 1972. doi : 10.1103/PhysRevLett.28.76. (Cited on page 46.)

J. M. Ottino. Mixing, Chaotic Advection, and Turbulence. *Annual Review of Fluid Mechanics*, 22(1) :207–254, 1990. doi : 10.1146/annurev.fl.22.010190.001231. (Cited on page 2.)

J. M. Ottino and R. Chella. Laminar mixing of polymeric liquids ; a brief review and recent theoretical developments. *Polymer Engineering & Science*, 23(7) :357–379, 1983. (Cited on page 2.)

A. Pantokratoras. Study of mhd boundary layer flow over a heated stretching sheet with variable viscosity : a numerical reinvestigation. *International Journal of Heat and Mass Transfer*, 51(1-2) :104–110, 2008. (Cited on page 18.)

B. Parent, J. P. Sislian, and J. Schumacher. Numerical investigation of the turbulent mixing performance of a cantilevered ramp injector. *AIAA journal*, 40(8) :1559–1566, 2002. (Cited on page 2.)

D. Pekurovsky. P3dfft : A framework for parallel computations of Fourier transforms in three dimensions. *SIAM Journal on Scientific Computing*, 34(4) :C192–C209, 2012. (Cited on page 47.)

A. Piel. *Plasma physics : an introduction to laboratory, space, and fusion plasmas.* Springer, 2017. (Cited on pages 123 and 124.)

R. W. Pitz and J. W. Daily. Combustion in a turbulent mixing layer formed at a rearward-facing step. *AIAA journal*, 21(11) :1565–1570, 1983. (Cited on page 2.)

M. Plesset. On the stability of fluid flows with spherical symmetry. *Journal of Applied Physics*, 25(1) :96–98, 1954. (Cited on pages 11 and 35.)

K. L. Polzin, J. M. Toole, J. R. Ledwell, and R. W. Schmitt. Spatial variability of turbulent mixing in the abyssal ocean. *Science*, 276(5309) :93–96, 1997. (Cited on page 2.)

S. B. Pope. *Turbulent Flows.* Cambridge University Press, 2000. ISBN 9780521598866. (Cited on page 101.)

O. Poujade and M. Peybernes. Growth rate of Rayleigh-Taylor turbulent mixing layers with the foliation approach. *Phys. Rev. E*, 81 :016316 (8 pages), Jan 2010. doi : 10.1103/PhysRevE.81.016316. (Cited on page 97.)

A. Pouquet, M. Lesieur, J. C. André, and C. Basdevant. Evolution of high Reynolds number two-dimensional turbulence. *J. Fluid Mech.*, 72 :305–319, 11 1975. ISSN 1469-7645. doi : 10.1017/S0022112075003369. (Cited on page 163.)

K. Prestridge. Experimental adventures in variable-density mixing. *Physical Review Fluids*, 3(11) :110501, 2018. (Cited on pages 22 and 23.)

A. Prosperetti. Viscous effects on perturbed spherical flows. *Quarterly of Applied Mathematics*, 34(4) :339–352, 1977. (Cited on page 36.)

P. Ramaprabhu, G. Dimonte, and M. J. Andrews. A numerical study of the influence of initial perturbations on the turbulent Rayleigh-Taylor instability. *Journal of Fluid Mechanics*, 536 :285–319, 2005. (Cited on pages 8 and 9.)

P. Ramaprabhu, V. Karkhanis, and A. G. W. Lawrie. The rayleigh-taylor instability driven by an accel-decel-accel profile. *Physics of Fluids*, 25(11) :115104, 2013. (Cited on page 10.)

P. Rao, C. P. Caulfield, and J. D. Gibbon. Nonlinear effects in buoyancy-driven variable-density turbulence. *Journal of Fluid Mechanics*, 810 :362–377, 2017. (Cited on pages 22, 113 and 119.)

J. W. S. Rayleigh. Investigation of the character of the equilibrium of an incompressible heavy fluid of variable density. *Proceedings of the London Mathematical Society*, s1-14(1) :170–177, 1882. doi : 10.1112/plms/s1-14.1.170. (Cited on page 4.)

R. D. Reitz. Use of detailed chemical kinetics to study hcci engine combustion with consideration of turbulent mixing effects. *J. Eng. Gas Turbines Power*, 124(3) : 702–707, 2002. (Cited on page 2.)

R. D. Richtmyer. Taylor instability in shock acceleration of compressible fluids. *Communications on Pure and Applied Mathematics*, 13(2) :297–319, 1960. (Cited on page 6.)

H. G. Rinderknecht, H. Sio, C. K. Li, A. B. Zylstra, M. J. Rosenberg, P. Amendt, J. Delettrez, C. Bellei, J. A. Frenje, M. Gatu Johnson, F. H. Séguin, R. D. Petrasso, R. Betti, V. Y. Glebov, D. D. Meyerhofer, T. C. Sangster, C. Stoeckl, O. Landen, V. A. Smalyuk, S. Wilks, A. Greenwood, and A. Nikroo. First observations of nonhydrodynamic mix at the fuel-shell interface in shock-driven inertial confinement implosions. *Phys. Rev. Lett.*, 112 :135001, Apr 2014a. doi : 10.1103/PhysRevLett.112.135001. (Cited on pages 122 and 150.)

H. G. Rinderknecht, H. Sio, C. K. Li, A. B. Zylstra, M. J. Rosenberg, P. Amendt, J. Delettrez, C. Bellei, J. A. Frenje, and M. G. Johnson. First observations of nonhydrodynamic mix at the fuel-shell interface in shock-driven inertial confinement implosions. *Physical review letters*, 112(13) :135001, 2014b. (Cited on page 15.)

R. S. Rogallo. Numerical experiments in homogeneous turbulence. Technical Report 81315, NASA, 1981. Memo. (Cited on pages 28, 30 and 157.)

Y. Saad and M. H. Schultz. Gmres : A generalized minimal residual algorithm for solving nonsymmetric linear systems. *SIAM Journal on scientific and statistical computing*, 7(3) :856–869, 1986. (Cited on page 51.)

P. Sagaut and C. Cambon. *Homogeneous Turbulence Dynamics*. Cambridge University Press, 2008. ISBN 9780521855488. (Cited on pages 28, 73, 74 and 82.)

H. Sakagami and K. Nishihara. Three-dimensional Rayleigh-Taylor instability of spherical systems. *Physical Review Letters*, 65(4) :432, 1990. (Cited on page 36.)

D. L. Sandoval. *The dynamics of variable-density turbulence.* PhD thesis, University of Washington, 1995. (Cited on pages 20, 31, 32, 64 and 96.)

M. M. Scase, K. A. Baldwin, and R. J. A. Hill. Rotating rayleigh-taylor instability. *Physical Review Fluids*, 2(2) :024801, 2017. (Cited on page 11.)

D. H. Sharp. Overview of Rayleigh-Taylor instability. Technical report, Los Alamos National Lab., NM (USA), 1983. (Cited on page 4.)

J. D. Slavin, J. M. Shull, and M. C. Begelman. Turbulent mixing layers in the interstellar medium of galaxies. *The Astrophysical Journal*, 407 :83–99, 1993. (Cited on page 2.)

J. P. Snyder. *Map projections–A working manual*, volume 1395. US Government Printing Office, 1987. (Cited on page 165.)

O. Soulard, J. Griffond, and B.-J. Gréa. Large-scale analysis of self-similar unstably stratified homogeneous turbulence. *Phys. Fluids*, 26(015110) :32 pages, 2014. (Cited on pages 71, 96 and 97.)

O. Soulard, J. Griffond, and B.-J. Gréa. Large-scale analysis of unconfined self-similar Rayleigh-Taylor turbulence. *Physics of Fluids*, 27(9) :095103, 2015. doi : http://dx.doi.org/10.1063/1.4930003. (Cited on pages 9 and 71.)

O. Soulard, F. Guillois, J. Griffond, V. Sabelnikov, and S. Simoëns. Permanence of large eddies in Richtmyer-Meshkov turbulence with a small Atwood number. *Physical Review Fluids*, 3(10) :104603, 2018. (Cited on pages 9 and 10.)

O. Soulard, J. Griffond, B.-J. Gréa, and G. Viciconte. Permanence of large eddies in variable-density homogeneous turbulence. *arXiv preprint arXiv :1904.06061*, 2019. (Cited on pages 97, 99, 118, 119 and 153.)

J. Stoer and R. Bulirsch. *Introduction to numerical analysis*, volume 12. Springer Science & Business Media, 2013. (Cited on pages 52 and 53.)

R. Tailleux. On the energetics of stratified turbulent mixing, irreversible thermodynamics, boussinesq models and the ocean heat engine controversy. *Journal of Fluid Mechanics*, 638 :339–382, 2009. (Cited on page 1.)

B. Talbot. *Mélange et dynamique de la turbulence en écoulements libres à viscosité variable.* PhD thesis, Rouen, INSA, 2009. (Cited on pages 18 and 19.)

G. I. Taylor. The instability of liquid surfaces when accelerated in a direction perpendicular to their planes. I. *Proceedings of the Royal Society of London. Series A, Mathematical and Physical Sciences*, 201(1065) :pp. 192–196, 1950. ISSN 00804630. URL `http://www.jstor.org/stable/98398`. (Cited on page 4.)

H. Tennekes and J. L. Lumley. *A first course in turbulence.* MIT press, 1972. (Cited on page 3.)

B. Thornber, D. Drikakis, D. Youngs, and R. Williams. The influence of initial conditions on turbulent mixing due to Richtmyer-Meshkov instability. *Journal of Fluid Mechanics*, 654 :99–139, 2010. (Cited on pages 9 and 10.)

B. Thornber, J. Griffond, O. Poujade, N. Attal, H. Varshochi, P. Bigdelou, P. Ramaprabhu, B. Olson, J. Greenough, Y. Zhou, et al. Late-time growth rate, mixing, and anisotropy in the multimode narrowband richtmyer–meshkov instability : The θ-group collaboration. *Physics of Fluids*, 29(10) :105107, 2017. (Cited on page 8.)

B. J. R. Thornber and D. Drikakis. Numerical dissipation of upwind schemes in low mach flow. *International Journal for Numerical Methods in Fluids*, 56(8) : 1535–1541, 2008. doi : 10.1002/fld.1628. (Cited on page 132.)

S. T. Thoroddsen, C. W. Van Atta, and J. S. Yampolsky. Experiments on homogeneous turbulence in an unstably stratified fluid. *Phys. Fluids*, 10(12) :3155–3167, 1998. doi : http://dx.doi.org/10.1063/1.869842. (Cited on page 96.)

C. Ticknor, J. D. Kress, L. A. Collins, J. Clérouin, P. Arnault, and A. Decoster. Transport properties of an asymmetric mixture in the dense plasma regime. *Physical Review E*, 93(6) :063208, 2016. (Cited on pages 69, 122, 124, 125, 142 and 150.)

J. S. Turner and I. H. Campbell. Convection and mixing in magma chambers. *Earth-Science Reviews*, 23(4) :255–352, 1986. (Cited on page 18.)

G. Viciconte, B.-J. Gréa, and F. S. Godeferd. Self-similar regimes of turbulence in weakly coupled plasmas under compression. *Physical Review E*, 97(2) :023201, 2018. (Cited on pages 30 and 137.)

N. Vladimirova and M. Chertkov. Self-similarity and universality in rayleigh–taylor, boussinesq turbulence. *Phys. Fluids*, 21(1) :015102, 2009. doi : http://dx.doi.org/10.1063/1.3054152. (Cited on page 96.)

L. Voivenel, E. Varea, L. Danaila, B. Renou, and M. Cazalens. Variable viscosity jets : Entrainment and mixing process. In *Whither Turbulence and Big Data in the 21st Century ?*, pages 147–162. Springer, 2017. (Cited on pages 19 and 20.)

E. L. Vold, A. S. Joglekar, M. I. Ortega, R. Moll, D. Fenn, and K. Molvig. Plasma viscosity with mass transport in spherical inertial confinement fusion implosion simulations. *Physics of Plasmas*, 22(11) :112708, 2015. doi : 10.1063/1.4935906. (Cited on pages 14, 36 and 122.)

C. Walsh, J. Chittenden, K. McGlinchey, N. Niasse, and B. Appelbe. Self-generated magnetic fields in the stagnation phase of indirect-drive implosions on the national ignition facility. *Physical Review Letters*, 118(15) :155001, 2017. (Cited on page 15.)

C. R. Weber, D. S. Clark, A. W. Cook, L. E. Busby, and H. F. Robey. Inhibition of turbulence in inertial-confinement-fusion hot spots by viscous dissipation. *Phys. Rev. E*, 89 :053106, May 2014a. doi : 10.1103/PhysRevE.89.053106. (Cited on pages 16, 20, 88, 93 and 122.)

C. R. Weber, N. S. Haehn, J. G. Oakley, D. A. Rothamer, and R. Bonazza. An experimental investigation of the turbulent mixing transition in the Richtmyer-Meshkov instability. *Journal of Fluid Mechanics*, 748 :457–487, 2014b. (Cited on page 10.)

C. R. Weber, D. T. Casey, D. S. Clark, B. A. Hammel, A. MacPhee, J. Milovich, D. Martinez, H. F. Robey, V. A. Smalyuk, and M. Stadermann. Improving ICF implosion performance with alternative capsule supports. *Physics of Plasmas*, 24 (5) :056302, 2017. (Cited on pages 16 and 122.)

A. J. White, L. A. Collins, J. D. Kress, C. Ticknor, J. Clérouin, P. Arnault, and N. Desbiens. Correlation and transport properties for mixtures at constant pressure and temperature. *Phys. Rev. E*, 95 :063202, Jun 2017. doi : 10.1103/PhysRevE.95.063202. (Cited on pages 142 and 150.)

J. P. Wilkinson and J. W. Jacobs. Experimental study of the single-mode three-dimensional Rayleigh-Taylor instability. *Physics of fluids*, 19(12) :124102, 2007. (Cited on page 5.)

C.-T. Wu, J. H. Ferziger, and D. R. Chapman. Simulation and modeling of homogeneous, compressed turbulence. Technical report, Stanford University ; Dept. of Mechanical Engineering. ; CA, United States, 1985. (Cited on pages 28 and 157.)

D. Youngs. Three-dimensional numerical simulation of turbulent mixing by Rayleigh-Taylor instability. *Physics of Fluids A : Fluid Dynamics*, 3(5) :1312–1320, 1991. (Cited on page 140.)

D. Youngs. Application of MILES to Rayleigh-Taylor and Richtmyer-Meshkov mixing. In *16th AIAA Computational Fluid Dynamics Conference*, page 4102, 2003. (Cited on page 9.)

D. L. Youngs. Numerical simulation of turbulent mixing by Rayleigh-Taylor instability. *Physica D : Nonlinear Phenomena*, 12(1-3) :32–44, 1984. ISSN 0167-2789. doi : http://dx.doi.org/10.1016/0167-2789(84)90512-8. (Cited on pages 5 and 9.)

D. L. Youngs. The density ratio dependence of self-similar Rayleigh-Taylor mixing. *Philosophical Transactions of the Royal Society A : Mathematical, Physical and Engineering Sciences*, 371(2003) :20120173, 2013. (Cited on pages 8 and 9.)

D. L. Youngs and R. J. R. Williams. Turbulent mixing in spherical implosions. *International Journal for Numerical Methods in Fluids*, 56(8) :1597–1603, 2008. (Cited on page 36.)

Y. Zhou. Rayleigh-Taylor and Richtmyer-Meshkov instability induced flow, turbulence, and mixing. I. *Physics Reports*, 720 :1–136, 2017a. (Cited on pages 4, 6, 8, 9, 10, 11 and 95.)

Y. Zhou. Rayleigh-Taylor and Richtmyer-Meshkov instability induced flow, turbulence, and mixing. II. *Physics Reports*, 723 :1–160, 2017b. (Cited on page 11.)

A. Zylstra, N. Hoffman, H. Herrmann, M. Schmitt, Y. Kim, K. Meaney, A. Leatherland, S. Gales, C. Forrest, V. Y. Glebov, et al. Diffusion-dominated mixing in moderate convergence implosions. *Physical Review E*, 97(6) :061201, 2018. (Cited on pages 122 and 150.)